ENERGY STORAGE MATERIALS: NEW TRANSITION METAL OXIDES, OXY-FLUORIDES AND PHOSPHATES

Ph.D. THESIS

by

NISHANT GAUTAM

DEPARTMENT OF CHEMISTRY
INDIAN INSTITUTE OF TECHNOLOGY ROORKEE
ROORKEE 247 667, (INDIA)
JULY, 2018

ENERGY STORAGE MATERIALS: NEW TRANSITION METAL OXIDES, OXY-FLUORIDES AND PHOSPHATES

A THESIS

Submitted in partial fulfilment of the requirements for the award of the degree

of

DOCTOR OF PHILOSOPHY

in

CHEMISTRY

by

NISHANT GAUTAM

DEPARTMENT OF CHEMISTRY
INDIAN INSTITUTE OF TECHNOLOGY ROORKEE
ROORKEE 247 667, (INDIA)
JULY, 2018

INDAIN INSTITUTE OF TECHNOLOGY ROORKEE ROORKEE

CANDIDATE'S DECLARATION

I hereby certify that the work which is being presented in the thesis entitled "**ENERGY STORAGE MATERIALS: NEW TRANSITION METAL OXIDES, OXY-FLUORIDES AND PHOSPHATES**" in partial fulfilment of the requirements for the award of the degree of Doctor of Philosophy and submitted in the Department of Chemistry of the Indian Institute of Technology Roorkee, Roorkee is an authentic record of my own work carried out during a period of January, 2013 to July, 2018 under the supervision of Dr. Tapas Kumar Mandal, Assistant Professor, Department of Chemistry, Indian Institute of Technology Roorkee, Roorkee.

The matter presented in the thesis has not been submitted by me for the award of any other degree of this or any other Institution.

(**NISHANT GAUTAM**)

This is to certify that the above statement made by the candidate is correct to the best of my knowledge.

(Tapas Kumar Mandal)
Supervisor

The Ph.D. Viva-Voce examination of **Mr. Nishant Gautam**, Research Scholar, has been held on **…….**

Chairman, SRC **Signature of External Examiner**

This is to certify that the student has made all the corrections in the thesis.

Signature of Supervisor (s) **Head of the Department**

Dated:

CONTENTS

ABSTRACT

Energy demands are increasing day by day due to rapid industrial and technological growth of developing nations along with a staggering growth of the world population. Considering the receding levels of fossil fuels, if the energy load is met mostly by fossil based fuels the world might have to see catastrophic consequences in addition to augmented adverse effects of global warming and climate change. Thus, increased use of clean and green energy with minimal environmental impact is a major challenge in the 21st century. To curtail the global warming and reduce our reliance on fossil fuel based energies, energy generation from renewable sources is imperative. But, the source and magnitude of renewable energy are intermittent in nature and variable in time; it varies during the span of a day or part of a year. Therefore, the electrical energy generated from such renewable sources needs to be stored using a suitable energy storage technology. While electromagnetic waves, electricity grid and chemical energy are among the major energy carriers, chemical energy storage in batteries is one of the most convenient forms of energy storage. Lithium-ion battery (LIB) technology has been proven to be one of the well-established technologies for energy storage. Moreover, lithium being the lightest metal in the periodic table, LIB offers highest energy densities among all other rechargeable battery technologies. Owing to the easy handling and portability, LIBs are used as power sources in portable electronics (e.g., cell phones and laptops), medical implants (e.g., pumps, pacemakers), power tools, defense, transportation and aerospace applications. Despite continuous efforts of the scientific community to improve lithium ion battery technology over the last four decades, current battery systems are still far behind to replace internal combustion engines in fully electric powered vehicles, because to compete with the driving distance per full gasoline tank for vehicles with internal combustion engines, nearly 5-fold increments in the energy density of the current batteries is necessary.

A great deal of research effort has been devoted during the last two decades to develop high capacity and high energy density batteries, but the electrode materials essentially remained the same as far the LIB technology is concerned. Various strategies and methodologies are being adopted by several research groups across the globe to improve the different components of LIBs. A large body of research exists mostly involving the study of oxides and phosphates with various structural families such as, rock-salt, spinel, olivine etc. Among the different series of compounds,

much attention has been paid to the transition metal oxides with the layered rock-salt and spinel structures and phosphates with the olivine type structure. For example, $LiCoO_2$, $LiNiO_2$, $LiNi_{0.5}Mn_{0.5}O_2$, $LiMnO_2$ and $LiNi_{1-x-y}Co_xMn_yO_2$ constitute the major class of materials that are largely being investigated as cathodes in Li-ion batteries. Similarly, in the spinel family, $LiMn_2O_4$ and $LiNi_{0.5}Mn_{1.5}O_4$ are the main candidates that have attracted attention as cathodes. The olivine type phosphates, on the other hand, comprising $LiFePO_4$, $LiMnPO_4$, $LiCoPO_4$ and $LiNiPO_4$, are also being investigated as cathode materials. In spite of vast studies and exploration of cathode materials, $LiCoO_2$ still remained the workhorse for the LIB technology. In addition, $LiNi_{0.8}Co_{0.15}Al_{0.05}O_2$, $LiNi_{1/3}Mn_{1/3}Co_{1/3}O_2$, $LiMn_2O_4$ or $LiFePO_4$ are also being used in conventional LIBs. But, a number of problems exist with most of them pertaining to issues, such as, high cost, toxicity, phase/structural transition, capacity fading due to electrolyte instability and transition metal dissolution (when cycled at higher potential, e. g., for $LiCoO_2$ above 4.2 V), to mention a few. Recently, $LiNi_{1-x-y}Co_xMn_yO_2$ (NCM), a layered oxide with rock-salt structure, has been considered as a viable cathode material for electrification of transport due to its high capacity and good rate capability, but, low thermal stability, Li/Ni mixing and high reactive surface are the main issues that limits its cathode performance.

With respect to anodes of LIBs only limited class of materials, such as, graphite and various forms of carbon, TiO_2 based oxides, $Li_4Ti_5O_{12}$ and Li_3VO_4, which are mostly of insertion/de-insertion types, are being investigated. While graphite is a low cost, high capacity and long life anode material, used in most of the commercialized Li-ion batteries, but slow Li-ion diffusion, structural collapse during cycling and dendritic Li-growth at low operating voltages limit its use in high power density applications. Low theoretical capacity, poor electrical conductivity and poor ionic diffusion are the main obstacles for TiO_2 based anodes in LIBs. Although, titanium based $Li_4Ti_5O_{12}$ has emerged as a feasible anode material for low power battery applications due to its high structural stability, minimum volume change upon insertion/de-insertion of Li-ions and flat voltage plateau, but low theoretical capacity (175 mAh g^{-1}) and low electronic conductivity prevents its use in high capacity battery applications. Recently, Li_3VO_4 has been considered as a promising anode material as a replacement to graphite in commercial LIB due to its high theoretical capacity (394 mAh g^{-1}) and suitable working potential. But, low ionic and electronic conductivities of Li_3VO_4 are the main drawbacks that essentially results in poor electrochemical

performance and prevents its commercial use. Research efforts are underway to alleviate the problems of poor electrical and ionic conductivity of Li_3VO_4. In the backdrop of contemporary issues with the present day cathode and anode materials of LIBs, **Chapter-1** gives a brief overview of them along with the working principle of LIBs and various active electrode materials.

Chapter-2 describes the synthetic methodologies and the details of all the characterization techniques used in the present study. The compounds were synthesized by solid state reaction, sol-gel or hydrothermal method employing high purity simple metal carbonates / oxalates / oxides, alkali hydroxides, alkali fluorides, metal nitrates, phosphates, pyrophosphates and citric acid or ethane glycol as complexing agents / solvents. The progress of reactions and formation of final products were monitored by powder X-ray diffraction (P-XRD) and the morphological and compositional characterizations were carried out by Field Emission-Scanning Electron Microscopy (FE-SEM), Transmission-Electron Microcopy (TEM) and Energy Dispersive X-ray Spectroscopy (EDS) analysis. The thermal stability of the compounds and the amount of carbon in the as synthesized compounds were evaluated using Thermo-gravimetric (TG) analysis. X-Ray Photoelectron Spectroscopy (XPS) was used to ascertain the oxidation states of the redox active metals in the compounds. The charge transfer resistance (R_{ct}) was estimated using Electrochemical Impedance Spectroscopy (EIS) data. Finally, Cyclic Voltammetry (CV) and Galvanostatic charge-discharge analysis were carried out in fabricated Teflon half-cells to evaluate the electrochemical performance of the materials presented here.

In **Chapter-3**, we report the synthesis and characterization of a nickel, cobalt, manganese (NCM) based rock-salt layered oxy-fluoride, $Li_{1.25}Ni_{0.25}Co_{0.25}Mn_{0.25}O_{1.5}F_{0.5}$. The compound is synthesized using solid state reaction. P-XRD pattern simulation and Rietveld refinement studies confirm the ordered rock-salt structure of the oxy-fluoride without Li/Ni cation disorder in the Li-only layer. While the anodic and cathodic peaks at 3.95 and 3.72 V, respectively, in the CV trace ascertain the intercalation/de-intercalation of Li-ions into/out of the lattice, the charge-discharge curves show the intercalation/de-intercalation potential at a slightly higher voltage (~ 3.91 V) than its oxide analogs. The observed higher working voltage is attributed to the incorporation of fluoride ions into the oxide lattice. A high charge capacity of 216 mAh g^{-1} and a discharge capacity of 148 mAh g^{-1} at 0.1 C for the first cycle are observed for $Li_{1.25}Ni_{0.25}Co_{0.25}Mn_{0.25}O_{1.5}F_{0.5}$. A high charge-discharge capacity is obtained at slow cycling rate, but substantial capacity fading is observed

when the cell is cycled at higher cycling rates. The present work is significant due to the fact that it demonstrates a large amount of fluoride doping in the oxide lattice of the Li-rich oxy-fluoride maintaining a completely ordered structure and avoiding any likely consequences of Li/Ni disorder in the Li-only layer.

Chapter-4 deals with synthesis, characterization and electrochemical properties of $Na_3Fe(PO_4)_2$, a layered phosphate based cathode material for Li-ion batteries. In search for new cathodes involving intercalation-deintercalation of multiple Li-ions, $Na_3Fe(PO_4)_2$ was identified as an interesting compound. The compound is prepared as phase pure by a sol-gel method within 24 h reaction time, which is much faster than that of the solid state method reported earlier (reaction time > 7 days). The phase purity, microstructure and composition of the synthesized compound are ascertained by P-XRD, FE-SEM and EDX studies, respectively. The presence of an anodic peak at 3.04 V in the CV trace suggests $Na_3Fe(PO_4)_2$ as potential cathode material for Li-ion batteries. The charge-discharge studies carried out between 1.5 – 4.0 V at different C rates (C/50, C/20, C/10 and C/5) confirm the electrochemically active nature as cathode material for Li-ion batteries, although the compound showed much reduced capacity than the theoretical (85 mAh g^{-1}). But, the excellent capacity retention at C/20 up to 100 charge-discharge cycles is noteworthy suggesting its structural robustness during electrochemical insertion-extraction of Li.

Chapter-5 describes the synthesis, characterization and electrochemical properties of nut-shaped hierarchical mesoporous Li_3VO_4 (HM-Li_3VO_4). A rapid template free hydrothermal method is developed for the synthesis of HM-Li_3VO_4. P-XRD analysis confirm the formation of single-phase Li_3VO_4 with an orthorhombic structure having lattice parameters, 6.3189(3), 5.4454(2) and 4.9468(2) Å. SEM images show formation of nut-shaped morphology that are hollow from inside and essentially composed of nano particles of Li_3VO_4 with sizes ranging from 50-100 nm. Combined HR-TEM and BET surface area analysis establish hierarchical mesoporous nature for the as prepared Li_3VO_4. The electrochemical charge-discharge studies employing a lithium metal half-cell with the bare HM-Li_3VO_4 as active anode show a discharge capacity of 615 mAh g^{-1} and a charge capacity of 384 mAh g^{-1} at 0.1 C rate for the first cycle. The discharge capacity of 332 mAh g^{-1} observed at the 2nd cycle for HM-Li_3VO_4 is superior to those reported in the literature for other Li_3VO_4 in its bare form. The improved anode performance of nut-shaped HM-Li_3VO_4 is attributed to the hierarchical mesoporous microstructure which facilitates faster Li^+

diffusion through the mesoporous channels and accommodates Li^+ ions within mesopores during intercalation-deintercalation process. However, capacity fade at higher rates are evident in the HM-Li_3VO_4 due to its poor electrical conductivity.

In an effort to improve both the ionic and electrical conductivity of Li_3VO_4, a simple, short and cheaper template free one-pot solvothermal method is developed to synthesize mesoporous Li_3VO_4 (M-Li_3VO_4) on graphene oxide (GO). Here again, growth of nut-shaped Li_3VO_4 on GO with nut sizes ranging from 2 μm to sub-micrometer levels with a multimodal mesopore distribution are confirmed by FE-SEM, TEM and BET surface area studies. HR-TEM analysis confirm the growth of Li_3VO_4 on GO. The presence of graphene oxide (GO) is further ascertained by D and G band features in the Raman spectra, in addition to crystalline Li_3VO_4 due to the bands at 785 and 818 cm^{-1}. The EIS data clearly indicate enhanced electrical conductivity of Li_3VO_4-GO as compared to HM-Li_3VO_4. The electrochemical charge-discharge studies employing a lithium metal half-cell with Li_3VO_4-GO as active anode material show a discharge capacity of 814 mAh g^{-1} and a charge capacity of 559 mAh g^{-1} at 0.1 C rate when cycled in the potential range 0.2 – 3V for the first cycle. Moreover, a capacity of 414 mAh g^{-1} after the second discharge at 0.5 C is achieved in the same potential range. A discharge capacity of 374 mAh g^{-1}, which is achieved at the fifth cycle at 0.5 C rate, is comparable or superior to those reported in the literature for other Li_3VO_4 samples with similar carbon contents. The enhanced anode performance with more than double reversible capacity at 0.5 C rate for M-Li_3VO_4-GO as compared to that of bare HM-Li_3VO_4 is due to superior ionic and electronic conductivity of the material. The results of these investigations are discussed in **Chapter-6**.

Chapter-7 presents the overall conclusions and future prospects of our current investigation. The present work gives valuable insights in finding new layered rock-salt based oxy-fluorides and phosphates with alkali metal rich compositions. This will have tremendous potential for the development of next generation high capacity, high energy density and high rate capable electrodes for Li/Na-ion batteries.

ACKNOWLEDGEMENTS

First and foremost I want to thank my supervisor Dr. Tapas Kumar Mandal for his guidance and all the useful discussions and brainstorming sessions, especially during the initial development stage in designing research problems. The entire work research carried out during the course of my Ph.D. was not possible without his innovative guidance and support. He has always made himself available to clarify my doubts despite of his busy schedules. He has provided solution to all the problems which I faced during the entire course with a clear visualization. It is because of his guidance and exceptional scientific knowledge, I am able to design and work on a research problem in the right direction. His enthusiasm and honesty towards work will always be motivational for me in my whole life. I consider it as a great opportunity to do my doctoral programme under his guidance. He has helped me a lot in my difficult times over the course of the analysis and the writing of the thesis and for that I sincerely thank him for his confidence in me.

I am highly obliged and express my sincere thanks to Prof. M. R. Maurya, Head of the Department of Chemistry and all other faculty members for their kindness and help. I am extremely indebted to the members of my SRC, Prof. P. Jeevanandam (Chairman), Dr. H. C. Kandpal (Internal member), Department of Chemistry and Dr. Tulika Maitra (External member), Department of Physics, IIT Roorkee for their valuable suggestions and encouragement to carry out this work.

I am highly indebted to Prof. Anjan Sil and Prof. Amitava Choudhury for allowing to carry out electrochemical measurements of my samples. I would like thank to Hari raj and Prashanth Sandineni for helping me in the electrochemical measurements.

I am extremely thankful to Head, Institute Instrumentation Centre (IIC) for providing all the necessary instrumental facilities. I greatly appreciate Mr. Shiv Kumar for his help during the FE-SEM measurements. I am also thankful to Mr. Shiv Kumar and Devender Sharma, in-charge of XRD and Mr. Mukesh, in-charge of TEM. I express my heartfelt thanks to Mr. Madan Pal, Department of Chemistry, who helped me a lot for the technical arrangements during my presentations in the department.

I would like to express my sincere thanks to Ministry of Human Resource Development, Government of India for providing me fellowship.

I would like to thank to all my lab colleague for their support and crating healthy environment in the lab. I want to thank Dr. Naresh for his kind nature and valuable discussion in the early days. Thank you Lalit for helping me a lot in thesis writing and structural refinement. Thanks to Sonia Rani, Vandana Meena, Vijay, Jaideep Malik and Shubham for the good time spent with you. Your hard work will hand you a better future with high accomplishment. All the best to you. I thank rest of the lab members Anupam, Kamini, Rita, Anowar, Ambikeshwar, Avnish, Poonam and Vishal for their support.

I would like to thank my friends Amarkant, Manoj (Monu), Amit, Anuj, Ankur, Ankur, Manoj, Vivak Sharma, Ravi, Avnish Malik, Mohit Choudhary, Ajay Panchal, Bhawna Rao, Manju Singh, Ashish Sharma and Himanshu Sharma for their moral support and motivation. I want to thank my friends at IIT Roorkee (during my M. Tech.) Bhanu Pratap Gangwar, Ashutosh Sukla, Umesh Sharma, Sandeep, Astha, Archita, Anuradha, Richa and Anju for the joyful time I spent with them.

Finally, I would like to pay homage to my parents, my father and mother, and my family members. Thank you very much for your support, care and endless love. Today, my father is not with me but the lesson he taught me will always be with be in my entire life. I want to thank my grandmother for her care and giving valuable suggestions at every stage of life. I want to thank my paternal and maternal grandfather and grandmothers and all elder of my family for their support and encouragement. I want to thank my sister and her husband for showing faith in me and prayers she did for the betterment of my life. I want to thank my all younger brothers and sisters for giving so much of joy to my life.

I owe thanks to my wife, Soniya, for making my life simple and joyful. Her care and understanding during tough time of Ph.D. made possible to achieve this goal easily. I appreciate my little superstar, Mitthu, for making me laugh every time whenever I was tensed.

(Nishant Gautam)

List of Figures

List of Tables

List of Publications/Patents:

1. **Nishant Gautam**, Paritosh Mohanty, Anjan Sil and Tapas Kumar Mandal*, *Indian Patent filed*, Application No. 201711038135 (**2017**).

2. **Nishant Gautam** and Tapas Kumar Mandal*, *Indian Patent filed* (PPA), Application No. 201811022066 (**2018**).

3. **Nishant Gautam**, Raeesh Muhammad, Hari Raj, Anjan Sil and Tapas Kumar Mandal, Hierarchical Mesoporosity in Li_3VO_4: Way to Superior Anode Performance in Li-Ion Batteries (**Submitted to ACS Energy Materials**).

4. **Nishant Gautam**, Prashanth Sandineni, Amitava Choudhury, and Tapas Kumar Mandal, A New Synthetic Route for $Na_3Fe(PO_4)_2$ Layered Phosphate: A Potential Cathode Material for Sodium and Lithium ion Batteries (To be submitted).

5. **Nishant Gautam,** Anjan Sil and Tapas Kumar Mandal Rock Salt Ordered Lithium-rich NCM Type Oxy-fluoride as High Voltage Cathode Material for Lithium-Ion Batteries (manuscripts under preparation)

List of Conference Proceedings/Presentations:

1. **Nishant Gautam**, Hariraj, Anjan Sil and Tapas Kumar Mandal, New Compositions in the Olivine Type $LiMnPO_4$: Potential Cathode Materials for High Voltage Li-ion Battery, CRSI-2016, Institute of Nano Science and Technology and Punjab University, Chandigarh, India, February 5th -7th, **2016.**

2. **Nishant Gautam**, Prashanth Sandineni, Amitava Choudhury, and Tapas Kumar Mandal, A New Synthetic Route for $Na_3Fe(PO_4)_2$ Layered Phosphate: A Potential Cathode Material for Sodium and Lithium ion Batteries, MMAD 2018, *National Institute of Technology, Kurukshetra, India*, January 20, **2018**.

CHAPTER – 1

Introduction

CHAPTER – 2

Characterization Techniques

CHAPTER – 3

Rock Salt Ordered Lithium-Rich NCM Type Oxy-Fluoride as High Voltage Cathode Material for Lithium-Ion Batteries

CHAPTER – 4

A New Synthetic Route for $Na_3Fe(PO_4)_2$ Layered Phosphate: A Potential Cathode Material for Lithium-Ion Batteries

CHAPTER – 5

Nut-Shaped Li_3VO_4 with Hierarchical Mesopores: A New Anode Material for High Capacity Li-Ion Batteries

CHAPTER – 6

One-Pot Synthesis of Mesoporous Li_3VO_4 on GO: A Viable Anode Material for Li-Ion Batteries

CHAPTER – 7

Conclusions and Future Prospects

References

1.1 Introduction

Energy demands are increasing day by day due to rapid industrial and technological growth of developing nations along with a staggering growth of the world population. The use of clean and green energy with minimal environmental impact is a major challenge in the 21st century [1]. Since last 250 years, the global energy demand was fulfilled by the exploitation of fossil fuels. The main reason of our dependency on fossil fuels for energy requirements was its easy availability, convenience of use and lower cost. Conversely, the use of fossil fuels emits vast amount of CO_2 which are responsible for global warming. Hydroelectric, nuclear, solar, wind and other renewable forms of energy are among the major contributors as alternatives to fossil fuel based energy. Despite being a source of clean energy, hydro-electric power have some restrictions such as, it requires storage of water in dams in confined areas and thus supply is mainly restricted over a limited area. On the other hand, the main challenge of nuclear energy is nuclear waste which will be radioactive for thousands of years. On the contrary, renewable energy sources such as, solar, wind and tidal offer clean energies with minimal impact on the environment [2]. The depletion of fossil fuel reserves together with adverse environmental effects have leads to the increased use of renewable forms of energy in order to reduce the greenhouse gas emissions as well as to reduce the dependency on fossil fuels [3]. The source and magnitude of renewable energy are intermittent in nature and variable in time; it varies during the span of a day or part of a year. Therefore, the use of renewable energy in the form of electricity requires a suitable energy storage technology. While electromagnetic waves, electricity grid and chemical energy are among the major energy carriers, chemical energy storage in batteries is one of the most convenient form of storage.

The two key types of batteries are primary (disposable) and secondary (rechargeable) batteries. The main conventional rechargeable battery technologies, such as nickel-cadmium, lead-acid and nickel-metal hydride batteries have limitations because of their size and weight. Moreover, the electrolyte used in these batteries put a restriction on the operational voltage up to1.5 V, therefore, restricting the development of high capacity batteries [4].

The advantages of rechargeable batteries are many. Once the chemical energy is stored, the battery can be used anywhere and anytime of the day. Among the various existing rechargeable battery technologies (Fig. 1.1), Li-ion batteries outperform other systems because of their high energy density and design flexibility, dominating the portable market nearly 63% of sales worldwide [5]. Lithium being the lightest metal in the periodic table, it offers highest energy densities in Li-ion batteries. Owing to the easy handling and portability of electrical energy, Li-ion batteries could be used as a power sources in different areas, such as portable electronics (e.g., cell phones and laptops), medical implants (e.g., pumps, pacemakers), power tools, defense, transportation and aerospace applications [6, 7].

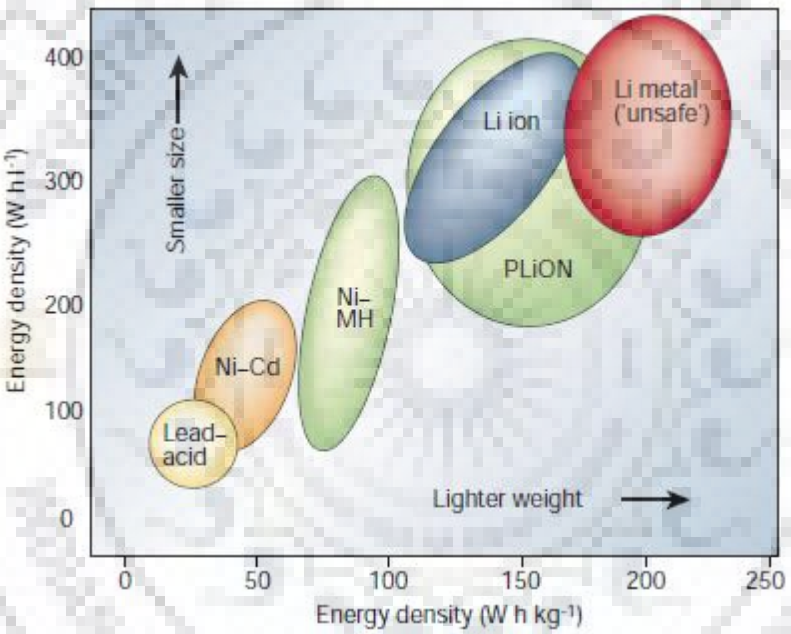

Figure 1.1 Volumetric and gravimetric energy density comparison of different battery technologies [5].

1.2 Working Principal of Li-ion Battery:

A battery is made up of one or more electrochemical cells connected in parallel or series. The main constituents of an electrochemical cell are anode, cathode and electrolyte. Anode and cathode are separated by the electrolyte which is electrically insulating.

In the charge process, an external voltage is required to shuttle out the lithium ion from the positive electrode (cathode) which pass through the electrolyte and gets intercalated

into the negative electrode (anode) with the movement of electron through an external circuit (one electron per Li^+) from cathode to anode side. The electrolyte used in Li-ion batteries would be electrically insulating while the diffusion of ions are allowed. However, due to insulating nature of the electrolyte, the electrons are forced to pass through an external circuit. During the charge process, the transition metal ion present in the cathode gets oxidized releasing a lithium ion that moves towards the negative electrode (generally graphite) through a Li-ion conducting electrolyte medium and gets intercalated into the negative electrode taking up an electron that travels through the external circuit to maintain the charge neutrality. In other words, reduction of Li-ion takes place at the negative electrode. Figure 1.2 depicts a schematic diagram describing the working principle of a Li-ion cell.

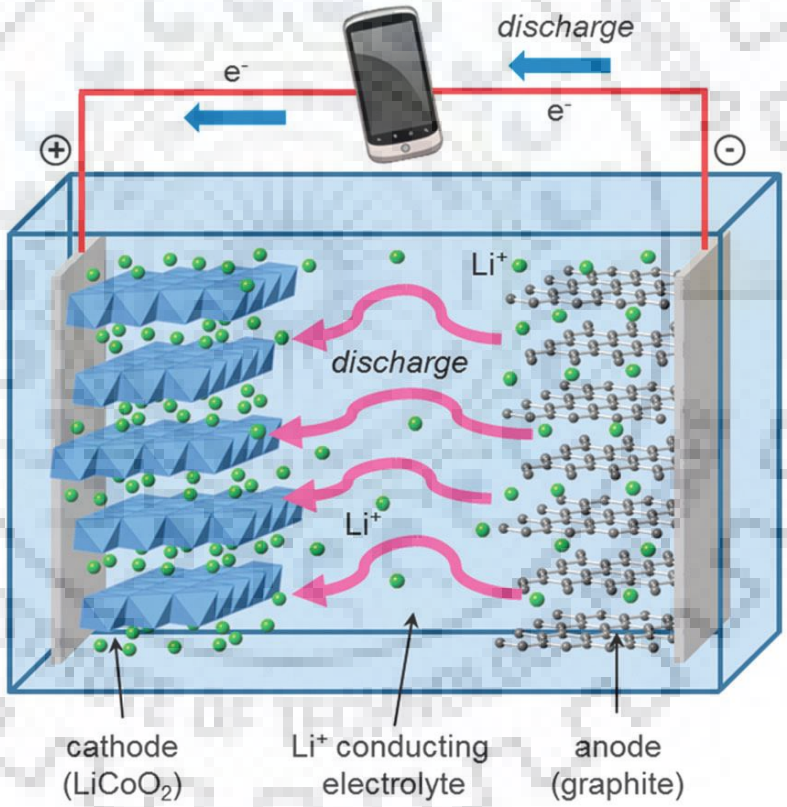

Figure 1.2 Schematic diagram of working principle of a Li-ion Battery [8].

Conversely, the discharge process of a Li-ion battery is just the reverse of charge process, where the Li-ion extracted from the negative electrode moves in the reverse direction through the electrolyte and gets intercalated into the positive electrode. In this process, there is a spontaneous flow of electron from negative electrode to the positive

electrode through an external circuit. At the positive electrode, the Li-ions get intercalated into the vacant Li-sites of the host structure and the electrons reduce the transition metal ions and maintain the electrical neutrality. The entire process describe above completes one full cycle of charge and discharge of a Li-ion battery. In the schematic diagram describing the working principle of Li-ion battery (Figure 1.2), lithium insertion and de-insertion is taking place in a reversible manner and $LiCoO_2$ balances this process by the oxidation and reduction of cobalt present in the lattice [8]. The electrochemical systems where lithium ion rock back from one side to another is termed as "rocking chair system or batteries". This concept was first given by B. Scrosati *et al.* in 1980, where they used lithium intercalated electrode material first time in place of lithium metal [9].

The electrode reactions (half-cell reactions) occurring at anode and cathode during the charge and discharge are shown below.

Charge:

Cathode: $LiCoO_2 \rightarrow Li_{1-x}CoO_2 + x\,Li^+ + x\,e^-$

Anode: $x\,Li^+ + 6\,C + x\,e^- \rightarrow Li_xC_6$

Discharge:

Cathode: $Li_{1-x}CoO_2 + x\,Li^+ + x\,e^- \rightarrow LiCoO_2$

Anode: $Li_xC_6 \rightarrow x\,Li^+ + 6\,C + x\,e^-$

Overall reaction at anode

$$xLi^+ + 6C + x\,e^- \leftrightarrow Li_xC_6$$

Overall reaction at cathode

$$LiCoO_2 \leftrightarrow Li_{1-x}CoO_2 + x\,Li^+ + x\,e^-$$

1.3 Brief Overview of Li-ion Battery:

The first ever battery was invented by Alessandro Volta in 1800 [10] and named voltaic pile. This invention opened the doors for the understanding of electrochemistry and functioning of batteries. After that synthesis of pure alkali metals was accomplished using voltaic pile via electrolysis [11]. The very first commercialized battery was the primary Leclanche cell which was used in telegraphy station and telephones. V. A. Kotsjejev

demonstrated the effect on Leclanche when its chemical and physical constituents were varied [12]. The concept of rechargeable battery was given by the Gaston Plante in mid-19th century and discovered lead acid battery, a first ever secondary battery which could be charged and discharged several times [13]. In the late 19th century, there was competition between electrical engines and combustion engines for the transportation [6]. The discovery of huge petroleum reserves in early 20th century smoothed the passage for the development of gasoline cars and on the other hand, reduced the research interests in electric engines.

In the late 20th century, the development of portable electronic gadgets renewed the interest in the battery field and gave a boost to the rechargeable battery research. At that time, the only available rechargeable lead acid battery was not suitable for these devices because they required light weight and high energy density battery. In the beginning, nickel-cadmium batteries were used as power sources in electronic devices due to their high energy density as compared to that of lead acid batteries.

The invention in lithium batteries started in early 1970s with lithium-iodine system. These lithium-iodine cells were successfully used in cardiac pace makers and are still in use because of their compact design [14]. However, it was soon realized that the low working potential of lithium metal is not suitable for long life of lithium batteries, although the lithium offered high energy density among all other anodes. In 1975, M. S. Wittingham *et al.* established a wet chemical method for the intercalation of lithium in different types of layered transition metal dichalcogenides using n-butyl lithium [15]. Out of many transition metal dichalcogenides, TiS_2 having a low molecular weight, good electronic conductivity and low cost, was emerged as a potential cathode candidate for lithium batteries [16]. The working potential of TiS_2 was found to be ~ 2 V along with high theoretical capacity of 240 $mAhg^{-1}$. In 1977, Exxon (full company name) tried to make secondary batteries in non-aqueous liquid electrolytes [17] using TiS_2 cathode and Li-metal as anode. The main drawbacks with Li/TiS_2 cell were (i) moisture sensitive nature of TiS_2 and (ii) dendrites formation on the Li-metal anode on battery cycling [18].

In 1980, a groundbreaking discovery of a layered transition metal oxide, $LiCoO_2$ by J. B. Goodenough *et al.* met the requirement of a high voltage and high energy density battery [19]. The layered $LiCoO_2$ formed by the alternate layers of lithium and cobalt

octahedra in a rock salt structure showed safe and reversible extraction of lithium-ion from the structure. Lithium can be intercalated and de-intercalated from the layered $LiCoO_2$ structure at a voltage of ~ 4.2 V leading to a high voltage battery [20]. After the discovery of $LiCoO_2$, much attention has been given to identify a safe and low voltage anode material. Basu *et al.* were the first group to report a liquid phase synthesis of lithium-graphite intercalation compounds [21]. Attempts were made to synthesize lithium intercalated graphite compounds by electrochemical methods in non-aqueous liquid electrolytes [22-24]. The lithium intercalated graphite compounds showed a large volume change and exfoliation of the material leading to high capacity fading [24]. In 1990, J. R. Dhan *et al.* demonstrated that lithium could be reversibly intercalated into graphite and petroleum coke using 1M $LiAsF_6$ in a 1:1 ratio of propylene carbonate (PC) and ethylene carbonate (EC) [25]. They showed that irreversible reactions which occur only on first discharge cycle are associated with electrolyte decomposition leading to the formation of passivating solid electrolyte interphase (SEI) on the surface of anode used (i.e., graphite and petroleum coke). The SEI works as a protective layer which allows lithium ion diffusion but restricts the electron diffusion. A number of research articles are reported in the literature describing the formation and nature of SEI on the graphite based anode materials [26-32].

The concept of lithium intercalation into the electrodes, $LiCoO_2$ cathode and graphite/petroleum coke anode, along with the stable SEI formation in ethylene carbonate (EC) containing electrolytes was used by Sony Corporation, Japan for the manufacture of Li-batteries. In 1991, Sony successfully commercialized a battery using $LiCoO_2$ cathode, a petroleum coke anode and 1 M $LiPF_6$ in PC: DEC (propylene carbonate: diethyl carbonate) as electrolyte [33]. The name of this battery as 'lithium ion battery' (LIB) was given for marketing purposes.

The efficacy of lithium ion batteries led to their adaptation in all types of portable electronic devices soon after its commercialization. The lithium ion batteries with high volumetric energy density (around 200 W h L^{-1}) outperform to other competing battery system such as nickel cadmium and nickel metal hydride batteries [34]. It was pointed out by A. Manthiram *et al.* that present day Li-ion battery system shows an accountable enhancement in the gravimetric and volumetric energy density up to 260 W h kg^{-1} and 780 W h L^{-1}, respectively [35]. The continuous improvement can be seen by comparing two

same size (18 mm in diameter and 65 mm in length) 18650 lithium-ion cells having the practical capacities of 0.9 Ah (cell used three decade back in Li-ion batteries) and 2.6 Ah (cell used in current Li-ion batteries), respectively [36]. On the other hand, electric vehicles (EVs) and plug-in hybrid electric vehicles (PHEVs) require not only a high capacity, high power and long life Li-ion battery but also with enhanced safety [37]. Despite continuous efforts made by the scientific community to improve lithium ion battery technology over the last four decades, current battery systems are still far behind to replace internal combustion engines in fully electric vehicles, because to compete with the driving distance per tank for vehicles with internal combustion engines nearly 5-fold increment in the energy density is necessary [38].

1.4 Components of a Li-ion Battery

Like any other batteries, the main components of a Li-ion battery, are cathode, anode and the electrolyte. All three major components are separately recognized and established as vast area of research in Li-ion battery. To be active components in Li-ion battery, certain criteria must be fulfilled by all the battery components. For example, the cathode materials for Li-ion batteries would be able to show reversible lithium insertion/de-insertion process. The structure of cathode materials must be stable and should not show any crystal structural transition or phase decomposition when cycled for a long time to achieve improved cycle life or over a wide potential range to achieve a high capacity. Moreover, the anode materials must have interstitial space to host lithium ions during charging and discharging of a Li-ion battery. The electrolyte should be an electrical insulator but allow easy diffusion of lithium ions.

1.4.1 Positive Electrode (Cathode) Materials

Cathode materials for Li-ion batteries mostly have host structures wherein a guest Li-ion could be inserted into or extracted reversibly [39]. A number of cathode materials for Li-ion batteries have been explored by the material chemists such as TiS_2 type dichalcogenides [16], $LiCoO_2$ type layered rock-salt oxides [40], spinel type $LiMn_2O_4$ [41] and olivine type $LiFePO_4$ [42]. The prime focus of a material chemist working in Li-ion battery field is to invent cathode materials with high energy density or material with high working voltage

because none of the available cathodes till date surpassed the practical capacities of more than 215 $mAhg^{-1}$ [43]. In this section we have reviewed the advantages and shortcomings of cathode materials used in Li-ion batteries.

1.4.1.1 Lithium Cobalt Oxide ($LiCoO_2$)

J. B. Goodenough *et al.* were the first to propose a material, Li_xCoO_2, with ordered rock-salt structure to be used as a cathode material for Li-ion batteries. The open circuit voltage of Li_xCoO_2 is nearly twice than that of TiS_2, still dominating the market of today's Li-ion batteries [19]. In the above study, they have showed that lithium can be removed reversibly within the range $0.067 \leq x \leq 1$. The layered Li_xCoO_2 structure shows good kinetic stability within this compositional range. Later, P. J. Wiseman *et al.* established the completely ordered rock-salt structure of $LiCoO_2$ containing alternate layers of cobalt and lithium atoms and crystallizing in hexagonal *R*–3*m* space group from powder neutron diffraction [44].

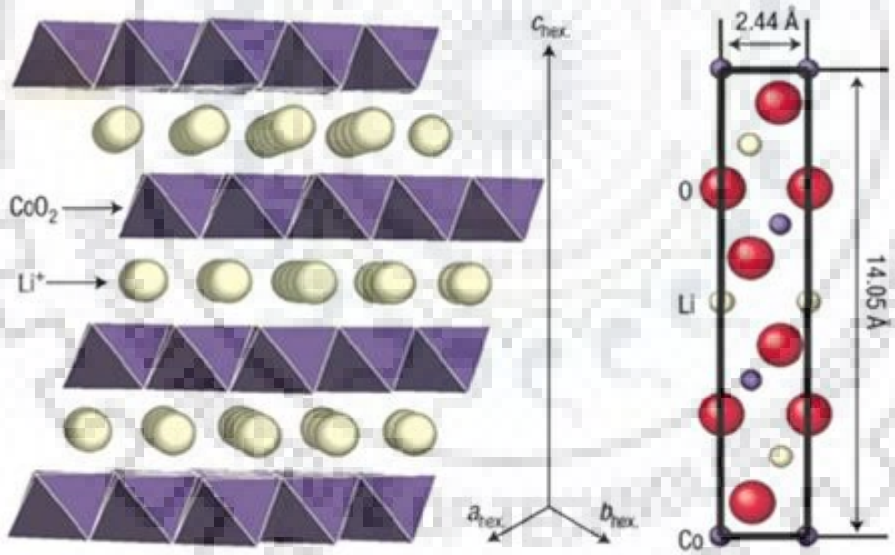

Figure 1.3 Structure of $LiCoO_2$ showing the layered rock-salt arrangement of cobalt as edge shared octahedra (in purple) and lithium atoms (in light yellow) [51].

Moreover, after its commercialization, rechargeable Li-ion batteries with $LiCoO_2$ cathode, non-graphitizable carbon anode and $LiPF_6$ containing propylene carbonate/diethyl carbonate electrolyte solution were thoroughly tested for its safety and abuse by Sony

Corporation [45]. The study also revealed excellent cycle performance even at a moderately high temperature because of the stability of $LiCoO_2$ and non-graphitizable carbon with respect to intercalation/deintercalation of Li-ion.

After the successful commercialization of Li ion battery with $LiCoO_2$ as a cathode material, much attention has been paid by the chemists to explore more on the structure of $LiCoO_2$. $LiCoO_2$ forms in the α-$NaFeO_2$ structure, a distorted rock-salt type structure, where the cations Li and Co are ordered in the alternating (111) planes of the cubic close packed oxygen lattice [46]. Depending on the preparation method and synthesis temperature $LiCoO_2$ shows two types of structure. While the high temperature lithium cobalt oxide (HT-$LiCoO_2$) crystallizes in a hexagonal layered structure, the low temperature oxide (LT-$LiCoO_2$) crystallizes in a cubic spinel structure [47]. Gummow *et al.* have shown that $LiCoO_2$ synthesized at lower temperature adopts a different structure that is not perfectly ordered. This is due to the fact that 6% of the cobalt resides in the octahedral (8a) sites of the lithium layers [48-49]. LT-$LiCoO_2$ is believed to adopt a spinel related structure making a large difference between the electrochemical performance of LT-$LiCoO_2$ and HT-$LiCoO_2$ [50]. Yang. S.-H. *et al.* have successfully demonstrated the determination of separate columns of cobalt, oxygen and lithium atoms in the layered $LiCoO_2$ using mid-voltage transmission electron microscope. This was not possible using simple X-ray and neutron powder diffraction techniques due to the low scattering power of lithium [51]. A large number of studies have also focused on the electrochemical performance of $LiCoO_2$ and related compounds [52-58].

Doping studies with other metals *viz.* Mn, Fe, Al, and Mg etc. have also been carried out to increase the specific capacity and stability of $LiCoO_2$. The performance of $LiCoO_2$ cathode was increased by coating Al_2O_3 onto the $LiCoO_2$ particle surfaces using a sol-gel method [59]. An appropriate explanation for the improved performance on Al_2O_3 coating was given by Dedryvère, R. *et al*. They have shown that on the introduction of aluminum into the structure, the surface basicity of $LiCoO_2$ decreases and ionicity of Co-O bond increases. This led to less cobalt dissolution into the electrolyte [60]. Later, much improved capacity retention was shown by Y. S. Jung *et al.* with 3-4 Å thick atomic layer deposition of Al_2O_3 on $LiCoO_2$ [61]. Fe-doped layered $LiCoO_2$ was prepared by Tabuchi, M. *et al*. using a hydrothermal method [62]. The electrochemical behavior of $LiCo_{1-x}Fe_xO_2$ showed

prominent capacity fading as the Fe content was increased from 0.05 to 0.25. The poor electrochemical performance of Li/$LiCo_{1-x}Fe_xO_2$ cells was attributed to insufficient atomic ordering of Li and transition metals in the structure [63]. S. Gopukumar *et al.* have synthesized Sn, Zn, Bi and Cr-doped $LiCoO_2$ by a simple solid state reaction. Among them, $LiCoO_2$ with 5% doping showed a high discharge capacity of ~ 155 $mAhg^{-1}$ at 0.2 C rate [64]. Recently, J. R. Dahn *et al.* established that even 1% doping of Mn/Mg in $LiCoO_2$ enhances the cycling performances along with reduced cell resistance [65]. Despite many advantages, $LiCoO_2$ cathodes do have some disadvantages, such as, Co solubility into the electrolyte during delithiation while charging and toxicity of Co. So, chemists are constantly exploring new oxides for the development of alternative to $LiCoO_2$ cathodes that are inexpensive, offer high capacity and enhanced safety.

1.4.1.2 Lithium Nickel Oxide ($LiNiO_2$)

It was initially thought that nickel based oxides, such as $LiNiO_2$ could be a better replacement of $LiCoO_2$ due to its inexpensive and environmental benign nature. $LiNiO_2$ with α-$NaFeO_2$ type layered structure is similar to $LiCoO_2$ with a theoretical capacity of 273 $mAhg^{-1}$. Though $LiNiO_2$ offers a high theoretical capacity and high operational potential ~ 3.9 V, it suffers from some other problems which limit its practical use. Firstly, $LiNiO_2$ is not easy to synthesize. It was stated that all synthesis methods employed to get a pure $LiNiO_2$ were complex in nature due to its thermal instability at higher temperature [67]. Secondly, any non-stoichiometry in $LiNiO_2$ leads to the mixing of lithium and nickel sites in the layers resulting in suppressed discharge capacity and cyclability [67-68]. T. Ohzuku *et al.* have demonstrated that layered $LiNiO_2$ (space group *R*–3*m*) gets converted easily and completely into cubic rock salt structured $LiNiO_2$ (space group *Fm*3*m*) due to its lattice resemblance. $LiNiO_2$ (*R*–3 *m*) when heated at 900 °C, it results in the formation of an electrochemically inactive phase [69]. Another problem was the structural change that occurs when lithium is extracted from $LiNiO_2$. S. Yamada *et al.* have shown that upon delithiation, $Li_{1-x}NiO_2$ transforms into a hexagonal phase with compositions $0 \leq x \leq 0.25$ while the same gets converted into a monoclinic phase in the composition range $0.25 \leq x \leq 0.55$ [70].

Many attempts have been made to improve the stability and cycle performance of $LiNiO_2$ by substituting nickel with other transition metal elements. Cobalt substituted phases, $LiNi_{1-y}Co_yO_2$, with suitable synthetic routes have been studied in depth. The substitution of cobalt in the entire composition range, $0 \geq y \geq 1$, stabilizes the layered rock-salt structure [71]. C. Delmes *et al.* have examined the electrochemical behavior of cobalt substituted $LiNiO_2$ phase and concluded that the compounds with $y \geq 0.2$ show enhanced electrochemical cycling performance [72]. Moreover, they have reported that a pure 2-D structure was formed for $y \geq 0.2$, resulting in the stabilization of the structure and improved electrochemical performance [73]. J. R. Dahn *et al.* have studied the partial substitution of nickel with manganese in $LiNiO_2$. They have shown that the Mn-substituted solid solutions were isostructural with $LiNiO_2$ with Mn/Ni mixing and the amount of reversibly extractable lithium were decreased with the increase of manganese content in the solid solutions [74]. However, the material with 50 % substitution of nickel by manganese, $LiNi_{1/2}Mn_{1/2}O_2$, with a high capacity and fairly low cost was shown to be of great interest. T. Ohzuku *et al.* have demonstrated $LiNi_{1/2}Mn_{1/2}O_2$ as an optimized cathode with substitution of nickel by manganese to have a high capacity and stable cycling performance and proposed $LiNi_{1/2}Mn_{1/2}O_2$ as an alternative to $LiCoO_2$ [75, 76]. G. Ceder *et al.* have demonstrated using first principle calculation that nickel is the electrochemically active ion in $LiNi_{1/2}Mn_{1/2}O_2$. They also argued that presence of Mn in +4 oxidation state renders stability to these materials and the high insertion voltage is partly due to changing Mn-Ni interaction on cycling [77]. On the other hand, Ni migration into the Li layers is responsible for reduced cyclic performance. G. Ceder *et al* have described the effect of Li/Ni mixing on the electrochemical performance by *ab initio* calculations. Generally, 8-12% of Li/Ni mixing was found in $LiNi_{1/2}Mn_{1/2}O_2$ synthesized using different types of synthetic routes. Even if, 8.3 % nickel gets migrated to the Li layer, it increases the activation energy barrier by 20 - 30 meV. This increase in activation energy significantly reduces both the Li-ion diffusivity and the cycle performance [78]. An improved rate capability and reduced cation mixing was observed when $LiNi_{0.5}Mn_{0.5}O_2$ was prepared by ion exchange of $NaNi_{0.5}Mn_{0.5}O_2$ [78, 79]. The reduced thermal stability and lack of appropriate synthetic methods were responsible for limiting the use of $LiNi_{0.5}Mn_{0.5}O_2$ in LIBs.

1.4.1.3 Lithium Manganese Oxide ($LiMnO_2$)

The search of cheaper and less toxic layered transition metal oxides were intense after the commercialization of $LiCoO_2$ cathode material for lithium ion batteries. In this regard $LiMnO_2$ was found to be a competitive candidate among the layered transition metal oxides because of its low cost and less toxic nature than cobalt and nickel based oxides. In the mid 1990's synthesis of stoichiometric $LiMnO_2$ remained unsuccessful despite many attempts [80-81]. $LiMnO_2$ crystallizes in two structures; the high temperature phase form in an orthorhombic space group (Pmnm) and is electrochemically inactive, while the low-temperature form is the electrochemically active layered variant that crystallizes in a monoclinic space group (C2/*m*) [82-84]. J. R. Dahn *et al.* have also demonstrated a low temperature synthesis for $LiMnO_2$ using an ion-exchange reaction between γ-MnOOH and 4 M LiOH in air at 100 °C and at 200 °C in argon atmosphere [85]. R. J. Gummow *et al.* have proposed a new synthetic route by reacting γ-MnO_2 and LiOH with a reducing agent under argon atmosphere [86]. I. J. Davidson *et al.* has shown that the high temperature orthorhombic form prepared in the early studies has good capacity and long life. X-ray diffraction and electrochemical results confirmed the structural change of orthorhombic $LiMnO_2$ to spinel $Li_{1-x}Mn_2O_4$, when the battery was charged beyond a certain limit [87].

Many attempts have been made to synthesize layered $LiMnO_2$ but most have resulted in the formation of off- stoichiometric phases with the presence of water and proton in the structure. The crystallinity of the off- stoichiometric compositions were very low and did not show stable charge/discharge studies [88, 89]. The synthesis of stoichiometric $LiMnO_2$ was carried out by P. G. Bruce *et al.* in two steps. First, $NaMnO_2$ was synthesized using a solid state reaction and refluxing $NaMnO_2$ with an excess of LiBr or LiCl in *n*-hexanol for 6-8 h at 145-150 °C, in the second step [90]. The charge/discharge studies of the stoichiometric $LiMnO_2$ thus prepared showed good stability over a long period. A more mild hydrothermal method at 160 °C was used to synthesize layered $LiMnO_2$ by M. S. Whittingham *et al.* but its capacity was reported to fade rapidly due to the diffusion of manganese from the MnO_2 layers to the interlayer region where generally the Li ions are located [91].

G. Vitins *et al.* thoroughly investigated lithium intercalation into the layered $LiMnO_2$ and concluded that lithium removal and reinsertion into the layered $LiMnO_2$ is not reversible

in nature. The structure of $LiMnO_2$ collapsed after a small amount of lithium was extracted resulting in a very low capacity. However, cycling up to a lower voltage shows a structural rearrangement to a spinel related structure which gave better cycling performance [92]. The finding of J. Molenda *et al.* also favored the conversion of orthorhombic $LiMnO_2$ to defective $Li_{1-x}Mn_2O_4$ spinel phase. Additionally, the spinel phase helped in improving the stability [93].

M. M. Thackeray *et al.* have confirmed the multiphase product formation by a systematic investigation of convergent beam electron diffraction data for the $LiMnO_2$ samples prepared by the ion exchange of α-$NaMnO_2$. The multiphase product was dominated by the layered $LiMnO_2$ phase whereas the lithiated spinel and orthorhombic phases were present in small amounts. Electrochemical data of this compound showed a better cycling performance than a pure spinel, $LiMn_2O_4$, phase [94]. However, the high capacity fading and structural transformation into spinel phase during cycling hindered its commercialization in Li-ion batteries. In order to improve the structural stability of the layered $LiMnO_2$, P. G. Bruce *et al.* have shown that 10 % substitution of manganese with cobalt is enough to reduce the Jahn-Teller distortion and stabilize the structure [95, 96].

1.4.1.4 Lithium Nickel Cobalt Manganese Oxide (NCM), $Li[Ni_{1-x-y}Co_xMn_y]O_2$

It was established in earlier discussion that partial substitution of nickel by cobalt and manganese in $LiNiO_2$ have profound effect in the stability and cyclability. These results motivated material chemists to discover high energy density electrode materials based on cobalt and manganese substitution in $LiNiO_2$ for lithium ion batteries. J. Cho *et al.* summarized the effect of doping of different types of metals in nickel rich layered transition metal oxides. Since last three decades, efforts have been made to develop an appropriate layered transition metal oxide cathode material with enhanced structural stability and improved electrochemical performance. Research outcomes suggested that cobalt substitution in nickel based cathode materials reduce the cation disordering effectively resulting in superior rate capability. Moreover, manganese and aluminum substitution were found to be very helpful in structural stabilization and enhancing the thermal properties of nickel based materials [97].

Initially, Z. Liu *et al.* have prepared a series of $LiNi_{1-x-y}Co_xMn_yO_2$, where x varies from $0 \leq x \leq 0.5$ and y varies from $0 \leq y \leq 0.3$, by heating $Ni_{1-x-y}Co_xMn_y(OH)_2$ with $LiNO_3$ in oxygen atmosphere. The electrochemical results of these compounds indicated decent capacity and improved performance for $LiNi_{0.7}Co_{0.2}Mn_{0.1}O_2$. However, increased manganese doping resulted in poor electrochemical performance [98]. The more appropriate composition, $LiNi_{1/3}Co_{1/3}Mn_{1/3}O_2$ (NMC111), was synthesized by T. Ohzuku *et al.* using a solid state reaction method. The electrochemical studies of $LiNi_{1/3}Co_{1/3}Mn_{1/3}O_2$ showed high rechargeable capacity of 150 $mAhg^{-1}$ when cycled between 3.5 - 4.2 V and the capacity increased up to 200 $mAhg^{-1}$ in the 3.5 - 5.0 V window. The thermal stability of this composition against electrolyte was much better than any other layered transition metal cathode [99, 100]. Later on, different synthetic methods such as, solid state, sol-gel, co-precipitation, hydrothermal, spray drying, molten salt and microwave synthesis were used to synthesize NMC111. Out of these methods, co-precipitation route is the most adopted method due to the advantages such as, ease of bulk material synthesis, easy controllability, homogeneous product formation ability and use of low temperature, over other synthetic methods [101-107].

Due to high capacity and good thermal stability nickel based cathode materials have attracted the attention of scientific community for a thoroughly scrutiny. It was found that increased capacities are attainable in compositions with high nickel contents. H. Cao *et al.* have synthesized a high nickel content composition, $LiNi_{0.6}Co_{0.2}Mn_{0.2}O_2$, by a simple co-precipitation method and demonstrated outstanding cycling stability at different rates when cycled between 2.8 and 4.2 V [108]. However, the major problem with the high nickel content sample was its air storage due to the presence of residual Li_2CO_3 and LiOH on the particle surfaces promoting self-reduction of Ni^{3+} and consequent phase changes. A series of composition with high nickel contents, $LiNi_{0.8}Co_{0.1+x}Mn_{0.1-x}O_2$ (x = 0, 0.03, and 0.06) was prepared by J. Cho *et al.* using co-precipitation method and it was shown that the amount of cobalt plays a significant role in improving the storage capacity in air and electrolyte at 90 °C. In the series, the composition with the highest cobalt content, $LiNi_{0.8}Co_{0.1+x}Mn_{0.1-x}O_2$ (x = 0.06), showed minimum LiOH and Li_2CO_3 formation in air and smaller Ni and Mn dissolution in electrolyte at 90 °C [109]. The other problem associated with the nickel rich cathode materials was their low thermal stability, which have been addressed in several

studies by adopting to a number of strategies including surface coating with $AlPO_4$ and AlF_3 [110, 111].

Due to the high specific capacity of NCM111 than $LiCoO_2$, NCM111 replaces $LiCoO_2$ in some high capacity applications such as, electric vehicles and hybrid electric vehicles. K. Amine *et al.* have analyzed the electrochemical performance of some full electrochemical cells with graphite as an anode and $Li_{1-x}Mn_{2-x}O_4$, $Li_{1+x}Ni_{1/3}Co_{1/3}Mn_{1/3}O_2$ or $LiNi_{0.8}Co_{0.15}Al_{0.05}O_2$ as cathode materials. Among the above, $Li_{1-x}Mn_{2-x}O_4$ cathode based full cell showed very high capacity loss upon cycling at 55 °C due to dissolution of manganese ions from the anode surface thereby increasing the charge transfer resistance at the anode/electrolyte interface. However, $Li_{1+x}Ni_{1/3}Co_{1/3}Mn_{1/3}O_2$ based full cell showed much improved cyclability and thermal stability when compared with $LiNi_{0.8}Co_{0.15}Al_{0.05}O_2$ based cell [112].

1.4.1.5 Lithium Iron Oxide ($LiFeO_2$)

α-$NaFeO_2$ type $LiMO_2$ (M: Co, $Ni_{1-x-y}Mn_xCo_y$ etc.) crystallizing in the ordered rock-salt structure were used as cathode materials in Li-ion batteries. Much attention has been paid to improve their capacity, stability and cycle life for fulfilling the requirements of use in high power applications. Although, Li-ion batteries with nickel and cobalt oxide based cathode materials were successfully commercialized but they have some economic and environmental problems [113]. Hence, all possibilities were explored to replace these cathodes with low cost and non-toxic or less toxic cathode materials. Therefore, iron based cathode materials with high capacity, good stability and long cycle life were thought to be a better choice as alternatives to other cathodes.

Lithium ferrite ($LiFeO_2$) is a non-toxic, low cost oxide made up with the most abundant metal in the world. Moreover, it has many advantages over other $LiMO_2$ (M = Co, Ni and Mn) type transition metal oxides [114, 115]. Three different forms of $LiFeO_2$ have been investigated, i.e., α, β and γ form [116]. While α-$LiFeO_2$ crystallizes in a cubic disordered rock salt structure in which Li^+ and Fe^{3+} ions randomly occupy the octahedral sites [116], γ-$LiFeO_2$ forms a tetragonal structure which contains an ordered arrangement of Li^+ and Fe^{3+} ions along the tetragonal *c*-axis. The remaining β-$LiFeO_2$ seems to be an intermediate structure that forms during the ordering process [117]. In spite of its non-toxic

nature, complex synthetic procedure and low operating voltages were the main problems associated with $LiFeO_2$, which impeded its development for practical uses [118-125]. Kim and Manthiram have reported a high discharge capacity of about 140 $mAhg^{-1}$ by lithium iron oxide with enhanced cyclability [126]. Sato *et al.* synthesized a nanocrystalline orthorhombic $LiFeO_2$ by a conventional solid state method at low temperature displaying good cycling performance [127]. Wang *et al.* reported a nanocrystalline, porous and high surface area α-$LiFeO_2$ prepared by molten salt method. They also demonstrated higher reversible capacity and stable cycle life for the α-$LiFeO_2$ nanocomposite electrode as compared to that of other $LiFeO_2$ [128]. Furthermore, there has been no such report that offers stable charge/discharge performance of the conventional $LiFeO_2$ (α, β and γ form) that could be used for practical purposes [129].

1.4.1.6 Spinel-type Lithium Manganese Oxide and its Derivatives

Rechargeable Li-batteries with $LiCoO_2$ based layered transition metal oxides as cathodes were commercialized for their use in most of the portable electronic devices till date but their high cost, toxicity and stability remained to be major issues of concern. Spinel-type lithium manganese oxides were found to intercalate/de-intercalate Li-ion reversibly without any major structural change [130]. M. M. Thackery *et al.* thoroughly investigated the structural and electrochemical behavior of $LiMn_2O_4$. $LiMn_2O_4$ crystallizes in a cubic spinel structure with space group *Fd3m*. In $LiMn_2O_4$ spinel, oxygen atoms are arranged in cubic close packing manner and occupy the 32*e* position. The Li-ions reside on tetrahedral 8*a* sites and the manganese ions on the octahedral 16*d* sites. The Li-ions are located in the interstitial space created by the face sharing tetrahedra and octahedra which helps in the three dimensional diffusion of Li-ions through the structure [41,130-132].

J. M. Tarascon *et al.* have studied the electrochemical performance of $LiMn_2O_4$ when cycled at high and low voltages and identified two voltage regions, one at ~ 4.1 V and the other at ~ 2.7 V. For the cell cycled at higher voltage region (4.1 V) good capacity and cyclability were observed, while inferior electrochemical performance was noticed when cycled at the lower voltage regime (2.7 V) [133]. Although $LiMn_2O_4$ was found to be a good cathode material with high operating voltage and good capacity but severe capacity fading during cycling limited its use in Li-ion batteries. The capacity fading mechanism was

extensively studied by M. Yoshio *et al.* using Li/1M-$LiPF_6$ + EC/DMC (1:2 by volume)/$LiMn_2O_4$ cell. The investigation carried out at different temperatures showed that the capacity fading is higher at higher temperature. This capacity fading was due to electrolyte decomposition and Mn^{3+} dissolution into the electrolytic solution [134]. D. Aurbach *et al.* have proposed two different mechanisms for the capacity fading, one was the formation of a new less symmetric, more disordered and electrochemically inactive phase when cycled between 3.5 – 4.2 V potential range whereas, the other involved the manganese dissolution when cycled at ~ 4.4 V [135]. The improved cycling performance have been achieved by doping other elements in place of manganese. The Al^{+3} doped solid solution, $LiAl_xMn_{2-x}O_4$ ($0.3 \geq x \geq 0.5$), displays higher discharge capacity retention due to enhanced structural stability and reduced strain during cycling [136, 137].

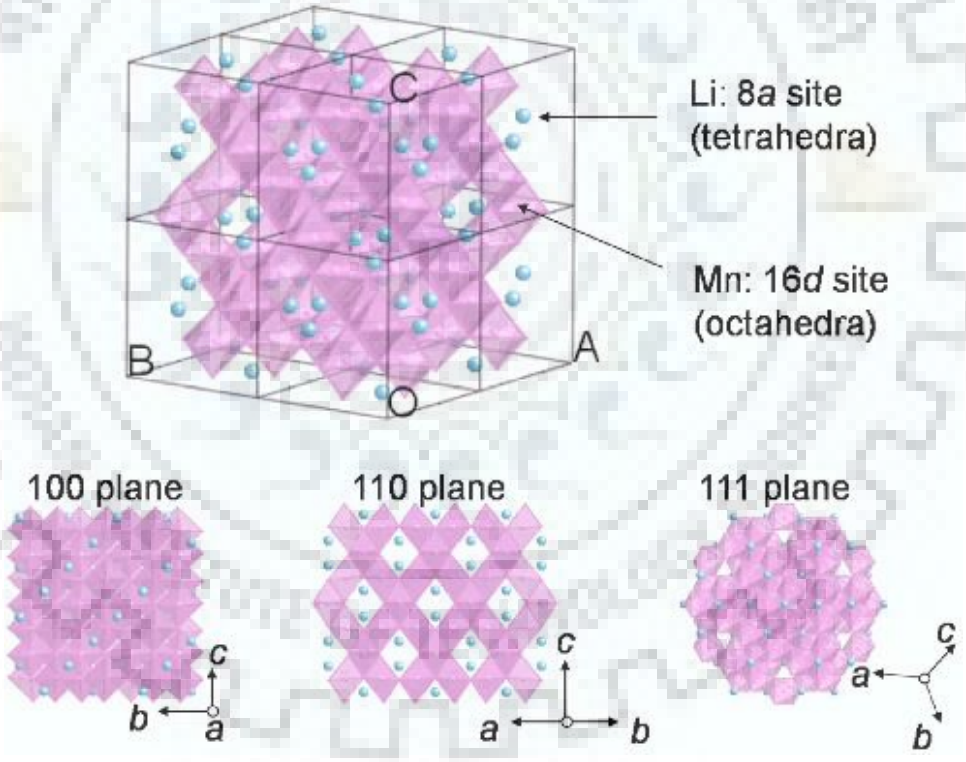

Figure 1.4 Structure of spinel $LiMn_2O_4$ with cross sectional views of 100, 110 and 111 planes [131].

It was established in the literature that the main reason behind capacity loss in manganese based spinel cathodes was Mn^{3+} ion dissolution in the electrolytic solution. To overcome this problem different kinds of coating using electro-chemically inert materials were investigated to minimize the contact area between the electrolyte and electrode materials such as MgO, CeO_2, ZnO, AlF_3, $AlPO_4$ and $LiAlO_2$ etc. [138-143]. A number of dopants were studied to increase the stability and cyclic performance of $LiMn_{2-x}M_xO_4$ (M = Ni, Cr, Co, Ti) solid solutions [144, 145]. In the case of nickel doped samples, $LiMn_{2-x}Ni_xO_4$ ($0 < x < 0.5$), a shift in the potential from 4.1 V to 4.7 V was observed and was attributed to the oxidation of Ni^{+2} to Ni^{+4}. This class was referred to the 5 V spinel cathodes for Li-ion batteries [145]. The $LiMn_{1.5}Ni_{0.5}O_4$ was found to crystallize into two different forms such as ordered spinel ($P4_332$) and disordered spinel (Fd–$3m$) [146]. Y. K. Sun *et al.* have shown that disordered spinels having Fd–$3m$ space group exhibit better electrochemical performance than the ordered phases with $P4_332$ space groups [147]. The Ti-substituted $LiMn_{1.5-x}Ti_xNi_{0.5}O_4$ showed better rate capability and faster Li-ion diffusion. Y. K. Sun *et al.* have argued that Ti-substitution into ordered $LiMn_{1.5}Ni_{0.5}O_4$ is responsible of the formation of face centered disordered spinel [148]. The high operating voltages beyond the stability limit of the electrolytes used in batteries is the main problem associated with $LiMn_{1.5}Ni_{0.5}O_4$ cathode materials [149]. A. Manthiram *et al.* have demonstrated the effect of surface modification of $LiMn_{1.42}Ni_{0.42}Co_{0.16}O_4$ with 2 wt % nanosized Al_2O_3, Bi_2O_3, ZnO and $AlPO_4$ to achieve improved cycling and better rate capability. The reduced electrochemical performance of bare $LiMn_{1.42}Ni_{0.42}Co_{0.16}O_4$ was due to the formation of thick SEI layer. It is understood that the surface coating reduces the thickness of SEI layer significantly, thus improving the electrochemical performance [150].

1.4.1.7 Olivine-type Lithium Metal Phosphate: ($LiMPO_4$: M = Fe, Co, Mn)

The ployanion based compounds as cathodes in Li-ion batteries have attracted attention due to their high operating voltage and fast lithium ion diffusion. The presence of polyanions such as $(PO_4)^{3-}$ and $(SO_4)^{2-}$ etc., induces an inductive effect resulting in enhanced redox energies [151, 152]. Among several polyanionic compounds iron based phosphate, $LiFePO_4$, satisfies many of the criteria required for a material to be used as a cathode material in Li-ion batteries. The $LiFePO_4$ crystallizes in an ordered olivine-type structure with space group *Pnma*. In the olivine structure, the oxygen atoms form a

hexagonal close-packed arrangement wherein lithium and iron occupies the octahedral 4*c* and 4*a* sites. The phosphorus atoms resides on tetrahedral sites and form a PO_4 tetrahedra. The corner connected FeO_6 octahedron forms zigzag planes in the *b*–*c* plane. Each LiO_6 octahedra are edge-shared and forms a linear chain along the *b*-axis. FeO_6 and LiO_6 octahedra are edge shared to each other. The PO_4 tetrahedra are corner and edge connected with FeO_6 and LiO_6 octahedra generating a stable three-dimensional structure [7, 154, 158].

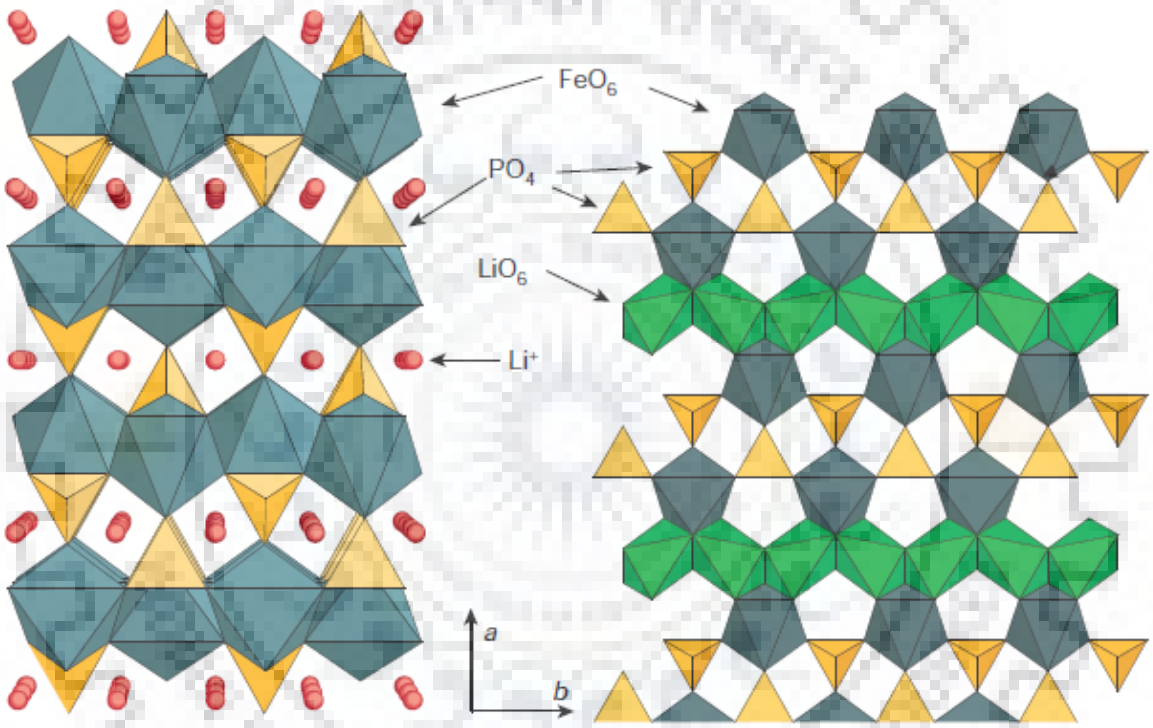

Figure 1.5 The crystal structure of $LiFePO_4$ along 001direction, grey color showing FeO_6 octahedra, yellow color showing PO_4 tetrahedra and red color showing lithium ions [5].

Padhi *et al.* were first to report electrochemical properties of $LiFePO_4$. They have shown reversible lithium extraction/insertion at 3.5 V *vs* Li^+ in $LiFePO_4$, which made this material a suitable cathode for low power Li-ion batteries [42]. The synthesis of $LiFePO_4$ is simple and can be prepared by solid state reaction [153], hydrothermal method [154], sol-gel method [155] or co-precipitation [156]. M. Wohlfahrt-Mehrens *et al.* have demonstrated much better electrochemical results of $LiFePO_4$ prepared by a co-precipitation method.

Unlike other cathode materials, $LiFePO_4$ showed better stability even in the charged state [156].

Although the theoretical capacity of $LiFePO_4$ is 170 $mAhg^{-1}$, only about 0.6 Li atom/formula unit can be extracted giving a specific capacity of ~ 110 $mAhg^{-1}$ [153]. Much attention has been paid to improve the capacity due to its potentially low cost and environmental benign nature. It is reported that $LiFePO_4$ synthesized at lower temperature delivered higher charge/discharge capacity than that for the higher temperature product due to lower particle sizes of the low temperature product [157]. The effect of temperature on charge/discharge characteristics revealed that at room temperature $LiFePO_4$ gives low capacity; however, high capacity can be achieved at elevated temperatures. Also there is no indication of any side reactions between the electrodes and electrolyte conforming to the stable nature of $LiFePO_4$ [157, 158]. However, the main problems associated with $LiFePO_4$ were sluggish lithium diffusion and low electrical conductivity. J. Maier *et al.* analyzed ionic conductivity, electronic conductivity and chemical diffusion using single crystalline of $LiFePO_4$. They have established smaller value of ionic conductivity than the electronic conductivity along all the three axis of $LiFePO_4$ [159].

Many research groups have tried to improve the electronic and ionic conductivities of $LiFePO_4$ cathodes [160-163]. M. Armand *et al.* were the first group to report electrochemical performance of carbon coated $LiFePO_4$. The carbon coating was achieved by a simple post treatment method which helped in increasing the electronic conductivity as well as improving capacity and long life [160]. L. F. Nazar *et al.* have proposed a method to synthesize small size particles of $LiFePO_4$ with very good carbon coating using resorcinol-formaldehyde and surface oxidized carbon as carbon source in their synthesis. This $LiFePO_4$/C nanocomposite showed a high capacity, excellent rate capability and improved stability [161]. H. Jang *et al.* demonstrated the performance of $LiFePO_4$ by incorporating carbon using three different carbon sources such as, graphite, carbon black and acetylene black. The carbon coating carried out by graphite showed superior electrochemical performance than the other type of carbon sources [162]. The effect of carbon coating thickness on the electrochemical performance was studied by R. Dominko *et al.* The thickness of carbon coating was controlled by the amount of materials used as carbon source. The results primarily established that the reversible capacity of the respective

material will be high as low is the thickness of carbon coating [163]. Different types of synthetic approaches have been applied to prepare $LiFePO_4$/C such as, solid state [164-167], co-precipitation [168, 169], sol-gel [170, 171], and spray pyrolysis [172, 173]. The nano-sized $LiFePO_4$ with appropriate carbon coating made this material a viable cathode for their use electric vehicles [174].

The other members of the olivine family such as, $LiMnPO_4$, $LiCoPO_4$ and $LiNiPO_4$ with operating voltage of 4.1, 4.8 and 5.1 V, respectively, have been investigated extensively. Though, their high operating voltages seemed to be very interesting for high power Li-ion batteries, the stability of the currently used electrolytes hindered their use as cathode materials in high power batteries [175-178].

1.4.2 Negative Electrode Materials

Metallic lithium is a choice for anode material due to its high theoretical specific capacity (3680 $mAhg^{-1}$) and lowest electrochemical potential (3.04 V vs. standard hydrogen electrode) [179]. The first secondary lithium battery discovered by M. S. Whittingham and co-workers was commercialized by Exxon used metallic lithium as anode active material [17]. But, one of the drawbacks of using metallic lithium as anode is uncontrollable growth of lithium dendrites during charge/discharge process leading to short circuits and fire incidents in the batteries [180]. Later on, graphite was found to be a better replacement for lithium metal anode. Graphite fulfilled all the criteria required to be used as an anode material in Li-ion batteries. The specific capacity of graphite is ~ 300 $mAhg^{-1}$ and the working potential is higher than that of metallic lithium [181]. The practical specific capacity of graphite is close to its theoretical capacity and cannot be increased further. Therefore, there is immense interest to find new anode materials with high capacity and low working voltage. A number of anode materials have been reported in the literature. These can be classified into three following categories.

I. Insertion/de-insertion anode materials
II. Alloy/de-alloy anode materials
III. Conversion anode materials

In this section we will shed light on the synthesis, characterization and electrochemical performance of insertion/de-insertion anode materials. The insertion/de-insertion anode materials are further classified into two major categories.

A. Carbon based anode materials
   (a) Hard carbon
   (b) Carbon nano-tubes (CNTs)
   (c) Graphene
B. Transition metal oxides based anode materials
   (a) TiO_2
   (b) $Li_4Ti_5O_{12}$
   (c) Li_3VO_4

1.4.2.1 Carbon Based Anode Materials

Carbonaceous materials show easy and reversible intercalation/de-intercalation of lithium ions during the repeated charge-discharge of a battery. Therefore, these materials seemed to be better choice for anode material in Li-ion batteries. Furthermore, carbon based materials with high capacity, high stability and improved kinetics could be a promising candidate for the replacement of commercial graphite.

1.4.2.1.1 Hard Carbon

The form of carbon which cannot be graphitized at any given temperature is known as hard carbon or non-graphitizable carbon [182]. Out of three commercialized carbon anode material such as, graphite, soft carbon and hard carbon, hard carbon was found to be most promising anode material for Li-ion batteries due to its high reversible capacity of ~ 600 $mAhg^{-1}$ [183]. The high reversible specific capacity delivered by hard carbon is due to its highly disordered structure. The highly irregular structure is formed by the single layer carbon atoms i.e., graphene, connected in a random fashion which provide more space to accommodate more lithium leading to a high specific capacity [184, 185]. A number of reports have been published in the literature comprising the synthesis, characterization and electrochemical performance of hard carbon as anode material for Li-ion batteries. The improved electrochemical performance of hard carbon as compared to graphite anode in

terms of high capacity, improved cycling behavior, longer life and enhanced safety have been established [186-192]. However, the high irreversible capacity and low pack density are the main drawbacks associated with hard carbon materials. A number of strategies have been applied to improve the columbic efficiency such as, fluorination, surface oxidation and metal coating [191, 193]. The high packing density and higher structural stability of spherical morphology was thought to be a way to increase the columbic efficiency of hard carbon materials. However, the preparation of hard carbon spheres through direct methods was difficult [194].

Huang *et al.* were the first group to report the preparation of spherical hard carbon using a hydrothermal method resulting controllable and monodisperse particle size with smooth surfaces [195]. The precursor concentrations (such as, sugar) have profound effect on the size of hard carbon spheres; the size can be controlled by varying the concentration of the precursor [196]. Y. Li *et al.* have prepared monodisperse colloidal carbon microspheres by hydrothermal reaction using glucose as the starting material [197]. S. Yu *et al.* have synthesized carbon hollow microspheres using starch and rice grains. In this synthesis, iron ions and iron oxide nanoparticles were used to catalyze the starch and rice grains under milder hydrothermal condition [198]. The electrochemical performance of the hard carbon spheres seemed to result much better reversible capacity, improved cycle life and upgraded safety as compared to other form of carbon anode materials such as, graphite, soft carbon and other hard carbons [191, 193 and 199].

1.4.2.1.2 Carbon Nano-tubes (CNTs)

Carbon nanotubes (CNT), an allotrope of graphite, are excellent choice for the replacement of graphite as anode in Li-ion batteries. Some of the unique properties of CNT which make them very competitive candidate for anode material are one dimensional structure, high conductivity {10^5 S m^{-1} at 300 K for single-walled carbon nano-tubes (SWCNTs) and > 10^6 S m^{-1} for multi-walled carbon nano-tubes (MWCNTs)}, high rigidity, low density and high tensile strength (up to 60 GPa) [200-203]. Many research groups have studied the lithium ion storage mechanism by computational methods. Y. Liu *et al.* have demonstrated the lithium adsorption in CNTs by first principle calculations. These results confirmed that lithium adsorption on sites present outside the CNTs are energetically more

favorable than those inside when the tube diameter is small [204]. An *ab-initio* calculation was carried out to investigate Li^+ insertion into SWCNTs containing different topological defects. In this study, they have investigated different types of defects which help in lithium diffusion [205]. An experimental and theoretical study has been carried out to compare the lithium intake capacity of metallic and semiconducting SWCNTs. This study revealed that metallic SWCNTs can better accommodate the lithium leading to higher capacity than that of the semiconducting SWCNTs [206].

The experimental capacity of as the prepared CNTs varies considerably depending on their structure and morphologies. A report by S. Kawasaki *et al.* have demonstrated that much improved capacity by metallic SWCNTs as compares to that by semiconducting SWCNTs. The metallic SWCNTs delivered five times greater lithium storage capacity when electrochemical charge/discharge measurements were carried out using metallic SWCNTs as anode material [207]. A number of reports showed enhanced cycle performance by short CNTs. The syntheses of CNTs include, controllable growth by appropriate method, ball milling and solid state cutting [208-211]. The enhancement in electrochemical performance is due to shorter lithium diffusion distance available in short CNTs. Doping with heteroatoms is another way to improve the electrochemical performance of CNTs. Generally nitrogen or boron is found to be a suitable element for doping into CNTs due to their appropriate atomic size [212]. It was proved both experimentally and theoretically that nitrogen doping can help in improving the electrochemical performance of CNTs as anode material in Li-ion batteries [213-216]. The nitrogen doped CNTs generate ample quantity of defects and change the electronic structure due to higher electronegativity of N-atom which helps in faster lithium diffusion. Furthermore, N-doping leading to more disordered carbon structure with extrinsic defects results in improved lithium intercalation. Moreover, N-doped CNTs demonstrated better electrochemical performance in terms of high capacity, improved cycle life and better stability [213, 217, and 218].

1.4.2.1.3 Graphene

Graphene is a basic structural unit of graphite and forms as a two-dimensional carbon sheet of one atom thickness. Graphene is the rising star material in a number of fields such as, chemical, biological, physical and engineering sciences. Furthermore, due to its

high electrical conductivity, high mechanical stability (Young's modulus ~ 1 T Pa), superior thermal conductivity (~ 5×10^3 W m^{-1} K^{-1}) and very high surface area (2600 m^2 g^{-1}) makes graphene a suitable candidate for anode material in Li-ion batteries [219-221]. Graphene can provide both of the surfaces, front and back, for hosting Li-ion via adsorption [222]. The theoretical capacities reported for graphene are quite controversial and vary significantly with synthetic methods. The experimental specific capacity of graphene has been achieved up to ~ 1000 $mAhg^{-1}$ which is much higher than commercialized graphite [223, 224]. This outstanding capacity is attributed to the random aggregation of graphene. The random aggregation of graphene creates more space or voids which are available for the intercalation/de-intercalation of extra lithium during charging and discharging.

D. Pan *et al.* have synthesized disordered graphene using different synthetic routes such as, hydrazine reduction, low temperature pyrolysis and electron beam irradiation to study the Li-storage properties systematically. The results presented by D. Pan *et al.* have confirmed the enhanced capacity, between 790 – 1050 $mAhg^{-1}$, as delivered by the disordered graphene mainly due to the availability of additional reversible storage sites such as, edges and other defects [223]. P. Lian *et al.* have obtained specific capacities as high as 1264 $mAhg^{-1}$ for the high quality sheets prepared from the oxidation of graphite powder followed by rapid thermal expansion in nitrogen atmosphere [225]. Graphene nano-sheets prepared by the exfoliation of bulk graphite powder showed a specific capacity of 540 $mAhg^{-1}$. The specific capacity could be further increased up to 730 $mAhg^{-1}$ and 784 $mAhg^{-1}$, respectively, by the incorporation of CNTs and fullerenes (C_{60}) into the graphene nanosheets [226]. X. Chen *et al.* have proposed a scalable self-assembled strategy to produce bio-inspired hierarchical structure of graphene nanosheets. With the hierarchical honeycomb structure a large specific capacity of ~ 1150 $mAhg^{-1}$ after 50 cycles was achieved [227]. Many research groups have studied the doping of heteroatom in graphene. These reports confirm the doping of heteroatoms such as, nitrogen, phosphorous, boron and sulfur to enhance the specific capacity and cyclability of graphene nanosheets [228-233].

Despite several advantages, the main problem associated with graphene that restricts its use as anode material in Li-ion batteries are (1) its large irreversible capacity at the first cycle and (2) the continuous capacity fading during cycling. However, all the reported

capacities for graphene anode material are much higher than commercial graphite, demonstrating its practicality in commercial Li-ion batteries [234, 235].

1.4.2.2 Transition Metal Oxide Based Anode Materials

1.4.2.2.1 Titanium Dioxide (TiO_2)

Titanium dioxide (TiO_2) was investigated extensively as an anode material for Li-ion batteries due to its low cost, ready availability and environmental benign nature. A number of polymorphic forms of TiO_2 exist. Among them, TiO_2-B (bronze), anatase and rutile are considered as promising anode material for Li-ion batteries [236-238]. The intercalation/de-intercalation of Li-ions in TiO_2 occurs in the voltage range of 1.4 – 1.8 V. The high theoretical capacity of 330 $mAhg^{-1}$ for TiO_2 corresponding to one electron transfer made TiO_2 a highly competitive candidate to replace graphite anodes in Li-ion batteries [239].

Based on high Li-ion insertion capacity and fast insertion-extraction reactions all the polymorphic forms, namely, anatase, rutile and TiO_2 (B) were investigated for their anode performance in Li-ion batteries. The reversible lithium insertion in the anatase phase at ~ 1.78 V with 0.6 lithiums provides a capacity of ~ 200 $mAhg^{-1}$ [240]. Although the rutile polymorph was first considered as poor lithium insertion material, however, nanosized rutile TiO_2 was reported with excellent capacities at higher rates [241-243]. TiO_2 (B), on the other hand, showed lithium insertion into the structure at 1.6 V. A high capacity, ~ 305 $mAhg^{-1}$, corresponding to 0.7 mol lithium per mol of TiO_2 has been reported for the first cycle with reversible capacities of 200–300 $mAhg^{-1}$ after 100 cycles [244-246].

The insertion of extra Li^+ ion is strictly related to nanosize, porosity and dimensions [252]. Moreover, bulk anatase was reported to have a reversible capacity of 168 $mAhg^{-1}$ corresponding to the transfer of 0.5 moles of Li per mole of TiO_2 [251, 253]. A number of studies such as downsizing the TiO_2 [254], preparing high surface area TiO_2 [255], carbon coating [256, 257], metal coating [258, 259] and making conductive network [260, 261] have been carried to enhance the electrochemical performance and specific capacity.

Rutile polymorph is the stable form among other polymorphs of TiO_2. Rutile form is formed by heating anatase TiO_2 at a temperature > 700 °C. Many research group studied the

Li transport mechanism in rutile TiO_2 and demonstrated the anisotropic nature of Li transport. The outcome of some experimental and theoretical studies showed that Li diffusion coefficient along *c*-axis is nearly 2.5 times greater than that of the *ab*-plane [262-265]. The lithium storage capacity of microcrystalline rutile TiO_2 is not considerable (< 0.1 Li per TiO_2), however, nanosized rutile TiO_2 shows that about 0.5 mole of Li per mole TiO_2 can be extracted in the voltage range 1-3 V [266, 267]. Hu *et al.* have reported significant improvements in the amount of inserted Li using nanosized needle like rutile TiO_2 [242]. Reddy *et al.* have showed that 1 mole Li per mole of TiO_2 could be inserted using nanosized rutile phase prepared by sol-gel method [243]. Jiang *et al.* have demonstrated reversible insertion/extraction in the range of 0.6 – 0.7 moles per mole of TiO_2 for the commercial nano powder with particle size of 15 nm while 0.4 and 0.15 mol lithium could be inserted/extracted for per mol of TiO_2 with 30 and 300 nm particles, respectively [268]. Besides, intercalation/de-intercalation in the nanosized and mesoporous rutile TiO_2 has been reported to show reversible insertion/extraction of lithium [269].

TiO_2-B is also an electroactive polymorph of TiO_2. TiO_2-B form an open framework structure consisting corrugated sheets of edge and corner shared TiO_6 octahedra. Due to lower intercalation/de-intercalation voltage of Li-ions and high reversible capacity, TiO_2-B is considered as an active anode material for Li-ion batteries [239]. Marchand *et al.* were the first group to report the synthesis of TiO_2-B by H^+ ion exchange in $K_2Ti_4O_9$ and then heating the prepared hydrogen titanate at 500 °C [270]. The maximum lithium uptake for bulk TiO_2-B was found up to 0.8 mole Li per mole of TiO_2 upon first discharge cycle with stable reversible capacity corresponding to 0.3 – 0.6 mol Li per mole of TiO_2 [271-273]. To improve the lithium intake, much attention has been given to the synthesis of nanostructured TiO_2-B. TiO_2-B nanowires and nanotubes were synthesized by a simplified hydrothermal method using anatase TiO_2 and NaOH as a precursor of sodium titanate followed by H^+ exchange and heating processes [246, 274]. They have also shown the effect of heating time and temperature to produce the nanowires or nanotubes. TiO_2-B nanowires showed lithium intake up to 0.91 mole of Li per mole of TiO_2 corresponding to a capacity of 305 $mAhg^{-1}$ which is superior to anatase TiO_2 [275]. The lithium insertion properties of TiO_2-B was found to be different from anatase TiO_2. Graetzel *et al.* have demonstrated that lithium

storage in TiO_2-B is controlled by a pseudo-capacitive faradic process, whereas in anatase TiO_2 it was governed by solid state diffusion of Li-ions [276].

1.4.2.2.2 Lithium Titanium Oxide ($Li_4Ti_5O_{12}$)

In 1983 Murphy *et al.* were the first group to report the lithium intercalation property of $Li_4Ti_5O_{12}$ [277]. After that much attention has been given to investigate $Li_4Ti_5O_{12}$ as anode material for Li-ion batteries. $Li_4Ti_5O_{12}$ was considered to be a promising anode material due to its outstanding features such as, highly stable voltage plateau at ~ 1.55 V vs Li/Li^+, no volume change on cycling, long life and easy fabrication [278-281]. $Li_4Ti_5O_{12}$ can insert up to three Li-ions into the structure resulting into a theoretical specific capacity of 175 $mAhg^{-1}$. $Li_7Ti_5O_{12}$ formed after insertion of three Li-ions showed a negligible volume change, therefore, termed as zero strain material [280]. Petr Novák *et al.* have observed an increase of Ti–O bond length due to the insertion of lithium into $Li_4Ti_5O_{12}$ accompanied by a small decrease in the cell parameters leading to a little volume expansion upon Li insertion [281]. In spite of higher safety and durability, $Li_4Ti_5O_{12}$ have many drawbacks to be used as anode material in commercialized Li-ion batteries. The major drawbacks are its low electronic conductivity (10^{-8}–10^{-13} S cm^{-1}) [282] and low lithium diffusivity (10^{-9}–10^{-16} cm^2 S^{-1}) [283]. Moreover, the problem of gas evolution during charging/discharging process results in swelling of the battery which could be unsafe while a battery is in use [284].

Therefore, a number of strategies have been employed to enhance the performance of $Li_4Ti_5O_{12}$ anode material such as, morphology control, size control [285-288], carbon coating [289-291], carbon composite formation [292-295] and element doping [296-302]. K Hsiao *et al.* have studied different forms of $Li_4Ti_5O_{12}$ powders as an anode material for Li-ion batteries. They have shown that porous $Li_4Ti_5O_{12}$ with smaller particle size and high surface area gives high specific capacity at higher rates due to high electronic conductivity and short diffusion distance [286]. K Poeppelmeier *et al.* have synthesized three dimensionally ordered mesoporous (3 DOM) $Li_4Ti_5O_{12}$ using a template based method. These 3 DOM structures were found to have noticeable impact on the rate capability when the voids of the templates were under filled or partly filled [287]. A. K. Shukla *et al.* have demonstrated synthesis and electrochemical performance of highly porous flaky $Li_4Ti_5O_{12}$.

The synthesis of flaky $Li_4Ti_5O_{12}$ with high porosity was carried out using single step solution combustion method. A high capacity of 170 $mAhg^{-1}$ at 0.5 C rate, closer to its theoretical value, was achieved when tested as anode material in Li-ion batteries [288]. Y. Y. Xia *et al.* have used thermal vapor decomposition (TVD) method for coating nanothickness graphitized carbon on $Li_4Ti_5O_{12}$ particle surface. They showed that 5 nm carbon coated $Li_4Ti_5O_{12}$ has a better electrical conductivity of 2.05 S cm^{-1} along with high rate capability [289, 290]. Z. Yu *et al.* have prepared $Li_4Ti_5O_{12}$/graphitized carbon nanotube composites using a solid state method. The addition of graphitized carbon nanotubes have been shown to enhance the electrochemical performance of $Li_4Ti_5O_{12}$ due to formation of smaller particles and uniform conductive network [292]. S. Aoyagi *et al.* have demonstrated the synthesis of a nanocrystalline $Li_4Ti_5O_{12}$ grafted on to carbon nano fibers. The prepared composite could be cycled at super high rate ~ 300 C [295].

The doping of various types of elements into $Li_4Ti_5O_{12}$ has been studied by different research groups. T. F. Yi. *et al.* have investigated the effect of Na doping into $Li_4Ti_5O_{12}$. The lattice parameter of $Li_4Ti_5O_{12}$ was increased after Na doping while the particle size of the crystallites were decreased. Na doped sample with composition, $Li_{3.85}Na_{0.15}Ti_5O_{12}$, showed better cycling performance when compared with the pristine $Li_4Ti_5O_{12}$ [296]. An improvement in electronic and ionic conductivity with enhanced electrochemical performance was observed when $Li_4Ti_5O_{12}$ was doped with K-ion [297]. A simple hydrothermal method was used to synthesize nanoparticles of Mg-doped $Li_4Ti_5O_{12}$. Mg-doped sample showed a high capacity and long term stability [298]. The excellent electrochemical performance was demonstrated when $Li_4Ti_5O_{12}$ was doped with Ca. The $Li_{3.9}Ca_{0.1}Ti_5O_{12}$ showed a discharge capacity of 162.4 $mAhg^{-1}$, 148.8 $mAhg^{-1}$ and 138.7 $mAhg^{-1}$ after 100 cycles at 1C, 5C and 10 C rate, respectively [299]. The electrochemical performance of $Li_4Ti_5O_{12}$ doped with Cu, La, F and Fe has also been investigated [300-302].

1.4.2.2.3 Lithium Vanadate (Li_3VO_4)

Lithium vanadate (Li_3VO_4), was first investigated by H. Q. Li *et al.* in 2013 [303], and proposed it as a promising anode material for Li-ion batteries due to its high capacity, safe voltage and low cost. The insertion/de-insertion of lithium ions into Li_3VO_4 occurs in between 0.5–1.0 V, thus alleviating the possible deposition of lithium metal on to the anode

side when the battery is being charged and discharged. The theoretical capacity of Li_3VO_4, 394 $mAhg^{-1}$, is higher than that of graphite and $Li_4Ti_5O_{12}$, which are the most successful anode materials used in commercialized Li-ion batteries [304]. Despite its low electronic conductivity [< 10^{-10} S m^{-1}] [305, 306], there is considerable enhancement in specific capacity and cycle life of Li_3VO_4 [303, 307]. The continuous improvement in the electrochemical performance of Li_3VO_4 is due to the research efforts made in improving the electrical conductivity and enhancing the Li-ion diffusivity. Here, we shed light on different methodologies which helps in improving the electrical conductivity and Li-ion diffusivity of Li_3VO_4.

Hollow structured Li_3VO_4 microboxes wrapped by the porous graphene nanosheets were prepared by Y. Shi *et al.* using one-pot hydrothermal method at 180 °C for 40 h [19]. The enhancement in the electrochemical performance of the hollow structured Li_3VO_4 microboxes has been attributed to its microstructure that allows extra space for lithium storage and shows less strain during insertion/de-insertion of Li and reduces the diffusion distances for lithium ion migration [305, 308]. Spherical shaped Li_3VO_4 with particle sizes 0.2 – 2 μm was prepared by W-T. Kim *et al.* using ultrasonic spray pyrolysis with post calcinations showing a discharge capacity of 250 $mAhg^{-1}$ after 10 cycles at 0.5 C rate [309]. Q. Li. et al. have reported a composite of Li_3VO_4 with carbon nanotubes by a simple hydrothermal method comprising 13.76 wt% carbon nano tubes. The obtained screw cap like open hollow Li_3VO_4 demonstrated a discharge capacity of 355 $mAhg^{-1}$ at 0.25 C rate and extremely high rate cycling and long life with a reversible capacity of 250 $mAhg^{-1}$ after 2000 cycles at a rate of 2 A g^{-1}, which is attributed to highly conductive network and hollow structure [310]. A facile self-template method was employed to synthesize hollow shell-controlled Li_3VO_4-reduced graphene oxide (RGO) composite [311]. The composite delivered outstanding rate capability (201 mAh g^{-1} at 120 C rate) and superior high temperature stability (364.2 mAh g^{-1} after 1000 cycle at 10 C rate and 60 °C).

J. Liu *et al.* have reported ultrathin Li_3VO_4 nanoribbon-graphene sandwich like nanostructures with high storage capacities and rate capabilities. The unique morphology in which nano belts Li_3VO_4 (thickness about 3 nm) were incorporated in graphene nanosheets layer by layer alternatively resulting the hierarchical structure was claimed to be responsible

for high capacity and superior rate capability. G. Shao *et al.* have used high temperature ceramic method to prepare bulk Li_3VO_4 followed by high energy ball milling to obtain nanosized Li_3VO_4. The so obtained nanosized Li_3VO_4 was further carbon coated uniformly by high temperature CVD method. Although, the uniform carbon coated Li_3VO_4 thus obtained showed capacity of only about 160 $mAhg^{-1}$ at 0.5 C rate [313]. The electrochemical performance of surface amorphous oxygen deficient $Li_3VO_{4-\delta}$ was reported by L. Chen et al. [314]. The electrochemical performance of $Li_3VO_{4-\delta}$ showed pronounced enhancement as compared to Li_3VO_4 powder but a discharge capacity of 300 mAh g^{-1} was only achieved at the end of fifth cycle at 0.5 C [314]. A facile freeze drying method was developed by D. Zhao *et al.* to synthesize Li_3VO_4 nanoparticles embedded in highly porous carbon conductive network. The obtained product showed improved electrochemical performance in terms of specific capacity, cycle stability and rate capability [315]. A number of articles have reported the synthesis of different types of carbon composites with Li_3VO_4 to enhance the electrical conductivity which is necessary for improved capacity retention, high rate cycling and long life of the batteries [306, 310, 316-319].

The market of portable electronics is growing very rapidly. This has resulted in enormous consumption (nearly one quarter of the world production) of lithium by the battery manufacturers [320]. Supplies of Li are likely to be even further constrained if Li-ion batteries are adopted for large scale energy storage. Therefore, sodium ion batteries (NABs) have attracted much attention for large scale energy storage due to huge abundance, non-toxic nature and low cost of sodium resources. However, higher weight and larger size of sodium ion leads to lesser gravimetric and volumetric energy densities in NABs than that of LIBs [321-323]. For large scale energy storage systems energy density is not an acute issue, however, investigating a suitable “rocking chair” Na-ion battery will be enough to find place in the market for large scale storage, which would not be possible with Li-ion systems due to high cost and low abundance [324]. Thus, finding suitable electrode materials for NABs are also of importance in the contemporary battery research.

1.5 Materials Synthesis

Various synthetic methods have been used for the synthesis of different types of electrode materials such as, metal oxides, oxy-fluorides, metal phosphates and metal sulphates. Following are few commonly used methods for their synthesis.

- Solid state reaction
- Sol-gel
- Hydrothermal / Solvothermal
- Reactive grinding
- Microwave
- Sonochemical

It is known that the electrochemical performance of a material crucially depends on the method of its synthesis. In our present work, compounds are synthesized using different synthetic methods such as, solid state reaction, sol-gel or hydrothermal method. Some of the methods that are being employed in this investigation are briefly discussed herein.

1.5.1 Solid State Reaction Method

The solid-state reaction method is one among the most popular methods used for the synthesis of inorganic solids. In this method, stoichiometric quantities of starting materials, such as, metal oxides / carbonates / oxalates / acetates are weighed and ground thoroughly in an agate mortar for nearly an hour. The ground mixture is then transferred to an alumina, silica or platinum containers (crucible / boat) followed by heating them in a muffle / tube furnace at various temperatures and durations. Generally, solid state reactions are carried out at higher temperatures because the reactions are mostly diffusion controlled. Usually, due to the low diffusion coefficients of the solids, (in the order of 10^{-12} cm^2 s^{-1}) lower temperatures are not suitable for the reaction to happen. Moreover, it is a common practice to carry out reactions involving air / redox sensitive compounds in controlled gas atmospheres (argon/nitrogen). Often the reactant mixtures are ground in between two heating steps to breakdown the diffusion barrier between the grains of starting reactants and products. The repeated grinding and heating steps during the course of a solid state reaction

helps in the synthesis of phase pure materials. The nucleation process in the solid state reaction is slightly difficult due to structural differences between reactants and products, thus large amount of structural reorganization takes place to get to the final product by bond braking, reforming and migration of constituent elements.

Even though, solid state reaction comprises many drawbacks such as, difficulty in complete homogenous mixing of the starting compounds, large diffusion distances of the reacting solids, the reaction conditions are being worked out by trial and error method, due to its simplicity and easy accessibility of furnaces, it remains to be one of the most widely used method for the exploratory synthesis of new mixed metal oxides even today.

1.5.2 Sol-gel Method

Sol-gel method is a wet chemical technique commonly employed in the field of material science for the preparation of solid materials from small molecules. As compared to the conventional solid state reaction, sol-gel method results in the formation of compounds with small particle sizes and sometimes better purity due to homogeneous atomic level mixing of the reactants in solution phase. In this method, the starting materials are first dissolved in water or suitable solvents in presence of a complexing agent. Subsequently, a gel like network is formed by aging process or evaporation of the water/solvent. The gel is further dried, decomposed and finally heated at elevated temperatures (generally lower than those employed for solid state reactions).

1.5.3 Hydrothermal / Solvothermal Method

The word hydrothermal was first used by geologist and mineralogists. In the hydrothermal method water /a solvent at a temperature above its boiling point and a pressure higher than the atmospheric pressure serve as a medium for speeding up the reactions between the solids. The water/solvent serve as reaction medium as well as generates pressure in the reaction vessel through its vaporization. The temperature employed in the hydrothermal/solvothermal synthesis are generally much lower (up to 200 °C mostly) than used in conventional solid state or sol-gel synthesis. A variety of compounds with controlled morphology and particle size can be obtained by hydrothermal/solvothermal methods by

changing reaction parameters such as, temperature, pH and concentration of the reactants. In a typical hydrothermal/solvothermal method, the starting materials are initially dissolved in water / any solvent. The resulting solution is then transferred into a Teflon lined autoclave and heated at a temperature above the boiling point of water/solvent for various durations. The heating can be carried out using a conventional oven.

1.6 Objective of the Present Study

In view of the foregoing, development of new oxides, oxy-fluorides and phosphates or improvement in the ionic-electronic conductivity of candidate electrode materials with enhanced electrochemical performance are timely and highly desirable in contemporary battery research. Toward this, efforts are being devoted for the synthesis of new layered oxy-fluorides based on NCM oxide compositions. Herein, Li-rich compositions together with large amount of fluoride incorporation in NCM based layered rock-salt oxide have been envisaged. For exploring new layered phosphates, electrochemical performance of a structurally characterized layered phosphate, namely, $Na_3Fe(PO_4)_2$, have been explored. Moreover, emphasis has also been given for the development of simple, short and faster synthetic routes that are easy to adopt for commercial purposes. Moreover, the usefulness of hydrothermal/solvothermal methods in exploiting the microstructural properties of oxides has been exercised for Li_3VO_4, a potential high capacity insertion anode material. Different synthetic methodologies are being employed depending on the type/nature of the compound and specific problem being addressed, such as, exploratory synthesis, microstructural modification or devising a faster alternative method. The outcomes of the systematic investigations are presented in subsequent chapters.

CHAPTER – 2

Characterization Techniques

Characterization Techniques

Various characterization techniques are used to characterize all the synthesized compounds such as metal oxides, oxy-fluorides and phosphates reported in the present study. These include powder X-ray diffraction (P-XRD), field-emission scanning electron microscopy (FE-SEM), energy dispersive X-ray spectroscopy (EDS), transmission electron microscopy (TEM), selected area electron diffraction (SAED), Raman spectroscopy, thermogravemetric analysis (TGA), X-ray photoelectron spectroscopy (XPS), cyclic voltammetry (CV) and galvanostatic charge-discharge studies. This chapter gives a brief overview of sample preparation and procedures of analysis using the above analytical techniques.

2.1 Powder X-Ray Diffraction (P-XRD)

P-XRD is the most frequently used non-destructive technique employed to characterize solid compounds. It is generally helpful in the differentiation of amorphous and crystalline compounds, confirming the phase purity of synthesized compounds, determination of crystal structure, crystallite size (grain size), and preferred orientation of the powdered solid samples. The diffraction data is recorded within a desired range of angle (2θ) and all the diffraction peaks present in the P-XRD pattern are analyzed. The analysis of the diffraction data is used to identify the crystal system and structure of solid samples since each compound with a definite crystal structure has a set of unique *d*-spacings. The relationship between the wavelength of the incident X-ray beam and the lattice spacing in the crystalline compound could be described by Bragg's Law:

$$n\lambda = 2d\ sin\theta \tag{2.1}$$

Where, n is an integer and it represents the order of diffraction, λ is the wavelength of the incident X-ray beam, d is the interplanar distance between atomic planes in a crystal, and θ is the angle of incidence [325].

In this study, P-XRD technique was used to monitor the reaction progress and to confirm the phase purity of the as synthesized samples. P-XRD data was collected for powder

samples at a scanning rate of 2° min^{-1} for the 2θ range of 10 – 90°. In the present study, P-XRD measurements were performed using a Bruker AXS D8 Advanced diffractometer equipped with graphite monochromatized CuKα (1.5406 Å) radiation and operated at 40 KV and 30 mA. The software EVA® and DIFFRAC^{plus} were used for data evaluation and input instrumental parameters. To collect P-XRD data, approximately, 0.5 g of sample was placed in the sample holder and a clean glass slide was used for making the sample surface smooth.

The obtained P-XRD patterns of the synthesized compounds were first compared with the standard powder diffraction files (PDFs) available in the JCPDS (Joint Committee on Powder Diffraction Standard) database to confirm the phase purity of the synthesized compound. P-XRD pattern indexing and least-squares refinement of the lattice parameters were performed using PROZSKI program [326]. Using the refined lattice parameters, the simulation of the P-XRD pattern was carried out using the POWDERCELL program [327]. The input data such as, positional and thermal parameters and site occupancy factors (SOFs) were used from reference structural model. In POWDERCELL program, the cation distribution and the SOFs were adjusted as per the relevant compositions.

The Rietveld structure refinements were performed with slow scan P-XRD data collected for ~ 8 h in 10 – 90° angular range with a step size of 0.0188° and a scan speed of 6 sec per step using FULLPROOF program suite [328]. In the refinement process, first the background co-efficient along with zero shift and cell parameters were refined. When the program shows divergence, profile and shape parameters were refined one at a time. At the final stage of refinement, positional and thermal parameters were refined systematically starting from the heavier atoms followed by the lighter ones. Sometimes thermal parameters of oxygen atoms were kept fixed (same as given for the reported model system) in the refinement to avoid the divergence. Finally, structure was drawn using refined atomic, positional and thermal parameters with the help of Diamond and Vesta softwares.

2.2 Field–Emission Scanning Electron Microscopy (FE-SEM) and Energy-dispersive X-ray Spectroscopy (EDX)

The morphology and chemical composition of the compounds were analyzed using FE-SEM, a type of electron microscopic technique, generally employed to study the microstructure of powder samples [329]. In this technique, the samples are bombarded with a beam of high energy electrons, and the signals are collected and identified from the coming secondary electrons, characteristics X-rays, back scattered electrons, transmitted electrons, lights or specimen currents. The secondary electrons that are produced on the sample surface were detected by the secondary electron detector. The amplitude of the secondary electron signal varies with time according to the topography of the specimen surface. Then, the signal is amplified and used to display the corresponding specimen surface information, which can offer very high resolution images revealing details less than 1 nm in size. The intensity of emitted X-rays by each element present in the sample was used to determine the elemental ratio and chemical composition.

In present work, morphological studies of the all compounds were performed with Zeiss FE-SEM, Ultra plus55, operating at an accelerating voltage of 20 kV. The elemental compositions and mapping analysis of the compounds were carried out using EDX technique. Initially, a large scanning area was selected for elemental analysis followed by reducing the scanning area to individual crystallites. Several locations were scanned taking spots and small rectangular areas to ascertain the local and overall compositional homogeneity in the analyzed samples. Further, the compositional homogeneity of each crystallite was established by analyzing several spot within the crystallite. The elemental mapping analyses were carried out in the scanned rectangular area to confirm the homogeneous distribution of all elements present in the sample. For the sample preparation, aluminum stubs were clean thoroughly with isopropyl alcohol and dried by hot dryer. The powder samples were tarnished on a carbon tape pasted on aluminum stubs and gold sputtering was carried out in the argon atmosphere to ensure gold coating for good electrical conductivity.

2.3 High Resolution Transmission Electron Microscopy (HR-TEM)

In HR-TEM, high energy electrons emitted from a tungsten filament of the electron gun, operated at an accelerating operating voltage of 300 kV, are allowed to pass through a thin layer of sample deposited on carbon coated copper grids [330]. The electron gun in HR-TEM instrument contains different types of electromagnetic lenses which are used to regulate the size and angular spread of electron beam to be focused on the material. The imaging of solid samples is carried out by the transmitted electrons from the thin layer of the sample. The lattice fringes obtained at high magnifications were analyzed to determine the lattice periodicity. Selected area electron diffraction (SAED) patterns were collected to confirm the amorphous and crystalline nature of the samples as well as to establish the crystal structure. While the presence of bright spots in the SAED patterns represents the crystalline nature, hollow ring signifies amorphous nature of samples. The indexing of diffraction spots were carried out to ascertain the crystal structures.

The TEM images and SAED patterns were recorded with a FEI TECNAI G^2 microscope operated at 300 kV. For the sample preparation, nearly 5 mg of finely powdered sample was dispersed in 2 – 3 mL of ethanol in a pestle mortar and ground slowly for 5- 10 minutes to prepare homogeneous suspension. Then, ~ 20 μL of the suspension was smeared on a carbon coated copper grid with the help of a micropipette and aged in air for drying.

2.4 Raman Spectroscopy

Raman spectroscopy is a vital spectroscopic technique used for the analysis of rotational, vibrational and other low frequency modes in molecular systems. It can be used as complementary tool of infrared spectroscopy (IR). The Raman spectroscopy is a light scattering technique, whereby the interaction between the photon of monochromatic light (usually from a laser) and the electron cloud of a sample produces scattered radiation of different wavelengths. The interaction of the monochromatic radiation with a solid sample results in both elastic (Rayleigh scattering) and inelastic scattering (Stokes and anti-Stokes Raman scattering). After this interaction, the shift in the energy of incident radiation is observed which could be higher or lower than the incident radiation. The energy shift is detected in the form of frequency or wavelength and used for investigating the chemical and structural features of the samples.

In the present study, Raman measurements were performed using a Renishaw inVia Raman spectrometer (Serial no. 021R88) equipped with an Argon ion laser (514 nm) having 1 cm^{-1} spectral resolution, a confocal microscope with different objective lenses and a CCD detector.

2.5 Thermogravimetric Analysis (TGA)

Thermogravimetric analysis (TGA) is a characterization technique used to determine change or loss in weight of a sample as a function of time and temperature in a particular atmosphere or vacuum. TGA can be used to determine the thermal stability of compounds as well as to measure the amount of carbon content. The carbon content in the composite materials can be determined by heating the samples at higher temperatures in the air atmosphere. From the TG curves, the weight loss is calculated and the corresponding carbon content is determined. If there is no weight loss or gain for a compound subjected to TG analysis, the compound is considered as thermally stable in the temperature range of study. In the present work, TGA analysis was carried out using SII 6300 EXSTAR at a heating rate 5° min^{-1} in air atmosphere.

2.6 X-Ray Photoelectron spectroscopy (XPS)

XPS is a versatile technique for the analysis of surface chemical composition of solid samples. Generally, the monochromatic low energy X-ray of 1486.6 eV (with Al−K_α radiation source) or 1253.3 eV (with Mg−K_α radiation source) are used to stimulate the emission of photoelectrons from the material surface. To extract information about the chemical composition and identification of elements present on the surface up to 10 nm thickness, kinetic energy of emitted photoelectrons is measured using a hemispherical analyzer.

In the present work, the chemical composition and oxidation state of the elements present in solid samples were investigated using "PHI-5000 Versa Probe III, ULVAC-PHI INC" XPS spectrophotometer equipped with hemispherical analyzer and a multichannel detector. For the analysis, sample was mounted on a carbon tape and kept in sample introduction chamber under vacuum for 12 h. The analysis was carried out under ultra-high vacuum condition using monochromatic Al−K_α radiation source ($h\nu$ = 1486.6 eV). The

binding energy scale for $V2p_{3/2}$, $Ni2p_{3/2}$, $Co2p_{3/2}$, $Mn2p_{3/2}$, O_{1s} and F_{1s}were referenced with respect to C_{1s} at 284.8 eV

2.7 Surface Area Measurement

Gas sorption is a well-recognized technique used to analyzing the textural properties such as specific surface area, pore volume and pore size distribution of the porous materials [331]. For textural analysis, generally N_2 and Ar inert gases have been used as a probe molecule at their boiling temperature i.e. 77 and 87 K, respectively. Brunauer–Emmett–Teller (BET) methods have been employed to estimate the specific surface area by calculating the amount of gas adsorbed over the surface of solid. The linear form of BET equation is expressed as shown in equation 2.2.

$$\frac{1}{V[(P_0/P)-1]} = \frac{C-1}{V_m C}\left(\frac{P}{P_0}\right) + \frac{1}{V_m C} \tag{2.2}$$

where, P_0 and P are the saturation and equilibrium pressure of adsorbate at the temperature of adsorption, V is the adsorbed gas quantity (in volume), V_m is the monolayer adsorbed gas quantity and C is the BET constant. The BET equation given below, equations 2.3 and 2.4, can be used to determine the total surface area (S_{total}) and specific surface area (SA_{BET}) of the samples.

$$S_{total} = \frac{V_m N_s}{V} \tag{2.3}$$

$$SA_{BET} = \frac{S_{total}}{a} \tag{2.4}$$

where, V is the adsorbate (probe as) molar volume, N is Avogadro's number, s is adsorbate cross section and a is adsorbent mass.

In the present investigation, Autosorb-iQ2, Quantachrome Instruments, USA gas sorption equipment was used to measure the N_2 sorption isotherms at 77 K using liquid N_2. Prior to gas adsorption analysis, the unwanted gases and moisture adsorbed on the adsorbent surface were removed by degassing the samples at 120 °C for 6 h. The range of relative pressure was obtained using Rouquerol plots, used for the calculation of SA_{BET} by BET model. The pore size distribution (PSD) profiles were drawn using Density functional theory (DFT) with suitable carnel. The estimation of total pore volume was carried out from adsorption branch at a relative pressure of 0.90 or 0.99.

2.8 Electrochemical Impedance Spectroscopy

Electrochemical impedance spectroscopy is a technique used to study electrochemical processes such as, electron transfer, mass transfer and chemical reactions. The impedance spectrum consists two main parts, one is low frequency semicircle resulting from kinetic processes and the other one is the high frequency tail due to the diffusion processes within the materials.

In the present work, electrochemical impedance measurements were performed using galvanostate/potentiostate (model Multi Autolab M204) based on a three electrode assembly in the frequency range 0.1 Hz to 100 kHz with ±10 mV applied potential perturbation. The three electrode assembly comprises synthesized materials mixed with graphite as working electrode, Ag/AgCl (3 M KCl) as the reference electrode, Pt wire as the counter electrode and 10 mM $K_3[Fe(CN)_6]$ containing 0.1 M KCl as the electrolyte solution.

2.9.1 Electrode Preparation and Coin Cell Assembly

To test the electrochemical performance of the samples, cathode films of the active materials were first made on an aluminum current collector. The active material was subjected to ball-milling thoroughly after mixing with super P conductive carbon in a SPEX 8000 miller for 3 hours to reduce the particle size. Poly-vinylidene fluoride (PVDF) was then added to the active material as the binder and an optimum amount of N-methyl-2-pyrrolidone (NMP) was

added to dissolve the PVDF. The resulting slurry was further ball milled for another 20 minutes to obtain a homogeneous viscous mixture. The ratio of the active material, conducting carbon, and the binder in the cathode mix was 75: 15: 10. The cathode mix was then spread as a film of uniform thickness with the help of a glass rod onto a flat sheet of carbon-coated aluminum current collector and transferred into a vacuum oven and dried overnight at 85°C.

For electrochemical tests, CR2032 type coin cells were fabricated. The composite cathode film was cut into circular disks (3/8 inch diameter) with 4.0 – 5.0 mg of active material loading and transferred into an argon filled glove box with an oxygen concentration below 2.0 ppm. The cathode disk and Li anode (0.75 mm thickness Li ribbon cut into circular disks) were assembled in the coin cell casing with a Celgard® 2325 circular sheet placed between the two electrodes as the separator. The electrolyte, 1 M solution of $LiPF_6$ in DMC–EC (1:1) was then added and the cell was sealed with a coin cell crimper. The prepared cells were aged for equilibration for about 12 hours before electrochemical testing.

2.9.2 Electrode Preparation and Teflon Cell Assembly

The electrochemical measurements were carried out on laboratory fabricated Teflon half-cells with Li-metal counter electrode, 1 M $LiPF_6$ in 1:1 (v/v) ethylene carbonate (EC)-dimethyl carbonate (DMC) (Mitsubishi Chemical Co., Japan) electrolyte solution and Polypropylene (Celgard 2300) as separator. The slurry of electrode materials was prepared by mixing 80 wt% of active material, 10 wt% of conducting agent (acetylene black) and 10 wt% of binder (polyvinylidene fluoride, PVDF). The obtained slurry was pasted onto copper foil followed by drying in a vacuum oven at 80 °C for 12 h to remove the solvent before pressing. After drying and pressing, the electrodes were cut into circular discs having a diameter of ~ 10 mm. Cells were assembled inside an Argon filled glove-box (MBRAUN, MB 200G Unilab, Germany) maintaining oxygen and moisture at a controlled level of < 1 ppm.

2.10 Electrochemical Characterization

2.10.1 Cyclic Voltammetry

Cyclic voltammetry (CV) has been employed to investigate the thermodynamics and kinetics of the electron transfer at the interface of working electrodes in an electrochemical reaction. In the CV measurement, current-voltage behavior of working electrode was analyzed within a fixed potential window at a constant potential scan rate. In a typical scan, the current increases slowly and peak features appear at appropriate potentials where redox reactions take place. In CV, scan rate is the change of potential as a function of time. The relationship between the scan rate and peak current (i_p) follows the Randles-Sevcik equation:

$$i_p = 2.65 \times 10^5 n^{3/2} A C D^{1/2} v^{1/2} \tag{2.5}$$

where, n is number of electrons involved in the half-reaction, A is electrode area, C is the analyte concentration, D is the analyte diffusion co-efficient, v is the potential sweep rate.

In the present study, Cyclic voltammograms were obtained using a PAR EG&G potentiostat-galvanostat model 273 and Arbin cycler (MB 200G, Arbin Instruments, USA) battery tester in the potential range of 1.5 – 4.0 V (vs. Li/Li^+) with a scan rate of 0.05 mV s^{-1}.

2.10.2 Galvanostatic Charge-Discharge Studies

The charge-discharge capacities of the working electrode can be calculated by the total charge in the form of current multiplied by the time of charge-discharge process. The parameters of charge-discharge process were chosen by the theoretical capacity of the analyzed materials. Here, voltage composition profiles were obtained using galvanostatic charge-discharge experiments on an Arbin Instruments battery tester, model BT2043 and Arbin cycler (MB 200G, Arbin Instruments, USA) battery tester, on the same potential limits as CV at various C-rates.

CHAPTER – 3

Rock Salt Ordered Lithium-Rich NCM Type Oxy-Fluoride as High Voltage Cathode Material for Lithium-Ion Batteries

Rock Salt Ordered Lithium-rich NCM Type Oxy-fluoride as High Voltage Cathode Material for Lithium-Ion Batteries

3.1 INTRODUCTION

Vision for the electrification of road transport is gaining momentum due to rapid depletion of fossil fuel reserves and to up keep the environmental health of densely populated cities by reducing the CO_2 levels in the air [332]. For this purposes, US Department of Energy (DoE) and automobile industries have set up a goal to develop a battery of high energy density, ~ 300 Wh/L and 250 Wh/Kg with a cost of $ 125/kWh, to drive a mid-sized sedan up to 300 miles [333]. Li-ion batteries, an established technology powering all type of portable electronic devices, are now ready to power the electric vehicles due their high gravimetric and volumetric energy density [334-339]. Further improvements in the energy density and low cost production are the major issues to achieve the goal. The anode, cathode and electrolyte materials are the key components that need to be improved to enhance overall performance of Li-ion batteries such as, energy density, power density, life time and safety [340, 341, 336-338]. It is imperative that new generation of electrode materials need to be developed or existing materials must be improved significantly for the use of LIB technology for large scale electric vehicles (EV) and energy storage systems or load leveling applications [342, 343]. Till date, a conventional Li-ion battery uses $LiCoO_2$, $LiNi_{0.8}Co_{0.15}Al_{0.05}O_2$, $LiNi_{1/3}Mn_{1/3}Co_{1/3}O_2$ or $LiMn_2O_4$ as cathode materials. Typically, a $LiCoO_2$ cathode can deliver a capacity of 150 mAh g^{-1} due to the utilization of ~ 55-60 % lithium in the structure [344, 345]. Therefore, relatively lower energy density of the presently used cathode materials is the main obstacle in the development of high energy density Li-ion batteries which could be used for large-scale transportation and stationary energy storage [345].

Since nearly three decades, electrochemists were trying to invent an alternative to conventional layered $LiCoO_2$, a high specific energy cathode material with long life and better safety. During the time, two other series of compounds, namely, the olivine type phosphates ($LiMPO_4$; M = Fe, Mn, Co and Ni) and the spinel type metal oxides (LiM_2O_4; M

= Mn, Ni and Co) were developed and added in the list of cathode materials. Although both the materials have found commercial application in transportation and utility scale stationary storage, they suffer from low capacity [346, 347]. Therefore, $LiMO_2$ type layered materials with high theoretical capacity, ~ 270 $mAhg^{-1}$, deserves further optimization to get high energy density Li-ion battery to meet the requirements of high energy applications. Layered $LiNiO_2$ [348-350] and $LiMnO_2$ [351-353] was considered promising cathode materials for Li-ion batteries due to their high theoretical capacity and low cost. $LiNiO_2$ have some major drawbacks such as, complex synthesis method to prepare stoichiometric compound and structural degradation during electrochemical cycling [354]. On the other hand, $LiMnO_2$ shows phase transition to spinel structure during charge-discharge cycling [355].

In recent times, a great success has been achieved in the investigation of high capacity cathode material with safe and long electrochemical cycling. The nickel based layered $LiM_{1-x-y}M_xM_yO_2$ (M = Ni, Co and Mn) compounds comprising nickel, cobalt and manganese in variable amounts are considered as promising cathode candidates for high capacity Li-ion batteries [356]. It was widely established that substitution of nickel by both cobalt and manganese have profound effect on the electrochemical performance of nickel based cathode materials such as, improving the reversible capacity retention by reducing Li/Ni mixing and enhancing the structural stability [357, 358]. Liu *et al.* were the first to prepare a solid solution, $LiNi_{1-x-y}Co_xMn_y$ ($0 \leq x \leq 0.5$, $0 \leq y \leq 0.3$), by heating $LiNi_{1-x-y}Co_xMn_y(OH)_2$ and $LiNO_3$ in oxygen atmosphere. Among the various compositions of $LiNi_{1-x-y}Co_xMn_y$ ($0 \leq x \leq 0.5$, $0 \leq y \leq 0.3$), $LiNi_{0.8}Co_{0.2}O_2$ and $LiNi_{0.7}Co_{0.2}Mn_{0.1}$ were found to have good initial capacity and cycle life [359]. After that, Ohzuku and Makimura synthesized $LiNi_{1/3}Co_{1/3}Mn_{1/3}O_2$ using solid state reaction method, showing a high capacity of 150 mAh g^{-1} when cycled in between 2.5 – 4.3 V and 200 mAh g^{-1} when cycled up to 4.6 V [360]. A number of synthetic methods were employed to improve the phase purity and uniform cation distribution of $LiNi_{1/3}Co_{1/3}Mn_{1/3}O_2$ such as, solid state [360], co-precipitation of triple hydroxides [361] and sol-gel [362, 363]. The ability of Ni^{2+} to oxidize easily up to Ni^{4+} without oxygen release in the nickel based ternary oxide cathode materials is responsible for their higher capacity as compared to $LiCoO_2$. Therefore, an increase in the amount of Ni content has mostly resulted in higher specific discharge capacity. But, the thermal stability and capacity retention decreases subsequently with increasing Ni content

[364, 365]. Beside these disadvantages, researchers have tried to optimize the compositions of nickel based layered transition metal oxides to get high energy density Li-ion battery with high safety and long life. Among them, $LiNi_{0.5}Co_{0.3}Mn_{0.2}O_2$ [366-369], $LiNi_{0.6}Co_{0.2}Mn_{0.2}O_2$ [370-372], $LiNi_{0.7}Co_{0.15}Mn_{0.15}O_2$ [373, 374] and $LiNi_{0.8}Co_{0.1}Mn_{0.1}O_2$ [375-378] are considered as most promising cathode candidates for next generation high energy density Li-ion batteries. Among different strategies, lithium-rich compositions, $Li_{1+x}MO_2$ and $Li_{1+x}(Ni,Co,Mn)O_2$ [379-381] are extensively being studied, in addition to anionic substitutions by fluoride to some extent [382, 383]. Herein, we envisage a new Li-rich NCM composition with a significant amount of fluoride substitution, to enhance the structural stability mediated by increased covalency of F^- and retain 2D order and reduce Li/Ni mixing by increasing Li-content. Furthermore, in absence of impeding Ni ions in the Li-layer in an ordered 2D structure, the Li^+ diffusion would be facilitated to a significant extent, thereby improving the cell performance. The details of its synthesis, structural and compositional characterization and the Galvanostatic charge-discharge studies in half-cell mode *vs* Li^+/Li are described in this chapter.

3.2 EXPERIMETAL SECTION

3.2.1 Materials and Synthesis

The synthesis of $Li_{1.25}Ni_{0.25}Co_{0.25}Mn_{0.25}O_{1.5}F_{0.5}$ was carried out using a conventional high temperature solid state reaction. For the synthesis of $Li_{1.25}Ni_{0.25}Co_{0.25}Mn_{0.25}O_{1.5}F_{0.5}$, stoichiometric amounts of Li_2CO_3 (Sigma-Aldrich, purity ≥ 98 %), LiF (Himedia, purity ≥ 98 %), $NiC_2O_4.H_2O$, $CoC_2O_4.H_2O$ and $MnC_2O_4.H_2O$ were taken in an agate mortar and ground thoroughly for one hour to ensure the homogeneous mixing of all the constituents. The resulting mixture was transferred to an alumina boat and heat treated at 500 °C for 6 h followed by 850 °C for 24 h with intermittent grinding. The reactions were carried out in air keeping the heating rate at 4 °C min^{-1} in the first step. Metal oxalates of nickel, cobalt and manganese were prepared by reacting nitrate salts of the corresponding metals (Nickel (II) nitrate hexahydrate, SRL, purity ≥ 99 %, Manganese (II) nitrate tetrahydrate, Sigma-Aldrich, purity ≥ 97 %, Cobalt (II) nitrate hexahydrate, Sigma-Aldrich, purity ≥ 98 %) with oxalic acid (Oxalic acid dihydrate, Merck, purity ≥ 99 %) in 1:1 molar ratio.

3.2.2 Electrochemical Measurement

For electrochemical measurements a half-cell was fabricated by following the procedures as described in Chapter-2. For the cell fabrication 1 M $LiPF_6$ in 1:1 (v/v) ethylene carbonate (EC)-dimethyl carbonate (DMC) (Mitsubishi Chemical Co., Japan) was used as electrolyte and Polypropylene membrane (Celgard 2300) was used as the separator. The slurry of the active electrode material was prepared by mixing 80 wt% active material with 10 wt% acetylene black (as conducting agent) and 10 wt % polyvinylidene fluoride (as binder). The obtained slurry was pasted onto aluminium foil followed by drying in a vacuum oven at 80°C for 12 h. Cells were assembled inside an argon gas-filled glove-box by following the same procedure as already discussed in Chapter-2.

3.3 RESULTS AND DISCUSSION

3.3.1 Powder-XRD Analysis

The progress of the solid state reaction between Li_2CO_3, LiF and the metal oxalates was monitored by recording P-XRD patterns after each heating step. The P-XRD patterns recorded after the heating steps are presented in Figure 3.1. The P-XRD pattern obtained after heating at 850 °C for 24 h shows formation of highly crystalline $Li_{1.25}Ni_{0.25}Co_{0.25}Mn_{0.25}O_{1.5}F_{0.5}$. All the diffraction peaks are indexable in a rhombohedral cell with an ordered rock-salt structure similar to that reported for $LiNiO_2$ (JCPDS PDF # 09-0063) [384]. Thus, absence of any additional reflections due to any other impurity phases ascertained single phase $Li_{1.25}Ni_{0.25}Co_{0.25}Mn_{0.25}O_{1.5}F_{0.5}$ samples. The rhombohedral lattice parameters, a = 2.8594(3) and c = 14.226(2) Å, were obtained after least-squares refinement of all the diffraction lines using the PROSZKI program. Table 3.1 shows the indexed P-XRD data.

For initial scrutiny of the ordering of Li and transition metals in the structure, P-XRD pattern simulation has been carried out using the Powder Cell program. For the simulation, the model layered rock-salt structure of $LiNiO_2$ was used. Several models were constructed with varying degrees of disorder (5%, 10% and 15%) of Ni in the Li-layer by adjusting the Li and Ni occupancy accordingly in both the layers, in addition to the completely ordered model. The atomic parameters, occupancy and thermal parameters used in the simulation are

given in Table 3.2. The simulated P-XRD patterns along with the observed pattern are shown in Figure 3.2.

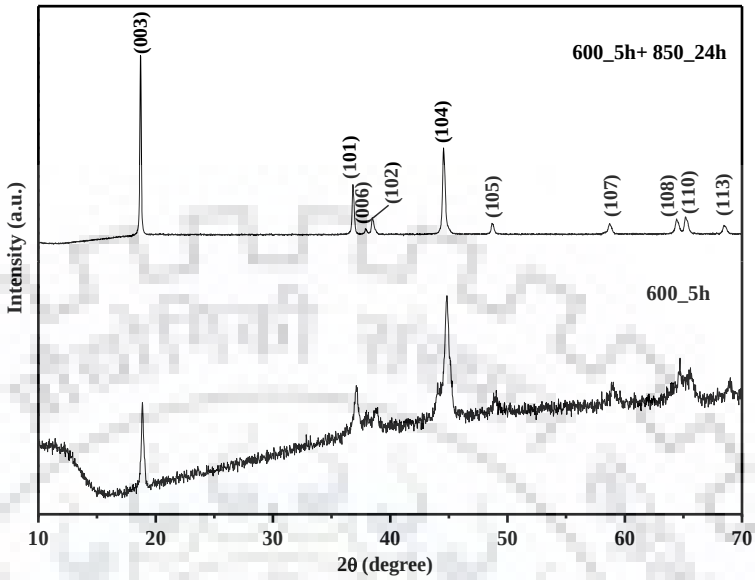

Figure 3.1 P-XRD pattern of $Li_{1.25}Ni_{0.25}Co_{0.25}Mn_{0.25}O_{1.5}F_{0.5}$.

Table 3.1 Indexed P-XRD data of $Li_{1.25}Ni_{0.25}Co_{0.25}Mn_{0.25}O_{1.5}F_{0.5}$

h k l	d_{obs}(Å)	d_{calc} (Å)	I_{obs}
0 0 3	5.416	5.444	100
1 0 1	4.109	4.122	36.8
0 0 6	3.879	3.892	2.5
1 0 2	3.649	3.659	9.1
1 0 4	3.156	3.166	47.7
1 0 5	2.726	2.721	5.9
1 0 7	2.468	2.471	5.8
1 0 8	2.387	2.384	7.2
1 1 0	2.228	2.230	8.3
1 1 3	2.117	2.119	4.8

a = 2.8594(3) and c = 14.226(2) Å.

Table 3.2 Atomic, Occupancy and Thermal Parameters used for the P-XRD Pattern Simulation of $Li_{1.25}Ni_{0.25}Co_{0.25}Mn_{0.25}O_{1.5}F_{0.5}$

For 0 % Ni in Li-layer

Atom	Wyckoff position	x	y	z
Li	3b	0.0000	0.0000	0.5000
Li	3a	0.0000	0.0000	0.0000
Mn	3a	0.0000	0.0000	0.0000
Co	3a	0.0000	0.0000	0.0000
Ni	3a	0.0000	0.0000	0.0000
O	6c	0.0000	0.0000	0.2575(3)
F	6c	0.0000	0.0000	0.2575(3)

For 5 % Ni in Li-layer

Atom	Wyckoff position	x	y	z
Li	3b	0.0000	0.0000	0.5000
Ni	3b	0.0000	0.0000	0.5000
Li	3a	0.0000	0.0000	0.0000
Mn	3a	0.0000	0.0000	0.0000
Co	3a	0.0000	0.0000	0.0000
Ni	3a	0.0000	0.0000	0.0000
O	6c	0.0000	0.0000	0.2575(3)
F	6c	0.0000	0.0000	0.2575(3)

The simulated data indicates that the intensity ratio, I_{003}/I_{104} decreases with increase in the Li/Ni-disorder, with the highest ratio observed for the completely ordered structure. This is consistent with the trends of intensity ratio with increased disorder already reported for other NCM based oxides [66, 385].

Table 3.2 Atomic, Occupancy and Thermal Parameters used for the P-XRD Pattern Simulation of $Li_{1.25}Ni_{0.25}Co_{0.25}Mn_{0.25}O_{1.5}F_{0.5}$ (continued)

For 10 % Ni in Li-layer

Atom	Wyckoff position	x	y	z
Li	3b	0.0000	0.0000	0.5000
Ni	3b	0.0000	0.0000	0.5000
Li	3a	0.0000	0.0000	0.0000
Mn	3a	0.0000	0.0000	0.0000
Co	3a	0.0000	0.0000	0.0000
Ni	3a	0.0000	0.0000	0.0000
O	6c	0.0000	0.0000	0.2575(3)
F	6c	0.0000	0.0000	0.2575(3)

For 15 % Ni in Li-layer

Atom	Wyckoff position	x	y	z
Li	3b	0.0000	0.0000	0.5000
Ni	3b	0.0000	0.0000	0.5000
Li	3a	0.0000	0.0000	0.0000
Mn	3a	0.0000	0.0000	0.0000
Co	3a	0.0000	0.0000	0.0000
Ni	3a	0.0000	0.0000	0.0000
O	6c	0.0000	0.0000	0.2575(3)
F	6c	0.0000	0.0000	0.2575(3)

A high I_{003}/I_{104} intensity ratio for the observed data hints for a completely ordered structure of the oxy-fluoride $Li_{1.25}Ni_{0.25}Co_{0.25}Mn_{0.25}O_{1.5}F_{0.5}$. In the literature, fluoride doping was reported only up to ~ 10% with phase pure materials, but was mostly associated with

some cation disorder involving either the existing transition metals or the co-doped cations and lithium. Here, the composition is designed with lower transition metal contents to make it lithium and fluoride rich.

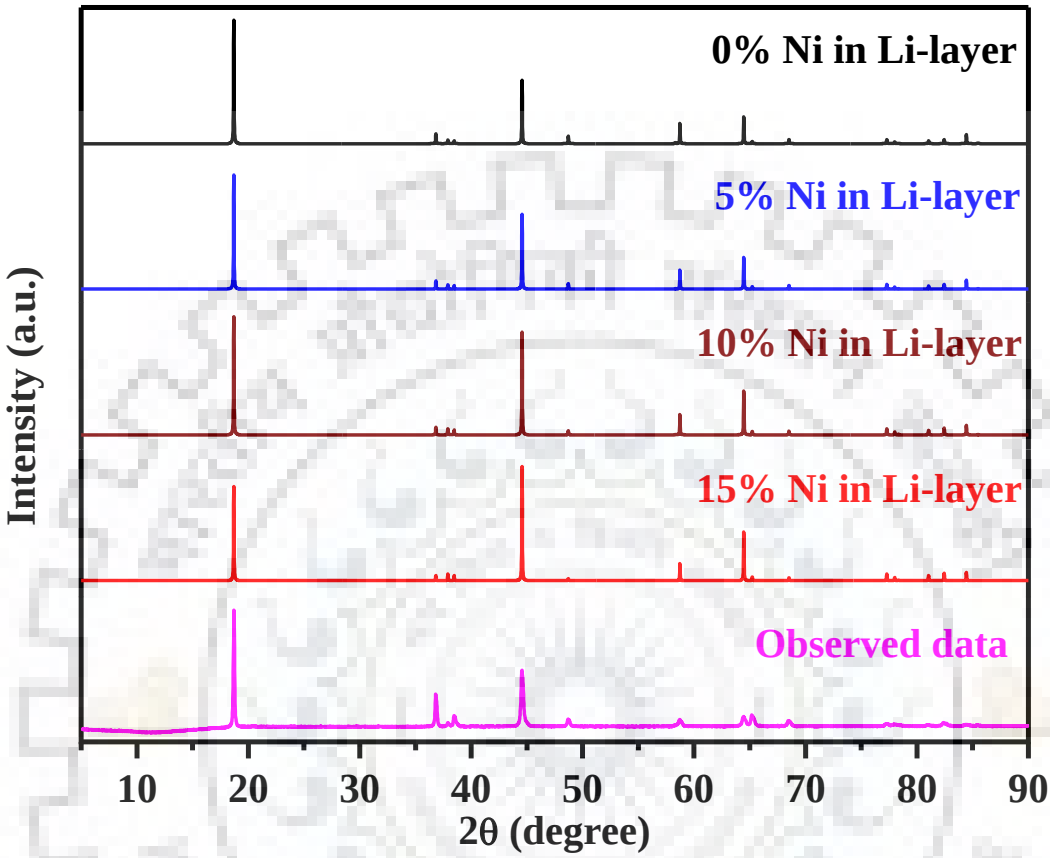

Figure 3.2 Simulated P-XRD patterns of $Li_{1.25}Ni_{0.25}Co_{0.25}Mn_{0.25}O_{1.5}F_{0.5}$ along with the observed data.

Further, Rietveld refinement of the structure of $Li_{1.25}Ni_{0.25}Co_{0.25}Mn_{0.25}O_{1.5}F_{0.5}$ has been carried out using the same model. The background, lattice, profile, atomic and thermal parameters were refined systematically in a stepwise manner until convergence was reached with reasonably good reliability indexes. The final refined profile is shown in Figure 3.3 and the refined atomic, occupancy and thermal parameters along with reliability indexes are given in Table 3.2. Crystal structures of the compound are drawn using the refined coordinates and are represented with both polyhedral and ball-stick model (Figure 3.4). The color codes in the ball-stick model indicate mixed cation occupancy by Li/Ni/Co/Mn in one layer leaving the other completely unmixed and occupied by Li.

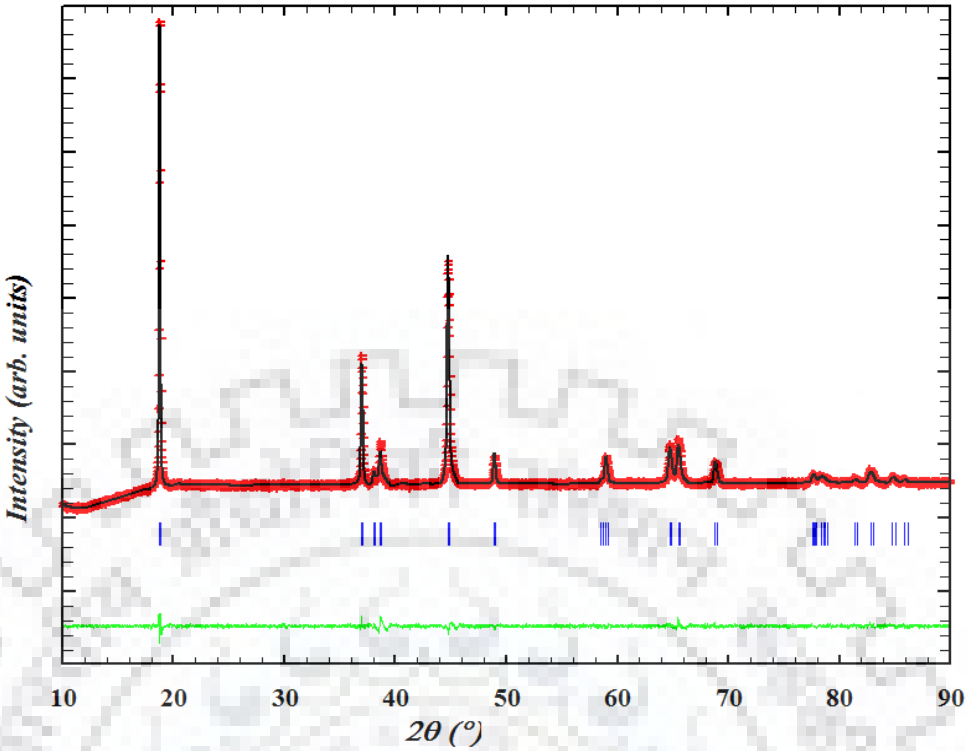

Figure 3.3 The calculated (black line), observed (red plus) and difference profiles (below, green line) of the Rietveld refinement of $Li_{1.25}Ni_{0.25}Co_{0.25}Mn_{0.25}O_{1.5}F_{0.5}$. Blue vertical bars represent the Bragg positions.

Table 3.3 Rietveld Refined Atomic Position, Site Occupancy and Thermal Parameters of $Li_{1.25}Ni_{0.25}Co_{0.25}Mn_{0.25}O_{1.5}F_{0.5}$

Atom	Wyckoff position	x	y	z	f_{occ}	B_{iso} (Å^2)
Li	3b	0.0000	0.0000	0.5000	1.0	0.25
Li	3a	0.0000	0.0000	0.0000	0.25	0.25
Mn	3a	0.0000	0.0000	0.0000	0.25	0.25
Co	3a	0.0000	0.0000	0.0000	0.25	0.25
Ni	3a	0.0000	0.0000	0.0000	0.25	0.25
O	6c	0.0000	0.0000	0.2579	1.5	5.775(4)
F	6c	0.0000	0.0000	0.2579	0.5	5.775(4)

Space group *R*-3*m* (No. 166), a = 2.8474(5) and c = 14.179 Å; R_{Bragg} = 2.49 %, R_f = 2.54 %, R_p = 0.89 %, R_{WP} = 2.54 %, and χ^2 = 1.65.

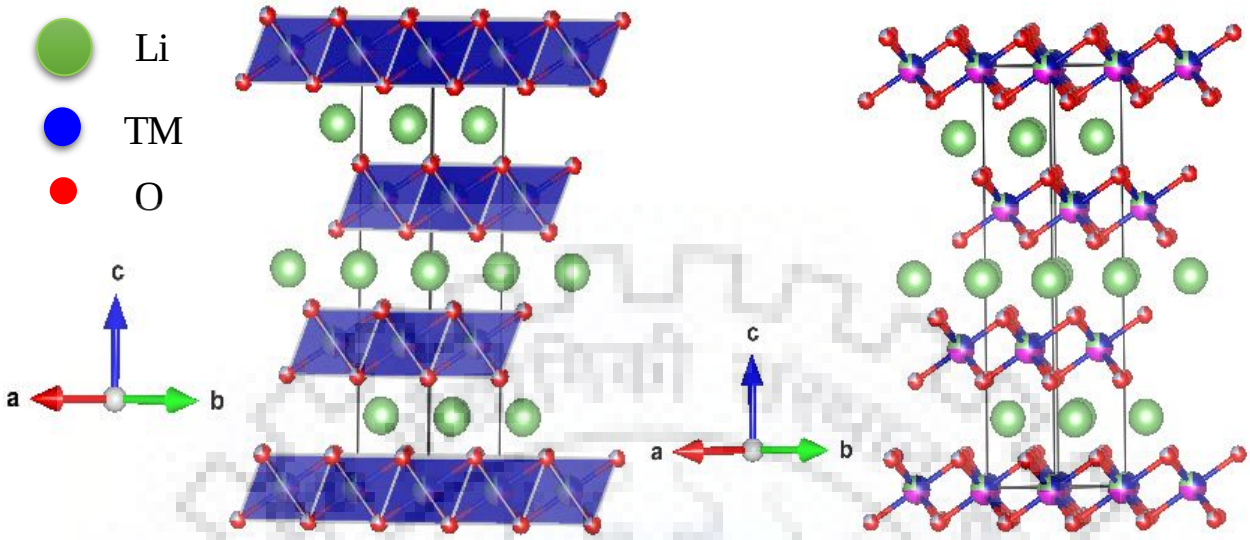

Figure 3.4 Crystal structure of $Li_{1.25}Ni_{0.25}Co_{0.25}Mn_{0.25}O_{1.5}F_{0.5}$, drawn using the refined atomic coordinates.

3.3.2 FE-SEM and EDS Analysis

FE-SEM images and corresponding EDS of $Li_{1.25}Ni_{0.25}Co_{0.25}Mn_{0.25}O_{1.5}F_{0.5}$ are shown in Figure 3.5. FE-SEM images taken at several locations of the sample show morphological homogeneity all through the analyzed areas. Moreover, the SEM images indicate that the particle sizes are in the range of few nanometers to several hundred nanometers. The compositional homogeneity of synthesized sample was checked by recording EDS at numerous crystallites of the imaged area. An analysis of elemental composition obtained from EDS demonstrated excellent compositional uniformity with the nominal elemental composition.

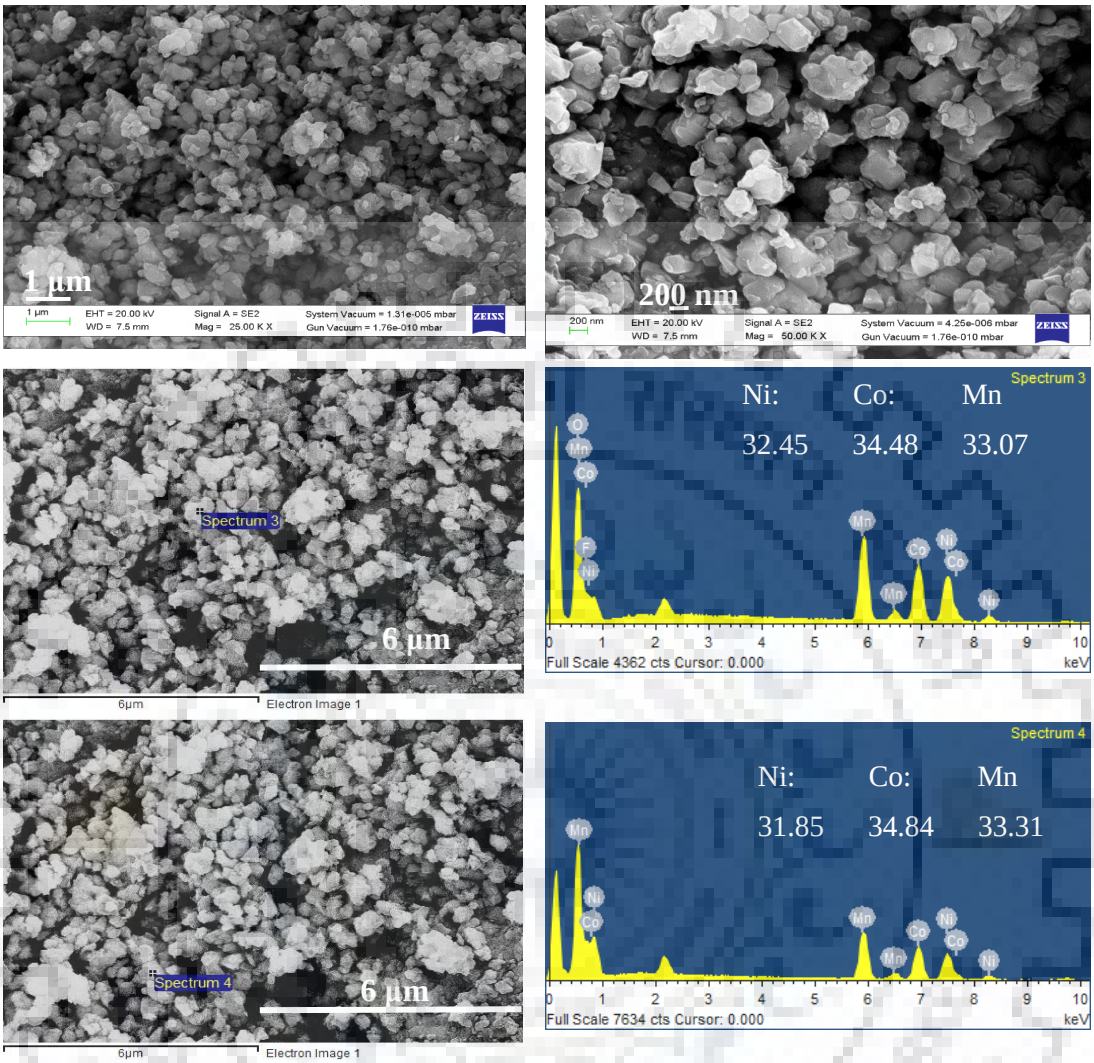

Figure 3.5 FE-SEM images and corresponding EDS of $Li_{1.25}Ni_{0.25}Co_{0.25}Mn_{0.25}O_{1.5}F_{0.5}$.

3.3.3 FE-SEM-EDS Elemental Mapping Analysis

An elemental mapping analysis was carried out at a selected rectangular area to examine the elemental distribution in the synthesized sample. The FE-SEM-EDS elemental mapping images are shown in Figure 3.6. The results of elemental mapping show that all the elements (oxygen, nickel, cobalt, manganese and fluorine) are homogeneously distributed in the scanned rectangular area of the sample. Further, the observed color contrasts for O and F are consistent with the corresponding bright-field SEM image given that O and F are lighter elements as compared to the transition metals.

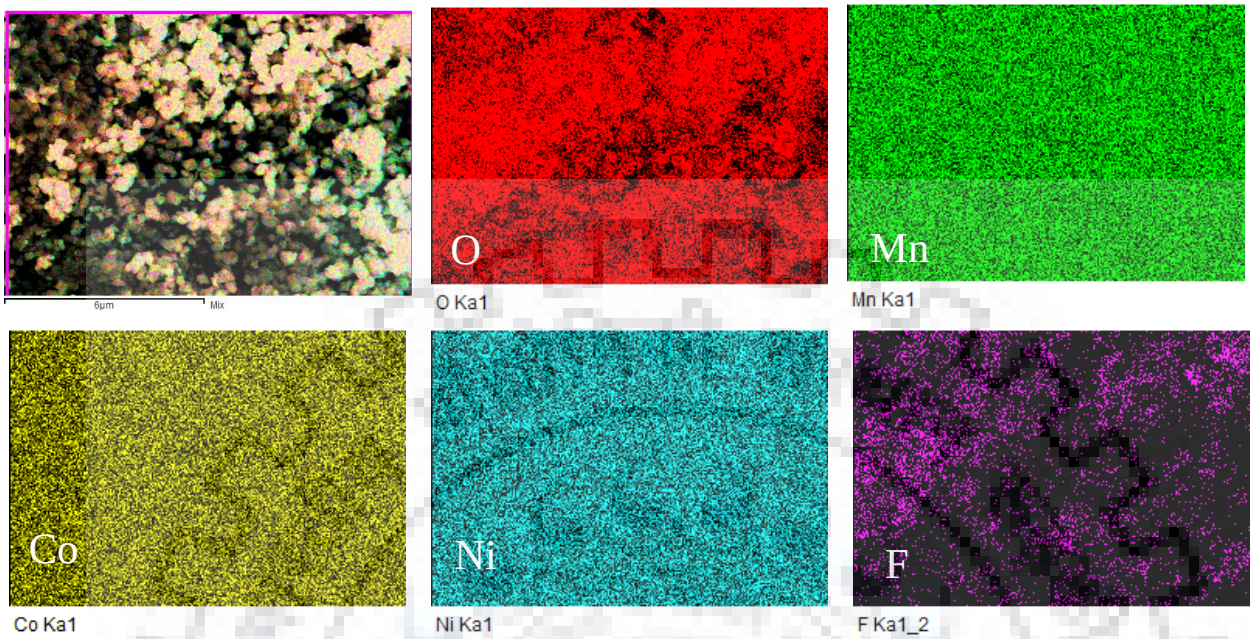

Figure 3.6 SEM image and the corresponding EDS elemental mapping for $Li_{1.25}Ni_{0.25}Co_{0.25}Mn_{0.25}O_{1.5}F_{0.5}$.

3.3.4 High-Resolution Transmission Electron Microscopy (HR-TEM) Analysis

The high resolution TEM (HR-TEM) images and ED pattern of $Li_{1.25}Ni_{0.25}Co_{0.25}Mn_{0.25}O_{1.5}F_{0.5}$ are shown in Figure 3.7. TEM images clearly show the crystallite sizes ranging from few hundred nm to several hundred nm. Clear lattice fringes observed in the HR-TEM image (Figure 3.7c) are indicative of highly crystalline nature of the sample and the distance of 4.7 Å corresponds to the spacing between the consecutive layers of transition metals. Three such layers with a distance of 14.1 (3× 4.7 Å) Å make up the *c*-parameter of the unit cell as can be clearly seen in the structure shown in Figure 3.4. The selected area electron diffraction (SAED) image shows bright diffraction spots confirming its highly crystalline nature as well. Indexing of the diffraction spot indicated in Figure 3.7d is in good agreement with the analyzed P-XRD data.

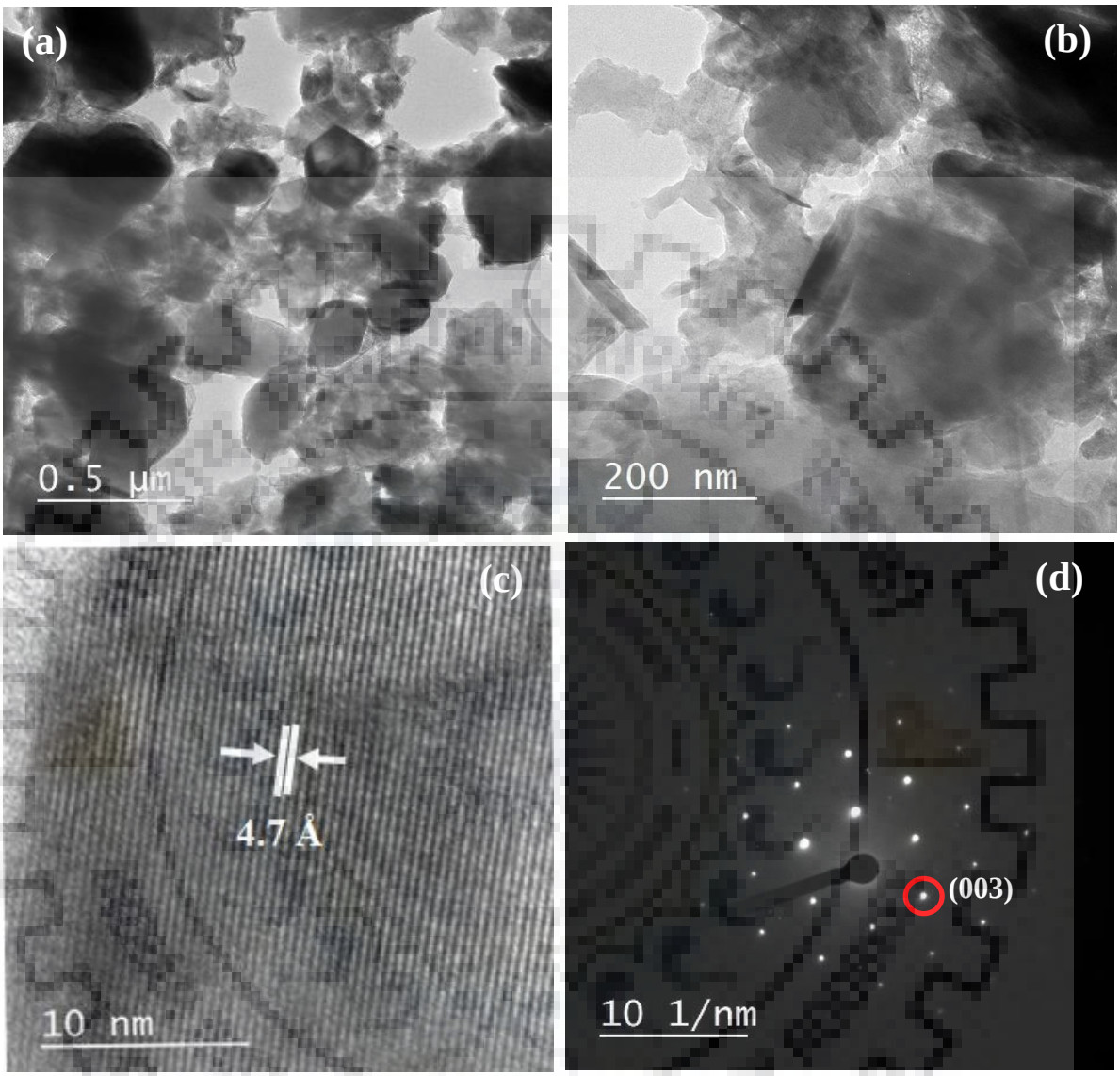

Figure 3.7 TEM micrographs (a, b), HR-TEM image (c) and SAED pattern (d) of $Li_{1.25}Ni_{0.25}Co_{0.25}Mn_{0.25}O_{1.5}F_{0.5}$.

3.3.5 Surface Area Analysis

The pore size distribution (PSD) and specific surface area of the as synthesized compound was analyzed using the nitrogen adsorption and desorption method. The PSD and surface area analysis data are shown in Figure 3.8 (c). The specific surface area of 20.7 m^2 g^{-1} for $Li_{1.25}Ni_{0.25}Co_{0.25}Mn_{0.25}O_{1.5}F_{0.5}$ calculated using the BET equation seems to be higher

than similar oxide analogs synthesized by solid state reactions. A relatively high surface area obtained for the oxy-fluoride here may probably be due to its porous nature. The isotherm, shown in Figure 3.8 (b), consists of a hysteresis loop up to a relative pressure ~ 0.9, which is a characteristics feature of mesoporous materials. The pore size distribution shown in Figure 3.8 (a) demonstrated that majority of the pores is centered at ~ 2.6 nm. The total pore volume of the compound is 0.21 cc g^{-1}.

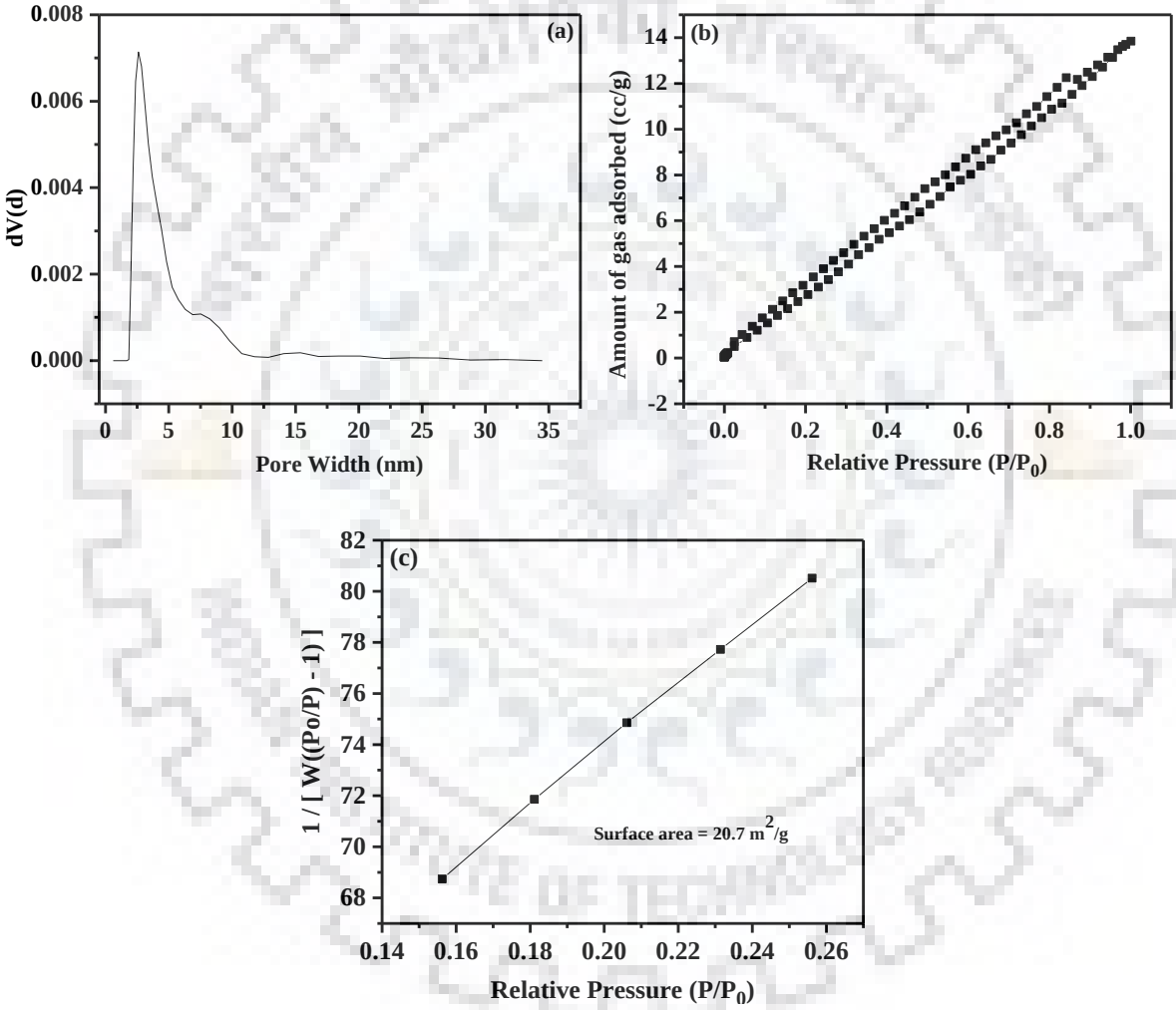

Figure 3.8 (a) Pore size distribution, (b) N_2 sorption isotherm and (c) surface area curve for $Li_{1.25}Ni_{0.25}Co_{0.25}Mn_{0.25}O_{1.5}F_{0.5}$.

3.3.6 X-Ray Photoelectron Spectroscopy (XPS)

The oxidation state of the transition metals present in $Li_{1.25}Ni_{0.25}Co_{0.25}Mn_{0.25}O_{1.5}F_{0.5}$ was probed by X-ray photoelectron spectroscopy (XPS) measurements. XPS spectra of Ni, Co, Mn and F are shown in Figure 3.9.

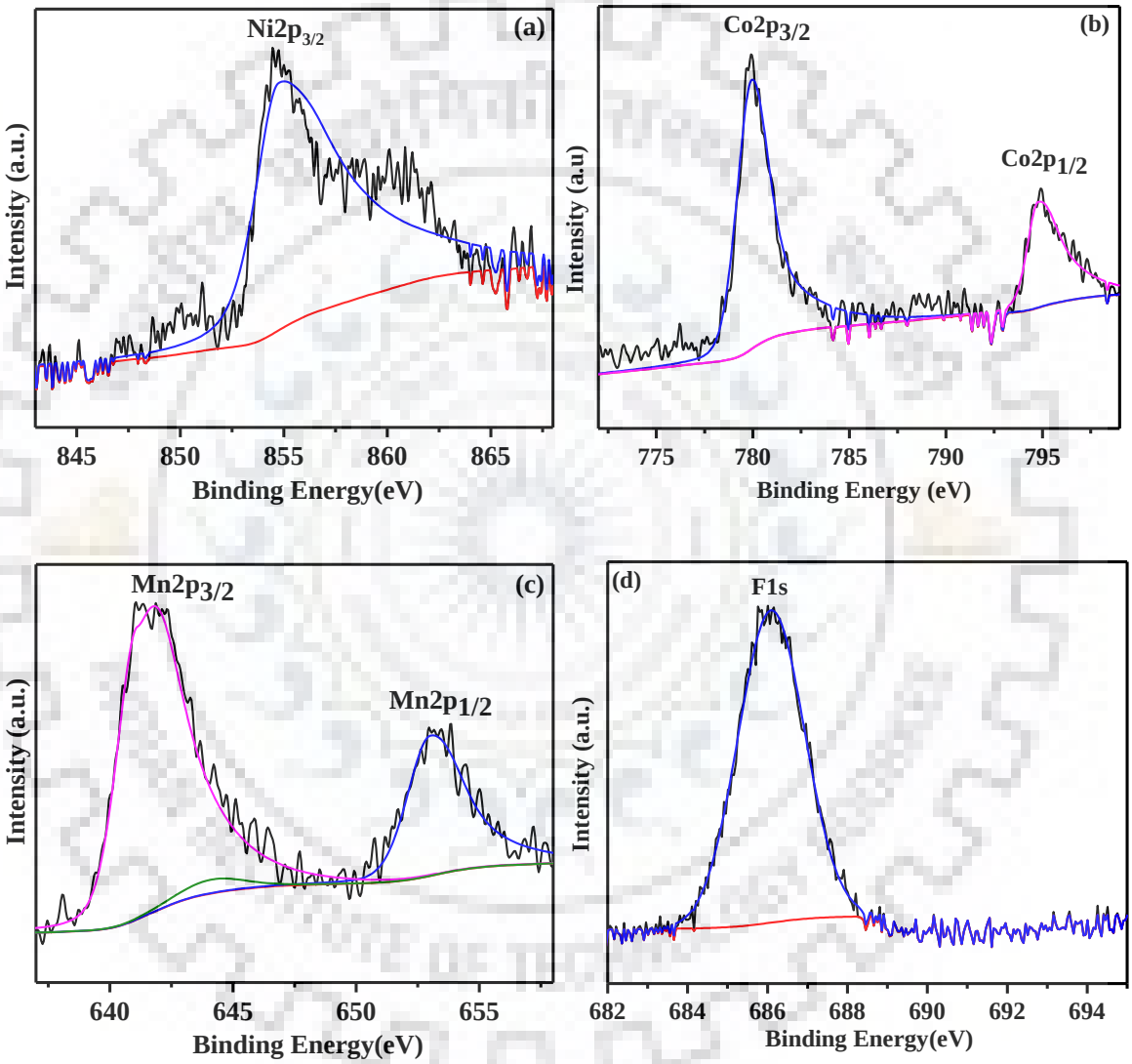

Figure 3.9 Deconvoluted $Ni2p_{3/2}$, $Co2p_{3/2}$, $Mn2p_{3/2}$ and F_{1s} XPS of $Li_{1.25}Ni_{0.25}Co_{0.25}Mn_{0.25}O_{1.5}F_{0.5}$.

A symmetrical peak due to Ni $2p_{3/2}$ at a binding energy of 854.6 eV confirms the presence of nickel as Ni^{2+} in $Li_{1.25}Ni_{0.25}Co_{0.25}Mn_{0.25}O_{1.5}F_{0.5}$. Similarly, Co $2p_{3/2}$ and Mn

$2p_{3/2}$ spectra shows peaks at binding energies of 779.8 and 641.9 eV, respectively conforming to the presence of cobalt and manganese as Co^{3+} and Mn^{4+} in $Li_{1.25}Ni_{0.25}Co_{0.25}Mn_{0.25}O_{1.5}F_{0.5}$. The peak at the binding energy of 686.0 eV is in accordance with that of F_{1s} of fluorine element, corresponding to inorganic fluorides. Thus, the XPS study confirms the incorporation of fluoride into the oxide lattice.

3.3.7 CV Analysis

The cyclic voltammogram (CV) of $Li_{1.25}Ni_{0.25}Co_{0.25}Mn_{0.25}O_{1.5}F_{0.5}$ is shown in Figure 3.10. The CV was recorded in a voltage range of 2 – 4.5 V at the scan rate of 0.1 mV/sec. The CV encompasses two peaks; an anodic peak at 3.95 V and the corresponding cathodic peak at 3.72 V. The absence of any other peak in the CV ascertains that only Ni^{2+}/Ni^{4+} redox couple is active in the compound. It was well established in the literature that among three transition metal elements present in NCM based oxides, only nickel and cobalt with oxidation states +2 and +3, respectively, are electrochemically active [386].

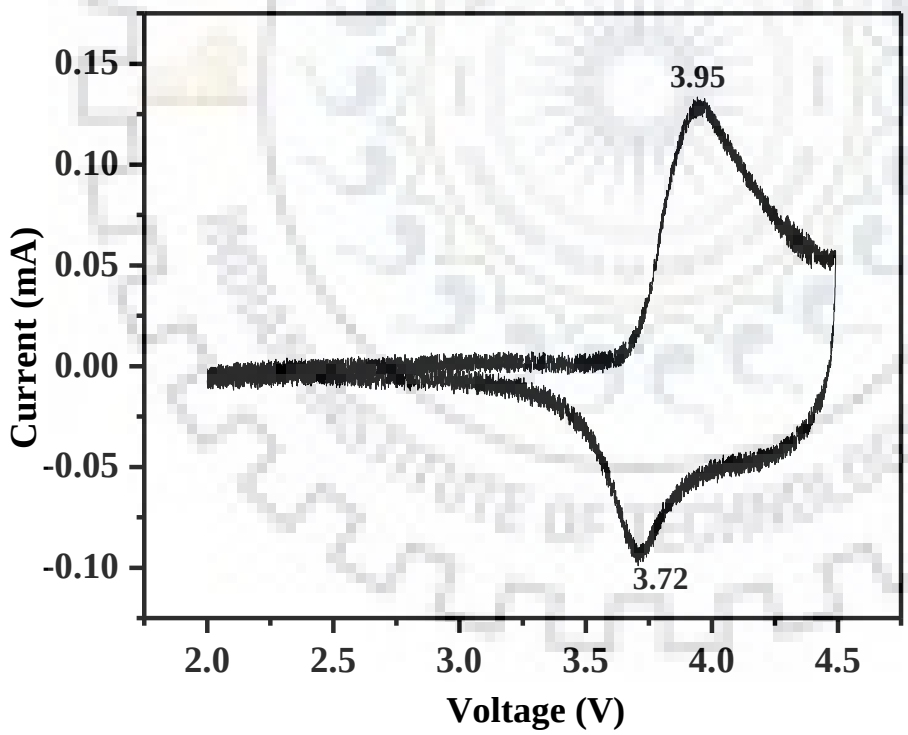

Figure 3.10 Cyclic volatammogram of $Li_{1.25}Ni_{0.25}Co_{0.25}Mn_{0.25}O_{1.5}F_{0.5}$ between 2.0 – 4.5 V at a scan rate of 0.1 mV/sec.

There is no sign of the presence of $Mn^{3+}/^{4+}$ redox couple due to the absence of a peak at 3.2 V. Mn seems to be present as electrochemically inactive Mn^{4+}, but to provide extra stability to the lattice. The peaks corresponding to $Co^{3+}/^{4+}$ redox couple generally appears at a voltage greater than 4.6 V [387]. Therefore, in the present study, peaks for $Co^{3+}/^{4+}$ couple is not observed due to the restricted upper voltage limit (up to 4.5 V) in the CV measurement.

3.3.8 Galvanostatic Charge-Discharge Analysis

First three charge-discharge cycles of $Li_{1.25}Ni_{0.25}Co_{0.25}Mn_{0.25}O_{1.5}F_{0.5}$ cathode material at 0.1 C cycling rate within a potential window of 3.0 – 4.49 V are shown in Figure 3.11 (a). The charge-discharge curve demonstrates that deintercalation-intercalation of lithium ions occurs mainly at ~ 3.9 V after first charge. This is higher than that of its oxide analog [386]. A high charge-discharge capacity of 216 mAh g^{-1} and 148 mAh g^{-1} are observed for the first cycle when cycled between 3.0 – 4.49 V at 0.1 C. These are much higher than other fluorine doped NCM cathode materials containing higher amounts of fluorine [385]. Although, the columbic efficiency for the first charge-discharge cycle is 68.5 %, it rose up to ~ 97% for the 2nd and 3rd charge-discharge cycles. A discharge capacity of 150 mAh g^{-1} is achieved at 0.2 C after 18 cycles. The discharge capacities obtained at 0.2 C demonstrated stable nature of the compound on electrochemical insertion-extraction of Li. A discharge capacity of 100 mAh g^{-1} obtained at 0.8 C after 70 cycles were further supported the structural robustness of the Li-rich NCM type oxy-fluoride reported here.

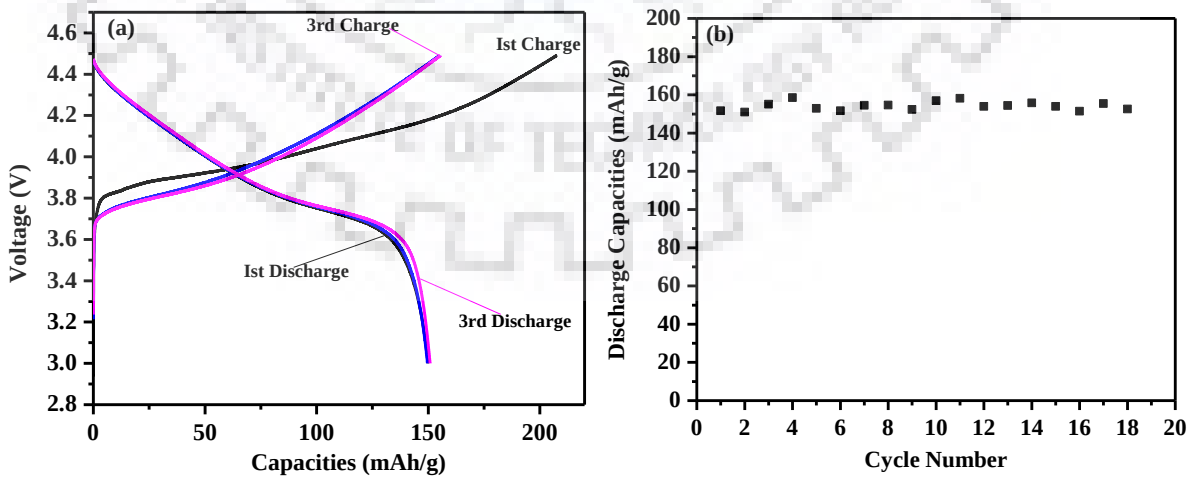

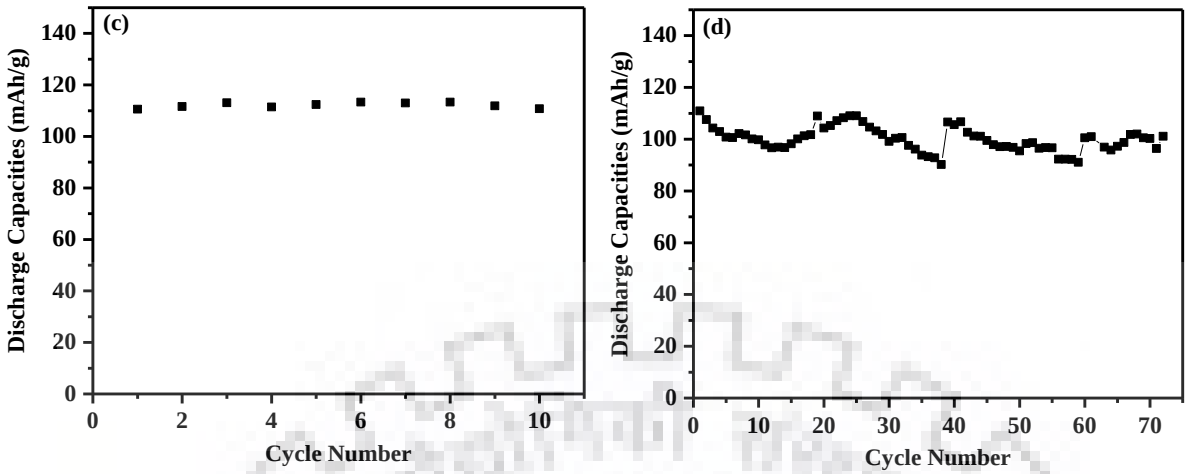

Figure 3.11 Galvanostatic charge-discharge studies of $Li_{1.25}Ni_{0.25}Co_{0.25}Mn_{0.25}O_{1.5}F_{0.5}$ at (a) 0.1 C, (b) 0.2 C, (c) 0.5 C and (d) 0.8 C in the potential range 3.0 - 4.49 V.

In summary, a new Li-rich NCM based rock-salt layered oxy-fluoride, namely, $Li_{1.25}Ni_{0.25}Co_{0.25}Mn_{0.25}O_{1.5}F_{0.5}$, was synthesized by solid state reaction and reported for the first time. P-XRD pattern simulation and Rietveld refinement studies confirmed the ordered rock-salt structure of the oxy-fluoride without Li/Ni cation disorder in the Li-only layer. In CV trace, while the anodic and cathodic peaks at 3.95 and 3.72 V, respectively, confirmed the intercalation/de-intercalation of Li-ions into/out of the lattice, the charge-discharge curves showed the intercalation/de-intercalation potential at a slightly higher voltage (~ 3.91 V) than its oxide analogs. The observed higher working voltage was attributed to the incorporation of fluoride ions into the oxide lattice. A high charge capacity of 216 mAh g^{-1} and a discharge capacity of 148 mAh g^{-1} at 0.1 C for the first cycle were observed for $Li_{1.25}Ni_{0.25}Co_{0.25}Mn_{0.25}O_{1.5}F_{0.5}$. A high charge-discharge capacity was obtained at slow cycling rate, but substantial capacity fading was observed when the cell was cycled at higher cycling rates. The present work is significant due to the fact that it demonstrates a large amount of fluoride doping in the oxide lattice of the Li-rich oxy-fluoride maintaining a completely ordered structure and avoiding any likely consequences of Li/Ni disorder in the Li-only layer.

CHAPTER – 4

A New Synthetic Route for $Na_3Fe(PO_4)_2$ Layered Phosphate: A Potential Cathode Material for Lithium-Ion Batteries

A New Synthetic Route for $Na_3Fe(PO_4)_2$ Layered Phosphate: A Potential Cathode Material for Sodium and Lithium-Ion Batteries

4.1 INTRODUCTION

Even though the development of battery technologies as storage devices started nearly 100 year back but the last three decades have witnessed a continuous development of battery technologies [388]. Li-ion batteries are considered most promising storage system and used as power sources in a number of devices such as, cell phones, laptops, power tools, digital cameras, pacemakers etc. due to their high energy density and long life. However, the use of Li-ion batteries in large scale applications such as automotive and stationary is not appropriate due to scarcity and high cost of lithium. Recently, sodium ion batteries (NABs) have attracted immense attention due to high natural abundance, low cost and environmental benign nature of sodium. There are advantageous for large scale manufacture of low-cost NABs over LIBs. Additionally, NABs could be a better choice to use in the large scale electrochemical energy storage applications due to replacement of cheap aluminum anode in place of copper as current collector [389]. A number of materials have been explored as possible host materials for Na-ion batteries. Among them transition metal oxides [390-394], hard carbon [395-398], phosphates [399-401], sulphates [402-405], ferrocyanides [406-408] and metal alloys [409-411] have been used as electrode material for NABs due to their substantial Na-ion storage capabilities. However, structural instability during extraction-insertion of Na-ion is the main problem associated with Na-ion batteries when a battery is charged and discharged repeatedly. The large size of Na^+ ion (~ 40 % larger than Li^+ ion) induces large stress in the host structure often resulting in structural collapse during intercalation/de-intercalation process [398].

In this context, phosphates have attracted immense interest due to their robust structure with high stability and open framework allowing easy intercalation/de-intercalation of Na-ions with minimal structural change. The phosphate containing compounds are rich in chemistries and forms variety of structures such as orthophosphates, pyrophosphates and mixed-phosphates [412]. Much attention has been given to explore the possibility of suitable cathode materials for NABs in the phosphate family. Recently many phosphate based

compounds such as $NaFePO_4$ [413], Na_2FePO_4F [414, 415], $Na_3Fe_3(PO_4)_4$ [416], $NaMnFe_2(PO_4)_3$ [417], $Na_3M(CO_3)(PO_4)$ (M = Mn, Fe) [418], $Na_2MP_2O_7$ (M = Mn, Fe) [419, 420], $Na_4Fe_3(PO_4)_2(P_2O_7)$ [421], $Na_7V_4(P_2O_7)_4(PO_4)$ [422, 423], $Na_4NiP_2O_7F_2$ [424] and $Na_3MnTi(PO_4)_3$ [425] have been reported to exhibit good electrochemical performance. Even though, the P-O bond offers good structural stability but the theoretical capacities of these high molecular weight compounds are low. Out of many phosphate-based compounds only few offer good capacity. The maricite, $NaFePO_4$, demonstrated a high capacity (~ 142 mAh g^{-1}) at the first cycle with improved cyclability. Carbon coated Na_2FePO_4F prepared using vitamin C as a green carbon source demonstrated a high reversible capacity of 117 mAh g^{-1} at a cycling rate of 0.1 C. The compound also exhibit ~ 85% capacity retention after 1000 charge-discharge cycles at 4 C rate [415]. More recently, M. Chen *et al.* have reported carbon coated $Na_{3.32}Fe_{2.34}(P_2O_7)_2$ that could deliver a capacity of ~ 100 mAh g^{-1} at 0.1 C with 92.3 % capacity retention after 300 cycles at 0.5 C [426]. Therefore, finding a suitable phosphate based cathode material for NABs with high capacity and good electrochemical performance is still challenging. In search of novel phosphate structures, we have identified herewith a layered double phosphate, $Na_3Fe(PO_4)_2$, which could be a possible cathode material for Na-ion batteries. The layered structure of $Na_3Fe(PO_4)_2$ is composed of $[Fe(PO_4)_2^{3-}]_n$ infinite layers, which are made up of corner shared PO_4 tetrahedra and FeO_6 octahedra. Each tetrahedral phosphate unit is linked to three iron atoms by three of its corners leaving the fourth oxygen unshared. Thus, each iron is octahedrally coordinated with six oxygens of six different phosphate groups and the fourth oxygen of phosphate tetrahedra points into the interlayer space and coordinates with the sodium atoms.

There are only few reports describing the complex synthesis of $Na_3Fe(PO_4)_2$. A. B. H. Amara *et al.* and V. A. Morozov *et al.* prepared $Na_3Fe(PO_4)_2$ by solid state reactions at 740–760 °C for 120 – 200 hours [427, 428]. The single crystals of $Na_3Fe(PO_4)_2$ have been grown using nitrate and chloride melts as media for crystal growth by O. Livitska *et al.* [429].

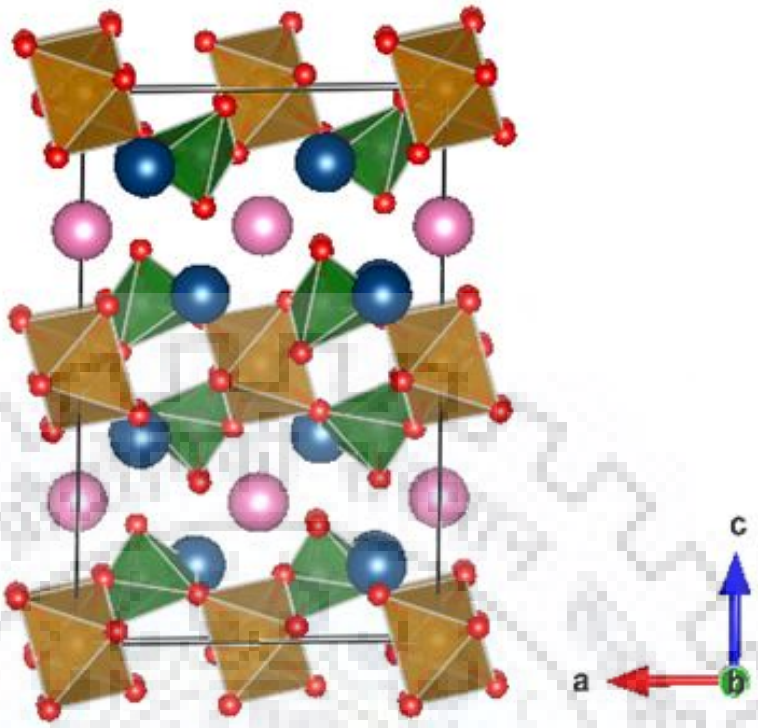

Figure 4.1 Structure of $Na_3Fe(PO_4)_2$ [428].

Here, we report a rapid synthetic method for the preparation of $Na_3Fe(PO_4)_2$ based on sol-gel technique. This method is fast (< 24 h) and simple as compared to earlier methods that takes more than 7 days to prepare $Na_3Fe(PO_4)_2$. The details of synthesis, characterization and electrochemical properties of $Na_3Fe(PO_4)_2$ are reported in this chapter.

4.2 EXPERIMETAL SECTION

4.2.1 Materials and Synthesis

Synthesis of $Na_3Fe(PO_4)_2$ was carried out by a sol-gel method (Scheme-I). For this purpose, citric acid (SDFCL, 99.0 %), $NaNO_3$ (Himedia, ACS reagent, 99.0 %), $Fe(NO_3)_3.9H_2O$ (Himedia, A. R, 98.0 %), $NH_4H_2PO_4$ (Himedia, A. R, 99.0 %) and $Na_4P_2O_7$ (Himedia, 97.5 %) were used as starting materials. In a typical synthesis, stoichiometric amounts (0.005 moles) of $NaNO_3$, $Fe(NO_3)_3.9H_2O$, and $NH_4H_2PO_4$ were dissolved in 50 ml of distilled water taken in a beaker. Citric acid (0.015 moles) and $Na_4P_2O_7$ (0.02 moles) were

dissolved in 30 ml of distilled water taken in separate beakers. The beaker containing citric acid solution was placed on a hot plate with stirrer and the temperature was adjusted at 60 °C. Then, the solution of ammonium dihydrogen phosphate and metal nitrates were transferred into the citric acid solution drop wise with constant stirring till a clear solution was obtained. After that, $Na_4P_2O_7$ solution was transferred into this clear solution. The resultant solution was evaporated at 80 °C to get a gel type product. This gel was dried completely at 120 °C to turn into a blackish powder. The blackish powder was collected and transferred into a platinum crucible for further calcinations. The powder was initially calcined at 500 °C for 5 h followed by 900 °C for 12 h to get pure phase $Na_3Fe(PO_4)_2$. Finally, the powder was washed with boiled water to remove excess alkali phosphates and gave a yellowish powder after drying that was used for further characterization and electrochemical studies.

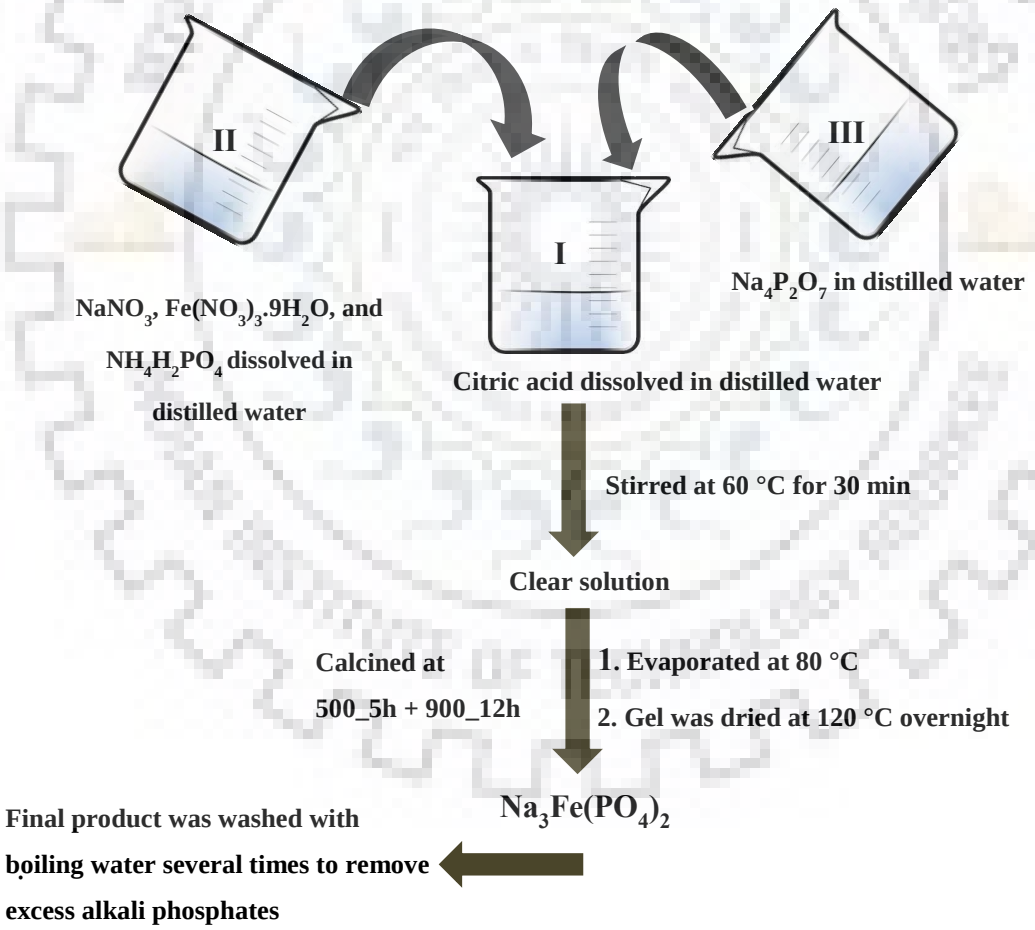

Scheme-I Schematic representation of the sol-gel synthesis of $Na_3Fe(PO_4)_2$.

4.3 RESULTS AND DISCUSSION

4.3.1 Powder-XRD Analysis

Phase evolution of $Na_3Fe(PO_4)_2$ by the reported solid state method and sol-gel method (developed herewith) is monitored by collecting P-XRD data after each heating step. The P-XRD patterns of the as obtained powders after each step of solid state reaction is shown in Figure 4.2. As can be seen, even after heating the final product with $Na_4P_2O_7$ at the last step, the solid state reaction results in the formation of $Na_3Fe(PO_4)_2$ with a small amount of $Na_3Fe_2(PO_4)_3$ impurity. In the initially developed sol-gel method, the reaction time is reduced to nearly 3 days (from 7 days), but the final product could not be freed from $Na_3Fe_2(PO_4)_3$ impurity even after heating with $Na_4P_2O_7$ in the last step (Figure 4.3). Based on the above observations, we have come up with a modified method wherein $Na_4P_2O_7$ is added at the very beginning of the sol-gel method described in the experimental section. The P-XRD pattern recorded for the final product is given in Figure 4.4. All the diffraction peaks observed in the pattern are indexable and in agreement with the reported JSPDS data of $Na_3Fe(PO_4)_2$ (JCPDS PDF # 51-0082) confirming the formation of phase pure compound with high crystallinity [427].

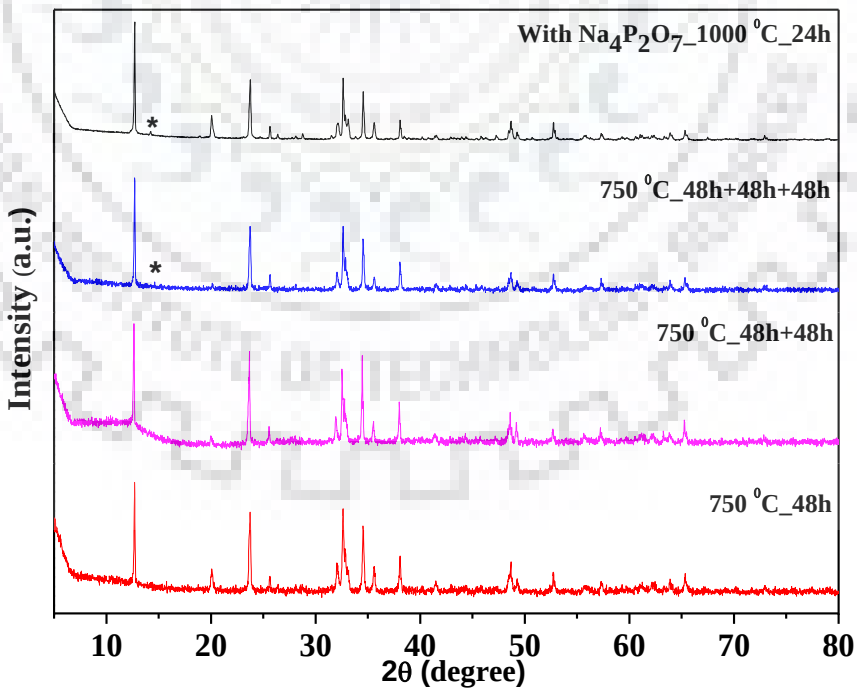

Figure 4.2 P-XRD patterns of $Na_3Fe(PO_4)_2$ at different stages of solid state synthesis.

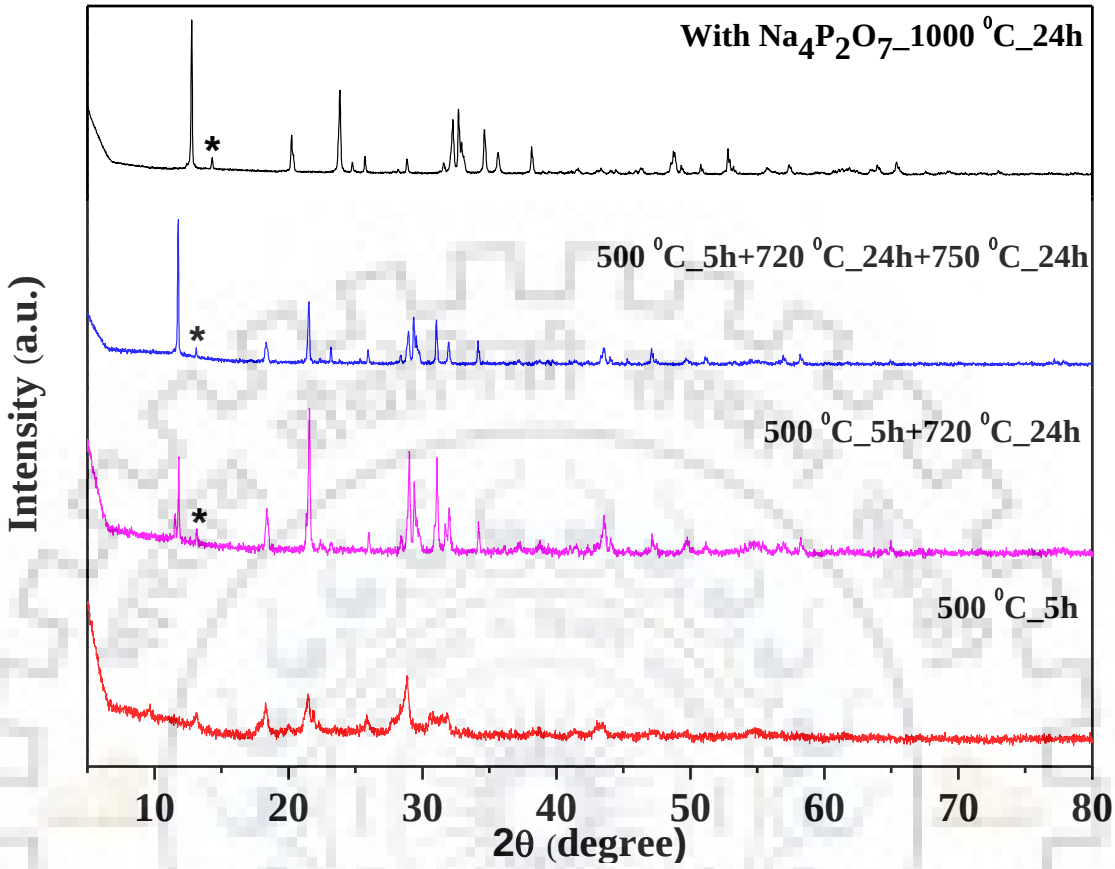

Figure 4.3 P-XRD patterns of $Na_3Fe(PO_4)_2$ at different stages of sol-gel synthesis when $Na_4P_2O_7$ is used at the last step.

Least-squares refinement of the lattice parameters are carried out with all the observed P-XRD lines using the PROZSKI program. The monoclinic cell parameters, a = 9.0698(5), b = 5.0343(7), c = 13.866(1) Å and β = 91.43(1)°, obtained after the least-squares refinement are in good agreement with the reported data. The indexed P-XRD data for $Na_3Fe(PO_4)_2$ are given in Table 4.1.

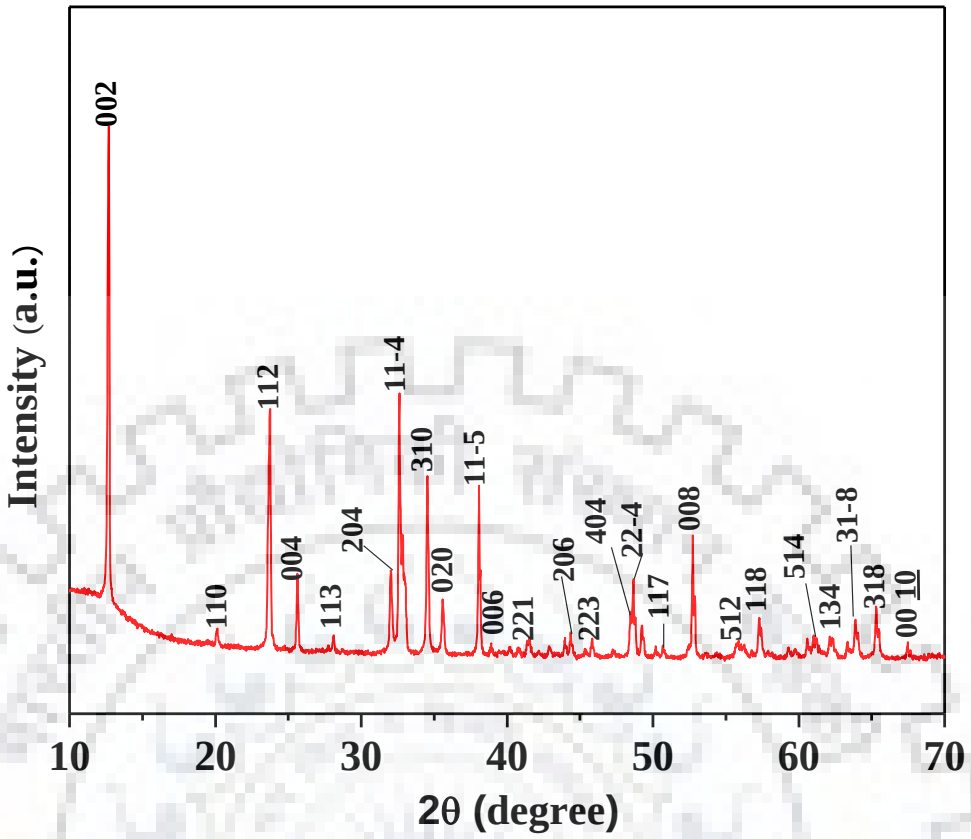

Figure 4.4 P-XRD pattern of $Na_3Fe(PO_4)_2$ using $Na_4P_2O_7$ at the beginning of sol-gel synthesis.

4.3.2 FE-SEM and EDS Analysis

The FE-SEM images of $Na_3Fe(PO_4)_2$ are shown in Figure 4.5. The images show morphological homogeneity over the analyzed regions of the sample with plate-like crystallites of few micrometers in length and width. Moreover, a high resolution image (Figure 4.5b) shows that the plate-like crystallites are actually made up of nanoparticles of $Na_3Fe(PO_4)_2$ with crystallite sizes down to ~ 10 nm and a fairly uniform distribution. The compositional homogeneity of the compound is checked by collecting EDS spectra at number of crystallites of the imaged area. The SEM images and corresponding EDS spectra with elemental compositions are shown in Figure 4.6. The elemental composition obtained experimentally is in good agreement with the expected elemental ratio for $Na_3Fe(PO_4)_2$ composition.

Table 4.1 Indexed P-XRD data of $Na_3Fe(PO_4)_2$

h k l	d_{obs}(Å)	d_{calc} (Å)	I_{obs}
0 0 2	6.933	6.931	100
1 1 0	4.402	4.401	4
1 1 –2	3.737	3.736	62
0 0 4	3.463	3.465	22
1 1 3	3.169	3.168	5
2 0 –4	2.787	2.787	23
1 1 –4	2.740	2.739	68
1 1 4	2.708	2.707	16
3 1 0	2.592	2.591	59
0 2 0	2.516	2.517	14
1 1 –5	2.359	2.359	40
2 2 –1	2.177	2.177	5
–2 2 4	1.868	1.868	6
2 2 4	1.847	1.847	18
0 0 8	1.732	1.732	8
5 1 2	1.647	1.647	38
1 1 8	1.605	1.605	14
3 1 –8	1.455	1.455	13
3 1 8	1.426	1.426	16

a = 9.0698(5), b = 5.0343(7), c = 13.866(1) Å and β = 91.43(1)°.

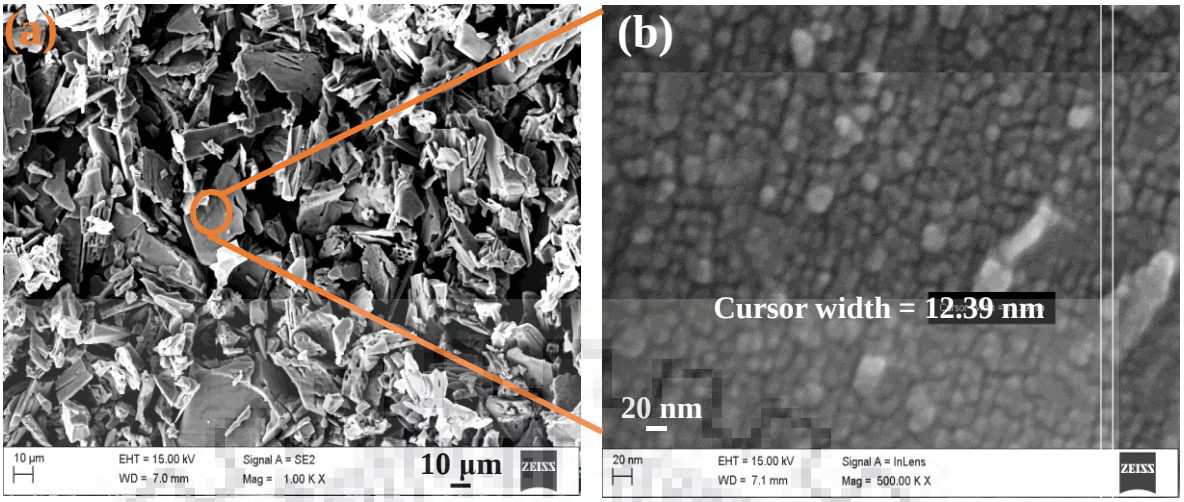

Figure 4.5 FE-SEM images of $Na_3Fe(PO_4)_2$ at (a) 1.00 KX and (b) 500.00 KX magnification.

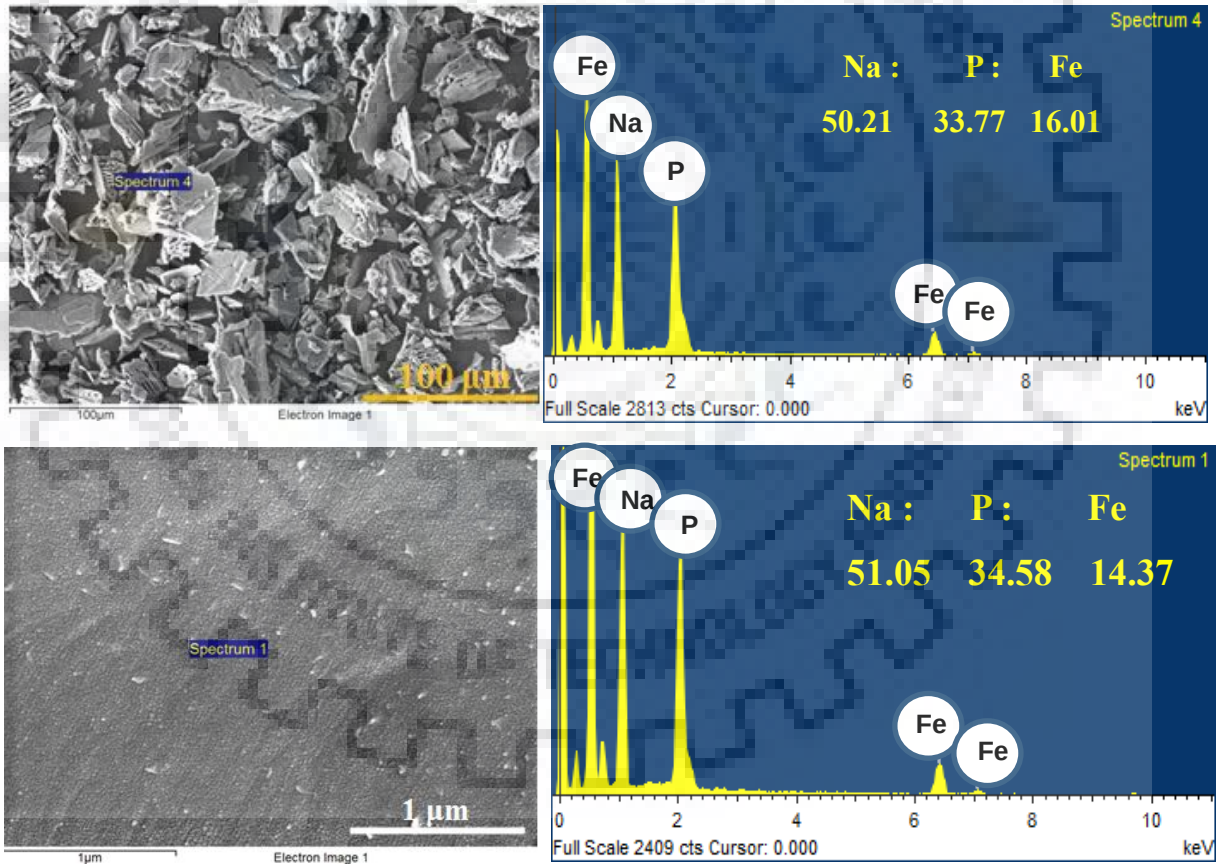

Figure 4.6 EDS data of $Na_3Fe(PO_4)_2$.

4.3.3 FE-SEM-EDS Elemental Mapping

To analyze the elemental distribution, the EDS elemental mapping is carried out at different areas of the sample. The FE-SEM-EDS elemental mapping results are shown in Figure 4.7. The homogeneous distribution of sodium, iron, phosphorous and oxygen elements present in the compound can be seen in the elemental mapping images presented here.

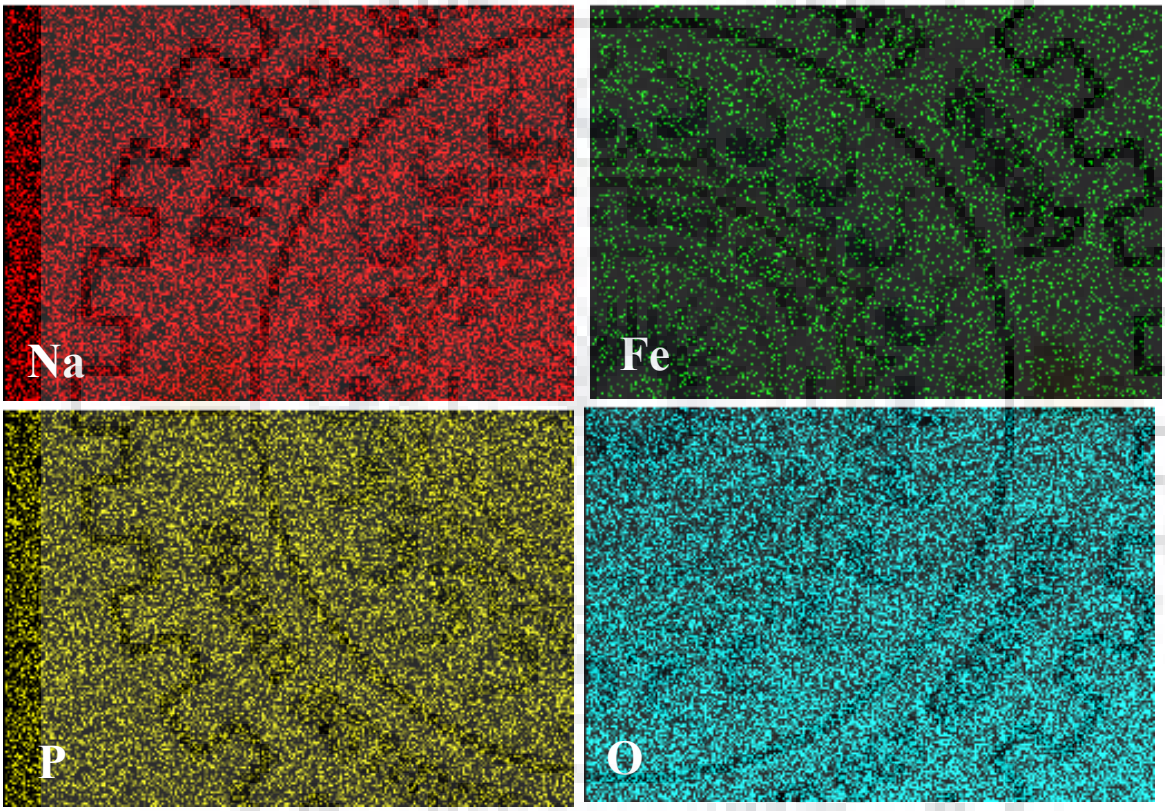

Figure 4.7 EDS elemental mapping of $Na_3Fe(PO_4)_2$.

4.3.4 TG Analysis

The thermal stability of the compound was checked by TG analysis. The TG curve of $Na_3Fe(PO_4)_2$ is shown in Figure 4.8. The TG data indicates that the compound is stable up to ~ 850 °C without any significant change in the weight on heating.

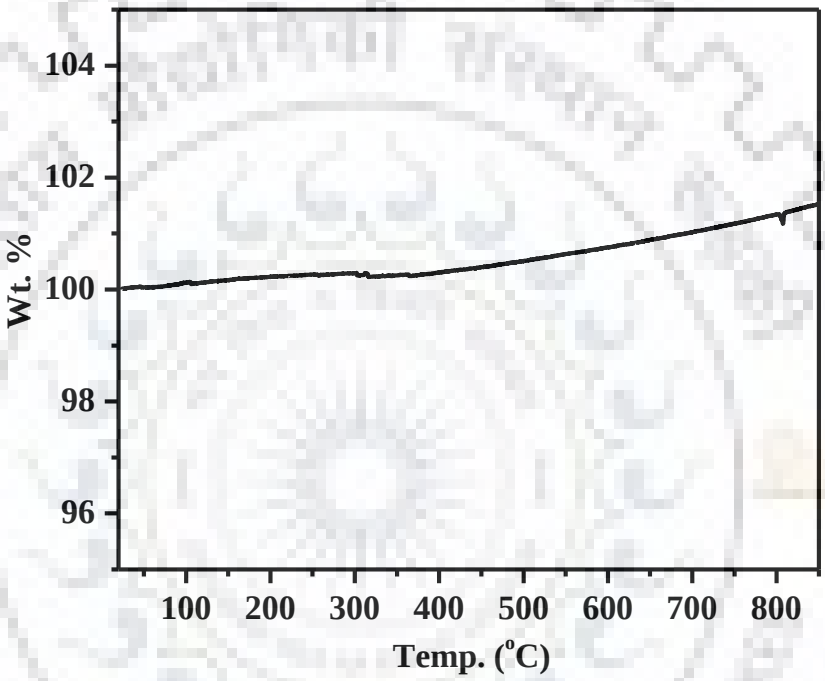

Figure 4.8 TG curve of $Na_3Fe(PO_4)_2$.

4.3.5 CV Analysis

Figure 4.9 shows four cycles of voltammograms of the Li-ion cells made from the title compound as cathode active material and metallic lithium as anode. The open circuit voltage (OCV) of the cell is 2.83 V. In the subsequent cycles the reduction onset (Li-insertion) is at ~ 3.25 V for all the cycles. The cathodic (Li-insertion) and anodic (Li-extraction) peaks are observed at 2.7 and 3.04 V, respectively, for $Na_3Fe(PO_4)_2$. The area under the cathodic and anodic peaks for $Na_3Fe(PO_4)_2$ are almost same suggesting good overall charge and discharge kinetic capabilities.

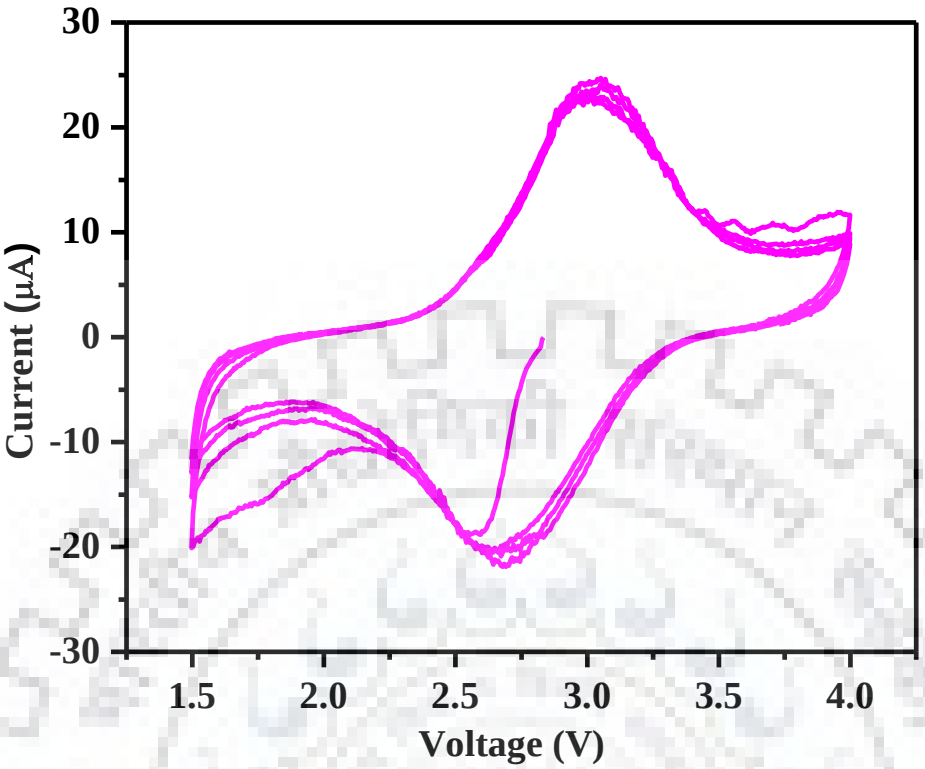

Figure 4.9 Cyclic voltammogram of $Na_3Fe(PO_4)_2$.

4.3.6 Galvanostatic Charge-Discharge Measurements

The galvanostatic charge-discharge experiments were done at various slow C-rates and the cut-off potentials were set in the range 1.5 – 4.0 V for all the tests (Figure 4.10). Assuming complete one electron process per Fe atom, insertion of 1 lithium ion per formula unit gives a theoretical capacity of 85.14 mAh g^{-1} for $Na_3Fe(PO_4)_2$. $Na_3Fe(PO_4)_2$ shows achievable capacity of 24.9 mAh g^{-1} (~ 29 % of theoretical capacity) at C/50 rate, which accounts for 0.29 Li insertion. However, it experiences an irreversible capacity loss of 5 % in the second cycle. At higher C-rates, the capacity achieved remains constant with 18.5 mAh g^{-1} at C/20, 17.4 mAh g^{-1} at C/10 and 16 mAh g^{-1} at C/5, respectively. Upon returning to a slower C-rate (C/50) after completing all the faster C-rates, it showed a constant capacity of 21.3 mAh g^{-1} (Figure 4.11 a). When cycled at C/10 rate for an extended cycle life testing it showed a constant capacity of 18.2 mAh g^{-1} up to 100 cycles without any capacity fading reinforcing the structural stability of $Na_3Fe(PO_4)_2$ during Li-ion intercalation and de-intercalation. The voltage–composition curves show lithiation starting at a potential of 3.25 V

as expected from the CV plot. The sloppy discharge profiles without any apparent plateau also point towards a solid-solution formation between the oxidized and reduced phases. Low experimentally observed capacity of ~25% may be due to its poor ionic and electrical conductivity.

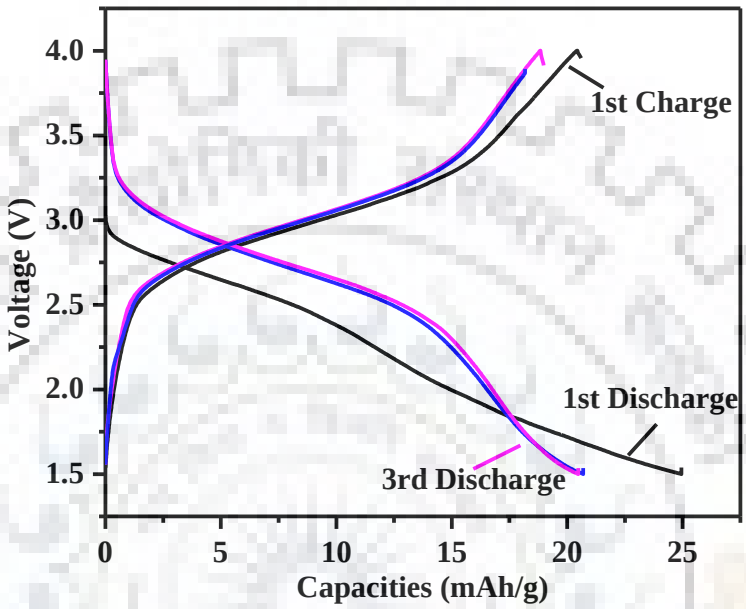

Figure 4.10 Charge-discharge curve of $Na_3Fe(PO_4)_2$ at C/50 when cycled between 1.5 – 4 V.

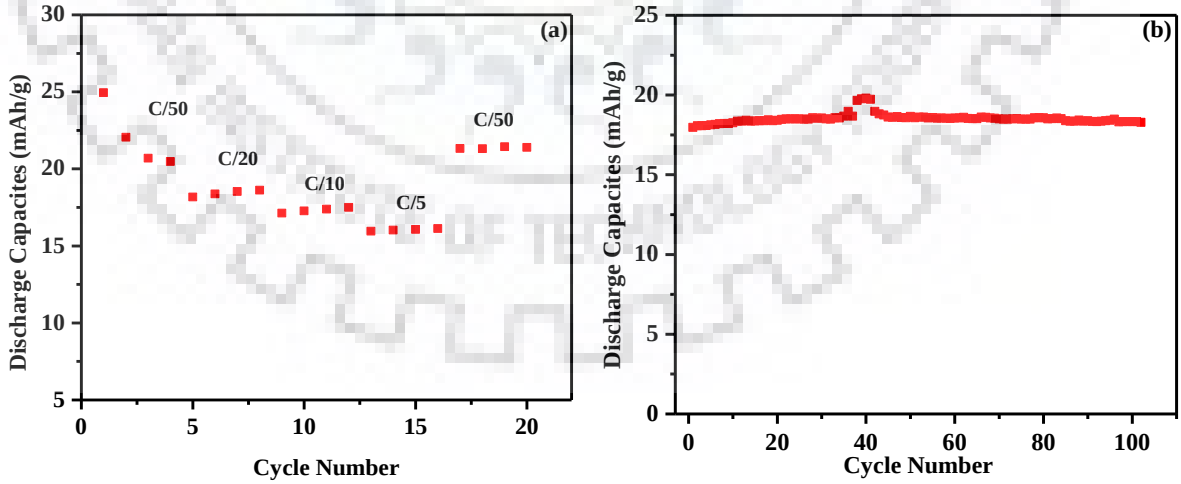

Figure 4.11 Charge-discharge curve of $Na_3Fe(PO_4)_2$ (a) at different cycling rate (b) 100 cycles at C/10.

In summary, a rapid synthetic method for the preparation of $Na_3Fe(PO_4)_2$ based on sol-gel technique within 24 h reaction time, much faster than the conventional solid state method is reported. The phase purity, microstructure and composition of the synthesized compound were ascertained by P-XRD, FE-SEM and EDX studies, respectively. The presence of an anodic peak at 3.04 V in the CV trace suggested $Na_3Fe(PO_4)_2$ as potential cathode material for Li-ion batteries. The charge-discharge studies carried out between 1.5 – 4.0 V at different C rates (C/50, C/20, C/10 and C/5) confirmed the electrochemically active nature of $Na_3Fe(PO_4)_2$ as cathode material for Li-ion batteries, although the compound showed much reduced capacity than the theoretical (85 mAh g^{-1}). But, the excellent capacity retention at C/20 up to 100 charge-discharge cycles is noteworthy suggesting its structural robustness during electrochemical insertion-extraction of Li.

CHAPTER – 5

Nut-Shaped Li_3VO_4 with Hierarchical Mesopores: A New Anode Material for High Capacity Li-Ion Batteries

Nut-shaped Li_3VO_4 with Hierarchical Mesopores: A New Anode Material for High Capacity Li-Ion Batteries

5.1 INTRODUCTION

Lithium Ion Battery (LIB) is a well-established technology used as power sources for all types of portable devices and large scale energy storage devices [430-435]. Yet, the technology is still far behind as cost-effective and safe to be used in electric vehicles (EVs), hybrid electric vehicles (HEVs) and plug in hybrid electric vehicles (PHEVs). While graphite is the most commonly used anode material in LIBs because of its excellent properties such as, flat and low working potential (~ 0.2 V vs. Li), low cost and high reversibility, it has many drawbacks as well. For example, graphite has slow lithium diffusion (10^{-9} – 10^{-7} cm^2 s^{-1}), which results in low power density battery as well as dendritic lithium growth at low potential that raises mainly safety issues [436]. There are efforts to replace graphite anode with other materials having higher capacity, energy density and power density. Despite having high energy densities, some conversion type electrodes are not suitable for replacing graphite because of large charge-discharge hysteresis [437]. $Li_4Ti_5O_{12}$, crystallizing in a spinel structure has been found to be a promising anode material for LIBs having good cyclability with minimal structural change upon lithiation-delithiation and higher safety [438, 439]. However, the energy density of $Li_4Ti_5O_{12}$ is limited by its high operating potential (~ 1.6 V) and low theoretical specific capacity (~ 170 mAh g^{-1}) [439]. So, there is a need to explore safer materials possessing high energy density, high specific capacity and good rate capabilities.

Recently, Li_3VO_4 has been investigated as a promising anode material for LIBs [440, 303, 316]. Li_3VO_4 showed intercalation-deintercalation of Li-ion in the voltage range 0.5 V–1.0 V versus Li^+/Li [303], which is lower than $Li_4Ti_5O_{12}$. Li-electroplating problem which causes dendritic lithium growth would not occur at this lithiation-delithiation potential. The theoretical specific capacity of Li_3VO_4 is 394 mAh g^{-1}, which is higher than that of the commercial graphite anode (370 mAh g^{-1}) [441]. Despite having many advantages such as, safe voltage, high specific capacity and reasonably high Li-ion conductivity (≈ 10^{-4} S m^{-1})

[442], low electrical conductivity is the main issue in using Li_3VO_4 as a capable anode material for LIBs. Moreover, large polarization resistance which arises due to low electrical conductivity of Li_3VO_4 reduces the performance of LIBs. Many attempts have been made to improve the electrical conductivity of Li_3VO_4 [443-445, 317, 446]. In addition to that, Li_3VO_4 synthesized by other synthetic methods such as, solid state [440, 303], sol-gel [445] and hydrothermal [443] results in larger particle sizes. The large particle sizes leads to low surface areas and slow Li-ion diffusion for the as prepared Li_3VO_4. S. Shi-Gang *et al.* have reported better cyclic performance of nanosized Li_3VO_4 [447]. A template based method producing Li_3VO_4 with hollow-cuboid morphology was developed by C. Guozhong *et al*. The high surface area and hollow structure of the above Li_3VO_4 shortened the Li-ion diffusion distance leading to excellent cycling performance [448].

In this chapter, we report a rapid hydrothermal method for the synthesis of hierarchically mesoporous Li_3VO_4 (HM-Li_3VO_4). The template free hydrothermal method in ethylene glycol - water (EG-H_2O 2:1 v/v) solvent system produces nut-shaped Li_3VO_4 at 170 °C in 5 hours. The nut-shaped Li_3VO_4 is highly porous and hollow from inside with hierarchical mesoporosity with an extended pore size distribution ranging between 3.0 and 30.0 (± 0.5) nm. The as synthesized Li_3VO_4 is highly crystalline in nature. The electrochemical charge-discharge shows improved anode performance with bare Li_3VO_4. The details of the investigations are reported in this chapter.

5.2 EXPERIMETAL SECTION

5.2.1 Materials and Synthesis

For the preparation of HM-Li_3VO_4 by hydrothermal method, first ethylene glycol-water (EG-H_2O; EG, extrapure AR purchased from SRL and Millipore water was used) solvent system was prepared by mixing EG:H_2O in 2:1 (v/v) ratio. Then stoichiometric quantities of V_2O_5 (Sigma-Aldrich, purity ≥ 99.6 %) and LiOH.H_2O (SRL, purity > 99 %) were weighed and transferred into two separate beakers containing the EG-H_2O solvent system. The beaker containing V_2O_5 was kept on a magnetic stirrer and the temperature was adjusted at 55 °C. LiOH.H_2O in the other beaker was stirred with a glass rod to make a clear suspension. The LiOH.H_2O suspension was then transferred into the V_2O_5 suspension and stirred for 30 minutes. A greenish color solution was resulted after 30 minutes. The resulting

solution was transferred into a Teflon lined autoclave (50 ml capacity) and hydrothermal treatments were carried out at 170 °C for various durations (3, 4, 5, 10 and 20 h). The compounds obtained after the hydrothermal reactions were filtered and thoroughly washed with ethanol. After washing, the products were dried in an air oven at 80 °C overnight. The powder products thus obtained were subjected to various analysis and measurements. For comparison, Li_3VO_4 powder was also prepared using solid state method (SS-Li_3VO_4), for which stoichiometric amounts of Li_2CO_3 and V_2O_5 were taken and ground in an agate mortar for one hour. The ground powder was then heated at 500 ºC for 5 h followed by intermittent grinding and heating at 750 ºC for 10 h to obtain phase pure Li_3VO_4 (SS-Li_3VO_4).

5.2.2 Electrochemical Measurement

For electrochemical measurements, a half-cell was fabricated using Li-metal as the counter electrode with HM-Li_3VO_4 as an active anode material and 1 M $LiPF_6$ in 1:1 (v/v) ethylene carbonate (EC)-dimethyl carbonate (DMC) (Mitsubishi Chemical Co., Japan) as the electrolyte. Electrochemical measurements were carried out using a laboratory made cylindrical Teflon cell with Polypropylene separator (Celgard 2300). The slurry of HM-Li_3VO_4 electrode was prepared by mixing 80 wt % of active material, 10 wt. % of conducting agent (acetylene black) and 10 wt. % of binder (polyvinylidene fluoride, PVDF). The obtained slurry was pasted onto copper foil followed by drying in a vacuum oven at 80°C for 12 h to remove the residual solvents before pressing. After drying and pressing, electrodes were cut into circular discs having a diameter of ~10 mm. Then, cells were assembled inside an argon gas-filled glove-box (MBRAUN, MB 200G Unilab, Germany) maintaining oxygen and moisture at a controlled level of < 1 ppm. Electrochemical measurements of all cells were carried out using Arbin Cycler (MB 200G, Arbin Instruments, USA) battery tester.

5.3 RESULTS AND DISCUSSION

5.3.1 Powder-XRD Analysis

P-XRD patterns of Li_3VO_4 synthesized under hydrothermal condition (HM-Li_3VO_4) for different durations (3, 4 and 5 h) are shown in Figure 5.1. The analysis of P-XRD

patterns indicated formation of single phase Li_3VO_4 that matches very well with the reported Li_3VO_4 (JCPDS PDF # 38-1247) for all the samples. All the diffraction peaks are indexable in the orthorhombic space group, $Pmn2_1$ [449]. The P-XRD pattern of Li_3VO_4 (Figure 5.2), prepared by the solid state method (SS-Li_3VO_4), also agrees well with the reported Li_3VO_4 confirming the formation of pure phase material.

To determine the refined unit cell parameters of HM-Li_3VO_4, least-squares refinement of all the observed diffraction lines was carried out in the orthorhombic $Pmn2_1$ space group (No. 31) using the PROSZKI program. The refined lattice parameters, a = 6.314(3), b = 5.469(3) and c = 4.968(4) Å, are in good agreement with that of the previous literature reports. The indexed P-XRD data is given in Table 5.1.

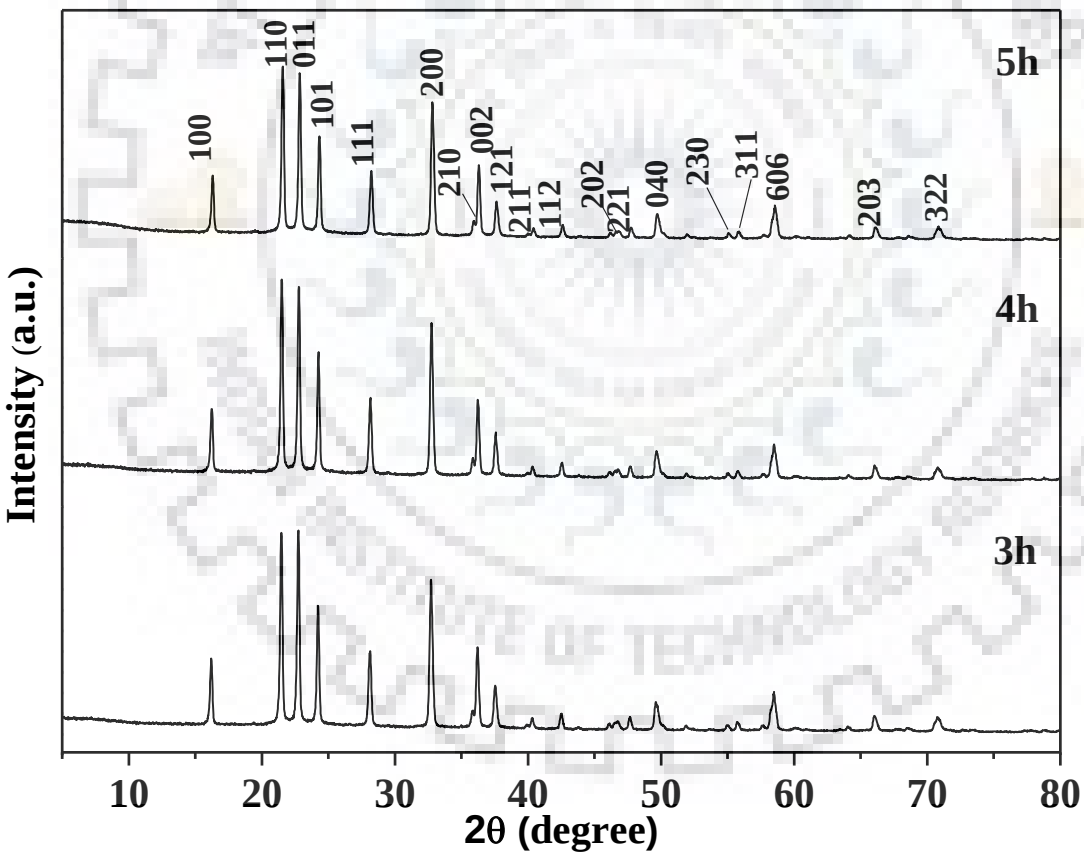

Figure 5.1 P-XRD patterns of HM-Li_3VO_4 obtained after 3, 4 and 5 h under hydrothermal condition.

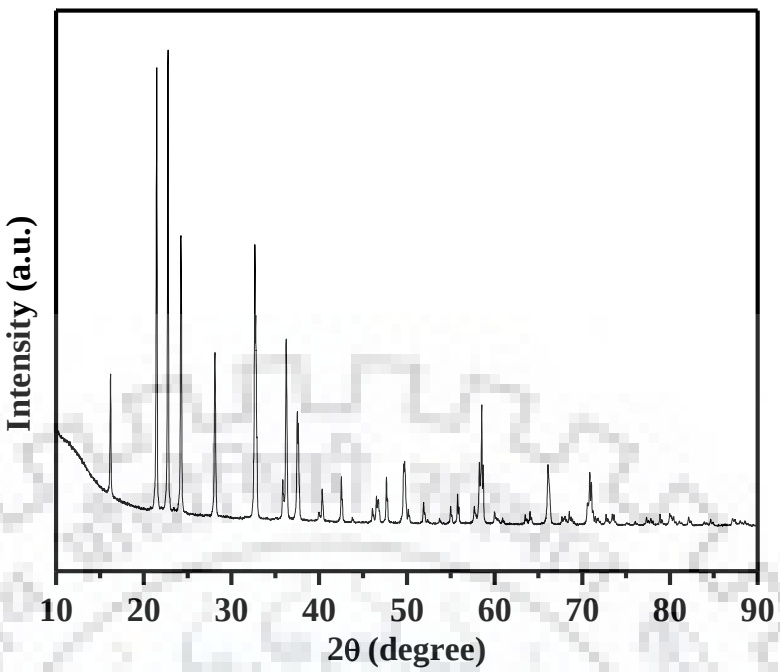

Figure 5.2 P-XRD pattern of SS-Li_3VO_4 synthesized by solid state method.

The crystal structure refinement of HM-Li_3VO_4 is carried out by the Rietveld method using FULLPROF program. The Rietveld refinement of the P-XRD data is performed in the $Pmn2_1$ space group using the positional, occupancy and thermal parameters reported in the literature [449] as inputs. A reliable fit between the calculated and observed P-XRD data is achieved with the reliability parameters, R_{Bragg} = 3.53%, R_f = 4.61% and χ^2 = 4.58 for HM-Li_3VO_4. The calculated, observed and difference profiles of the Rietveld refinement is shown in Figure 5.3. The refined atomic positions and thermal parameters along with occupancy are given in Table 5.2. The Rietveld refined cell parameters, a = 6.3189(3), b = 5.4454(2) and c = 4.9468(2) Å and V = 169.87 $Å^3$ are in good agreement with the previously reported data. The structure of HM-Li_3VO_4 based on the positional parameters obtained after the Rietveld refinement is presented in Figure 5.4.

The structure of Li_3VO_4 is a distorted ordered wurtzite-type, which can be described as made up of distorted hexagonal packing of oxygen ions with half the tetrahedral sites occupied by Li and V. In the polyhedral presentation, rows of $Li(1)O_4$ tetrahedra alternate with rows of $Li(2)O_4$-VO_4-$Li(2)O_4$ tetrahedra in a corner shared three-dimensional network, which could be viewed as a hollow lantern-like structure. In this three-dimensional

arrangement, only half of the tetrahedral sites are occupied and the remaining half are vacant, which are favorable for lithium insertion.

Table 5.1 Indexed P-XRD data of HM-Li_3VO_4

h k l	d_{obs}(Å)	d_{calc} (Å)	I_{obs}
1 0 0	5.416	5.444	32
1 1 0	4.109	4.122	100
0 1 1	3.879	3.892	99
1 0 1	3.649	3.659	59
1 1 1	3.156	3.166	36
2 0 0	2.726	2.721	69
0 0 2	2.468	2.471	41
2 0 1	2.387	2.384	23
2 1 1	2.228	2.230	6
1 1 2	2.117	2.119	9
0 3 1	1.936	1.936	5
2 2 1	1.901	1.902	8
2 0 2	1.831	1.829	15
2 1 2	1.756	1.757	4
2 3 0	1.664	1.664	3
3 1 1	1.644	1.644	5
3 2 0	1.573	1.573	24
1 3 2	1.537	1.537	3
1 4 1	1.450	1.449	3
2 0 3	1.411	1.409	13
3 2 2	1.327	1.327	12

a = 6.314(3), b = 5.469(3) and c = 4.968(4) Å

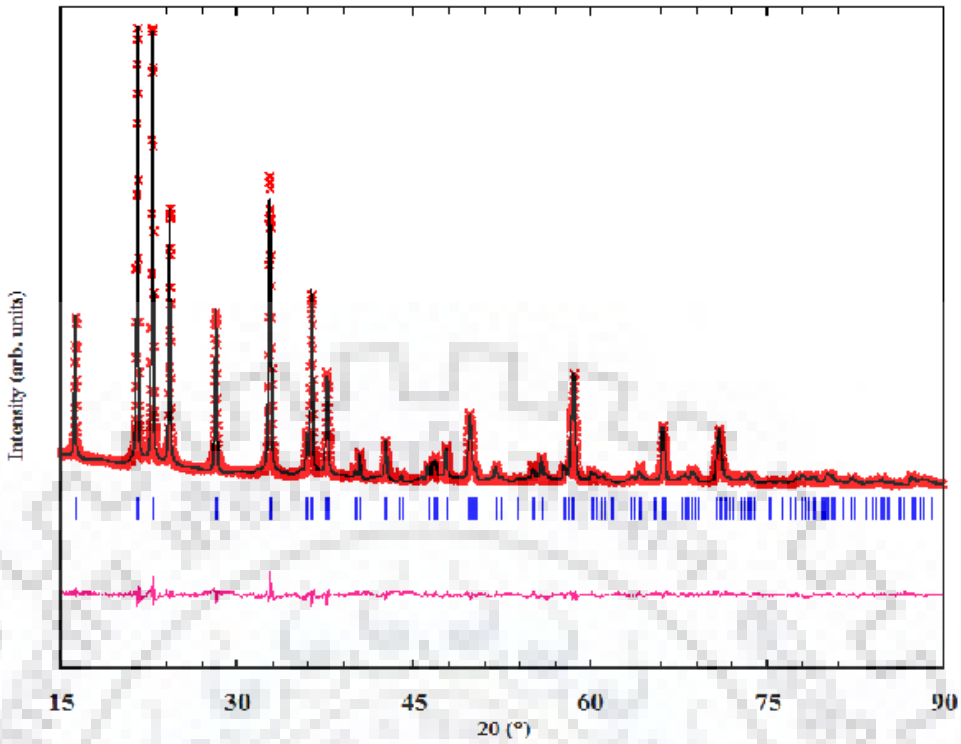

Figure 5.3 The calculated (black line), observed (red cross) and difference profiles (below, pink line) of the Rietveld refinement of HM-Li_3VO_4.

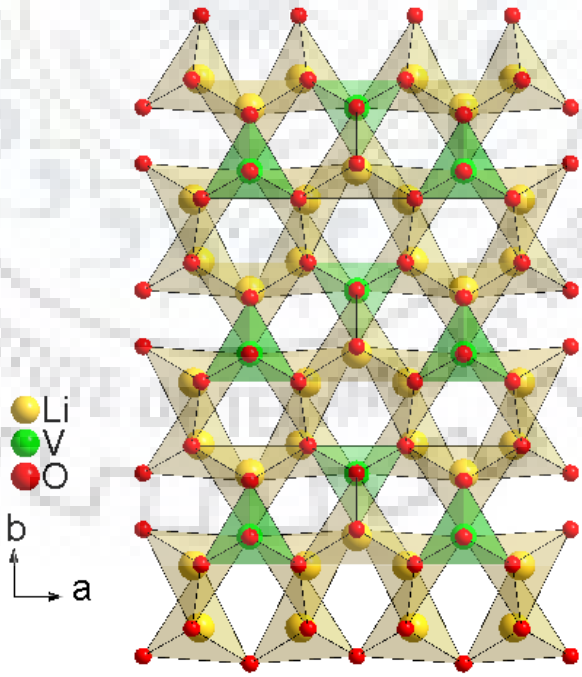

Figure 5.4 Crystal structure of HM-Li_3VO_4 drawn from the refined atomic positions.

Table 5.2 Refined Atomic Position, Site Occupancy and Thermal Parameters Obtained After Rietveld Refinement of the Structure of HM-Li_3VO_4

Atoms	*x*	*y*	*z*	B (Å^2)	Occ.
Li1	0.236(1)	0.327(5)	0.973(7)	3.0(4)	2.0
Li2	0.5000	0.826(3)	0.99(1)	1.8	1.0
V	0.0000	0.8269(3)	0.0000	3.46(7)	1.0
O1	0.2272(5)	0.6752(9)	0.906(1)	2.4(1)	2.0
O2	0.0000	0.132(1)	0.90(1)	0.03(1)	1.0
O3	0.5000	0.173(1)	0.859(1)	0.97(8)	1.0

Space group $Pmn2_1$ (No. 31), a = 6.3189(3), b = 5.4454(2) and c = 4.9468(2) Å; R_{Bragg} = 3.53%, R_f = 4.61%, R_p = 13.7%, R_{WP} = 11.5%, and χ^2 = 4.58.

5.3.2 FE-SEM Analysis

FE-SEM images of the HM-Li_3VO_4 obtained after 3, 4, 5, 10 and 20 h hydrothermal treatments are shown in Figures 5.5 and 5.6. The images clearly reveal that the nut-shaped particles start to form as early as 3 h of reaction. It is apparent from the images that the number and uniformity of nut-shaped particles increases from 3 to 5 h, although the P-XRD pattern showed highly crystalline nature for all the samples. With extended reaction times, from 10 to 20 h, the nut-shaped particles get converted into some sort of agglomerates. Notably, the nut-shaped Li_3VO_4 particles obtained after 5 h hydrothermal reaction are not completely dense, rather hollow from inside, as can be seen in one of the high magnification SEM images (Figure 5.6 c). The porous nature of the Li_3VO_4 is clearly seen (Figure 5.6 d) when FE-SEM images were collected with thoroughly ground samples. Thus, it can be concluded from the SEM imaging studies that the nut-shaped Li_3VO_4 synthesized here is

highly porous and formed by aggregation of small sized particles of Li_3VO_4. All the electrochemical measurements are carried out on the samples obtained after 5 h of hydrothermal reaction.

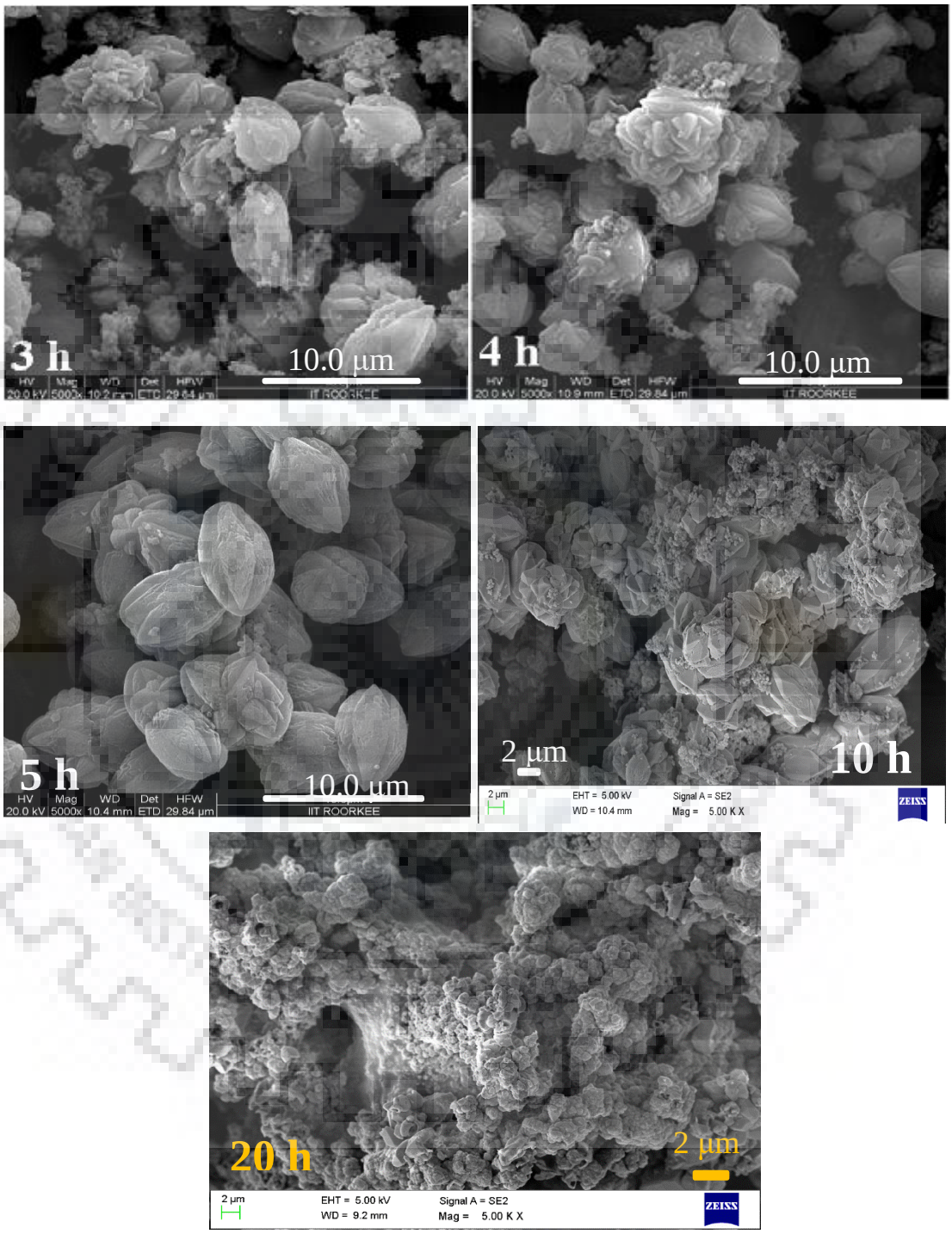

Figure 5.5 FE-SEM images of untreated HM-Li_3VO_4 obtained after 3, 4, 5, 10 and 20 h of hydrothermal treatment.

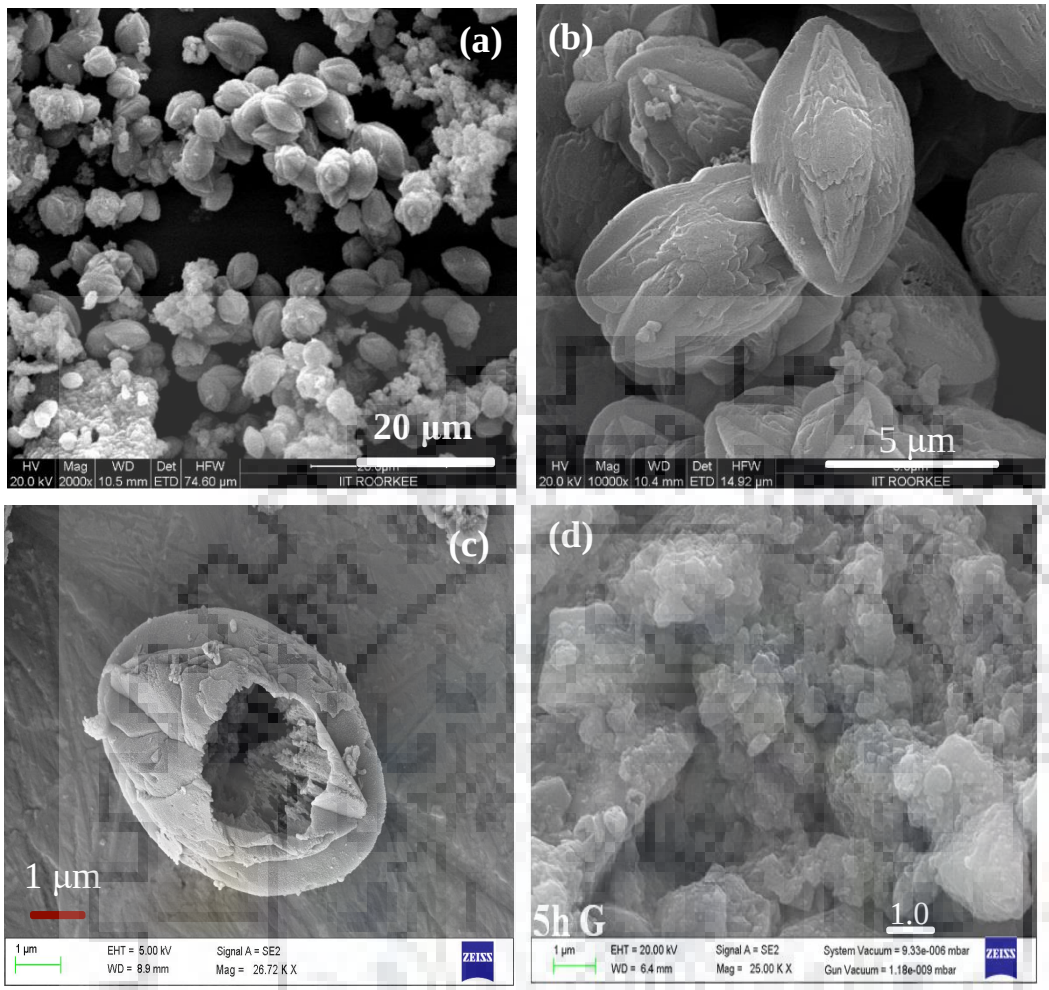

Figure 5.6 FE-SEM images of untreated HM-Li_3VO_4 obtained after 5 h of hydrothermal treatment at different magnification.

5.3.3 TEM Analysis

TEM images (taken at different magnifications) and ED patterns of HM-Li_3VO_4 are shown in Figure 5.7. Rings in the ED pattern signify the polycrystalline nature of the sample. The first four rings (indexed) in the ED pattern are in excellent agreement with the 2nd, 3rd, 4th and 5th (*hkl*) reflections observed in the P-XRD pattern. Analysis of TEM images at different magnifications shows that the large nut-shaped Li_3VO_4 particles are basically composed of nanoparticles of Li_3VO_4 with sizes ranging from 50-100 nm. Moreover, the observed pore sizes also range from few nanometers to ~ 30 nm.

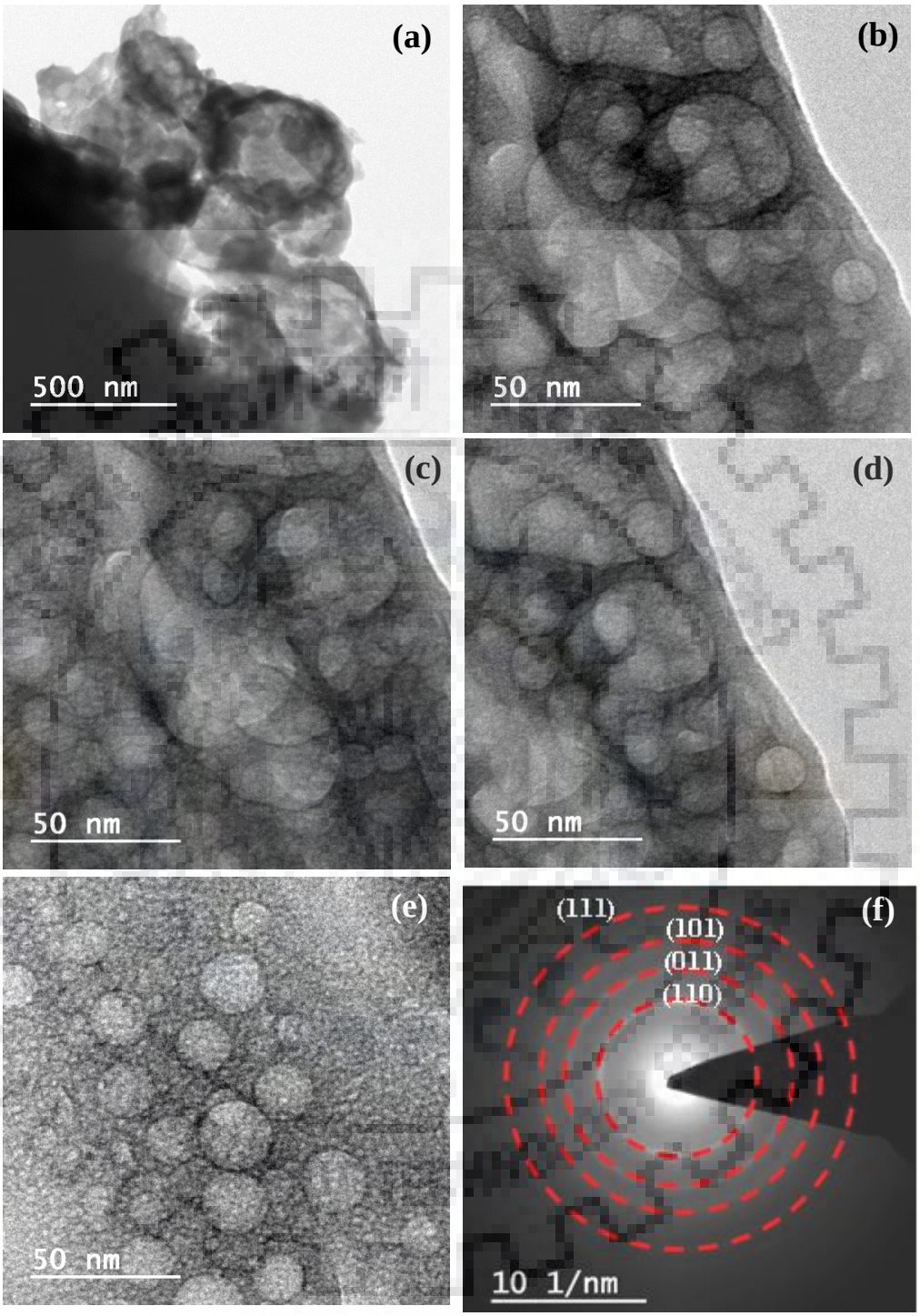

Figure 5.7 TEM images (a-e) and ED pattern (f) of HM-Li_3VO_4 obtained after 5 h of hydrothermal reaction.

To elucidate the nature of pores present in the nut-shaped Li_3VO_4, a histogram is constructed from the TEM images. The histogram shown in Figure 5.8 gives a clearer picture about the pore size distribution. It is seen that majority of the pores are in 0-5 nm range while the number of pores decreases gradually with the increase of pore diameter, thus clearly indicating a multimodal pore distribution and hierarchy in the pore structure of HM-Li_3VO_4. Moreover, the irregular sized pores seem to be arranged in a three-dimensional interconnected fashion with closed walls.

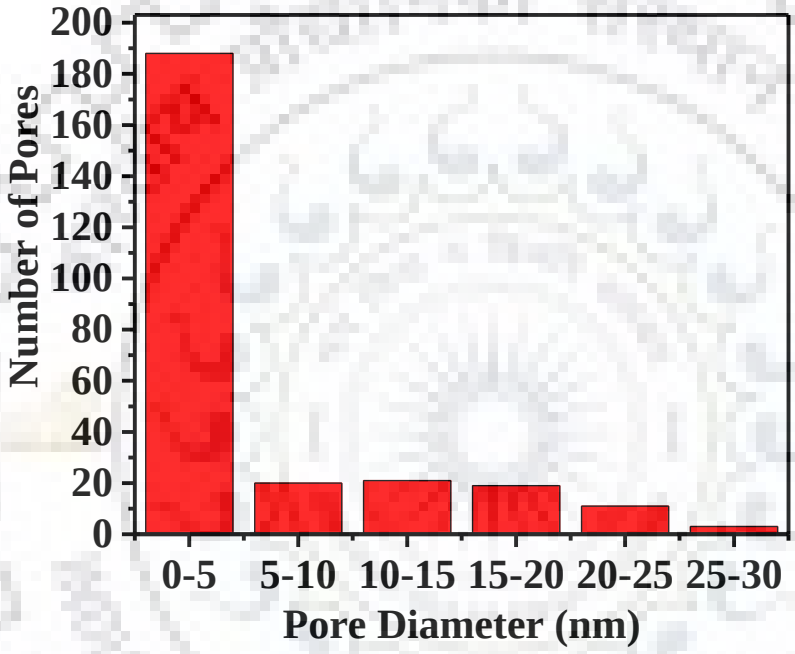

Figure 5.8 Pore size distribution in nut-shaped HM-Li_3VO_4 estimated from TEM images.

5.3.4 Surface Area Analysis

Nitrogen sorption is carried out to analyze the surface area and porosity of the samples. The BET surface area and total pore volume of the as synthesized HM-Li_3VO_4 are 6.3 $m^2\ g^{-1}$ and 0.008 cc g^{-1}, respectively. The bare HM-Li_3VO_4 shows a type IV isotherm, which is typical for mesoporous materials with irregular pore systems [450]. The pore size distribution showed that the diameters of the majority of the pores are between 3 and 4 nm (Figure 5.9). However, the tail of the major peak extends up to ~ 10 nm with additional maxima at ~ 4.5, 6, and 8 nm.

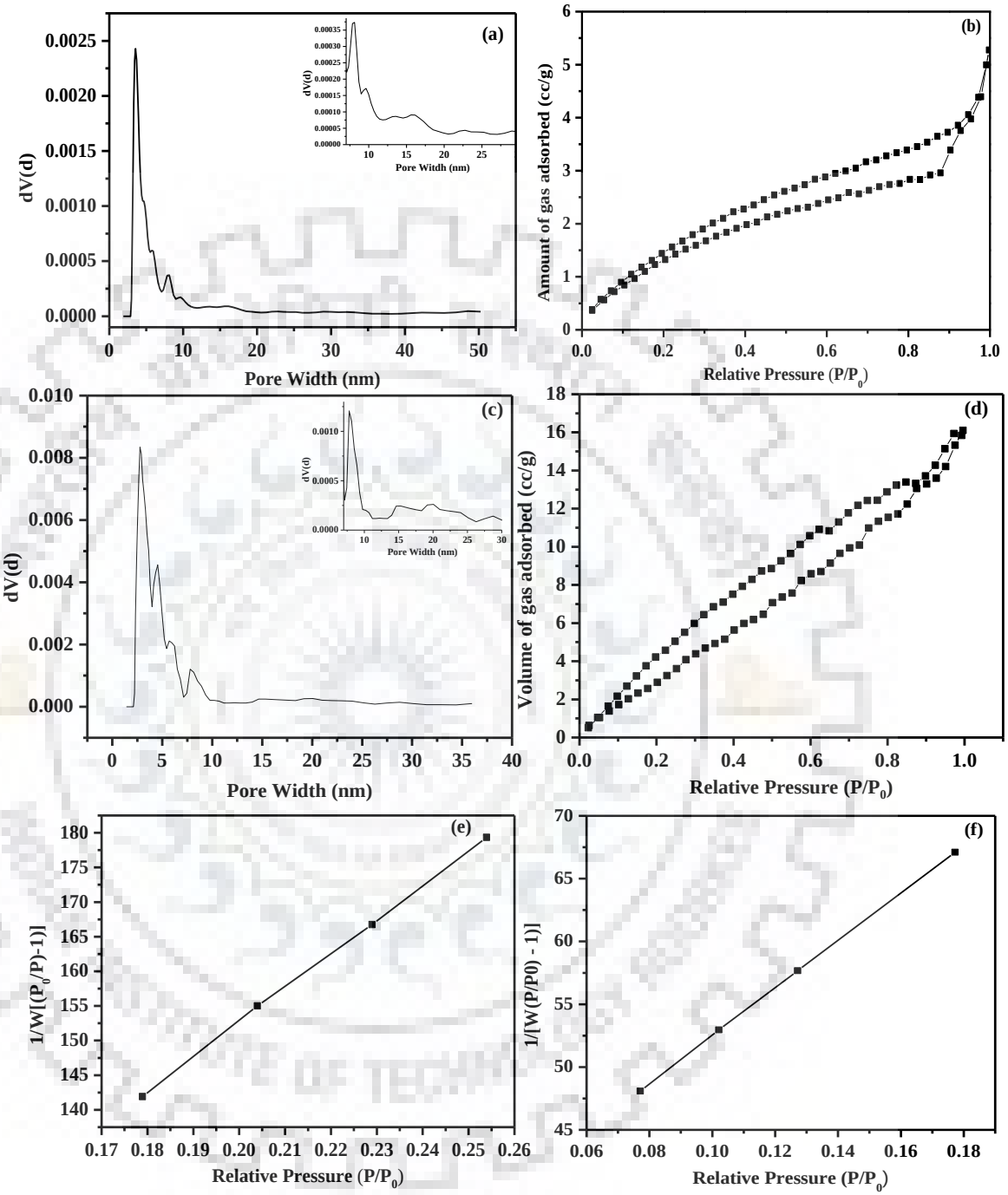

Figure 5.9 Pore size distribution of HM-Li_3VO_4 (a) before and (c) after grinding. Nitrogen sorption isotherms of HM-Li_3VO_4 (c) before and (d) after grinding. Surface area of HM-Li_3VO_4 (e) before and (f) after grinding.

Moreover, multiple numbers of low intense maxima with broad features are also seen beyond 10 nm that extends up to ~ 30 nm (see inset of Figures 5.9a). Thus, complete pore analysis data clearly indicates the pore size distribution as multimodal and ascertains a hierarchical distribution consistent with the TEM analysis. The observed small surface area clearly reveals that all the pores are not accessible in the nut-shaped HM-Li_3VO_4. Therefore, BET surface area and pore size analysis were carried out after grinding the powder thoroughly to enhance the accessibility of pores. The BET surface area and total pore volume after grinding the pristine sample are 15.66 $m^2\ g^{-1}$ and 0.03 cc g^{-1}, respectively. The surface area and pore volume becomes nearly three times than that of the pristine samples after grinding mainly due to enhanced accessibility of the mesopores. But, the pore size distribution data essentially remained the same even after grinding. It is interesting to note the multiple step features in the isotherm (Figure 5.9d), which probably indicates overlay of several type-IV isotherms corresponding to the hierarchy of an array of mesopores.

5.3.5 XPS Analysis

The high resolution XPS of $V2p_{3/2}$, $V2p_{1/2}$ and O_{1s} are shown in Figure 5.10. The binding energies of 517.2 and 525.0 eV correspond to the pentavalent $V2p_{3/2}$ and $V2p_{1/2}$, respectively, while the peak at 529.8 eV is due to O_{1s}. The observed XPS peaks are in agreement with earlier reports [451]. The XPS study carried out on HM-Li_3VO_4 confirms the presence of vanadium as V^{5+}.

5.3.6 Thermogravimetric Analysis

The TG curve of HM-Li_3VO_4 is shown in Figure 5.11. TG analysis shows that ~ 2.3 % weight loss up to 600 °C for the as synthesized sample. The weight loss might be due to some ethylene glycol solvent that might have got trapped in the pores of the nut-shaped HM-Li_3VO_4 even after washing and drying. The sample showed a nearly stable nature beyond 600 °C indicating its high thermal stability up to 800 °C.

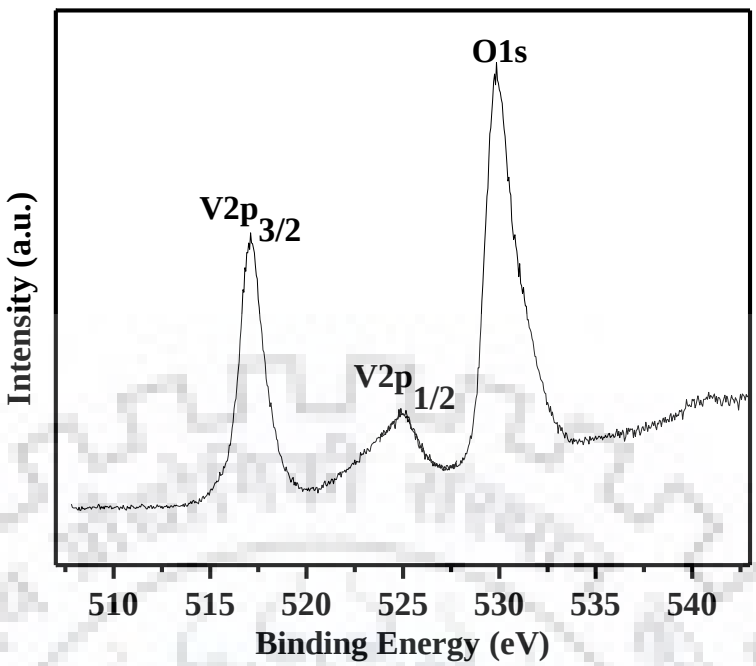

Figure 5.10 XPS of HM-Li_3VO_4 synthesized under hydrothermal condition at 170 °C for 5 h.

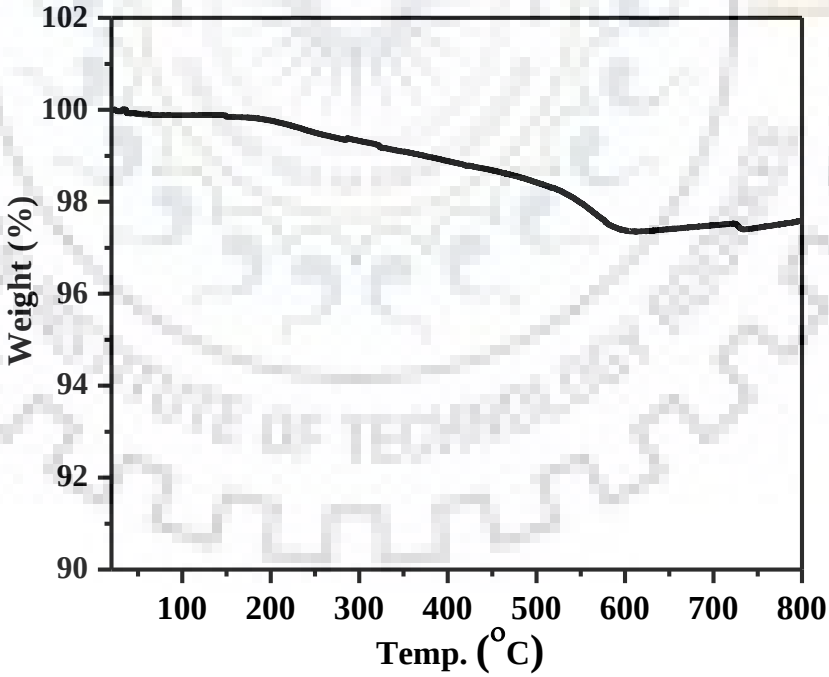

Figure 5.11 TG curve of HM-Li_3VO_4 synthesized under hydrothermal condition at 170 °C for 5 h.

5.3.7 Electrochemical Measurements

The electrochemical performance of bare HM-Li_3VO_4 (without any carbon coatings etc.) is analyzed in a cylindrical Teflon cell configuration. The Galvanostatic charge-discharge studies are carried out under different charge rates (0.1 C – 1 C) in between 0.2 to 2 V. The charge-discharge curves shown in Figure 5.12a confirmed the lithium intercalation mainly in the voltage range 1.0 and 0.5 V vs. Li/Li^+. The cell displayed a high discharge capacity of 615 mAh g^{-1} and charge capacity of 385 mAh g^{-1} at 0.1 C for the first cycle (Figure 5.12 a).

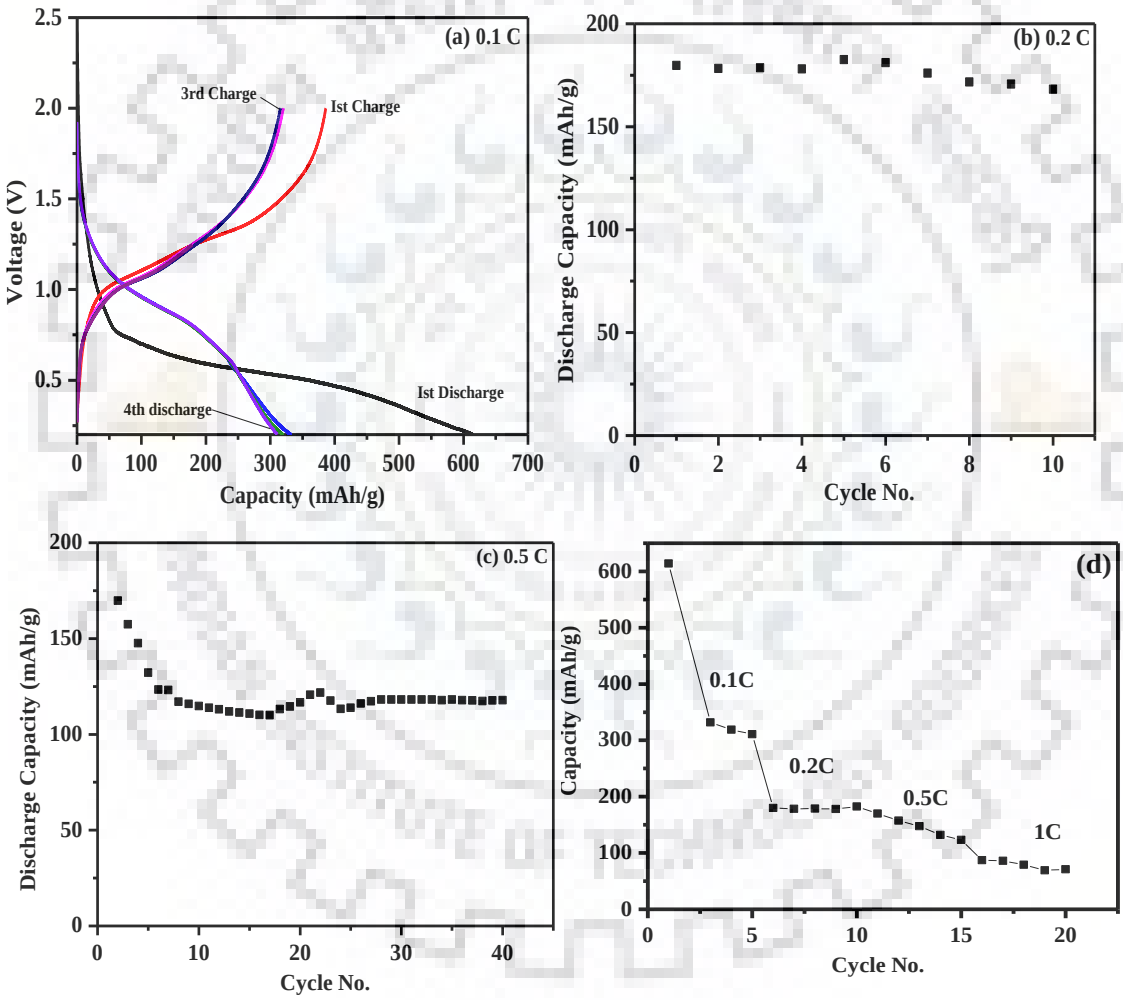

Figure 5.12 (a) Charge-discharge cycles at 0.1 C, (b) discharge capacities at 0.2 C (c) discharge capacities at 0.5 C and (d) discharge capacities at different C rates with increasing cycle numbers.

The relatively low coulombic (~ 62.4 %) efficiency for the first discharge-charge cycle is attributed to the occurrence of side reaction on the electrode surface and interfaces due to the formation of SEI [452]. After the first charge-discharge cycle HM-Li_3VO_4 shows stable performance with a high columbic efficiency of 96.3%. This indicates that the side reactions occur mostly in the first cycle. A discharge capacity 319 mAh g^{-1} at 0.1 C can be obtained after the 4th cycle which is 86.44 % of the capacity of the second discharge cycle. The discharge capacity is 168 mAh g^{-1} after 10 cycles at 0.2 C and 117 mAh g^{-1} after 40 cycles at 0.5 C. The charge-discharge data for bare HM-Li_3VO_4 presented here are comparable or superior to the previous reports [440, 303, 316, 451, 453-455, 313, 318].

5.3.7 CV Analysis

The cyclic voltammetric curve of HM-Li_3VO_4 was collected in a voltage range of 0.2 to 2.5 V at a scan rate of 0.1 mV s^{-1}. The first four cycles of CV profiles are shown in Figure 5.13. There is a marked difference between the 1st and other three subsequent cycles. During the first cathodic scan, the peak observed at 0.34 V is attributed to SEI formation, while that at 0.58 V is due to lithium intercalation.

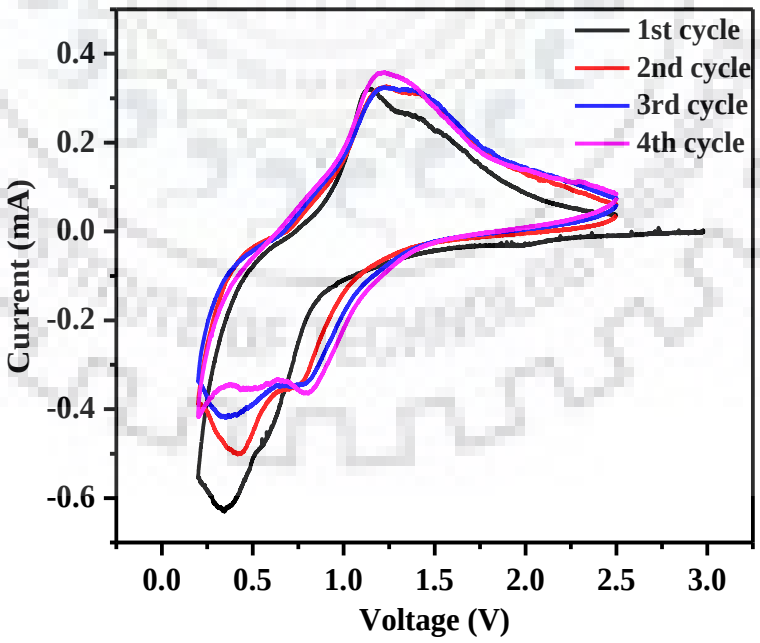

Figure 5.13 Cyclic voltammetric curve of HM-Li_3VO_4 at a scan rate of 0.1 mV s^{-1}.

The voltage plateau in the first discharge curve (Figure 5.12a) is consistent with the reduction peak observed in the first cathodic scan. A remarkable shift in the reduction peaks to 0.50 V and 0.81 V, respectively, in the 4th cycle is attributed to the activation of Li_3VO_4. The peak at 1.2 V in the anodic scan of the 4th cycle is attributed to the lithium extraction process.

The electrochemical charge-discharge cycles of SS-Li_3VO_4 are shown in Figure 5.14. The comparison between charge-discharge data of HM-Li_3VO_4 and SS-Li_3VO_4 shows a noticeable difference. The charge-discharge data presented here for SS-Li_3VO_4 are carried out at 0.1 C rate cycled between the same voltage window (0.2 – 2 V) and compared with the charge-discharge data at 0.1 C rate for the nut-shaped HM-Li_3VO_4. SS-Li_3VO_4 shows a discharge capacity of 320 mAh g^{-1} for the first cycle and 102 mAh g^{-1} for the second discharge cycle which is much lower than that of the nut-shaped HM-Li_3VO_4. The low columbic efficiency of ~ 35 % for SS-Li_3VO_4 in the first discharge and charge cycles might be due to the SEI formation, side reactions that occur on the electrode-electrolyte interface and poor ionic and electronic conductivity of SS-Li_3VO_4.

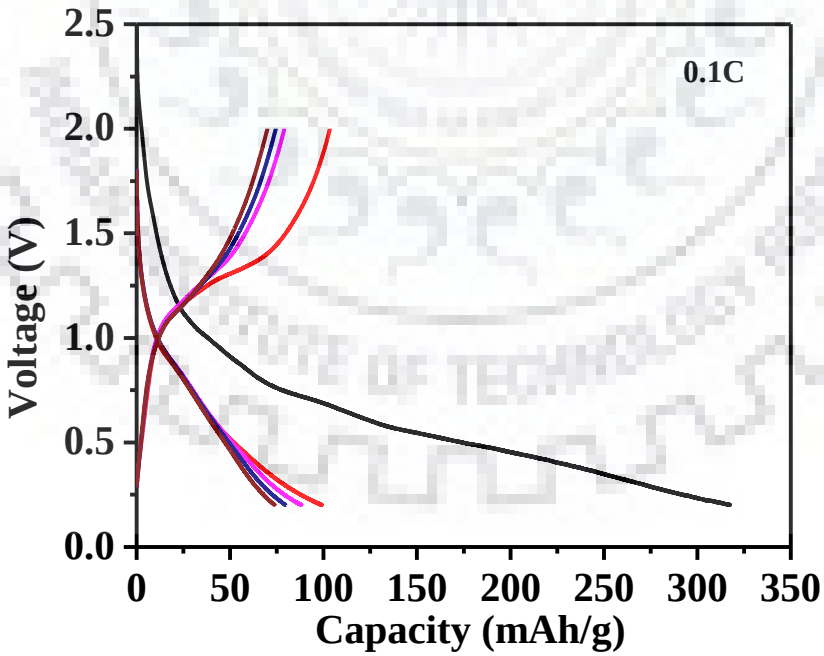

Figure 5.14 Charge-discharge cycles of SS-Li_3VO_4 at 0.1 C cycled between 0.2 – 2 V.

In summary, a rapid template free hydrothermal method was developed for the synthesis of nut-shaped hierarchical mesoporous Li_3VO_4 (HM-Li_3VO_4). P-XRD analysis confirmed formation of single-phase Li_3VO_4 with an orthorhombic structure having lattice parameters, 6.3189(3), 5.4454(2) and 4.9468(2) Å. SEM images showed formation of nut-shaped morphology that are hollow from inside and essentially composed of nano particles of Li_3VO_4 with sizes ranging from 50-100 nm. Combined HR-TEM and BET surface area analysis established hierarchical mesoporous nature of the as prepared Li_3VO_4. The electrochemical charge-discharge studies employing a lithium metal half-cell with the bare HM-Li_3VO_4 as active anode showed a discharge capacity of 615 mAh g^{-1} and a charge capacity of 384 mAh g^{-1} at 0.1 C rate for the first cycle. The discharge capacity of 332 mAh g^{-1} observed at the 2nd cycle for HM-Li_3VO_4 was superior to those reported in the literature for other Li_3VO_4 in its bare form. The improved anode performance of nut-shaped HM-Li_3VO_4 is attributed to the hierarchical mesoporous microstructure which facilitates faster Li^+ diffusion through the mesoporous channels and accommodates Li^+ ions within the mesopores during intercalation-deintercalation process. However, capacity fade at higher rates was evident in the HM-Li_3VO_4 due to its poor electrical conductivity.

CHAPTER – 6

One-Pot Synthesis of Mesoporous Li_3VO_4 on GO: A Viable Anode Material for Li-Ion Batteries

One-Pot Synthesis of Mesoporous Li_3VO_4 on GO: A Viable Anode Material for Li-ion Batteries

6.1 INTRODUCTION

High energy density and high rate capability are probably the two major requirements along with safety for the Li-ion batteries to be used in electric vehicles (EVs), hybrid electric vehicles (HEVs) and plug in hybrid electric vehicles (PHEVs). Although, Li-ion batteries provide high gravimetric and volumetric energy densities [456-460], they can further be improved by inventing new high capacity cathode and anode materials. Furthermore, the decomposition of conventional electrolytes above 4.2 V is again one of the main obstacles in the development of high voltage cathode materials [461-463]. Although, graphite is the workhorse among the anode materials used in Li-ion batteries but severe safety issues, such as, dendritic growth of Li (due to low operational voltage ~ 0.2 V) on the surface of graphite when charged at high rates, limits its use in large size Li-ion batteries [464]. $Li_4Ti_5O_{12}$, on the other hand has emerged as a competitor of graphite anode due to highly flat plateau at 1.5 V vs. Li^+/Li and minimal volume change during lithium intercalation [465]. However, the low theoretical capacity (~ 170 mAh g^{-1}) and high operating potential (~ 1.5 V) of $Li_4Ti_5O_{12}$ anode results in low energy density and low power Li-ion batteries. Therefore, an anode material with high capacity and safe charge-discharge cycles over a long period is essential for vehicular applications. Thus, when combined with high voltage, high capacity and fast rate capable anode, the battery can provide high power density for longer driving distance on a single charge as well as faster recharge in charging stations.

In Chapter-5, we have reported the synthesis of hierarchical mesoporous Li_3VO_4, wherein the mesoporous microstructure and the pore hierarchy has enabled us to achieve enhanced Li-ion mobility and thereby improved electrochemical performance of Li_3VO_4 as compared to most of the Li_3VO_4 reported in its bare form (without carbon composite). However, the electrical conductivity remained poor thus leading to capacity fading with cycling and low discharge capacity at higher C rates. Efforts are being made by several

research groups across the globe to improve both the ionic and electrical conductivity of Li_3VO_4 to achieve high capacity retention and fast rate capability (see Chapter-1). A number of articles have reported the synthesis of different types of carbon composites with Li_3VO_4, which are already reviewed in Chapter-1, to enhance the electrical conductivity for better electrochemical performance of the batteries in terms of capacity retention, high rate cycling and long life . However, most of the synthetic methods reported involved multiple steps and laborious procedures and controlled atmosphere annealing or longer reaction times, which may not be suitable from commercial point of view. Very recently, a high temperature form of Li_3VO_4, namely, γ-Li_3VO_4, which possess higher inherent ionic conductivity, have been reported. Smoothed Li-ion insertion and extraction with enhanced cycle stability have been reported by γ- Li_3VO_4 with Si-doing but the reported reversible capacity was far lower than its theoretical capacity. Therefore, low electrical conductivity, poor rate performance and low cycle life of Li_3VO_4 anodes remained to be the major issues that require to be addressed to realize the full potential of Li_3VO_4 as an advanced anode material.

In the light of the foregoing and our work described in Chapter-5, it is relaized that nanostructuring along with incorporation of hierarchical mesoporosity will alleviate the problems of Li-ion diffusion to a significant extent. Therefore, it is envisaged that enhancement of the electronic conductivity of nanostructured and hierarchical mesoporous Li_3VO_4 can lead to higher capacity retention and rate capable Li-ion batteries. In order to overcome the problems of ionic and poor electronic conductivity of Li_3VO_4 in one go, we have developed herewith a simple, short and template free one-pot synthetic method for the synthesis of mesoporous Li_3VO_4 grown on GO (M-Li_3VO_4-GO) that can deliver 95% to near complete theoretical capacity reversibly with good rate capability. We describe the synthesis, characterization and electrochemical performance of M-Li_3VO_4-GO in this chapter.

6.2 EXPERIMETAL SECTION

6.2.1 Materials and Synthesis

First, graphene oxide (GO) was prepared by a modified Hummer's method. The synthesis of Li_3VO_4 on GO was carried out by a one pot solvothermal method. A unique solvent system prepared by mixing ethylene glycol (EG) and water (EG-H_2O, EG, extrapure

AR, purchased from SRL and Millipore water were used) in a 2:1 (v/v) ratio was used for the synthesis of Li_3VO_4 on GO. GO was first transferred into a beaker containing EG-H_2O solvent and soaked for overnight. After soaking overnight, this solution was sonicated for about 45 minutes. Then stoichiometric quantity of V_2O_5 (Sigma-Aldrich, purity ≥ 99.6 %) were weighed and transferred into a beaker containing GO and EG-H_2O solvent system. This beaker was kept on a magnetic stirrer and temeperature was adjusted to 55 °C. In another beaker stoichiometric quantity of $LiOH.H_2O$ (SRL, purity > 99 %) were weighed and stirred with a glass rod to make a clear suspension. The clear $LiOH.H_2O$ suspension was then transferred into the V_2O_5 suspension and stirred for 30 minutes. A greyish color solution was obtained after 30 minutes. The resulting solution was then transferred into a Teflon lined autoclave (50 ml capacity) and hydrothermal-solvothermal treatments were carried out at 170 °C for 5 h. The compound obtained after the hydrothermal reaction was filtered and thoroughly washed with ethanol. After washing, the product was dried in an air oven at 80 °C overnight. The powder product obtained after drying was subjected to various analysis and measurements.

6.2.2 Electrochemical Measurement

Electrochemical measurements were carried out using a half-cell, fabricated with Li-metal as the counter electrode and M-Li_3VO_4-GO as the active anode material. Electrochemical measurements were peroformed on a laboratory made half-cell with 1 M $LiPF_6$ in 1:1 (v/v) ethylene carbonate (EC)-dimethyl carbonate (DMC) (Mitsubishi Chemical Co., Japan) as the electrolyte and Polypropylene (Celgard 2300) as separator. The composition and procedure for the preparation of slurry of M-Li_3VO_4-GO, its pasting, drying, cutting and assembling of half-cells were same as described in Chapter-5. A battery tester, Arbin Cycler MB 200G, Arbin Instruments, USA was used to carry out the electrochemical measurements of the assembled cells.

6.3 RESULTS AND DISCUSSION

6.3.1 Powder-XRD Analysis

The P-XRD pattern of GO synthesized by modified Hummer's method is shown in Figure 6.1. The peak at 10.6 Å is characterstic of GO, confirming the formation of graphite oxide (GO) from the commercial graphite. The P-XRD pattern of Li_3VO_4-GO synthesized by the one pot hydro-solvothermal method is shown in Figure 6.2. Analysis of the P-XRD data reveals formation of single phase Li_3VO_4, similar to that reported in the literature (JCPDS PDF # 38-1247) and in the previous chapter. All the diffraction peaks are indexable in the orthorhombic space group, $Pmn2_1$ (No. 31), reported for Li_3VO_4 [449]. The characteristic diffraction peaks due to GO are not visible. This is due to poor scattering by the constituent atoms of GO and presence of a comparatively small quantity in the composite. To determine the refined unit cell parameters of Li_3VO_4-GO, least-squares refinement of all the observed diffraction lines is carried out in an orthorhombic system using the PROSZKI program. The refined lattice parameters, a = 6.314(2), b = 5.469(3) and c = 4.968(4) Å, are in agreement with the earlier reports. The indexed P-XRD data of Li_3VO_4-GO is given in Table 6.1.

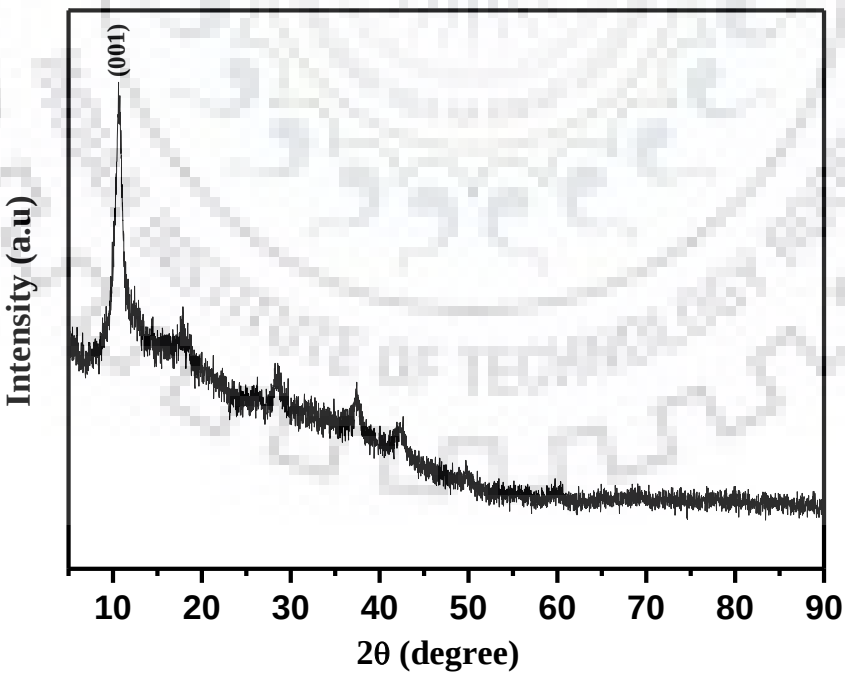

Figure 6.1 P-XRD pattern of GO synthesized using modified Hummer's method.

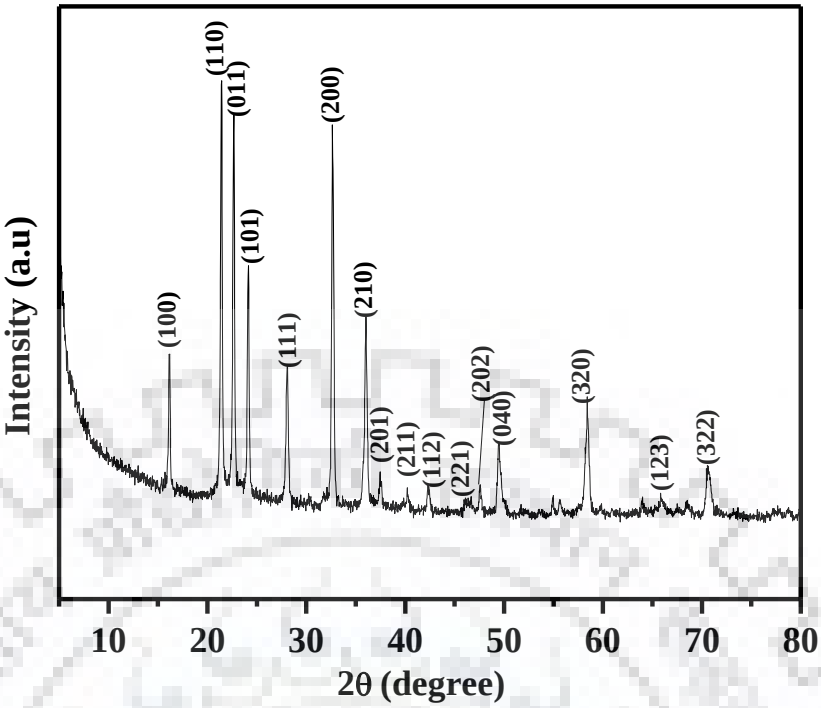

Figure 6.2 P-XRD pattern of Li_3VO_4-GO synthesized under hydrothermal condition.

6.3.2 FE-SEM Analysis

The morphological homogeneity of the as synthesized Li_3VO_4-GO was checked by recording FE-SEM images. The FE-SEM images of Li_3VO_4-GO are shown in Figure 6.3. The images clearly reveals formation of nut-shaped particles grown on the GO sheets. The size of the nut-shaped particles of Li_3VO_4 vary from sub-micrometer to 2 μm range and are much smaller than those obtained in the previous synthesis reported in Chapter-5. The FE-SEM images taken at different areas of the sample ascertained the morphological homogeneity of Li_3VO_4-GO throughout the analyzed area of the sample. Moreover, the size and shape distribution of the Li_3VO_4 particles synthesized by the present one-pot method seems to be relatively narrow and monodisperse as compared to that described in the previous chapter. This may be due to differences in the growth mechanisms in the absence and presence of GO.

Table 6.1 Indexed P-XRD data of Li_3VO_4-GO

h k l	d_{obs}(Å)	d_{calc} (Å)	I_{obs}
1 0 0	5.479	5.469	32
1 1 0	4.138	4.134	100
0 1 1	3.917	3.904	90
1 0 1	3.681	3.677	54
1 1 1	3.156	3.178	36
2 0 0	2.742	2.734	87.3
0 0 2	2.486	2.484	38.1
2 0 1	2.399	2.395	13.9
2 1 1	2.238	2.240	5.7
1 1 2	2.129	2.129	7.4
1 3 0	1.964	1.964	5.1
2 2 1	1.909	1.908	7.8
2 0 2	1.838	1.838	18.5
2 3 0	1.670	1.668	4.6
3 1 1	1.650	1.651	5.0
0 4 0	1.578	1.578	29.2
3 2 2	1.331	1.332	14

a = 6.314(2), b = 5.469(3) and c = 4.968(4) Å.

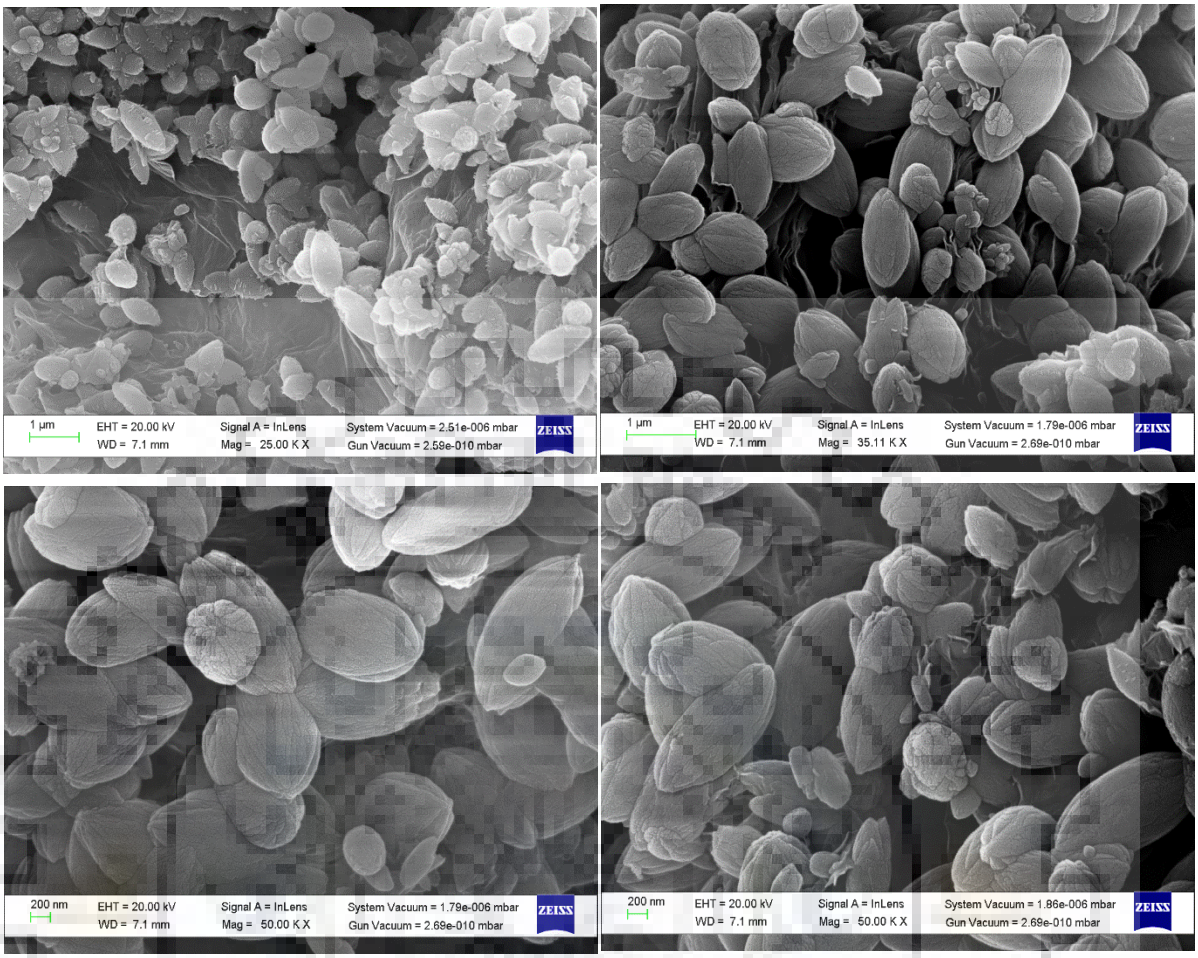

Figure 6.3 FE-SEM images of Li_3VO_4-GO synthesized by hydrothermal reaction for 5 h.

6.3.3 TEM Analysis

TEM images at different magnifications for Li_3VO_4-GO are shown in Figure 6.4. A closer look at the images clearly reveals intimate contacts of Li_3VO_4 particles with the GO. The presence of mesopores with different sizes is clearly evident in the HR-TEM taken at higher magnifications (Figure 6.4d). It is further pointed out that the nut-shaped particles are indeed made up of smaller nanoparticles of Li_3VO_4, similar feature to what was observed in HM-Li_3VO_4 reported in Chapter-5.

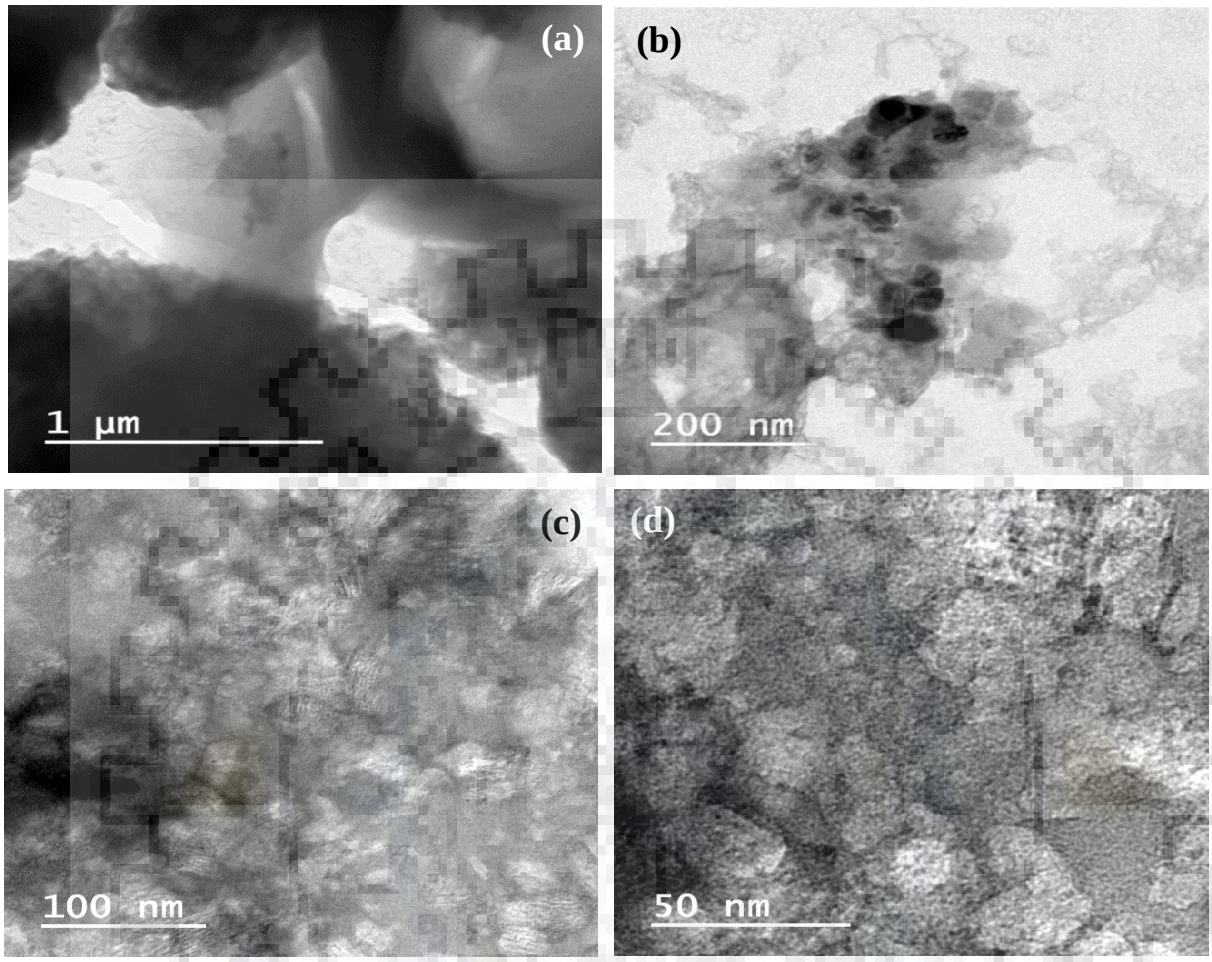

Figure 6.4 HR-TEM images of Li_3VO_4 obtained after 5 h of hydrothermal treatment.

6.3.4 TG Analysis

The amount of carbon content in the Li_3VO_4-GO composite is determined using TG analysis. The TG curve, shown in Figure 6.5, indicates a total weight loss of 8.2 % up to 400 °C. It is seen that the weight loss starts at ~ 50 °C and ~ 1% of weight loss is observed up to 100 °C. The weight loss occurred up to ~ 100 °C is attributed to the moisture adsorbed on the surface of the Li_3VO_4-GO. Further weigth loss observed between 300 – 400 °C is due to carbons present in the form of GO in Li_3VO_4-GO composites. Therefore, the total amount

of carbon content calculated by TG analysis is 7.2 %. Beyond 400 °C no futher weight loss is observed, which confirms the stable nature of Li_3VO_4 up to 800 °C.

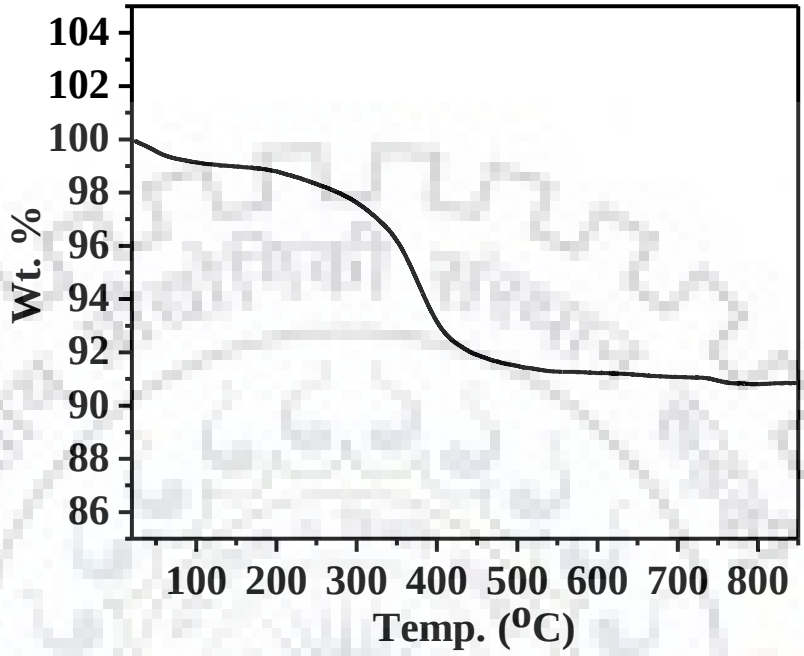

Figure 6.5 TG curve of as synthesized Li_3VO_4-GO.

6.3.5 EIS Measurement

The EIS measurements are carried out to probe the electrical conductivity and charge transfer resistance (R_{ct}) of Li_3VO_4-GO composite in camparison to bare Li_3VO_4. The EIS spectra of bare Li_3VO_4 and Li_3VO_4-GO are shown in Figure 6.6. The Nyquist plots display semicircles in the high to medium frequency range corresponding to the charge transfer resistance (R_{ct}). The diameter of the semicircle is related to the charge transfer resistance, i.e., higher the diameter of the semicircle higher will be the R_{ct}. The R_{ct} value for bare Li_3VO_4 and Li_3VO_4-GO composite are 432 and 195 Ω, respectively. By growing Li_3VO_4 on GO the charge transfer resistance has been reduced to less than half of its value in case of the bare Li_3VO_4, indicating a substantial improvement in the electrical conductivity of Li_3VO_4.

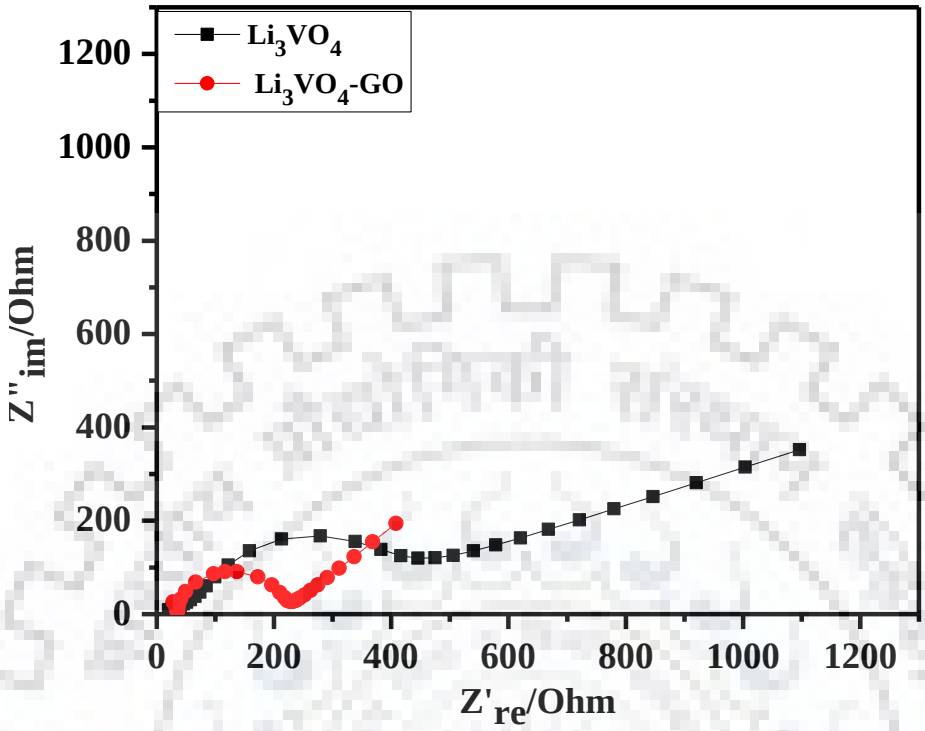

Figure 6.6 Nyquist plots of HM-Li_3VO_4 and M-Li_3VO_4-GO.

6.3.6 XPS Analysis

The high resolution XPS spectra of $V2p_{3/2}$, $V2p_{1/2}$, $O1s$ are shown in Figure 6.7a. The binding energy at 517.3 and 525.2 eV can be ascribed to $V2p_{3/2}$ and $V2p_{1/2}$, respectively, for vanadium in the pentavalant oxidation state, while the peak at 529.9 eV corresponds to $O1s$. In the high resolution XPS spectra of $C1s$ (Figure 6.7b), three peak features are observed, namely, at 284.7, 285.7 and 288.7 eV, respectively. The strong peak at 284.7 eV is attributed to C-C graphitic carbon. The peak at 285.7 and 288.7 eV are due to oxygenated carbon atoms. While the first one corresponds to C-OH linkages, the other one corresponds to C-O linkage. The XPS analysis clearly reveals the presence of graphene oxide confirming the formation of Li_3VO_4-GO composite.

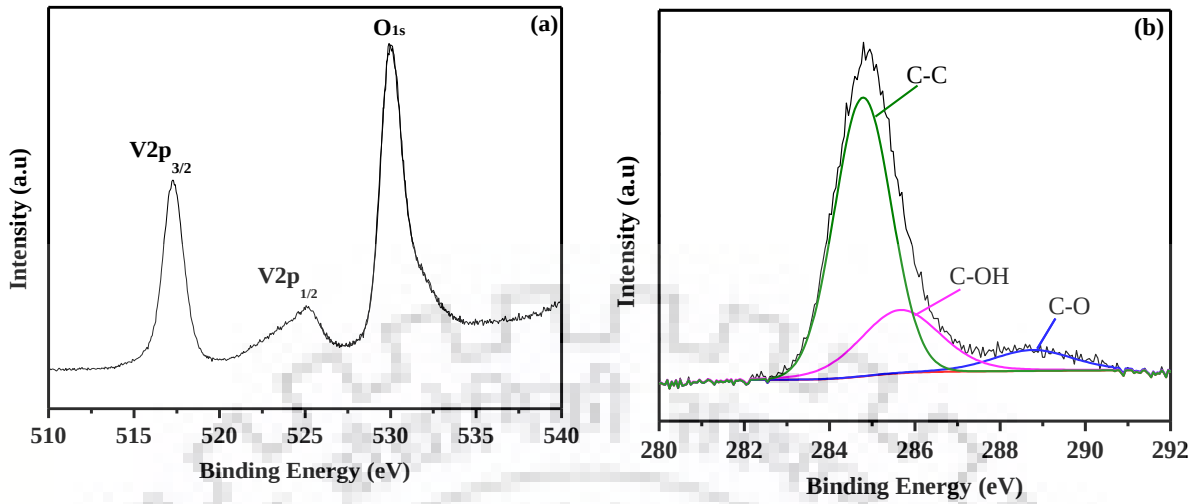

Figure 6.7 (a) $V2p_{3/2}$, $V2p_{1/2}$and O_{1s} spectra of Li_3VO_4-GO. (b) C_{1s} spectra of Li_3VO_4-GO. showing characteristic features of C-C, C-OH and C-O linkages.

6.3.7 Raman Analysis

Raman analysis is carried out to confirm the presence of graphitic carbon in the Li_3VO_4-GO composite. The Raman spectra of Li_3VO_4-GO is shown in Figure 6.8. The Raman bands at 817.7 and 784.9 cm^{-1} are assigned to the characterstic peaks of Li_3VO_4, whereas, those at 1356 and 1596 cm^{-1} are assigned to the characterstic D- (for defects and disordered carbon) and G-bands (graphitic carbon) [466] of graphene oxide. The nearly equal intensity of the G and D bands substantiates the formation of few layer thick GO as mostly obtained by standard and modified Hummer's method.

6.3.8 Surface Area Analysis

The porosity and surface area of the pristine Li_3VO_4-GO are measured by employing nitrogen adsorption-desorption isotherms. The BET surface area and total pore volume of the mesoporous Li_3VO_4-GO are 7.7 $m^2\ g^{-1}$ and 0.02 cc g^{-1}, respectively. The as synthesized Li_3VO_4-GO shows a slightly higher surface area than that of the bare Li_3VO_4.

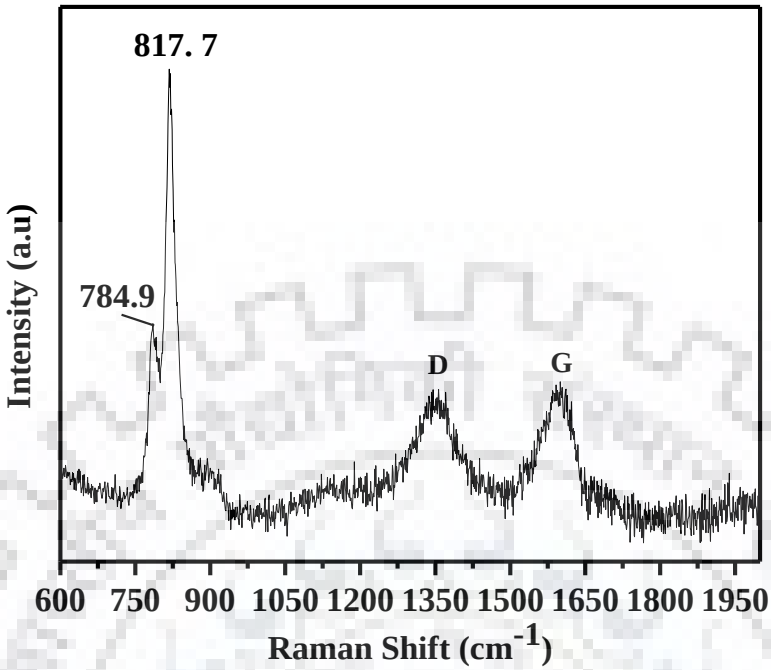

Figure 6.8 Raman spectrum of M-Li_3VO_4-GO.

The isotherm shown in Figure 6.9 (b) is a type IV isotherm which confirms the mesoporous nature of Li_3VO_4-GO. The pore distribution curve shown in Figure 6.9a indicates that the diameter of majority of the pores are centered at ~ 2.7 and 30 nm, while the pore size distribution covers a wide range with pore sizes in between the two limits representing the hierarchical nature of porosity in the material. The nut-shaped Li_3VO_4-GO are hollow and porous from inside as seen in the TEM analysis, but the surface areas are not great enough. It is likely that some of the pores are not accessible during the gas adsorption studies, which may be due to the blocked pores. Thus, to have a more clear picture of pore distribution, the BET surface area and pore size analysis is carried out once again with thoroughly ground powders. The BET surface area of the thoroughly ground Li_3VO_4-GO samples increased to 10.1 $m^2\ g^{-1}$, while the total pore volume decreased to 0.01 cc g^{-1} on grinding. The may be attributed to the breaking down of some of the pore walls, thus decreasing the number of blocked pores and enhancing the pore accessibility.

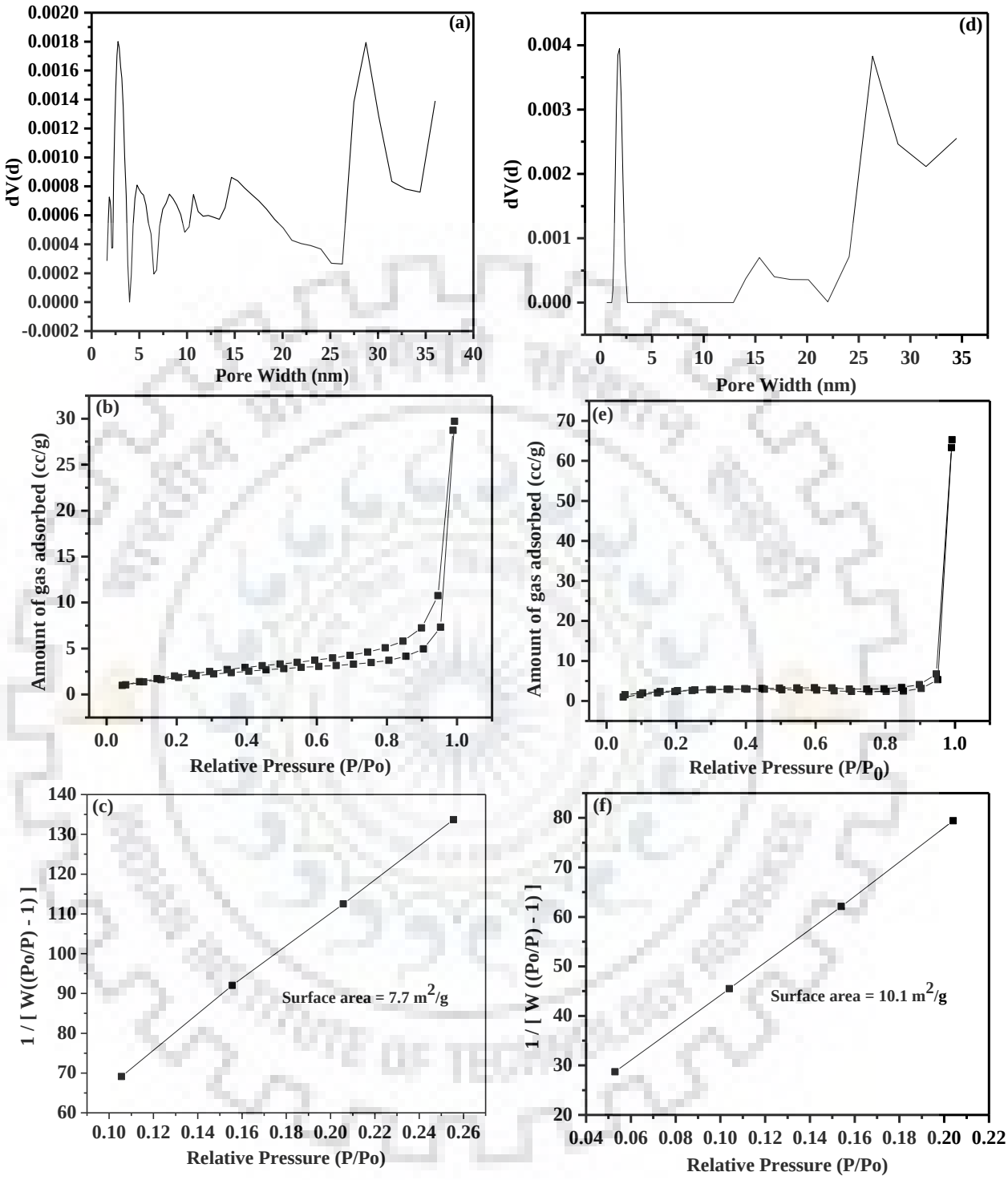

Figure 6.9 (a), (b), (c) are the pore size distribution, N_2 sorption isotherm and surface area curve for as obtained Li_3VO_4-GO (before grinding), and (d), (e), (f) are the pore size distribution, N_2 sorption isotherm and surface area curve for thoroughly ground Li_3VO_4-GO.

6.3.9 Electrochemical Measurements

Electrochemical measurements of Li_3VO_4-GO are performed on a laboratory made half-cell vs. Li/Li^+. The galvanostatic charge-discharge cycling behavior of the half-cells fabricated using the Li_3VO_4-GO as anode are analyzed between 0.2 – 2 V and 0.2 – 3 V at different charge-discharge rates (0.1 C – 1C). The charge-discharge curves at different C rates are shown in Figure 6.10 when cycled between 0.2 – 2 V. The lithium intercalation-deintercalation occurs mainly in between 1.0 and 0.5 V. Charge-discharge studies carried out at 0.1 C rate reveals enhanced electrochemical performance of the cell with a high discharge capacity of 674 mAh g^{-1} and a charge capacity of 398.3 mAh g^{-1} for the first discharge and charge cycle, respectively (Figure 6.10a).

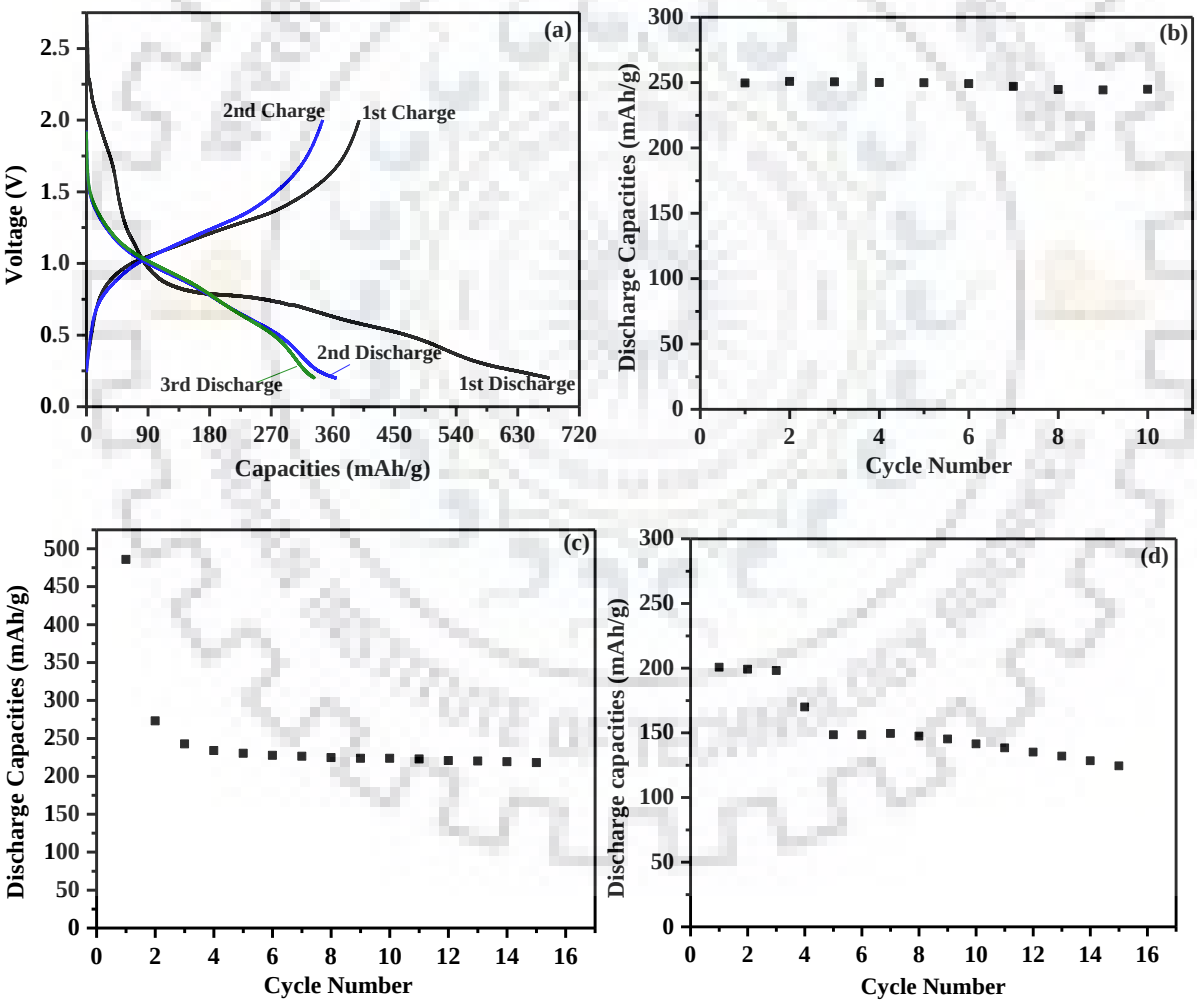

Figure 6.10 Charge-discharge cycles of Li_3VO_4–GO at (a) 0.1 C (b) 0.5 C (c) 0.75 C and (d) 1 C cycling rate when cycled between 0.2 – 2 V.

There is a substantial enhancement in the first discharge and charge capacities for Li_3VO_4-GO anodes as comparred to that of bare HM-Li_3VO_4 described in the previous chapter. Furthermore, a discharge capacity of 364 mAh g^{-1} for the second discharge cycle is also higher than that of the bare Li_3VO_4. However, first charge-discharge cycle displayed a large irreversibility which could be due to the formation of solid electrolyte interface (SEI) and other side reactions occuring on the electrode-electrolyte interfaces in addition to some phase transformations resulting in low coloumbic efficiency (~ 59 %) [347].

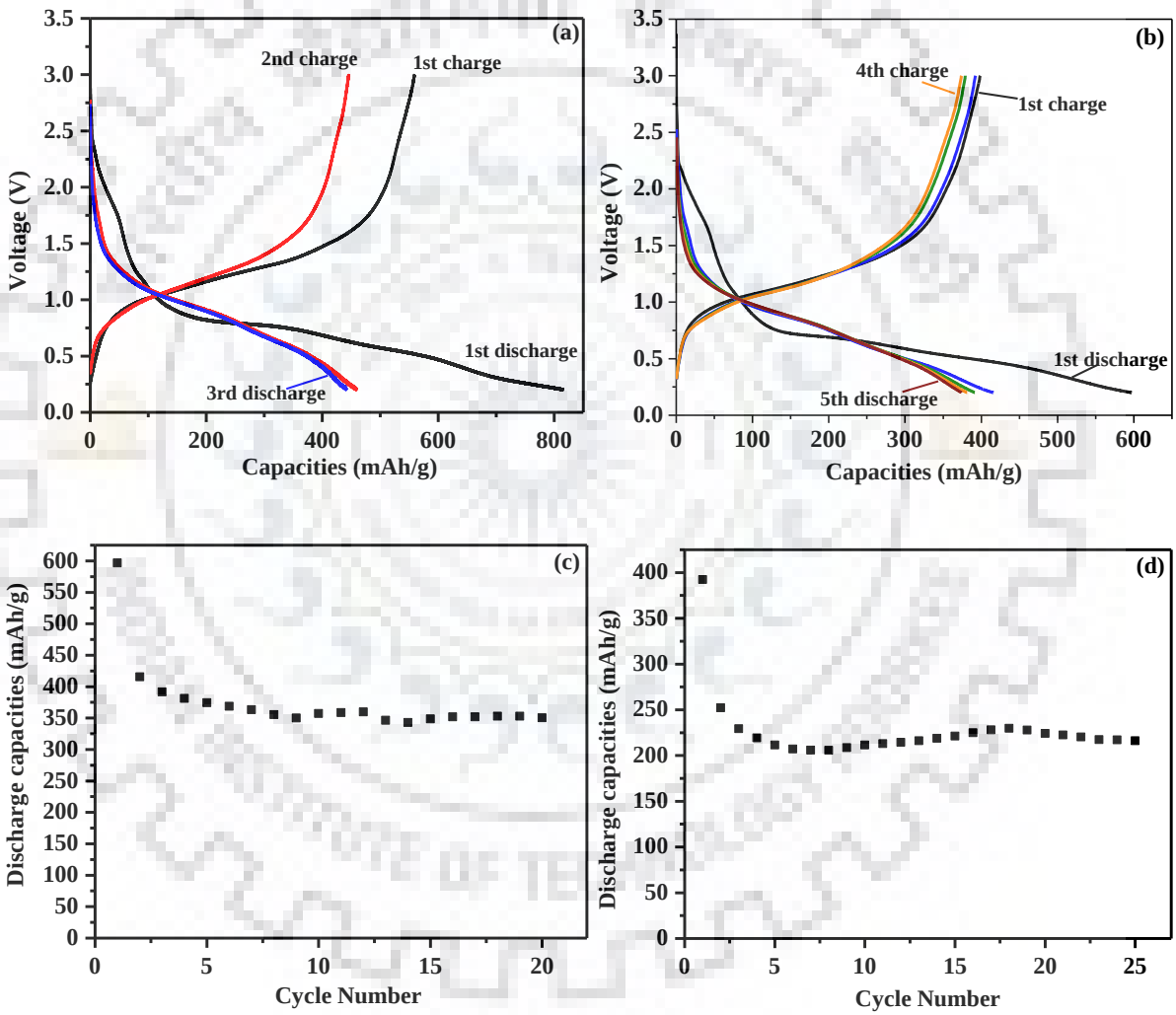

Figure 6.11 Charge-discharge cycles of Li_3VO_4-GO at (a) 0.1 C, (b) and (c) 0.5 C, (d) 1 C cycling rate when cycled between 0.2 – 3 V.

The enhancement in coloumbic efficiency from 59 % to 94 % in the second charge-discharge cycle confirmes that the initial capacity loss probably occurred only during the first charge-discharge. The electrochemical performance of Li_3VO_4-GO shows an enhancement when cycled between 0.2 – 3 V window (Figure 6.11). A discharge capacity of 458 mAh g^{-1} at 0.1 C rate is achieved after first cycle (Figure 6.11b), much higher than the cell cycled between 0.2 – 2 V. A discharge capacity of 374 mAh g^{-1} achieved after the 5th cycle at 0.5 C rate (Figure 6.11b) is superior or comparable to that of all the previous studies with cells cycled in the same voltage window [305, 310, 467, 311, 317, 453, 468]. Moreover, high discharge capacities of 351 and 221 mAh g^{-1} sustained at 0.5 and 1 C, respectively, confirms the high rate capabable nature of the Li_3VO_4-GO anode. Further, the first discharge-charge cycles of Li_3VO_4-GO are compared to that with bare HM-Li_3VO_4 synthesized under hydrothermal condition and Li_3VO_4 synthesized using solid state reaction (SS-Li_3VO_4) (Figure 6.12). The electrochemical data demonstrates excellent enhancements in the discharge-charge capacities for the first cycle. A comparison of the discharge capacities of Li_3VO_4-GO (black squares) with bare HM-Li_3VO_4 (red circles) at 1 C cycled between 0.2 – 2 V shows enhanced capacity retention and much improved rate capability for cells with Li_3VO_4-GO anodes.

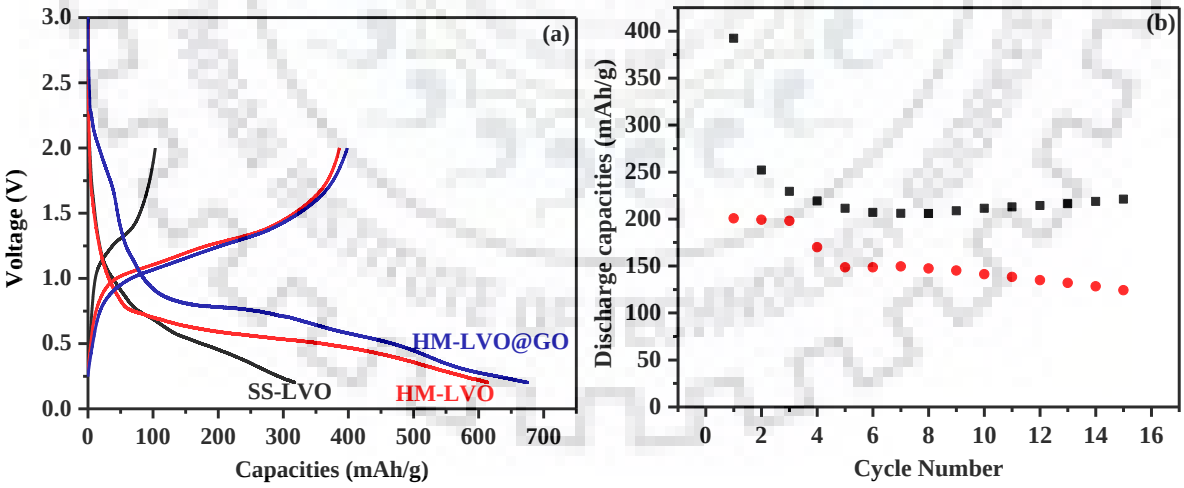

Figure 6.12 (a) First discharge-charge cycle of SS-Li_3VO_4 (SS-LVO), HM-Li_3VO_4 (HM-LVO) and Li_3VO_4-GO (HM-LVO@GO) at 0.1 C rate. (b) Discharge capacities of HM-LVO (red circles) and HM-LVO@GO (black squares) at 1C whan cycled between 0.2 – 2 V.

The enhancement in the galvanostatic charge-discharge capacity and cycling performance of Li_3VO_4-GO is due to the intimate contact between nanosized Li_3VO_4 particles with GO resulting in higher electronic conductivity and the hierarchical mesoporosity ensuing faster Li-ion diffusion.

6.3.10 CV Analysis

The cyclic voltammetric analysis of Li_3VO_4-GO are carried out in 0.2 to 3 V range at a scan rate of 0.1 mV s^{-1}. The cyclic voltammetric curves of the first four cycles for Li_3VO_4-GO are shown in Figure 6.13. In the first cycle, three reduction peaks are seen at a voltage of 0.44, 0.59 and 1.99 V, in the cathodic scan. The peaks at 0.44 and 0.59 V are due to the reduction of V^{5+} into V^{3+}. The peak at 1.99 V is attributed to the electrolyte decomposition and side reactions at the electrode surface and electrode-electrolyte interface that leads to SEI formation in addition to some phase transformations [447, 469]. In the second cycle, the peaks at 0.44 and 0.59 V are shifted to 0.51 and 0.81 V, respectively. However, in the 3rd and 4th cycle, the reduction peaks get nearly stabilized around 0.51 and 0.90 V indicating stabilization of the Li_3VO_4 electrode in consecutive cycles, consistent with the CV data reported in the literature [447, 469]. Moreover, the peak observed at 1.17 V in the first anodic more or less remain intact in consecutive cycles conforming to the smoth extraction of Li-ion from Li_3VO_4.

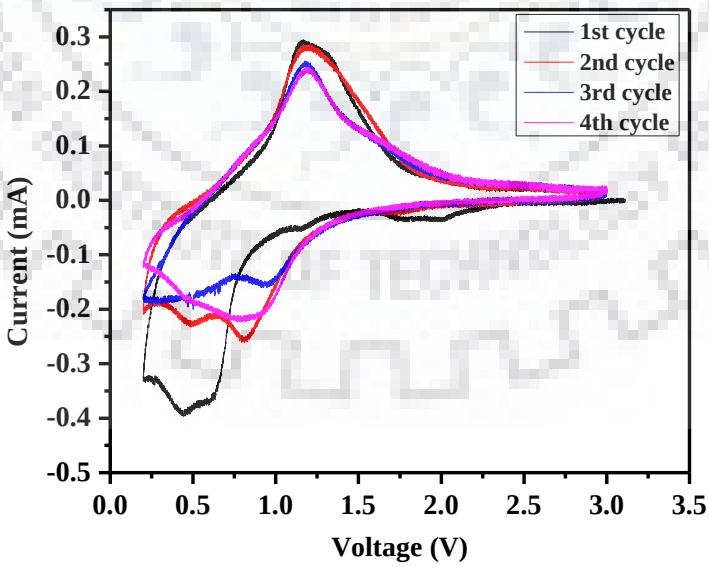

Figure 6.13 Cyclic Voltammetric curve of Li_3VO_4-GO at a scan rate of 0.1 mV sec^{-1}.

In summary, we have devised a simple, short and cheaper template free one-pot solvothermal method to synthesize nut-shaped Li_3VO_4-GO. The FE-SEM images showed formation of nut-shaped Li_3VO_4 grown on GO with particle sizes ranging from 2 μm to sub-micrometer level. The P-XRD analysis indicated formation of crystalline phase pure Li_3VO_4 with orthorhombic structure and gave refined lattice parameters of 6.314(3), 5.469(3) and 4.968(4) Å. BET surface area analysis confirmed presence of mesopores with a multimodal pore distribution. HR-TEM analysis confirmed the growth of Li_3VO_4 on GO. Raman spectroscopic investigation confirmed the presence of graphene oxide (GO) by the presence of D and G bands in addition to crystalline Li_3VO_4 by the presence of bands at 785 and 818 cm^{-1}. The EIS data clearly indicated enhanced electrical conductivity of Li_3VO_4-GO as compared to the bare HM-Li_3VO_4. The electrochemical charge-discharge studies employing a lithium metal half-cell with Li_3VO_4-GO as active anode material showed a discharge capacity of 814 mAh g^{-1} and a charge capacity of 559 mAh g^{-1} at 0.1 C rate when cycled in 0.2 – 3 V range for the first cycle. Moreover, a capacity of 414 mAh g^{-1} after the second discharge at 0.5 C was achieved within the same potential range. A discharge capacity of 374 mAh g^{-1} achieved at the fifth cycle at 0.5 C rate is comparable or superior to those reported in the literature for other Li_3VO_4 samples with similar carbon contents. Finally, the important position hold by Li_3VO_4 in the 'Ragone plot' shown below is noteworthy.

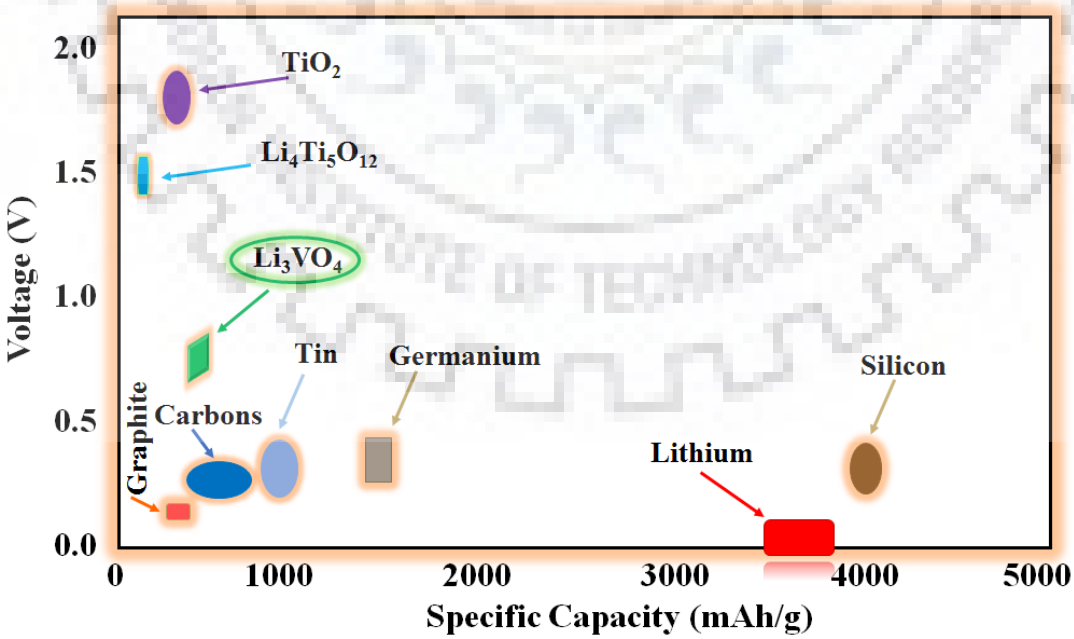

CHAPTER – 7

Conclusions and Future Prospects

Conclusions and Future Prospects

The present investigation is aimed at the energy storage materials mostly involving the Li-ion battery technology, which is perceived to be the most well established energy storage medium being commercialized and used extensively for powering portable electronic devices. It is being used not only in personal gadgets like mobile phones, laptops, audio players etc. but, in many other hand-held devices, medical implants (e. g., pumps and pacemakers), power tools and devices for aerospace applications. Extending its wide use in various other sectors like transportation and large-scale stationary energy storage systems, the specific capacity, energy density and rate capability of the batteries need to be improved further. This requires improvement in the performance of the existing materials as well as development of new class of high capacity and high rate capable anode and cathode materials. Moreover, looking at their large-scale use, one need not only consider earth abundant and cheap component materials, but need to minimize the environmental impacts and enhance device safety.

It is apparent that the rock-salt based layered transition metal oxides are the most extensively studied system for cathode materials in Li-ion batteries. For example, $LiCoO_2$, $LiNiO_2$, $LiNi_{0.5}Mn_{0.5}O_2$, $LiMnO_2$ and $LiNi_{1-x-y}Co_xMn_yO_2$ constitute the major class of cathode materials that are largely being investigated. In spite of vast studies and exploration, $LiCoO_2$ still remained the workhorse cathode for the LIB technology. Besides, $LiCoO_2$, $LiNi_{0.8}Co_{0.15}Al_{0.05}O_2$, $LiNi_{1/3}Mn_{1/3}Co_{1/3}O_2$, $LiMn_2O_4$ and $LiFePO_4$ are among the alternate cathode materials used in conventional Li-ion batteries. But, one or the other issues are of concern with most of them, such as, high cost, toxicity, low capacity, phase transition or structural transition. Moreover, capacity fading due to electrolyte instability and transition metal dissolution is common in some of them when the battery is cycled at higher potentials (e. g., for $LiCoO_2$ above 4.2 V). In the NCM based oxides, low thermal stability, Li/Ni mixing and high reactive surface limit their cathode performance for longer use.

To come up with cheaper and earth abundant materials, we envisaged an NCM based cathode with reduced transition metal contents. Furthermore, the composition is enriched with Li to have subsequent co-doping of the oxide with fluoride to enhance the chemical and structural stability in the charged state. We have established that a large amount of fluorine

can be incorporated into the oxide lattice keeping the structure intact. Moreover, Li-rich composition ensured an ordered rock-salt structure completely preventing the Li/Ni disorder in the Li-only layer. The new oxy-fluoride, $Li_{1.25}Ni_{0.25}Co_{0.25}Mn_{0.25}O_{1.5}F_{0.5}$, has shown good capacity as cathode in a Li-ion half-cell, despite having lesser transition metal contents. While the anodic and cathodic peaks at 3.95 and 3.72 V, respectively, in the CV trace confirmed the intercalation/de-intercalation of Li-ions into/out of the lattice, the charge-discharge curve showed the intercalation/de-intercalation potential at a slightly higher voltage (~ 3.91 V) than its oxide analogs. The observed higher working voltage is attributed to the incorporation of fluoride ions into the oxide lattice. A high charge capacity of 216 mAh g^{-1} and a discharge capacity of 148 mAh g^{-1} at 0.1 C for the first cycle are observed for $Li_{1.25}Ni_{0.25}Co_{0.25}Mn_{0.25}O_{1.5}F_{0.5}$. The present work is significant in the context that a large amount of fluoride can be doped in the Li-rich oxy-fluoride maintaining a completely ordered structure, avoiding any likely consequences of Li/Ni disorder in the Li-only layer thus ensuring better electrochemical performance of the NCM based oxy-fluorides. It is believed that improving the microstructural characteristics of NCM oxy-fluoride may help in materializing its full capacity (235 mAh g^{-1}) and prevent substantial capacity fading.

In search for new structure types as potential cathodes for Li-ion batteries involving intercalation-deintercalation of multiple Li-ions, we have identified a phosphate, namely, $Na_3Fe(PO_4)_2$, which has been reported with an interesting layered structure. A new synthetic approach is developed for the synthesis of phase pure $Na_3Fe(PO_4)_2$ by a sol-gel method within 24 h reaction time, which is much faster than that of the solid state method reported earlier (reaction time > 7 days). The cyclic voltammetry trace with an anodic peak around 3 V and electrochemical charge-discharge studies carried out at different C rates between 1.5 – 4.0 V confirmed the electrochemically active nature of $Na_3Fe(PO_4)_2$ and its potential as cathode material in Li-ion batteries, although the compound showed much reduced capacity than the theoretical (85 mAh g^{-1}). This is attributed to several factors including reduced ionic and electronic conductivities, structural constraints or poor microstructural properties. But, the excellent capacity retention at C/20 up to 100 charge-discharge cycles was noteworthy suggesting its structural robustness during electrochemical insertion/extraction of Li.

With respect to anodes of LIBs only limited class of materials, such as, graphite and various forms of carbon, TiO_2 based oxides, $Li_4Ti_5O_{12}$ and Li_3VO_4, which are mostly of

insertion/de-insertion types, are being investigated. While graphite is a low cost, high capacity and long life anode material, used in most of the commercialized Li-ion batteries, but slow Li-ion diffusion, structural collapse during cycling and dendritic Li-growth at low operating voltages limited its use in high power density applications. Low theoretical capacity, poor electrical conductivity and poor ionic diffusion are the main obstacles for TiO_2 based anodes in LIBs. Although, titanium based $Li_4Ti_5O_{12}$ has emerged as a feasible anode material for low power battery applications due to its high structural stability, minimum volume change upon insertion/de-insertion of Li-ions and flat voltage plateau, but low theoretical capacity (175 mAh g^{-1}) and low electronic conductivity prevents its use in high power and high capacity battery applications. Recently, Li_3VO_4 was considered as a promising anode material as a replacement to graphite in commercial LIBs due to its high theoretical capacity (394 mAh g^{-1}) and suitable working potential. But, low ionic and electronic conductivities of Li_3VO_4 were the main drawbacks that essentially resulted in poor electrochemical performance. In the backdrop of contemporary issues with the present day cathode and anode materials of LIBs, it is realized that in addition to poor theoretical capacity of the anodes, slow Li-ion diffusion and electronic conductivity are general problems with most of the anode materials. In this dissertation, efforts are being devoted to alleviate the problems of slow Li-ion diffusion and poor electrical conductivity of Li_3VO_4 anode.

A rapid template free hydrothermal method is developed to synthesize nut-shaped hierarchical mesoporous Li_3VO_4 (HM-Li_3VO_4) without any post-synthetic calcinations. The micro-sized nut-shaped Li_3VO_4 particles are basically composed of nanoparticles of Li_3VO_4 with sizes ranging from 50-100 nm. Moreover, the nut-shaped particles are hollow from inside and highly porous. HR-TEM together with BET surface area analysis confirmed presence of mesoporosity and multimodal pore distribution in the nut-shaped HM-Li_3VO_4. The electrochemical charge-discharge studies employing a lithium metal half-cell with HM-Li_3VO_4 in its bare form as the active anode material showed a discharge capacity of 615 mAh g^{-1} and a charge capacity of 384 mAh g^{-1} at 0.1 C rates for the first cycle. The discharge capacity of 332 mAh g^{-1} observed at the 2nd cycle is superior to those reported in the literature for other Li_3VO_4 in its bare form. The demonstrated enhanced electrochemical performance of bare HM-Li_3VO_4 as anode material is claimed to be due to mesoporous microstructure and pore hierarchy. It is believed that the mesoporous microstructure facilitates faster Li^+ diffusion

through the mesoporous channels, thus substantially improves the Li-ion mobility and helps in accommodating the Li^+ ions within mesopores, which may also reduce the structural strain during intercalation-deintercalation process. However, capacity fade at higher rates are evident in the HM-Li_3VO_4 due to its poor electrical conductivity.

Finally, in our effort to improve both the ionic and electrical conductivity of Li_3VO_4, a simple, short and cheaper template free one-pot solvothermal method is developed to synthesize mesoporous Li_3VO_4 (M-Li_3VO_4) on graphene oxide (GO). Here again, growth of nut-shaped Li_3VO_4 on GO with nut sizes ranging from 2 μm to sub-micrometer levels with a multimodal mesopore distribution are confirmed. Formation of crystalline phase pure Li_3VO_4 with orthorhombic structure and refined lattice parameters of 6.314(3), 5.469(3) and 4.968(4) Å are confirmed by P-XRD. The presence of graphene oxide (GO) is confirmed by D and G band features in the Raman spectra, in addition to crystalline Li_3VO_4 due to the bands at 785 and 818 cm^{-1}. An enhanced electrical conductivity of M-Li_3VO_4-GO as compared to that of pure HM-Li_3VO_4 is clearly evidenced by the EIS data. The electrochemical charge-discharge studies employing a lithium metal half-cell with M-Li_3VO_4-GO showed a discharge capacity of 814 mAh g^{-1} and a charge capacity of 559 mAh g^{-1} at 0.1 C rate when cycled in the potential range 0.2 – 3 V for the first cycle. Moreover, a capacity of 414 mAh g^{-1} is shown after the second discharge at 0.5 C in the same potential range. Furthermore, it is demonstrated that the discharge capacity of 374 mAh g^{-1} achieved at the fifth cycle at 0.5 C rate is comparable or superior to those reported in the literature for other Li_3VO_4 samples with similar carbon contents. The enhanced anode performance with more than double reversible capacity at 0.5 C rate for M-Li_3VO_4-GO as compared to that of bare HM-Li_3VO_4 is due to superior ionic and electronic conductivity of the material.

The present work has focused on the issues related to the reduced electrochemical performance of electrode materials due to poor ionic and electronic conductivity. With Li_3VO_4 insertion type anode, it has been demonstrated that formation of hierarchical mesoporosity along with nanostructuring alleviated the problem of slow Li-ion diffusion. Moreover, the growth of mesoporous Li_3VO_4 on GO demonstrated superior capacity retention due to improved electrical conductivity. Thus, we believe the incorporation of hierarchical mesopores within the structure and growth on GO has a general applicability for the microstructure design of other transition metal oxides to improve the ionic and electronic

conductivity and enhance the electrochemical performance of the electrodes. This may well be adopted as a general strategy for the development of high energy density, high capacity and high rate capable electrode materials.

The idea of layered phosphates with multiple Na or Li and multi redox active metals can give rise to high capacity cathodes and new electrodes for Li/Na-ion batteries. Further work is necessary to fully understand the system, difficulty in extracting its full capacity, ion mobilities, structural changes if any and microstructural effects. But, given the excellent capacity retention at C/20 up to 100 charge-discharge cycles and its structural robustness during electrochemical insertion-extraction of Li, the layered phosphate, $Na_3Fe(PO_4)_2$, requires further investigation.

Along the line of NCM based Li-rich oxy-fluorides development of new Ni-rich compositions or incorporation of multiple redox active cations may further enhance the gravimetric energy density and power density of the cathode materials. Moreover, the large amount of fluoride incorporation in the Li-rich oxy-fluoride would widen the possibility of exploring many more compositions with other transition metals as well. To have more insights into the structure in terms of the actual amount of fluoride incorporation and accurate determination of atomic positions a neutron diffraction study would be necessary. The future work may help in deeper understanding of the Li- and F-rich compounds and the dependence of their compositional, structural and microstructural properties on the electrochemical performance with respect to capacity retention, rate capability and long cycle life.

References

REFERENCES

1. Smith, P. F.; Takeuchi, K. J.; Marschilok, A. C.; Takeuchi, E. S. Holy Grails in Chemistry: Investigating and Understanding Fast Electron/Cation Coupled Transport within Inorganic Ionic Matrices. *Acc. Chem. Res.* **2017**, *50*, 544−548.

2. Thackeray, M. M.; Wolverton, C.; Isaacs, E. D. Electrical Energy Storage for Transportation-Approaching the Limits of, and Going Beyond, Lithium-Ion Batteries. *Energy Enviorn. Sci.* **2012**, *5*, 7854-7863.

3. Poizot, P.; Dolhem, F. Clean Energy New Deal for a Sustainable World: From Non-CO_2 Generating Energy Sources to Greener Electrochemical Storage Devices. *Energy Enviorn. Sci.* **2011**, *4*, 2003-2019.

4. Yoshino, A. The Birth of the Lithium-Ion Battery. *Angew. Chem. Int. Ed.* **2012**, *51*, 5798-5800.

5. Tarascon, J. M.; Armand, M. Issues and Challenges Facing Rechargeable Lithium Batteries. *Nature* **2001**, *41*, 359-367.

6. Goodenough, J. B.; Kim, Y. Challenges for Rechargeable Li Batteries. *Chem. Mater.* **2010**, *22*, 587–603.

7. Winter, M.; Brodd, R. J. What Are Batteries, Fuel Cells, and Supercapacitors? *Chem. Rev.* **2004**, *104*, 4245-4269.

8. Islam, M. S.; Fisher, C. A. J. Lithium and Sodium Battery Cathode Materials: Computational Insights into Voltage, Diffusion and Nanostructural Properties. *Chem. Soc. Rev.* **2014**, *43*, 185-204.

9. Scrosati, B. Lithium Rocking Chair Batteries: An Old Concept? *J. Electrochem. Soc.* **1992**, *139*, 2776-2781.

10. Schiffer, H.; Guerra, A. Electricity and Vital Force: Discussing the Nature of Science through a Historical Narrative. *Sci & Educ.* **2015**, *24*, 409-434.

11. Russel, C. A. The Electrochemical Theory of Sir Humphry Davy Part I: The Voltaic Pile and Electrolysis. *Ann. of Sci.* **1961**, *15*, 1-13.

12. Kostjejev, V. A. Effect of Various Factors on the Output of Leclanche Cells. *Transactions of the American Electrochemical Society* **1930**, *58*, 305-325.

13. Kurzweil, P. Gaston Planté and His Invention of the Lead-Acid Battery- The Genesis of the First Practical Rechargeable Battery. *Journal of Power Sources* **2010**, *195*, 4424-4434.

14. Greatbatch, W. Lithium-Iodine Battery. *Google Patent* **1975**.

15. Whittingham, M. S.; Gamble, F. R. The Lithium Intercalates of The Transition Metal Dichalcogenides. *Mater. Res. Bull.* **1975**, *10*, 363-371.

16. Whittingham, M. S. Electrical Energy Storage and Intercalation Chemistry, *Science* **1976**, *192*, 1126-1127.

17. Whittingham, M. S. Chalcogenide Battery. *Google Patents* **1977**.

18. Yamaki, J.; Tobishima, S.; Hayashi, K.; Saito, K.; Nemoto, Y.; Arakawa, M. A Consideration of the Morphology of Electrochemically Deposited Lithium in an Organic Electrolyte. *Journal of Power Sources* **1998**, *74*, 219-227.

19. Mizushima, K.; Jones, P. C.; Wiseman, P. J.; Goodenough, J. B. Li_xCoO_2 ($0< x \leq L$): A New Cathode Material for Batteries of High Energy Density. *Mat. Res. Bull.* **1980**, *15*, 783-789.

20. Amatucci, G. G.; Tarascon, J. M.; Klein, L. C. CoO_2, the End Member of the $LiCoO_2$ Solid Solution. *J. Electrochem. Soc.* **1996**, *143*, 1114-1123.

21. Basu, S.; Zeller, C.; Flanders, P. J.; Fuerst, C. D.; Johnson, W. D.; Fischer, J. E. Synthesis and Properties of Lithium-Graphite Intercalation Compounds. *Materials Science and Engineering* **1979**, *38*, 275-283.

22. Besenhard, J. O. The Electrochemical Preparation and Properties of Ionic Alkali Metal-And NR_4, Graphite Intercalation Compounds in Organic Electrolytes. *Carbon* **1976**, *14*, 111-115.

23. Takada, Y.; Fujii, R.; Matsuo, K. On the Graphite Intercalation Compound Prepared Electrochemically in $LiClO_4$-Propylene Carbonate Electrolyte. *Tanso*, **1983**, *114*, 120-123.

24. Dunning, J. S.; Tiedemann, W. H.; Hsueh, L.; Bennio, D. N. A Secondary, Nonaqueous Solvent Battery. *J. Electrochem. Soc.***1971**, *118*, 1886-1890.

25. Fong, R.; Sacken, U. V.; Dahn, J. R. Studies of Lithium Intercalation into Carbons Using Nonaqueous Electrochemical Cells. *J. Electrochem. Soc.* **1990**, *137*, 2009-2013.

26. Verma, P.; Maire, P.; Novák, P. A Review of the Features and Analyses of the Solid Electrolyte Interphase in Li-Ion Batteries. *Electrochimica Acta*. **2010**, *55*, 6332-6341.

27. Aurbach, D. Review of Selected Electrode-Solution Interactions Which Determine the Performance of Li and Li Ion Batteries. *Journal of Power Sources* **2000**, *89*, 206-218.

28. Aurbach, D.; Markovsky, B.; Shechter, A.; Ein-Eli, Y. A Comparative Study of Synthetic Graphite and Li Electrodes in Electrolyte Solutions Based on Ethylene Carbonate-Dimethyl Carbonate Mixtures. *J. Electrochem. Soc*. **1996**, *143*, 3809-3820.

29. Besenhard, J. O.; Winter, M.; Yang, J.; Biberacher, W. Filming Mechanism of Lithium-Carbon Anodes in Organic and Inorganic Electrolytes. *Journal of Power Sources* **1995**, *54*, 228-231.

30. Aurbach, D.; Ein-Eli, Y.; Markovsky, B.; Zaban, A. The Study of Electrolyte Solutions Based on Ethylene and Diethyl Carbonates for Rechargeable Li Batteries. *J. Electrochem. Soc*. **1995**, *142*, 2882-2890.

31. Ein-Eli, Y.; Markovsky, B.; Aurbach, D.; Carmeli, Y.; Yamin, H.; Lusk, S. The Dependence of the Performance of Li-C Intercalation Anodes for Li-Ion Secondary Batteries on the Electrolyte Solution Composition. *Electrochim. Acta*

1994, *39*, 2559-2569.

32. Aurbach, D.; Ein-Eli, Y.; Orit Chusid, O. The Correlation between the Surface Chemistry and the Performance of Li-Carbon Intercalation Anodes for Rechargeable "Rocking-Chair" Type Batteries. *J. Electrochern. Soc.* **1994**, *141*, 603-611.

33. Nagaura, T.; Tozawa, K. *Prog. Battereis Solar Cells*, **1990**, *9*, 209.

34. Shukla, A. K.; Venugopalan, S.; Hariprakash, B. Nickel-Based Rechargeable Batteries. *Journal of Power Sources* **2001**, *100*, 125-148.

35. Li, W.; Song, B.; Manthiram, A. High-Voltage Positive Electrode Materials for Lithium-Ion Batteries. *Chem. Soc. Rev*. **2017**, *46*, 3006-3059.

36. Choi, N-S.; Chen, Z.; Freunberger, S. A.; Ji, X.; Sun, Y.; Amine, K.; Yushin, G.; Nazar, L. F.; Cho, J.; Bruce, P. G. Challenges Facing Lithium Batteries and Electrical Double-Layer Capacitors. *Angew. Chem. Int. Ed.* **2012**, *51*, 9994-10024.

37. Deng, D. Li- Ion Batteries: Basics, Progress, and Challenges. *Energy Science and Engineering* **2015**, *3*, 385-418.

38. Erickson, E. M.; Ghanty, C.; Aurbach, D. New Horizons for Conventional Lithium Ion Battery Technology. *J. Phys. Chem. Lett.* **2014**, *5*, 3313-3324.

39. Nitta, N.; Wu, F.; Lee, J. T.; Yushin, G. Li-Ion Battery Materials: Present and Future. *Materials Today* **2015**, *18*, 252-264.

40. Ohzuku, T.; Ueda, A. Solid State Redox Reactions of $LiCoO_2$ (*R*–3 *m*) for 4 Volt Secondary Lithium Cells. *J. Electrochem. Soc*. **1994**, *141*, 2972-2977.

41. Thackeray, M. M.; Johnson, P. J.; Picciotto, L. A. D. Electrochemical Extraction of Lithium from $LiMn_2O_4$. *Mat. Res. Bull*. **1984**, *19*, 179-187.

42. Padhi, A. K.; Nanjundaswamy, K. S.; Goodenough, J. B. Phospho-olivines as Positive-Electrode Materials for Rechargeable Lithium Batteries. *J. Electrochem. Soc*. **1997**, *144*, 1188-1194.

43. Sun, Y. K.; Chen, Z.; Noh, H. J.; Lee, D. J.; Jung, H. G.; Ren, Y.; Wang, S.;Yoon, C. S.; Myung, S. T.; Amine, K. Nanostructured High-Energy Cathode Materials For Advanced Lithium Batteries. *Nature Materials* **2012**, *11*, 942-947.

44. Orman, H. J.; Wiseman, P. J. Cobalt (III) Lithium Oxide, $CoLiO_2$: Structure Refinement by Powder Neutron Diffraction. *Acta Cryst*. **1984**, *40*, 12-14.

45. Ozawa, K. Lithium-Ion Rechargeable Batteries with $LiCoO_2$ and Carbon Electrodes: The $LiCoO_2$/C System. *Solid State Ionics* **1994**, *69*, 212-221.

46. Akimoto, J.; Gotoh, Y.; Oosawa, Y. Synthesis and Structure Refinement of $LiCoO_2$ Single Crystals. *Journal of Solid State Chemistry* **1998**, *141*, 298-302.

47. Antolini, E. LiCoO2: Formation, Structure, Lithium and Oxygen Nonstoichiometry, Electrochemical Behaviour and Transport Properties. *Solid State Ionics* **2004**, *170*, 159-171.

48. Gummow, R. J.; Thackeray, M. M.; David, W. I. F.; Hull, S. Structure and Electrochemistry of Lithium Cobalt Oxide Synthesised At 400 ºC. *Mat. Res. Bull*. **1992**, *27*, 327-337.

49. Gummow, R. J.; Thackeray, M. M. Lithium-Cobalt-Nickel-Oxide Cathode Materials Prepared At 400 °C for Rechargeable Lithium Batteries. *Solid State Ionics* **1992**, *53-56*, 681-687.

50. Rossen, E.; Reimers. J. N.; Dahn, J. R. Synthesis and Electrochemistry of Spinel LT-$LiCoO_2$. *Solid State Ionics* **1993**, *62*, 53-60.

51. Horn, Y. S.; Croguennec, L.; Delmas, C.; Nelson, E. C.; O' keefe, M. A. Atomic Resolution of Lithium Ions in $LiCoO_2$. *Nature Materials* **2003**, *2*, 464-467.

52. Striebel, K. A.; Deng, C. Z.; Wen, S. J.; Cairns, E. J. Electrochemical Behavior of $LiMn_2O_4$ and $LiCoO_2$ Thin Films Produced with Pulsed Laser Deposition. *J. Electrochem. Soc*. **1996**, *143*, 1821-1827.

53. Takada, K.; Aotani, N.; Iwamoto, K.; Kondo, S. Electrochemical Behavior Of Li, MO, (M = Co, Ni) In All Solid State Cells Using A Glass Electrolyte. *Solid State Ionics* **1995**, *79*, 284-287.

54. Rabou, L. P. L. M.; Roskam, A. Cycleilife Improvement of Li/$LiCoO_2$ Batteries. *Journal of Power Sources* **1995**, *54*, 316-318.

55. Yazami, R.; Lebrun, N.; Bonneau, M.; Molteni, M. High Performance $LiCoO_2$ Positive Electrode Material. *Journal of Power Sources* **1995**, *54*, 389-392.

56. Nohma, T.; Kurokawa, H.; Uehara, M.; Takahashi, M.; Nishio, K.; Saito, T. Electrochemical Characteristics of $LiNiO_2$ and $LiCoO_2$ as A Positive Material for Lithium Secondary Batteries. *Journal of Power Sources* **1995**, *54*, 522-524.

57. Kim, H. S.; Cho, B. W.; Kim, J. T.; Yun, K. S.; Chun, H. S. Electrochemical Properties And Performance Of Poly (Acrylonitrile)-Based Polymer Electrolyte for Li/LiCoO2 Cells. *Journal of Power Sources* **1996**, *62*, 21-26.

58. Fragnaud, P.; Brousse, T.; Schleich, D. M. Characterization of Sprayed and Sputter Deposited $LiCoO_2$, Thin Films for Rechargeable Microbatteries. *Journal of Power Sources* **1996**, *63*, 187-191.

59. Cho, J.; Kim, Y. J.; Park, B. Novel $LiCoO_2$ Cathode Material with Al_2O_3 Coating for a Li Ion Cell. *Chem. Mater*. **2000**, *12*, 3788-3791.

60. Dahéron, L.; Dedryvère, R.; Martinez, H.; Flahaut, D.; Ménétrier, M.; Delmas, C.; Gonbeau, D. Possible Explanation for the Efficiency of Al-Based Coatings on $LiCoO_2$ Surface Properties of $LiCo_{1-x}Al_xO_2$ Solid Solution. *Chem. Mater*. **2009**, *21*, 5607-5616.

61. Jung, Y. S.; Cavanagh, A. S.; Dillon, A. C.; Groner, M. D.; George, S. M.; Lee, S. H. Enhanced Stability of $LiCoO_2$ Cathodes in Lithium-Ion Batteries Using Surface Modification by Atomic Layer Deposition. *J. Electrochem. Soc*. **2010**, *157*, 75-81.

62. Tabuchi, M.; Ado, K.; Kobayashi, H.; Sakaebe, H.; Kageyama, H.; Masquelier, C.; Yonemura, M.; Hirano, A.; Kanno, R. Preparation of $LiCoO_2$ and $LiCo_{1-x}Fe_xO_2$ Using Hydrothermal Reactions. *J. Mater. Chem*. **1999**, *9*, 199-204.

63. Kobayashi, H.; Shigemura, H.; Tabuchi, M.; Sakaebe, H.; Ado, K.; Kageyama, H.; Hirano, A.; Kanno, R.; Wakita, M.; Morimoto, S.; Nasu, S. Electrochemical Properties of Hydrothermally Obtained $LiCo_{1-x}Fe_xO_2$ as a Positive Electrode Material for Rechargeable Lithium Batteries. *J. Electrochem. Soc*. **2000**, *147*, 960-969.

64. Zou, M.; Yoshio, M.; Gopukumar, S.; Yamaki, J. I. Performance of $LiM_{0.05}Co_{0.95}O_2$ Cathode Materials in Lithium Rechargeable Cells When Cycled up to 4.5 V. *Chem. Mater*. **2005**, *17*, 1284-1286.

65. Liu, A.; Li, J.; Shunmugasundaram, R.; Dahn, J. R. Synthesis of Mg and Mn Doped $LiCoO_2$ and Effects on High Voltage Cycling. *J. Electrochem. Soc*. **2017**, *164 (7)*, A1655-A1664.

66. Ohzuku, T.; Ueda, A.; Nagayama, M. Electrochemistry and Structural Chemistry of $LiNiO_2$ ($R\bar{3}m$) for 4 Volt Secondary Lithium Cells. *J. Electrochem. Soc*. **1993**, *140*, 1862-1870.

67. Delmas, C.; Pérès, J. P.; Rougier, A.; Demourgues, A.; Weill, F.; Chadwick, A.; Broussely, M.; Perton, F.; Biensan, P.; Willmann, P. On the Behavior of the Li_xNiO_2 System: An Electrochemical and Structural Overview. *Journal of Power Sources* **1997**, *68*, 120-125.

68. Sacken, U. V.; Michal, C. A. Structure and Electrochemistry of $Li_{l\pm y}NiO_2$ and A New Li_2NiO_2 Phase with the Ni $(OH)_2$ Structure. *Solid State Ionics* **1990**, *44*, 87-97.

69. Ohzuku, T.; Ueda, A.; Nagayama, M.; Iwakoshi, Y.; Komori, H. Comparative Study of $LiCoO_2$, $LiNi_{1/2}Co_{l/2}O_2$ And $LiNiO_2$ For 4 Volt Secondary Lithium Cells. *Electrochemica Acta* **1993**, *38*, 1159-1167.

70. Yamada, S.; Fujiwara, M.; Kanda, M. Synthesis and Properties of LiNiO2 as Cathode Material for Secondary Batteries. *Journal of Power Sources* **1995**, *54*, 209-213.

71. Zhecheva, E.; Stoyanova, R. Stabilization of the Layered Crystal Structure of $LiNiO_2$ by Co-Substitution. *Solid State Ionics* **1993**, *66*, 143-149.

72. Delmas, C.; Saadoune, I. Electrochemical and Physical Properties of the $Li_xNi_{1-y}Co_yO_2$ Phases. *Solid State Ionics* **1992**, *53-56*, 370-375.

73. Rougier, A.; Saadoune, I.; Gravereau, P.; Willmann, P.; Delmas, C. Effect of Cobalt Substitution on Cationic Distribution in $LiNi_{1-y}Co_yO_2$ Electrode Materials. *Solid State Ionics* **1996**, *90*, 83-90.

74. Rossen, E.; Jones, C. D. W.; Dahn, J. R. Structure and Electrochemistry of $Li_xMn_yNi_{l-y}O_2$. *Solid State Ionics* **1996**, *57*, 311-318.

75. Ohzuku, T.; Makimura, Y. Layered Lithium Insertion Material of $LiNi_{1/2}Mn_{1/2}O_2$ A Possible Alternative to $LiCoO_2$ for Advanced Lithium-Ion Batteries. *Chemistry Letters* **2001**, *8*, 744-745.

76. Makimura, Y.; Ohzuku, T. Lithium Insertion Material of $LiNi_{1/2}Mn_{1/2}O_2$ for Advanced Lithium-Ion Batteries. *Journal of Power Sources*. **2003**, *119-121*, 156-160.

77. Reed, J.; Ceder, G. Charge, Potential, and Phase Stability of Layered $Li(Ni_{0.5}Mn_{0.5})O_2$. *Electrochem. Solid State Lett.* **2002**, *5(7)*, A145-A148.

78. Kang, K.; Meng, Y. S.; Bréger, J.; Grey, C. P.; Ceder, G. Electrodes with High Power and High Capacity for Rechargeable Lithium Batteries. *Science* **2006**, *311*, 977-980.

79. Hwang, B. J.; Yu, T. H.; Chenga, M. Y.; Santhanam, R. Rapid Microwave-Enhanced Ion Exchange Process For The Synthesis of $LiNi_{0.5}Mn_{0.5}O_2$ And Its Characterization As The Cathode Material For Lithium Batteries. *J. Mater. Chem*. **2009**, *19*, 4536-4544.

80. Leroux, F.; Guyomard, D.; Piffard, Y. The 2D Rancieite-Type Manganic Acid and Its Alkali-Exchanged Derivatives: Part I - Chemical Characterization and Thermal Behavior. *Solid State Ionics* **1995**, *80*, 299-306.

81. Paulsen, J. M.; Thomas, C. L.; Dahn, J. R. Layered Li-Mn-Oxide with the O2 Structure: A Cathode Material for Li-Ion Cell Which Does Not Convert to Spinel. *J. Electrochem. Soc*. **1999**, *146*, 3560-3565.

82. Capitaine, F.; Gravereau, P.; Delmas, C. A New Variety of $LiMnO_2$ with a Layered Structure. *Solid State Ionics* **1996**, *89*, 197-202.

83. Bruce, P. G.; Armstrong, A. R.; Gitzendanner, R. L. New Intercalation Compounds for Lithium Batteries: Layered $LiMnO_2$. *J. Mater. Chem*. **1999**, *9*, 193-198.

84. Pistoia, G.; Antonini, A.; Zane, D. Synthesis of $LiMnO_2$ and Its Characterization as A Cathode for Rechargeable Li Cells. *Solid State Ionics* **1995**, *78*, 115-122.

85. Reimers, J. N.; Fuller, E. W.; Rossen, E.; Dahn, J. R. Synthesis and Electrochemical Studies of $LiMnO_2$ Prepared at Low Temperatures. *J. Electrochem. Soc*. **1993**, *140*, 3396-3401.

86. Gummow, R. J.; Liles, D. C.; Thackeray, M. M. Lithium Extraction from Orthorhombic Lithium Manganese Oxide and the Phase Transformation to Spinel. *Mat. Res. Bull*. **1993**, *28*, 1249-1256.

87. Davidson, I. J.; McMillan, R. S.; Murray, J. J.; Greedan, J. E. Lithium-Ion Cell Based On Orthorhombic $LiMnO_2$. *Journal of Power Sources* **1995**, *54*, 232-235.

88. Rossouw, M. H.; Liles, D. C.; Thackeray, M. M. Synthesis and Structural Characterization of A Novel Layered Lithium Manganeses Oxide, $Li_{0.36}Mn_{0.91}O_2$, and Its Lithiated Derivative, $Li_{1.09}Mn_{0.91}O_2$. *J. Solid State Chem*. **1993**, *104*, 464-466.

89. Komaba, S.; Myung, S. T.; Kumagai, N.; Kanouchi, T.; Oikawa, K.; Kamiyama, T. Hydrothermal Synthesis of High Crystalline Orthorhombic $LiMnO_2$ as A Cathode Material for Li-Ion Batteries. *Solid State Ionics* **2002**, 152-153, 311-318.

90. Armstrong, A. R.; Bruce, P. G. Synthesis of Layered $LiMnO_2$ as an Electrode for Rechargeable Lithium Batteries. *Nature* **1996**, *381*, 499-500.

91. Chen, R.; Whittingham, M. S. Cathodic Behavior of Alkali Manganese Oxides from Permanganate. *J. Electrochem. Soc*. **1997**, *144*, L64-L67.

92. Vitins, G. West, K. Lithium Intercalation into Layered $LiMnO_2$. *J. Electrochem. Soc*. **1997**, *144*, 2587-2592.

93. Molenda, J.; Ziemnicki, M.; Marzec, J.; Zając, W.; Molenda, M.; Bućko, M. Electrochemical and High Temperature Physicochemical Properties of Orthorhombic $LiMnO_2$. *Journal of Power Sources* **2007**, *173*, 707-711.

94. Horn, Y. S.; Hackney, S. A.; Armstrong, A. R.; Bruce, P. G.; Gitzendanner, R.; Johnson, C. S.; Thackeray, M. M. Structural Characterization of Layered $LiMnO_2$ Electrodes by Electron Diffraction and Lattice Imaging. *J. Electrochem. Soc*. **1999**, *146 (7)*, 2404-2412.

95. Armstrong, A. R.; Robertson, A. D.; Gitzendanner, R.; Bruce, P. G. The Layered Intercalation Compounds $Li(Mn_{1-y}Co_y)O_2$: Positive Electrode Materials for Lithium-Ion Batteries. *J. Solid State Chem*. **1999**, *145*, 549-556.

96. Armstrong, A. R.; Robertson, A. D.; Bruce, P. G. Structural Transformation On Cycling Layered $Li(Mn_{1-y}Co_y)O_2$ Cathode Materials. *Electrochim. Acta* **1999**, *45*, 285-294.

97. Liu, W.; Oh, P.; Liu, X.; Lee, M. J.; Cho, W.; Chae, S.; Kim, Y.; Cho, J. Nickel-Rich Layered Lithium Transition-Metal Oxide for High-Energy Lithium-Ion Batteries. *Angew. Chem. Int. Ed*. **2015**, *54*, 4440-4457.

98. Liu, Z.; Yu, A.; Lee, J. Y. Synthesis and Characterization of $LiNi_{1-x-y}Co_xMn_yO_2$ as The Cathode Materials of Secondary Lithium Batteries. *Journal of Power Sources* **1999**, *81-82*, 416-419.

99. Ohzuku, T.; Makimura, Y. Layered Lithium Insertion Material of $LiCo_{1/3}Ni_{1/3}Mn_{1/3}O_2$ for Lithium-Ion Batteries. *Chemistry Letters* **2001**, *30*, 642-643.

100**.** Yabuuchi, N.; Ohzuku, T. Novel Lithium Insertion Material of $LiCo_{1/3}Ni_{1/3}Mn_{1/3}O_2$ for Advanced Lithium-Ion Batteries. *Journal of Power Sources* **2003**, *119-121*, 171-174.

101. Yang, Z.; Lu, J.; Bian, D.; Zhang, W.; Yang, X.; Xia, J.; Chen, G.; Gu, H.; Ma, G. Stepwise Co-Precipitation to Synthesize $LiNi_{1/3}Co_{1/3}Mn_{1/3}O_2$ One-Dimensional Hierarchical Structure for Lithium Ion Batteries. *Journal Power Sources* **2014**, *272*, 144-151.

102. Meng, H.; Huang, B.; Yin, J.; Yao, X.; Xu, X. Synthesis and Electrochemical Properties of $LiNi_{1/3}Co_{1/3}Mn_{1/3}O_2$ Cathodes in Lithium-Ion and All-Solid-State Lithium Batteries. *Ionics* **2015**, *21*, 43–49.

103. Ryu, W. H.; Lim, S. J.; Kim, W. K.; Kwon, H. 3-D Dumbbell-Like $LiNi_{1/3}Mn_{1/3}Co_{1/3}O_2$ Cathode Materials Assembled with Nano-Building Blocks for Lithium-Ion Batteries. *Journal of Power Sources* **2014**, *257*, 186-191.

104. Lin, B.; Wen, Z.; Gu, Z.; Huang, S. Morphology and Electrochemical Performance of $Li[Ni_{1/3}Co_{1/3}Mn_{1/3}]O_2$ Cathode Material by a Slurry Spray Drying Method. *Journal of Power Sources* **2008**, *175*, 564-569.

105. Zheng, W.; Shui, M.; Shu, J.; Gao, S.; Xu, D.; Chen, L.; Feng, L.; Ren, Y. GITT Studies on Oxide Cathode $LiNi_{1/3}Co_{1/3}Mn_{1/3}O_2$ Synthesized by Citric Acid Assisted High-Energy Ball Milling. *Bull. Mater. Sci*. **2013**, *36*, 495–498.

106. Miao, X.; Yan, Y.; Wang, C.; Cui, L.; Fang, J.; Yang, G. Optimal Microwave-Assisted Hydrothermal Synthesis of Nanosized $xLi_2MnO_3.(1-x)LiNi_{1/3}Co_{1/3}Mn_{1/3}O_2$ Cathode Materials for Lithium Ion Battery. *Journal of Power Sources* **2014**, *247*, 219-227.

107. Jan, S.S.; Nurgul, S.; Shi, X.; Xia, H.; Pang, H. Improvement of Electrochemical Performance of $LiNi_{0.8}Co_{0.1}Mn_{0.1}O_2$ Cathode Material by Graphene Nanosheets Modification. *Electrochim. Acta* **2014**, *149*, 86–93.

108. Cao, H.; Zhang, Y.; Zhang, J.; Xia, B. Synthesis and Electrochemical Characteristics of Layered $LiNi_{0.6}Co_{0.2}Mn_{0.2}O_2$ Cathode Material for Lithium Ion Batteries. *Solid State Ionics* **2005**, *176*, 1207– 1211.

109. Eom, J.; Kim, M. G.; Cho, J. Storage Characteristics of $LiNi_{0.8}Co_{0.1+x}Mn_{0.1-x}O_2$ (x = 0, 0.03, and 0.06) Cathode Materials for Lithium Batteries. *J. Electrochem. Soc*. **2008**, *155*, A 239-A 245.

110. Cho, J.; Kim, T.-J.; Kim, J.; Noh, M.; Park, B. *J. Electrochem. Soc*. **2004**, *151*, A1899-A1904.

111. Myung, S. T.; Lee, K. S.; Yoon, C. S.; Sun, Y. K.; Amine, K.; Yashiro, H. Effect of AlF_3 Coating on Thermal Behaviour of Chemically Delithiated $Li_{0.35}[Ni_{1/3}Co_{1/3}Mn_{1/3}]O_2$. *J. Phys. Chem. C* **2010**, *114*, 4710–4718.

112. Amine, K.; Liu, J.; Belharouak, I.; Kang, S. H.; Bloom, I.; Vissers, D.; Henriksen, G. Advanced Cathode Materials for High-Power Applications. *Journal of Power Sources* **2005**, *146*, 111–115.

113. Li, J.; Li, J.; Luo, J.; Wang, Li.; He, X. Recent Advances in the $LiFeO_2$-based Materials for Li-ion Batteries. *Int. J. Electrochem. Sci*. **2011**, *6*, 1550 – 1561.

114. Uzunova, S.; Uzunov, I.; Kovacheva, D.; Momchilov, A.; Puresheva, B. A Low External Temperature Method for Synthesis of Active Electrode Materials for Li Batteries – Part B: Synthesis of Lithium Iron Oxides $Li_xFe_yO_z$. *J. Appl. Electrochem.* **2006**, *36*, 1333–1339.

115. Lee, Y. S.; Yoon, C. S.; Sun, Y. K.; Kobayakawa, K.; Sato, Y. Synthesis of Nano-Crystalline $LiFeO_2$ Material with Advanced Battery Performance. *Electrochem. Commun.* **2002**, *4*, 727–731.

116. Morales, J.; Pena, J. S. Highly Electroactive Nanosized α-$LiFeO_2$. *Electrochem. Commun.* **2007**, *9*, 2116–2120.

117. Anderson, J. C.; Schieber, M. Order-Disorder Transitions in Heat-Treated Rock-Salt Lithium Ferrite. *J. Phys. Chem. Solids Pergamon Press* **1964**, *25*, 961-968.

118. Kanno, R.; Shirane, T.; Shirane, Y.; Takeda, Y.; Takana, M.; Ohashi, M.; Yamaguchi, Y. Synthesis, Structure, and Electrochemical Properties of a New Lithium Iron Oxide, $LiFeO_2$, with a Corrugated Layer Structure. *J. Electrochem. Soc.* **1996**, *143*, 2435-2442.

119. Ado, K.; Tabuchi, M.; Kobayashi, H.; Kageyama, H.; Nakamura, O.; Inaba, Y.; Kanno, R.; Takagi, M.; Takeda, Y. Preparation of $LiFeO_2$ with Alpha-$NaFeO_2$-Type Structure Using a Mixed-Alkaline Hydrothermal Method. *J. Electrochem. Soc.* **1997**, *144*, L177 - L180.

120. Sakurai, Y.; Arai, H.; Okada, S.; Yamaki, J. I. Low Temperature Synthesis and Electrochemical Characteristics of $LiFeO_2$ Cathodes. *Journal of Power Sources* **1997**, *68*, 711-715.

121. Tabuchi, M.; Tsutsui, S.; Masquelier, C.; Kanno, R.; Ado, K.; Matsubara, I.; Nasu, S.; Kageyama, H. Effect of Cation Arrangement on the Magnetic Properties of Lithium Ferrites ($LiFeO_2$) Prepared by Hydrothermal Reaction and Post-annealing Method. *J. Solid State Chem.* **1998**, *140*, 159-167.

122. Tabuchi, M.; Ado, K.; Sakaebe, H.; Masquelier, C.; Kageyama, H.; Nakamura, O. Preparation of AFeO, (A = Li, Na) by Hydrothermal Method. *Solid State Ionics* **1995**, *79*, 220-226.

123. Shirane, T.; Kanno, R.; Kawamoto, Y.; Takeda, Y.; Takano, M.; Kamiyama, T.; Izumi, F. Structure and Physical Properties of Lithium Iron Oxide, $LiFeO_2$, Synthesized by Ionic Exchange Reaction. *Solid State Ionics* **1995**, *79*, 227-233.

124. Tabuchi, M.; Masquelier, C.; Takeuchi, T.; Ado, K.; Matsubara, I.; Shirane, T.; Kanno, R.; Tsutsui, S.; Nasu, S.; Sakaebe, H.; Nakamura, O. Li+/Na+ Exchange from α-$NaFeO_2$, Using Hydrothermal Reaction. *Solid State Ionics* **1996**, *90*, 129-132.

125. Sakurai, Y.; Arai, H.; Yamaki, J. I. Preparation of Electrochemically Active α-$LiFeO_2$ at Low Temperature. *Solid State Ionics* **1998**, *113–115*, 29–34.

126. Kim, J.; Manthiram, A. Synthesis and Lithium Intercalation Properties of Nanocrystalline Lithium Iron Oxides. *J. Electrochem. Soc.* **1999**, *146*, 4371-4374.

127. Lee, Y. S.; Sato, S.; Sun, Y. K.; Kobayakawa, K.; Sato, Y. A New Type of Orthorhombic $LiFeO_2$ with Advanced Battery Performance and its Structural Change During Cycling. *Journal of Power Sources* **2003**, *119–121*, 285–289.

128. Rahman, M. M.; Wang, J. Z.; Hassan, M. F.; Chou, S.; Chen, Z.; Liu, H. K. Nanocrystalline Porous a-$LiFeO_2$–C Ccomposite- an Environmentally Friendly Cathode for the Lithium-Ion Battery. *Energy Environ. Sci.*, **2011**, *4*, 952–957.

129. Lee, Y.S.; Sato, S.; Tabuchi, M.; Yoon, C. S.; Sun, Y. K.; Kobayakawa, K.; Sato, Y. Structural Change and Capacity Loss Mechanism in Orthorhombic Li/$LiFeO_2$ System During Cycling. *Electrochem. Commun.* **2003**, *5*, 549–554.

130. Thackeray, M. M.; David, W. I. F.; Bruce, P. G.; Goodenough, J. B. Lithium Insertion into Manganese Spinels. *Mat. Res. Bull*. **1983**, *18*, 461-472

131. Hirayama, M.; Sonoyama, N.; Ito, M.; Minoura, M.; Mori, D.; Yamada, A.; Tamura, K.; Mizuki, J. I.; Kanno, R. Characterization of Electrode/Electrolyte Interface with X-Ray Reflectometry and Epitaxial-Film $LiMn_2O_4$ Electrode. *J. Electrochem. Soc.* **2007**, *154*, A1065-A1072.

132. Thackeray, M. M.; De Kock, A. Synthesis and Structural Characterization of Defect Spinels in the Lithium-Manganese-Oxide System. *Mat. Res. Bull*. **1993**, *28*, 1041-1049.

133. Tarascon, J. M.; Wang, E.; Shokoohi, F. K.; McKinnon, W. R.; Colson, S. The Spinel Phase of $LiMn_2O_4$ as a Cathode in Secondary Lithium Cells. *J. Electrochem. Soc.* 1991, 138, 2859-2864.

134. Xia, Y.; Zhou, Y.; Yoshio, M. Capacily Fading on Cycling of 4 V Li/$LiMn_2O_4$ Cells. *J Electrochem. Soc*. **1997**, *144*, 2593-2600.

135. Aurbach, D.; Levi, M. D.; Gamulski, K.; Markovsky, B.; Salitra, G.; Levi, E.; Heider, U.; Heider, L.; Oesten, R. Capacity Fading of Li_x Mn_2O_4 Spinel Electrodes Studied by XRD and Electroanalytical Techniques. *Journal of Power Sources* **1999**, *81–82*, 472–479.

136. Myung, S. T.; Komaba, S.; Kumagai, N. Enhanced Structural Stability and Cyclability of Al-Doped $LiMn_2O_4$ Spinel Synthesized by the Emulsion Drying Method. *J. Electrochem. Soc*. **2001**, *148*, A482-A489.

137. Lee, Y. S.; Kumada, N.; Yoshio, M. Synthesis and Characterization of Lithium Aluminium- doped Spinel ($LiAl_xMn_{2-x}O_4$) for Lithium secondary Battery. *Journal of Power Sources* **2001**, *96*, 376-384.

138. Gnanaraj, J. S.; Pol, V. G.; Gedanken, A.; Aurbach, D. Improving the High-Temperature Performance of $LiMn_2O_4$ Spinel Electrodes by Coating the Active Mass with MgO via a Sonochemical Method. *Electrochem. Commun.* **2003**, *5*, 940–945.

139. Ha, H.W.; Yun, N. G.; Kim, K. Improvement of Electrochemical Stability of $LiMn_2O_4$ by CeO_2 Coating for Lithium-Ion Batteries. *Electrochim. Acta* **2007**, *52*, 3236–3241.

140. Sun, Y. K.; Hong, K. J.; Prakash, J. The Effect of ZnO Coating on Electrochemical Cycling Behavior of Spinel $LiMn_2O_4$ Cathode Materials at Elevated Temperature. *J. Electrochem. Soc.* **2003**, *150*, A970-A972.

141. Liu, H.; Tang, D. The Effect of Nanolayer AlF3 Coating on $LiMn_2O_4$ Cycle Life in High Temperature for Lithium Secondary Batteries. *Russ. J. Electrochem.* **2009**, *45*, 762–764.

142. Liu, D.; He, Z.; Liu, X. Increased Cycling Stability of $AlPO_4$-Coated $LiMn_2O_4$ for Lithium Ion Batteries. *Matt. Lett.* **2007**, *61*, 4703–4706.

143. Kim, H. S.; Kim, Y.; Kim, S.; Martin, S. W. Enhanced Electrochemical Properties of $LiNi_{1/3}Co_{1/3}Mn_{1/3}O_2$ Cathode Material by Coating with $LiAlO_2$ Nnanoparticles. *Journal of Power Sources* **2006**, *161*, 623–627.

144. Hernan, L.; Morales, J.; Sanchez, L.; Santos, J. Use of Li–M–Mn–O [M= Co, Cr, Ti] Spinels Prepared by a Sol-Gel Method as Cathodes in High-Voltage Lithium Batteries. *Solid State Ionics* **1999**, *118*, 179–185.

145. Zhong, Q.; Bonakclarpou, A.; Zhan, M.; Gao, Y.; Dahn, J. R. Synthesis and Electrochemistry of $LiNi_xMn_{2-x}O_4$. *J. Electrochem. Soc.* **1997**, *144*, 205-213.

146. Kim, J. H.; Myung, S. T.; Yoon, C. S.; Kang, S. G.; Sun, Y. K. Comparative Study of LiNi0.5Mn1.5O4-δ and LiNi0.5Mn1.5O4 Cathodes Having Two Crystallographic Structures: *Fd*–3*m* and $P4_332$. *Chem. Mater.* **2004**, *16*, 906-91.

147. Wang, L.; Li, H.; Huang, X.; Baudrin, E. A Comparative Study of *Fd*–3*m* and $P4_332$ "$LiNi_{0.5}Mn_{1.5}O_4$. *Solid State Ionics* **2011**, *193*, 32-38.

148. Kim, J. H.; Myung, S. T.; Yoon, C. S.; Oh, I. H.; Sun, Y. K. Effect of Ti Substitution for Mn on the Structure of $LiNi_{0.5}Mn_{1.5}À_xTi_xO_4$ and Their Electrochemical Properties as Lithium Insertion Material. *J. Electrochem. Soc.* **2004**, *151*, A1911-A1918.

149. Pieczonka, N. P. W.; Liu, Z.; Lu, P.; Olson, K. L.; Moote, J.; Powell, B. R.; Kim, J. H. Understanding Transition-Metal Dissolution Behavior in $LiNi_{0.5}Mn_{1.5}O_4$ High-Voltage Spinel for Lithium Ion Batteries. *J. Phys. Chem. C* **2013**, *117*, 15947−15957.

150. Liu, J.; Manthiram, A. Understanding the Improvement in the Electrochemical Properties of Surface Modified 5 V $LiMn_{1.42}Ni_{0.42}Co_{0.16}O_4$ Spinel Cathodes in Lithium-ion Cells. *Chem. Mater.* **2009**, *21*, 1695–1707.

151. Nanjundaswamya, K. S.; Padhi, A. K.; Goodenough, J. B.; Okada, S.; Ohtsuka, H.; Arai, H.; Yamaki, J. Synthesis, Redox Potential Evaluation and Electrochemical Characteristics of NASICON-related-3D Framework Compounds. *Solid State Ionics* **1996**, *92*, 1-10.

152. Manthiram, A.; Goodenough, J. B. Lithium Insertion into $Fe_2(SO_4)_3$ Frameworks. *Journal of Power Sources* **1989**, *26*, 403 – 408.

153. Padhi, A. K.; Nanjunclaswamy, K. S.; Masquelier, C.; Okada, S.; Goodenough, J. B. Effect of Structure on the Fe^{3+}/Fe^{2+} Redox Couple in Iron Phosphates. *J. Electrochem. Soc.* **1997**, *144*, 1609-1613.

154. Yang, S.; Zavalij, P. Y.; Whittingham M. S. Hydrothermal Synthesis of Phosphate Cathodes. *Electrochem. Commun.* **2001**, *3*, 505-508.

155. Hu, Y.; Doeff, M. M.; Kostecki, R.; Finones, R. Electrochemical Performance of Sol-Gel Synthesized $LiFePO_4$ in Lithium Batteries. *J. Electrochem. Soc.* **2004**, *151*, A1279-A1285.

156. Arnold, G.; Garche, J.; Hemmer, R.; Strobele, S.; Vogler, C.; Mehrens, M. W. Fine-Particle Lithium Iron Phosphate $LiFePO_4$ Synthesized by a New Low-Cost Aqueous Precipitation Technique. *Journal of Power Sources* **2003**, *119–121*, 247–251.

157. Takahashi, M.; Tobishima, S.; Takei, K.; Sakurai, Y. Characterization of $LiFePO_4$ as the Cathode Material for Rechargeable Lithium Batteries. *Journal of Power Sources* **2001**, *97–98*, 508-511.

158. Andersson, A. S.; Thomas, J. O.; Kalska, B.; Häggström, L. Thermal Stability of $LiFePO_4$-Based Cathodes. *Electrochem. Solid-State Lett.* **2000**, *3*, 66-68.

159. Amin, R.; Balaya, P.; Maier, J. Anisotropy of Electronic and Ionic Transport in LiFePO4 Single Crystals. *Electrochem. Solid State Lett.* **2007**, *10*, A13-A16.

160. Ravet, N.; Chouinard, Y.; Magnan, J. F.; Besner, S. Gauthier, M.; Armand, M. Electroactivity of Natural and Synthetic Triphylite *J. Power Sources* **2001**, *97–98*, 503-507.

161. Huang, H.; Yin, S. C.; Nazar, L. F.; Approaching Theoretical Capacity of $LiFePO_4$ at Room Temperature at High Rates. *Electrochem. Solid State Lett.* **2001**, *4*, A170-A172.

162. Chung, S. Y.; Bloking, J. T.; Chiang, Y. M. Electronically Conductive Phospho-Olivines as Lithium Storage Electrodes. *Nat. Mat.* **2002**, *1*, 123-128.

163. Dominko, R.; Bele, M.; Gaberscek, M.; Remskar, M.; Hanzel, D.; Pejovnik, S.; Jamnik, J. Impact of the Carbon Coating Thickness on the Electrochemical Performance of $LiFePO_4$/C Composites. *J. Electrochem. Soc.* **2005**, *152*, A607-A610.

164. Wang, K.; Cai, R.; Yuan, T.; Yu, X.; Ran, R.; Shao, Z. Process Investigation, Electrochemical Characterization and Optimization of $LiFePO_4$/C Composite from Mechanical Activation using Sucrose as Carbon Source. *Electrochim. Acta* **2009**, *54*, 2861-2868.

165. Zaghib, K.; Ravet, N.; Gauthier, M.; Gendron, F.; Mauger, A.; Goodenough, J. B.; Julien, C. M. Optimized Electrochemical Performance of $LiFePO_4$ at 60 ◦C with Purity Controlled by SQUID Magnetometry. *Journal of Power Sources* **2006**, *163*, 560-566.

166. Herle, P. S.; Ellis, B.; Coombs, N.; Nazar, L. F. Nano-Network Electronic Conduction in Iron and Nickel Olivine Phosphates. *Nat. Mat.* **2004**, *3*, 147-152.

167. Barker, J.; Saidi, M. Y.; Swoyer, J. L. Lithium Iron (II) Phospho-olivines Prepared by a Novel Carbothermal Reduction Method. *Electrochem. Solid State Lett.* **2003**, *6*, A53-A55.

168. Laffont, L.; Delacourt, C.; Gibot, P.; Wu, M. Y.; Kooyman, P.; Masquelier, C.; Tarascon, J. M. Study of the $LiFePO_4$/$FePO_4$ Two-Phase System by High-Resolution Electron Energy Loss Spectroscopy. *Chem. Mater.* **2006**, *18*, 5520-5529.

169. Zheng, J. C.; Li, X. H.; Wang, Z. X.; Guo, H. J.; Zhou, S. Y. $LiFePO_4$ with Enhanced Performance Synthesized by a Novel Synthetic Route. *Journal of Power Sources* **2008**, *184*, 574-577.

170. Dominko, R.; Bele, M.; Goupil, J. M.; Gaberscek, M.; Hanzel, D.; Arcon, I.; Jamnik, J. Wired Porous Cathode Materials: A Novel Concept for Synthesis of $LiFePO_4$. *Chem. Mater.* **2007**, *19*, 2960-2969.

171. Iltchev, N.; Chen, Y.; Okada, S.; Yamaki, J. I. LiFePO4 Storage at Room and Elevated Temperatures. *Journal of Power Sources* **2003**, *119-121*, 749-754.

172. Yang, M. R.; Teng, T. H.; Wu, S. H. $LiFePO_4$/Carbon Cathode Materials Prepared by Ultrasonic Spray Pyrolysis. *Journal of Power Sources* **2006**, *159*, 307-311.

173. Konarova, M.; Taniguchi, I. Preparation of $LiFePO_4$/C Composite Powders by Ultrasonic Spray Pyrolysis Followed by Heat Treatment and Their Electrochemical Properties. *Mater. Res. Bull.* **2008**, *43*, 3305-3317.

174. Gu, Y. J.; Zeng, C. S.; Wu, H. K.; Cui, H. Z.; Huang, X. W.; Liu, X. B.; Wang, C. L.; Yang, Z. N.; Liu, H. Enhanced Cycling Performance and High Energy Density of $LiFePO_4$ Based Lithium Ion Batteries. *Mat. Lett.* **2007**, *61*, 4700-4702.

175. Li, G.; Azuma, H.; Tohda, M.; $LiMnPO_4$ as the Cathode for Lithium Batteries. *Electrochem. Solid State Lett.* **2002**, *5*, A135-A137.

176. Martha, S. K.; Grinblat, J.; Haik, O.; Zinigrad, E.; Drezen, T.; Miners, J. H.; Exnar, I.; Kay, A.; Markovsky, B.; Aurbach D. $LiMn_{0.8}Fe_{0.2}PO_4$: An Advanced Cathode Material for Rechargeable Lithium Batteries. *Angew. Chem. Int. Ed.* **2009**, *48*, 8559 –8563.

177. Amine, K.; Yasuda, H.; Yamachi, M. Olivine $LiCoPO_4$ as 4.8 V Electrode Material for Lithium Batteries. *Electrochem. Solid State Lett.* **2000**, *3*, 178-179.

178. Wolfenstine, J.; Allen, J. Ni^{3+}/Ni^{2+} Redox Potential in $LiNiPO_4$. *J. Power Sources* **2005**, *142*, 389-390.

179. Xu, W.; Wang, J.; Ding, F.; Chen, X.; Nasybulin, E.; Zhang, Y.; Zhang, J. G. Lithium Metal Anodes for Rechargeable Batteries. *Energy Environ. Sci.* **2014**, *7*, 513-537.

180. Lin, D.; Liu, Y.; Cui, Y. Reviving the Lithium Metal Anode for High-Energy Batteries. *Nat. Nanotech.* **2017**, *12*, 194-206.

181. Eftekhari, A. Low Voltage Anode Materials for Lithium-Ion Batteries. *Energy Storage Materials* **2017**, *7*, 157–180.

182. Dahn,J. R.; Zheng,T.; Liu, Y.; Xue, J. S. Mechanisms for Lithium Insertion in Carbonaceous Materials. *Science* **1995**, *270*, 590-593.

183. Azuma, H.; Imoto, H.; Yamada, S. I.; Sekai, K. Advanced Carbon Anode Materials for Lithium Ion Cells. *Journal of Power Sources* **1999**, *81-82*, 1-7.

184. Buiel, E.; Dahn, J. R. Li-Insertion in Hard Carbon Anode Materials for Li-Ion Batteries. *Electrochim. Acta* **1999**, *45*, 121-130.

185. Ni, J.; Huang, Y.; Gao, L. A High-Performance Hard Carbon for Li-Ion Batteries and Supercapacitors. Application *Journal of Power Sources* **2013**, *223*, 306-311.

186. Hu, J.; Li, H.; Huang, X. Electrochemical Behavior and Microstructure Variation of Hard Carbon Nano-Spherules as Anode Material for Li-Ion Batteries. *Solid State Ionics* **2007**, *178*, 265–271.

187. Lee, J. H.; Lee, H. Y.; Oh, S. M.; Lee, S. J.; Lee, K. Y.; Lee, S. M. Effect of Carbon Coating on Electrochemical Performance of Hard Carbons as Anode Materials for Lithium-Ion Batteries. *Journal of Power Sources* **2007**, *166*, 250-254.

188. Sun, H.; He, X.; Ren, J.; Li, J.; Jiang, C.; Wan, C. Hard Carbon/Lithium Composite Anode Materials for Li-Ion Batteries. *Electrochim. Acta* **2007**, *52*, 4312–4316.

189. Guo, B.; Shu, J.; Tang, K.; Bai, Y.; Wang, Z.; Chen, L. Nano-Sn/Hard Carbon Composite Anode Material with High-Initial Coulombic Efficiency. *Journal of Power Sources* **2008**, *177*, 205-210.

190. Haruna, H.; Itoh, S.; Horiba, T.; Seki, E.; Kohno, K. Large-Format Lithium-Ion Batteries for Electric Power Storage. *Journal of Power Sources* **2011**, *196*, 7002-7005.

191. Fujimoto, H.; Tokumitsu, K.; Mabuchi, A.; Chinnasamy, N.; Kasuh, T. The Anode Performance of the Hard Carbon for the Lithium Ion Battery Derived from the Oxygen-Containing Aromatic Precursors. *Journal of Power Sources* **2010**, *195*, 7452-7456.

192. Liu, J. L.; Wang, J.; Xia, Y. Y. A New Rechargeable Lithium-Ion Battery with a $xLi_2MnO_3\cdot(1-x)LiMn_{0.4}Ni_{0.4}Co_{0.2}O_2$ Cathode and a Hard Carbon Anode. *Electrochim. Acta* **2011**, *56*, 7392-7396.

193. Wang, J.; Liu, J. L.; Wang, Y. G.; Wang, C. X.; Xia, Y. Y. Pitch Modified Hard Carbons as Negative Materials for Lithium-Ion Batteries. *Electrochim. Acta* **2012**, *74*, 1-7.

194. Li, B. H.; Wang, Z.; Chen, L.; Huang, X. Research on Advanced Materials for Li-ion Batteries. *Adv. Mater.* **2009**, *21*, 4593-4607.

195. Wang, Q.; Li, H.; Chen, L.; Huang, X. Monodispersed Hard Carbon Spherules with Uniform Nanopores. *Carbon* **2001**, *39*, 2211-2214.

196. Wang, Q.; Li, H.; Chen, L.; Huang, Novel Spherical Microporous Carbon as Anode Material for Li-Ion Batteries. *Solid State Ionics* **2002**, *152-153*, 43-50.

197. Sun, X.; Li, Y. Colloidal Carbon Spheres and Their Core/Shell Structures with Noble-Metal Nanoparticles. *Angew. Chem. Int. Ed.* **2004**, *43*, 597-601.

198. Cui, X.; Antonietti, M.; Yu, S. H.; Structural Effects of Iron Oxide Nanoparticles and Iron Ions on the Hydrothermal Carbonization of Starch and Rice Carbohydrates. *Small* **2006**, *2*, 756-759.

199. Li, W.; Chen, M.; Wang, C. Spherical hard carbon prepared from potato starch using as anode material for Li-ion batteries. *Mat. Lett.* **2011**, *65*, 3368-3370.

200. Thess, A.; Lee, R.; Nikolaev, P.; Dai, H.; Petit, P.; Robert, J.; Xu, C.; Lee, Y. H.; Kim, S. G.; Rinzler, A. G.; Colbert, D. T.; Scuseria, G. E.; Tomanek, D.; Fischer, J. E.; Smalley, R. E. Crystalline Ropes of Metallic Carbon Nanotubes. *Science* **1996**, *273*, 483-487.

201. Ando, Y.; Zhao, X.; Shimoyama, H.; Sakai, G.; Kaneto, K. Physical Properties of Multiwalled Carbon Nanotubes. *Int. J. Inorg. Mater.* **1999**, *1*, 77-82.

202. Lier, G. V.; Alsenoy, C. V.; Doren, V. V.; Geerlings, P. Ab Initio Study of the Elastic Properties of Single-Walled Carbonnanotubes and Graphene. *Chem. Phys. Lett.* **2000**, *326*, 181−185

203. Yu, M.-F.; Lourie, O.; Dyer, M. J.; Moloni, K.; Kelly, T. F.; Ruoff, R. S. Strength and Breaking Mechanism of Multiwalled Carbon Nanotubes Under Tensile Load. *Science* **2000**, *287*, 637−640.

204. Liu, Y.; Yukawa, H.; Morinaga, M. First-Principles Study on Lithium Absorption in Carbon Nanotubes. *Comput. Mater. Sci.* **2004**, *30*, 50–56.

205. Garau, C.; Frontera, A.; Quiñonero, D.; Costa, A.; Ballester, P.; Deyà, P. M. Lithium Diffusion in Single-Walled Carbon Nanotubes: A Theoretical Study. *Chem. Phys. Lett.* **2003**, *374*, 548−555.

206. Jaber-Ansari, L.; Iddir, H.; Curtiss, L. A.; Hersam, M. C. Influence of Electronic Type Purity on the Lithiation of Single-Walled Carbon Nanotubes. *ACS Nano* **2014**, *8*, 2399−2409.

207. Kawasaki, S.; Hara, T.; Iwai, Y.; Suzuki, Y. Metallic and Semiconducting Single-Walled Carbon Nanotubes as the Anode Material of Li Ion Secondary Battery. *Mater. Lett.* **2008**, *62*, 2917− 2920.

208. Pierard, N.; Fonseca, A.; Konya, Z.; Willems, I.; VanTendeloo, G.; Nagy, J. B. Production of Short Carbon Nanotubes with Open Tips by Ball Milling. *Chem. Phys. Lett.* **2001**, *335*, 1−8.

209. Wang, X. X.; Wang, J. N.; Chang, H.; Zhang, Y. F.; Preparation of Short Carbon Nanotubes and Application as an Electrode Material in Li-Ion Batteries. *Adv. Funct. Mater.* **2007**, *17*, 3613–3618.

210. Yang, S.; Huo, J.; Song, H.; Chen, X. A Comparative Study of Electrochemical Properties of Two Kinds of Carbon Nanotubes as Anode Materials for Lithium-Ion Batteries. *Electrochim. Acta* **2008**, *53*, 2238−2244.

211. Wang, X. X.; Wang, J. N.; Su, L. F. Preparation and Electrochemical Performance of Ultra-Short Carbon Nanotubes. *Journal of Power Sources* **2009**, *186*, 194-200.

212. Terrones, M.; Jorio, A.; Endo, M.; Rao, A. M.; Kim, Y. A.; Hayashi, T.; Terrones, H.; Charlier, J. C.; Dresselhaus, G.; Dresselhaus, M. S. New Direction in Nanotube Science. *Mater. Today* **2004**, *7*, 30−45.

213. Czerw, R.; Terrones, M.; Charlier, J.-C.; Blase, X.; Foley, B.; Kamalakaran, R.; Grobert, N.; Terrones, H.; Tekleab, D.; Ajayan, P. M. Identification of Electron Donor States in N-Doped Carbon Nanotubes. *Nano Lett.* **2001**, *1*, 457−460.

214. Xiao, K.; Liu, Y.; Hu, P.; Yu, G.; Sun, Y.; Zhu, D. *n*-Type FieldEffect Transistors Made of an Individual Nitrogen-Doped Multiwalled Carbon Nanotube. *J. Am. Chem. Soc.* **2005**, *127*, 8614−8617.

215. Wang, H.; Zhang, C.; Liu, Z.; Wang, L.; Han, P.; Xu, H.; Zhang, K.; Dong, S.; Yao, J.; Cui, G. Nitrogen-Doped Graphene Nanosheets with Excellent Lithium Storage Properties. *J. Mater. Chem.* **2011**, *21*, 5430−5434.

216. Lim, S. H.; Li, R.; Ji, W.; Lin, J. Effects Of Nitrogenation on Single-Walled Carbon Nanotubes within Density Functional Theory. *Phys. Rev. B* **2007**, *76*, 195406.

217. Bulusheva, L. G.; Okotrub, A. V.; Kurenya, A. G.; Zhang, H.; Zhang, H.; Chen, X.; Song, H. Electrochemical Properties of Nitrogen doped Carbon Nanotube Anode in Li-Ion Batteries. *Carbon* **2011**, *49*, 4013−4023.

218. Li, X.; Zhu, X.; Zhu, Y.; Yuan, Z.; Si, L.; Qian, Y. Porous Nitrogen-Doped Carbon Vegetable-Sponges with Enhanced Lithium Storage Performance. *Carbon* **2014**, *69*, 515−524.

219. Lee, C.; Wei, X. D.; Kysar, J. W.; Hone, J. Measurement of the Elastic Properties and Intrinsic Strength of Monolayer Graphene. *Science* **2008**, *321* (5887), 385−388.

220. Balandin, A. A.; Ghosh, S.; Bao, W.; Calizo, I.; Teweldebrhan, D.; Miao, F.; Lau, C. N. Superior Thermal Conductivity of SingleLayer Graphene. *Nano Lett.* **2008**, *8*, 902−907.

221. Stankovich, S.; Dikin, D. A.; Dommett, G. H. B.; Kohlhaas, K. M.; Zimney, E. J.; Stach, E. A.; Piner, R. D.; Nguyen, S-B. T.; Ruoff, R. S. Graphene-Based Composite Materials. *Nature* **2006**, *442*, 28-286.

222. Su, D. S.; Schlögl, R. Nanostructured Carbon and Carbon Nanocomposites for Electrochemical Energy Storage Applications. *Chem Sus Chem* **2010**, *3*, 136.

223. Pan, D.; Wang, S.; Zhao, B.; Wu, M.; Zhang, H.; Wang, Y.; Jiao, Z. Li Storage Properties of Disordered Graphene Nanosheets. *Chem. Mater.* **2009**, *21*, 3136−3142.

224. Hwang, H. J.; Koo, J.; Park, M.; Park, N.; Kwon, Y.; Lee, H. Multilayer Graphynes for Lithium Ion Battery Anode. *J. Phys. Chem. C* **2013**, *117*, 6919−6923.

225. Lian, P.; Zhu, X.; Liang, S.; Li, Z.; Yang, W.; Wang, H. Large Reversible Capacity of High Quality Graphene Sheets as an Anode Material for Lithium-Ion Batteries. *Electrochim. Acta* **2010**, *55*, 3909− 3914.

226. Yoo, E.; Kim, J.; Hosono, E.; Zhou, H.-s.; Kudo, T.; Honma, I. Large Reversible Li Storage of Graphene Nanosheet Families for Use in Rechargeable Lithium Ion Batteries. *Nano Lett.* **2008**, *8*, 2277− 2282.

227. Yin, S.; Zhang, Y.; Kong, J.; Zou, C.; Li, C. M.; Lu, X.; Ma, J.; Boey, F. Y. C.; Chen, X. Assembly of Graphene Sheets into Hierarchical Structures for High-Performance Energy Storage. *ACS Nano* **2011**, *5*, 3831−3838.

228. Reddy, A. L. M.; Srivastava, A.; Gowda, S. R.; Gullapalli, H.; Dubey, M.; Ajayan, P. M. Synthesis of Nitrogen-Doped Graphene Films for Lithium Battery Application. *ACS Nano* **2010**, *4*, 6337−6342.

229. Zhang, C.; Mahmood, N.; Yin, H.; Liu, F.; Hou, Y. Synthesis of Phosphorus-Doped Graphene and its Multifunctional Applications for Oxygen Reduction Reaction and Lithium Ion Batteries. *Adv. Mater*. **2013**, *25*, 4932−4937.

230. Ma, X.; Ning, G.; Sun, Y.; Pu, Y.; Gao, J. High Capacity Li Storage in Sulfur and Nitrogen Dual-Doped Graphene Networks. *Carbon* **2014**, *79*, 310−320.

231. Ma, X.; Ning, G.; Qi, C.; Xu, C.; Gao, J. Phosphorus and Nitrogen Dual-Doped Few-Layered Porous Graphene: A High-Performance Anode Material for Lithium-Ion Batteries. *ACS Appl. Mater. Interfaces* **2014**, *6*, 14415−14422.

232. Liu, Y.; Wang, X.; Dong, Y.; Wang, Z.; Zhao, Z.; Qiu, J. Nitrogen-Doped Graphene Nanoribbons for High-Performance Lithium Ion Batteries. *J. Mater. Chem. A* **2014**, *2*, 16832−16835.

233. Jiang, Z.-J.; Jiang, Z. Fabrication of Nitrogen-Doped Holey Graphene Hollow Microspheres and Their Use as an Active Electrode Material for Lithium Ion Batteries. *ACS Appl. Mater. Interfaces* **2014**, *6*, 19082−19091.

234. Liang, M.; Zhi, L. Graphene-Based Electrode Materials for Rechargeable Lithium Batteries. *J. Mater. Chem.* **2009**, *19*, 5871-5878.

235. Raccichini, R.; Varzi, A.; Passerini, S.; Scrosati, B. The Role of Grapheme for Electrochemical Energy Storage. *Nat. Mater.* **2015**, *14*, 271− 279.

236. Xu, J.; Jia, C.; Cao, B.; Zhang, W. F. Electrochemical Properties of Anatase TiO_2 Nanotubes as an Anode Material for Lithium-Ion Batteries. Electrochim. Acta **2007**, *52*, 8044–8047.

237. Zachau-Christiansen, B.; West, K.; Jacobsen, T.; Atlung, S. Lithium Insertion in Different TiO_2 Modifications. *Solid State Ionics* **1988**, *28-30*, 1176-1182.

238. Dambournet, D.; Belharouak, I.; Amine, K. Tailored Preparation Methods of TiO_2 Anatase, Rutile, Brookite: Mechanism of Formation and Electrochemical Properties. *Chem. Mater.* **2010**, *22*, 1173−1179.

239. Yang, Z.; Choi, D.; Kerisit, S.; Rosso, K. M.; Wang, D.; Zhang, J.; Graff, G.; Liu, J. Nanostructures and Lithium Electrochemical Reactivity of Lithium Titanites and Titanium Oxides: A Review. *Journal of Power Sources* **2009**, *192*, 588−598.

240. Ohzuku, T.; Kodama, T.; Hirai, T. Electrochemistry of Anatase Titanium Dioxide in Lithium Nonaqueous Cells. *Journal of Power Sources* **1985**, *14*, 153−166.

241. Kubiak, P.; Pfanzelt, M.; Geserick, J.; Hörmann, U.; Hüsing, N.; Kaiser, U.; Wohlfahrt-Mehrens, M. Electrochemical Evaluation of Rutile TiO_2 Nanoparticles as Negative Electrode for Li-ion Batteries *Journal of Power Sources* **2009**, *194*, 1099−1104.

242. Hu, Y.-S.; Kienle, L.; Guo, Y.-G.; Maier, J. High Lithium Electroactivity of Nanometer-Sized Rutile TiO_2. *Adv. Mater.* **2006**, *18*, 1421−1426.

243. Reddy, M. A.; Kishore, M. S.; Pralong, V.; Caignaert, V.; Varadaraju, U. V.; Raveau, B. Room Temperature Synthesis and Li Insertion into Nanocrystalline Rutile TiO_2. *Electrochem. Commun.* **2006**, *8*, 1299–1303.

244. Armstrong, A. R.; Armstrong, G.; Canales, J.; Garcia, R.; Bruce, P. G. Lithium-Ion Intercalation Into TiO_2-B Nanowires. *Adv. Mater.* **2005**, *17*, 862−865.

245. Beuvier, T.; Richard-Plouet, M.; Granvalet, M. M.-L.; Brousse, T.; Crosnier, O.; Brohan, L. TiO_2(B) Nanoribbons As Negative Electrode Material for Lithium Ion Batteries with High Rate Performance. *Inorg. Chem.* **2010**, *49*, 8457–8464.

246. Armstrong, A. R.; Armstrong, G.; Canales, J.; Bruce, P. G. TiO_2-B Nanowires. *Angew. Chem. Int. Ed.* **2004**, *43*, 2286 –2288.

247. Van de Krol, R.; Goossens, A.; Meulenkamp, E. A. In Situ X-Ray Diffraction of Lithium Intercalation in Nanostructured and Thin Film Anatase TiO_2. *J. Electrochem. Soc.* **1999**, *146*, 3150−3154.

248. Stashans, A.; Lunell, S.; Bergstrom, R.; Hagfeldt, A.; Lindquist, S. E. Theoretical Study of Lithium Intercalation in Rutile and Anatase. *Phys. Rev. B: Condens. Matter Mater. Phys.* **1996**, *53*, 159−170.

249. Lindstroem, H.; Soedergren, S.; Solbrand, A.; Rensmo, H.; Hjelm, J.; Hagfeldt, A.; Lindquist, S.-E. Li^+ Ion Insertion in TiO_2 (Anatase). 1. Chronoamperometry on CVD Films and Nanoporous Films. *J. Phys. Chem. B* **1997**, *101*, 7710-7716.

250. Wagemaker, M.; Kentgens, a P. M.; Mulder, F. M. Equilibrium Lithium Transport between Nanocrystalline Phases in Intercalated TiO_2 Anatase. *Nature* **2002**, *418*, 397−399.

251. Wagemaker, M.; Borghols, W. J. H.; Mulder, F. M. Large Impact of Particle Size on Insertion Reactions. A Case for Anatase Li_xTiO_2. *J. Am. Chem. Soc.* **2007**, *129*, 4323−4327.

252. Wang, J.; Polleux, J.; Lim, J.; Dunn, B. Pseudocapacitive Contributions to Electrochemical Energy Storage in TiO_2 (Anatase) Nanoparticles. *J. Phys. Chem. C* **2007**, *111*, 14925−14931.

253. Sudant, G.; Baudrin, E.; Larcher, D.; Tarascon, J.-M. Electrochemical Lithium Reactivity with Nanotextured Anatase-Type TiO_2. *J. Mater. Chem.* **2005**, *15*, 1263−1269.

254. Jiang, C.; Wei, M.; Qi, Z.; Kudo, T.; Honma, I.; Zhou, H. Particle Size Dependence of the Lithium Storage Capability and High Rate Performance of Nanocrystalline Anatase TiO_2 Electrode. *Journal of Power Sources* **2007**, *166*, 239−243

255. Saravanan, K.; Ananthanarayanan, K.; Balaya, P. Mesoporous TiO_2 with High Packing Density for Superior Lithium Storage. *Energy Environ. Sci.* **2010**, *3*, 939−948.

256. Ishii, Y.; Kanamori, Y.; Kawashita, T.; Mukhopadhyay, I.; Kawasaki, S. Mesoporous Carbon–Titania Nanocomposites for High-Power Li-Ion Battery Anode Material. *J. Phy. Chem. Solids* **2010**, *71*, 511–514.

257. Zhang, J. J.; Huang, T.; Yu, A. S. Synergistic Effect of Amorphous Carbon Coverage and Enlarged Voltage Window on the Superior Lithium Storage Performance of Nanostructured Mesoporous Anatase TiO_2: Emphasis on Interfacial Storage Phenomena. *J. Alloys Compd.* **2014**, *606*, 61−67.

258. Mancini, M.; Kubiak, P.; Geserick, J.; Marassi, R.; Hüsing, N.; Wohlfahrt-Mehrens, M. Mesoporous Anatase TiO_2 Composite Electrodes: Electrochemical Characterization and High Rate Performances. *Journal of Power Sources* **2009**, *189*, 585−589.

259. Mancini, M.; Kubiak, P.; Wohlfahrt-Mehrens, M.; Marassi, R. Mesoporous Anatase TiO_2 Electrodes Modified by Metal Deposition: Electrochemical Characterization and High Rate Performances. *J. Electrochem. Soc.* **2010**, *157*, A164−A170.

260. He, B. L.; Dong, B.; Li, H. L. Preparation and Electrochemical Properties of Ag-Modified TiO_2 Nanotube Anode Material for Lithium− Ion Battery. *Electrochem. Commun.* **2007**, *9*, 425−430.

261. Guo, Y. G.; Hu, Y. S.; Sigle, W.; Maier, J. Superior Electrode Performance of Nanostructured Mesoporous TiO_2 (Anatase) Through Efficient Hierarchical Mixed Conducting Networks. *Adv. Mater.* **2007**, *19*, 2087−2091.

262. Koudriachova, M. V.; Harrison, N. M.; Leeuw, S. W. Effect of Diffusion on Lithium Intercalation in Titanium Dioxide. *Phys. Rev. Lett.* **2001**, *86*, 1275−1278.

263. Johnson, O. W. One-Dimensional Diffusion of Li in Rutile. *Phys. Rev.* **1964**, *136*, A284−A290.

264. Gligor, F.; de Leeuw, S. W. Lithium Diffusion in Rutile Structured Titania. *Solid State Ionics* **2006**, *177*, 2741−2746.

265. Stashans, A.; Lunell, S.; Bergstrom, R.; Hagfeldt, A.; Lindquist, S. E. Theoretical Study of Lithium Intercalation in Rutile and Anatase. *Phys. Rev. B: Condens. Matter Mater. Phys.* **1996**, *53*, 159−170.

266. Ohzuku, T.; Takehara, Z.; Yoshizawa, S. Nonaqueous Lithium/ Titanium Dioxide Cell. *Electrochim. Acta* **1979**, *24*, 219−222.

267. Kavan, L.; Fattakhova, D.; Krtil, P. Lithium Insertion into Mesoscopic and Single-Crystal TiO_2 (Rutile) Electrodes. *J. Electrochem. Soc.* **1999**, *146*, 1375−1379.

268. Jiang, C.; Honma, I.; Kudo, T.; Zhou, H. Nanocrystalline Rutile TiO_2 Electrode for High-Capacity and High-Rate Lithium Storage. *Electrochem. Solid State Lett.* **2007**, *10*, A127−A129.

269. Wang, D.; Choi, D.; Yang, Z.; Viswanathan, V. V.; Nie, Z.; Wang, C.; Song, Y.; Zhang, J.-G.; Liu, J. Synthesis and Li-Ion Insertion Properties of Highly Crystalline Mesoporous Rutile TiO_2. *Chem. Mater.* **2008**, *20*, 3435-3442.

270. Marchand, R.; Brohan, L.; Tournoux, M. TiO_2(B) A New Form Of Titanium-Dioxide and the Potassium Octatitanate $K_2Ti_8O_{17}$. *Mater. Res. Bull.* **1980**, *15*, 1129− 1133.

271. Zachau-Christiansen, B.; West, K.; Jacobsen, T.; Atlung, S. Lithium Insertion in Different TiO_2 Modifications. *Solid State lonics* **1988**, *28-30*, 1176-1182.

272. Zachau-Christiansen, B.; West, K.; Jacobsen, T.; Skaarup, S. Lithium Insertion in Isomorphous MO_2 (B) Structures. *Solid State Ionics* **1992**, *53-56*, 364-369.

273. Inaba, M.; Oba, Y.; Niina, F.; Murota, Y.; Ogino, Y.; Tasaka, A.; Hirota, K. TiO_2(B) as a Promising High Potential Negative Electrode for Large-size Lithium-ion Batteries. *Journal of Power Sources* **2009**, *189*, 580− 584.

274. Armstrong, G.; Armstrong, A. R.; Canales, J.; Bruce, P. G. Nanotubes with the TiO_2-B Structure. *Chem. Commun.* **2005**, 2454− 2456.

275. Armstrong, A. R.; Armstrong, G.; Canales, J.; Bruce, P. G. TiO_2-B Nanowires as Negative Electrodes for Rechargeable Lithium Batteries. *J. Power Sources* **2005**, *146*, 501−506.

276. Zukalová, M.; Kalbáč, M.; Kavan, L.; Exnar, I.; Graetzel, M. Pseudocapacitive Lithium Storage in TiO_2 (B). *Chem. Mater.* **2005**, *17*, 1248−1255.

277. Murphy, D. W.; Cava, R. J.; Zahurak, S. M.; Santoro, A. Ternary Li_xTiO_2 Phases from Insertion Reactions. *Solid State Ionics* **1983**, *9*, 413−417.

278. Ohzuku, T.; Ueda, A.; Yamamoto, N. Zero-Strain Insertion Material of $Li[Li_{1/3}Ti_{5/3}]O_4$ for Rechargeable Lithium Cells. *J. Electrochem. Soc.* **1995**, *142*, 1431−1435.

279. Scharner, S.; Weppner, W.; Schmid-Beurmann, P. Evidence of Two-Phase Formation upon Lithium Insertion into the $Li_{1.33}Ti_{1.67}O_4$ Spinel. *J. Electrochem. Soc.* **1999**, *146*, 857−861.

280. Ronci, F.; Reale, P.; Scrosati, B.; Panero, S.; Rossi Albertini, V.; Perfetti, P.; di Michiel, M.; Merino, J. M. High-Resolution In-Situ Structural Measurements of the $Li_{4/3}Ti_{5/3}O_4$ "Zero-Strain" Insertion Material. *J. Phys. Chem. B* **2002**, *106*, 3082−3086.

281. Ariyoshi, K.; Yamato, R.; Ohzuku, T. Zero-Strain Insertion Mechanism of $Li[Li_{1/3}Ti_{5/3}]O_4$ for Advanced Lithium-Ion (Shuttlecock) Batteries. *Electrochim. Acta* **2005**, *51*, 1125−1129.

282. Chen, C. H.; Vaughey, J. T.; Jansen, A. N.;* Dees, D. W.; Kahaian, A. J.; Goacher, T.; Thackeray, M. M. Studies of Mg-Substituted $Li_{4-x}Mg_xTi_5O_{12}$ Spinel Electrodes ($0 \leq x \leq 1$) for Lithium Batteries. *J. Electrochem. Soc.* **2001**, *148*, A102-A104.

283. Stenina, I. A.; Il'in, A. B.; Yaroslavtsev, A. B. Synthesis and Ionic Conductivity of $Li_4Ti_5O_{12}$. *Inorg. Mater.* **2015**, *51*, 62−67.

284. Belharouak, I.; Koenig, G. M.; Tan, T.; Yumoto, H.; Ota, N.; Amine, K. Performance Degradation and Gassing of $Li_4Ti_5O_{12}$/ $LiMn_2O_4$ Lithium-Ion Cells. *J. Electrochem. Soc.* **2012**, *159*, A1165−A1170.

285. Amatucci, G. G.; Badway, F.; Du Pasquier, A.; Zheng, T. J. An Asymmetric Hybrid Nonaqueous Energy Storage Cell. *J. Electrochem. Soc.* **2001**, *148*, A930−A939.

286. Hsiao, K.-C.; Liao, S.-C.; Chen, J.-M. Microstructure Effect on the Electrochemical Property of $Li_4Ti_5O_{12}$ as an Anode Material for Lithium-Ion Batteries. *Electrochim. Acta* **2008**, *53*, 7242−7247.

287. Sorensen, E. M.; Barry, S. J.; Jung, H.-K.; Rondinelli, J. R.; Vaughey, J. T.; Poeppelmeier, K. R. Three-Dimensionally Ordered Macroporous $Li_4Ti_5O_{12}$: Effect of Wall Structure on Electrochemical Properties. *Chem. Mater.* **2006**, *18*, 482−489.

288. Prakash, A. S.; Manikandan, P.; Ramesha, K.; Sathiya, M.; Tarascon, J.-M.; Shukla, A. K. Solution-Combustion Synthesized Nanocrystalline $Li_4Ti_5O_{12}$ As High-Rate Performance Li-Ion Battery Anode. *Chem. Mater.* **2010**, *22*, 2857−2863.

289. Cheng, L.; Li, X.-L.; Liu, H.-J.; Xiong, H.-M.; Zhang, P.-W.; Xia, Y.-Y. Carbon-Coated $Li_4Ti_5O_{12}$ as a High Rate Electrode Material for Li-Ion Intercalation. *J. Electrochem. Soc.* **2007**, *154*, A692−A697.

290. Zhu, G.-N.; Wang, C.-X.; Xia, Y.-Y. A Comprehensive Study of Effects of Carbon Coating on $Li_4Ti_5O_{12}$ Anode Material for Lithium Ion Batteries. *J. Electrochem. Soc.* **2011**, *158*, A102−A109.

291. Wang, Y. G.; Liu, H. M.; Wang, K. X.; Eiji, H.; Wang, Y. R.; Zhou, H. S. Synthesis and Electrochemical Performance of Nano-Sized $Li_4Ti_5O_{12}$ with Double Surface Modification of Ti(III) and Carbon. *J. Mater. Chem.* **2009**, *19*, 6789−6795.

292. Li, X.; Qu, M. Z.; Yu, Z. L. Preparation and Electrochemical Performance of $Li_4Ti_5O_{12}$/Graphitized Carbon Nanotubes Composite. *Solid State Ionics* **2010**, *181*, 635−639.

293. Huang, J. J.; Jiang, Z. Y. The Preparation and Characterization of $Li_4Ti_5O_{12}$/Carbon Nano-Tubes for Lithium Ion Battery. *Electrochim. Acta* **2008**, *53*, 7756−7760.

294. Shen, L.; Yuan, C.; Luo, H.; Zhang, X.; Xu, K.; Zhang, F. In Situ Growth Of $Li_4Ti_5O_{12}$ on Multi-Walled Carbon Nanotubes: Novel Coaxial Nanocables for High Rate Lithium Ion Batteries. *J. Mater. Chem.* **2011**, *21*, 761−767.

295. Naoi, K.; Ishimoto, S.; Isobe, Y.; Aoyagi, S. High-Rate Nano-Crystalline $Li_4Ti_5O_{12}$ Attached on Carbon Nano-Fibers for Hybrid Supercapacitors. *Journal of Power Sources* **2010**, *195*, 6250−6254.

296. Yi, T.-F.; Yang, S.-Y.; Li, X.-Y.; Yao, J.-H.; Zhu, Y.-R.; Zhu, R.-S. Sub-Micrometric $Li_{4-x}Na_xTi_5O_{12}$ ($0 \leq x \leq 0.2$) Spinel as Anode Material Exhibiting High Rate Capability. *Journal of Power Sources* **2014**, *246*, 505−511.

297. Gu, F. Electrochemical Performances of $Li_{4-x}K_xTi_5O_{12}$ (X=0.02, 0.04, 0.06) As Anode Materials for Lithium Ion Battery. *Adv. Mat. Res.* **2013**, *712-715*, 313-316.

298. Wang, W.; Jiang, B.; Xiong, W. Y.; Wang, Z.; Jiao, S. Q. A Nanoparticle Mg-Doped $Li_4Ti_5O_{12}$ for High Rate Lithium-Ion Batteries. *Electrochim. Acta* **2013**, *114*, 198−204.

299. Zhang, Q.; Zhang, C.; Li, B.; Kang, S.; Li, X.; Wang, Y. Preparation and Electrochemical Properties of Ca-Doped $Li_4Ti_5O_{12}$ as Anode Materials in Lithium-Ion Battery. *Electrochim. Acta* **2013**, *98*, 146−152.

300. Lin, C.; Ding, B.; Xin, Y.; Cheng, F.; Lai, M. O.; Lu, L.; Zhou, H. Advanced Electrochemical Performance of $Li_4Ti_5O_{12}$-Based Materials for Lithium-Ion Battery: Synergistic Effect of Doping and Compositing. *Journal of Power Sources* **2014**, *248*, 1034−1041.

301. Ji, M.; Xu, Y.; Zhao, Z.; Zhang, H.; Liu, D.; Zhao, C.; Qian, X.; Zhao, C. Preparation and Electrochemical Performance of La^{3+} And F^{-} co-doped $Li_4Ti_5O_{12}$ Anode Material for Lithium-Ion Batteries. *Journal of Power Sources* **2014**, *263*, 296-303.

302. Reale, P.; Panero, S.; Ronci, F.; Rossi Albertini, V.; Scrosati, B. Iron-Substituted Lithium Titanium Spinels: Structural and Electrochemical Characterization. *Chem. Mater.* **2003**, *15*, 3437−3442.

303. Li, H. Q.; Liu, X. Z.; Zhai, T.; Li, Y. D.; Zhou, H. S. Li_3VO_4:A Promising Insertion Anode Material for Lithium-Ion Batteries. *Adv. Energy Mater.* **2013**, *3*, 428−432.

304. Liaoa, C.; Zhanga, Q.; Zhaia, T.; Lia, H.; Zhoub, H. Development and Perspective of the Insertion Anode Li_3VO_4 for Lithium-Ion Batteries. *Energy Storage Materials* **2017**, *7*, 17–31.

305. Shi, Y.; Wang, J. Z.; Chou, S. L.; Wexler, D.; Li, H. J.; Ozawa, K.; Liu, H. K.; Wu, Y. P. Hollow Structured Li_3VO_4 Wrapped with Graphene Nanosheets in Site Prepared by a One-Pot Template-Free Method as an Anode for Lithium-Ion Battery. *Nano Lett.* **2013**, *13*, 4715−4720.

306. Shen, L.; Chen, S.; Maier, J.; Yu, Y. Carbon-Coated Li_3VO_4 Spheres as Constituents of an Advanced Anode Material for High-Rate Long-Life Lithium-Ion Batteries. *Adv. Mater.* **2017**, *29*, 1701571.

307. Ni, S.; Zhang, J.; Ma, J.; Yang, X.; Zhang, L.; Li, X.; Zeng, H. Approaching the Theoretical Capacity of Li_3VO_4 via Electrochemical Reconstruction. *Adv. Mater. Interfaces* **2016**, *3*, 1500340.

308. Shi, Y.; Gao, J.; Abruña, H. D.; Li, H.-J.; Liu, H.-K.; Wexler, D.; Wang, J.-Z.; Wu, Y. The Mechanism of the One-Step Synthesis of Hollow-Structured Li_3VO_4 as an Anode for Lithium-Ion Batteries. *Chem. Eur. J.* **2014**, *20*, 5608−5612.

309. Kim, W.-T.; Min, B.-K.; Choi, H. C.; Lee, Y. J.; Jeong, Y. U. Lithium Intercalation and Crystal Chemistry of Li_3VO_4 Synthesized by Ultrasonic Nebulization as a New Anode Material for Secondary Lithium Batteries. *J. Electrochem. Soc.* **2014**, *161*, A1302−A1305.

310. Li, Q.; Sheng, J.; Wei, Q.; An, Q.; Wei, X.; Zhang, P.; Mai, L. A Unique Hollow Li_3VO_4/Carbon Nanotube Composite Anode for High Rate Long-Life Lithium-Ion Batteries. *Nanoscale* **2014**, *6*, 11072−11077.

311. Li, Q.; Wei, Q.; Wang, Q.; Luo, W.; An, Q.; Xu, Y.; Niu, C.; Tang, C.; Mai, L. Self-Template Synthesis of Hollow Shell-Controlled Li_3VO_4 as a High-Performance Anode for Lithium-Ion Batteries. *J. Mater. Chem. A* **2015**, *3*, 18839−18842.

312. Liu, J.; Lu, P.; Liang, S.; Liu, J.; Wang, W.; Lei, M.; Tang, S.; Yang, Q. Ultrathin Li_3VO_4 Nanoribbon/Graphene Sandwich-Like Nanostructures with Ultrahigh Lithium Ion Storage Properties. *Nano Energy* **2015**, *12*, 709−724.

313. Shao, G.; Gan, L.; Ma, Y.; Li, H.; Zhai, T. Enhancing the Performance of Li_3VO_4 by Combining Nanotechnology and Surface Carbon Coating for Lithium Ion Batteries. *J. Mater. Chem. A* **2015**, *3*, 11253−11260.

314. Chen, L.; Jiang, X.; Wang, N.; Yue, J.; Qian, Y.; Yang, J. Surface Amorphous and Oxygen-Deficient $Li_3VO_{4-\delta}$ as a Promising Anode Material for Lithium-Ion Batteries. *Adv. Sci.* **2015**, *2*, 1500090.

315. Zhao, D.; Cao, M. Constructing Highly Graphitized Carbon Wrapped Li_3VO_4 Nanoparticles with Hierarchically Porous Structure as a Long Life and High Capacity Anode for Lithium-Ion Batteries. *ACS Appl. Mater. Interfaces* **2015**, *7*, 25084−25093.

316. Zhang, C.; Song, H.; Liu, C.; Liu, Y.; Zhang, C.; Nan, X.; Cao, G. Fast and Reversible Li Ion Insertion in Carbon-Encapsulated Li_3VO_4 as Anode for Lithium-Ion Battery. *Adv. Funct. Mater.* **2015**, *25*, 3497−3504.

317. Yang, Y.; Li, J.; He, X.; Wang, J.; Sun, D.; Zhao, J. A Facile Spray Drying Route for Mesoporous Li_3VO_4/C Hollow Spheres as an Anode for Long Life Lithium Ion Batteries. *J. Mater. Chem. A* **2016**, *4*, 7165− 7168.

318. Hu, S.; Song, Y. F.; Yuan, S. Y.; Liu, H. M.; Xu, Q. J.; Wang, Y. G.; Wang, C. X.; Xia, Y. Y. A Hierarchical Structure of Carbon-Coated Li_3VO_4 Nanoparticles Embedded in Expanded Graphite for High Performance Lithium Ion Battery. *Journal of Power Sources* **2016**, *303*, 333− 339.

319. Shen, L.; Lv, H.; Chen, S.; Kopold, P.; Aken, P. A. van; Wu, X.; Maier, J.; Yu, Y. Peapod-like Li_3VO_4/N-Doped Carbon Nanowires with Pseudocapacitive Properties as Advanced Materials for High-Energy Lithium-Ion Capacitors. *Adv. Mater.* **2017**, *1700142*, 1-8.

320. "Lithium" in Mineral Commodity Summaries, U.S. Geological Survey, Reston, VA, **2012**, p. 94.

321. Palomares, V.; Serras, P.; Villaluenga, I.; Hueso, K. B.; Carretero-González, J.; Rojo, T. Na-Ion Batteries, Recent Advances and Present Challenges to Become Low Cost Energy Storage Systems. *Energy Environ. Sci.* **2012**, *5*, 5884−5901.

322. Slater, M. D.; Kim, D.; Lee, E.; Johnson, C. S. Sodium-Ion Batteries. *Adv. Funct. Mater.* **2013**, *23*, 947–958.

323. Kim, S.-W.; Seo, D. H.; Ma, X.; Ceder, G.; Kang, K. Electrode Materials for Rechargeable Sodium-Ion Batteries: Potential Alternatives to Current Lithium-Ion Batteries. *Adv. Energy Mater.* **2012**, *2*, 710−721.

324. Pan, H.; Hu, Y.-S.; Chen, L. Room-temperature Stationary Sodium-ion Batteries for Large-scale Electric Energy Storage. *Energy Environ. Sci.* **2013**, *6*, 2338−2360.

325. West, A. R. Solid State Chemistry and Its Applications. Wiley Publishers, **2011**.

326. Losocha, W.; Lewinski, K. PROSZKI- A System of Programs for Powder Diffraction Data Analysis. *J. Appl. Crystallogr.***1994**, *27*, 437-438.

327. Kraus, W.; Nolze, G. *POWDER CELL* - A Program for the Representation and Manipulation of Crystal Structures and Calculation of the Resulting X-ray Powder Patterns. *J. Appl. Crystallogr.***1996**, *29*, 301-303.

328. Wetzig, K.; Schulze, D. *In Situ* Scanning Electron Microscopy in Materials Research. *AkademieVerlag* **1995**.

329. Chandler, G. W.; Seraphin, S.; Ed. Kaufmann, E. N. Scanning Electron Microscopy. *Characterization of Materials* **2003**, *2*, 1050-1063.

330. Pennycook, S. J.; Eds. Williams, D. B.; Carter, C. B. Transmission Electron Microscopy: A Text Book for Materials Science. *Microscopy and Microanalysis* **2010**, *16*, 111-111.

331. Brunauer, S.; Deming, L. S.; Deming, W. E.; Teller, E. On a Theory of the van der Waals Adsorption of Gases. *J. Am. Chem. Soc*. **1940**, *62*, 1723-1732.

332. Viswanathan, V. Fundamental Challenges Facing Next-Generation Li Ion Batteries. *J. Phys. Chem. Lett.***2015**, *6*, 4673−4674.

333. Liu, J.; Zhang, J-G.; Yang, Z.; Lemmon, J. P.; Imhoff, C.; Graff, G. L.; Li, L.; Hu, J.; Wang, C.; Xiao, J.; Xia, G.; Viswanathan, V. V.; Bhaskaran, S.; Sprenkle, V.; Li, X.; Shao, Y.; Schwenzer, B. Materials Science and Materials Chemistry for Large Scale Electrochemical Energy Storage: From Transportation to Electrical Grid. *Adv. Funct. Mater.* **2013**, *23*, 929–946.

334. Manthiram, A. An Outlook on Lithium Ion Battery Technology. *ACS Cent. Sci*. **2017**, *3*, 1063-1069.

335. Manthiram, A. Materials Challenges and Opportunities of Lithium Ion Batteries. *J. Phys. Chem. Lett*. **2011**, *2*, 176–184.

336. Hayner, C. M.; Zhao, X.; Kung, H. H. Materials for Rechargeable Li-Ion Batteries. Annu. Rev. Chem. Biomol. Eng. **2012**, *3*, 445-471.

337. Lu, L.; Han, X.; Li, J.; Hua, J.; Ouyang, M. A Review on the Key Issues for Lithium-Ion Battery Management in Electric Vehicles. *Journal of Power Sources*. **2013**, *226*, 272–288.

338. Croguennec, L.; Palacin, M. R.; Recent Achievements on Inorganic Electrode Materials for Lithium-Ion Batteries. *J. Am. Chem. Soc.* **2015**, *137*, 3140−3156.

339. Choi, N.-S.; Chen, Z.; Freunberger, S. A.; Ji, X.; Sun, Y-K.; Amine, K.; Yushin, G.; Nazar, L.F.; Cho, J.; Bruce, P. G.; Challenges Facing Lithium Batteries and Electrical Double-Layer Capacitors. *Angew. Chem. Int. Ed*. **2012**, *51*, 9994 – 10024.

340. Melot, B. C.; Tarascon, J.-M.; Design and Preparation of Materials for Advanced Electrochemical Storage. *Acc. Chem. Res.* **2013**, *46*, 1226–1238.

341. Goodenough, J.B.; Evolution of Strategies for Modern Rechargeable Batteries. *Acc. Chem. Res.* **2013**, *46*, 1053-1061.

342. Kim, T-H.; Park, J-S.; Chang, S.K.; Choi, S.; Ryu, J.H.; Song, H-K.; The Current Move of Lithium Ion Batteries Towards the Next Phase. *Adv. Energy Mater.* **2011**, *2*, 860–872.

343. Etacheri, V.; Marom, R.; Elazari, R.; Salitra, G.; Aurbach, D.; Challenges in the Development of Advanced Li-ion batteries: A Review. *Energy Environ. Sci.* **2011**, *4*, 3243-3262.

344. Zhou, L.; Zhang, K.; Hu, Z.; Tao, Z.; Mai, L.; Kang, Y.-M.; Chou, S.-L.; Chan, J. Recent Developments on and Prospects for Electrode Materials with Hierarchical Structures for Lithium-Ion Batteries. *Adv. Energy Mater.* **2018**, *8*, 1701415.

345. Marom, R.; Amalraj, S.F.; Leifer, N.; Jacob, D.; Aurbach, D.; A Review of Advanced and Practical Lithium Battery Materials. *J. Mater. Chem.* **2011**, *21*, 9938-9954.

346. Xu, B.; Qian, D.; Wang, Z.; Meng, Y.S.; Recent Progress in Cathode Materials Research for Advanced Lithium Ion Batteries. *Materials Science and Engineering R*. **2012**, *73*, 51-65.

347. Ohzuku, T.; Brodd, R.J.; An Overview of Positive-Electrode Materials for Advanced Lithium-Ion Batteries. *Journal of Power Sources.* **2007**, *174*, 449–456.

348. Kalyani, P.; Kalaiselvi, N.; Various Aspects of $LiNiO_2$ Chemistry: A Review. *Science and Technology of Advanced Materials*, **2005**, *66*, 689-703.

349. Delmas, C.; Ménétrier, M.; Croguennec, L.; Saadoune, I.; Rougier, A.; Pouillerie, C.; Prado, G.; Grüne, M.; Fournès, L.; An Overview of the $Li(Ni,M)O_2$ Systems: Syntheses, Structures and Properties. *Electrochimica Acta*. **1999**, *45*. 243-253.

350. Spahr, M.E.; Novák, P.; Schnyder, B.; Haas, O.; Nesper, R.; Characterization of Layered Lithium Nickel Manganese Oxides Synthesized by a Novel Oxidative Coprecipitation Method and Their Electrochemical Performance as Lithium Insertion Electrode Materials. *J. Electrochem. Soc.* **1998**, *145*, 1113-1121.

351. Armstrong, A.R.; Bruce, P.G.; Electrochemistry Beyond Mn^{4+} in $Li_xMn_{1-y}Li_yO_2$. *Electrochemical and Solid-State Letters*. **2004**, ***7*** *(1)*, A1-A4.

352. Eriksson, T.A.; Doeff. M.M.; A Study of Layered Lithium Manganese Oxide Cathode Materials. *Journal of Power Sources*. **2003**, *119–121*, 145–149.

353. Shaju, K.M.; Rao G.V.S.; Chowdari B.V.R.; Layered Manganese Oxide with O_2 Structure, $Li_{(2/3)+x)}(Ni_{1/3}Mn_{2/3})O_2$ as Cathode for Li-ion Batteries. *Electrochemistry Communications.* **2002**, *4*, 633–638.

354. Stoyanova, R.; Zhecheva, E.; Alcántara, R.; Tirado, J.L.; Bromiley, G.; Bromiley, F.; Ballaran, T.B.; Lithium/nickel Mixing in the Transition Metal Layers of lithium nickelate: High-Pressure Synthesis of Layered $Li[Li_xNi_{1-x}]O_2$ Oxides as Cathode Materials for Lithium-Ion Batteries. *Solid State Ionics*. **2003**, *161*, 197– 204.

355. Reed, J.; Ceder, J.; Van Der Van, A.; Layered-to-Spinel Phase Transition in Li_xMnO_2. *Electrochemical and Solid-State Letters*, **2001**, *4 (6)*, A78-A81.

356. Xu, J.; Lin, F.; Doeff, M.M.; Tong, W.; A Review of Ni-based Layered Oxides for Rechargeable Li-ion batteries. *J. Mater. Chem. A*, **2017**, *5*, 874–901.

357. Rougier, A.; Saadoune, I.; Gravereau, P.; Willmannb, P.; Delmas, C.; Effect of Cobalt Substitution on Cationic Distribution in $LiNi_{1-y}Co_yO_2$ Electrode Materials. Solid State Ionics. **1996,** *90*, 83-90.

358. Arai, H.; Okada, S.; Sakurai, Y.; Yamaki, J-I.; Electrochemical and Thermal Behavior of $LiNi_{1-Z}M_ZO_Z$. *J. Electrochem. Soc.* **1997**, *144(9)*, 3117-3125.

359. Liu. Z.; Yu, A.; Lee, J.Y.; Synthesis and Characterization of $LiNi_{1-x-y}Co_xMn_yO_2$ as the Cathode Materials of Secondary Lithium Batteries. *Journal of Power Sources*. **1999**, *81–82*, 416–419.

360. Ohzuku, T.; Makimura, Y.; Layered Lithium Insertion Material of $LiCo_{1/3}Ni_{1/3}Mn_{1/3}O_2$ for Lithium-Ion Batteries. *Chemistry Letters*. **2001,** 642-643.

361. Yabuuchi, N.; Ohzuku, Y.; Novel lithium Insertion Material of $LiCo_{1/3}Ni_{1/3}Mn_{1/3}O_2$ for Advanced Lithium-Ion Batteries. *Journal of Power Sources*. 2003, *119–121*, 171–174.

362. Hwang, B.J.; Tsai, Y.W.; Carlier, D.; Ceder, G.; A Combined Computational/Experimental Study on $LiNi_{1/3}Co_{1/3}Mn_{1/3}O_2$. *Chem. Mater*. **2003,** *15*, 3676-3682.

363. Chen, C-H.; Wang, C-J.; Hwang, B-J.; Electrochemical Performance of Layered $Li[Ni_xCo_{1-2x}Mn_x]O_2$ Cathode Materials Synthesized by a Sol–Gel Method. *Journal of Power Sources*. **2005**, *146*, 626–629.

364. Noh, H-J.; Youn, S.; Yoon, C.S.; Sun, Y-K.; Comparison of the Structural and Electrochemical Properties of Layered $Li[Ni_xCo_yMn_z]O_2$ (x = 1/3, 0.5, 0.6, 0.7, 0.8 and 0.85) Cathode Material for Lithium-Ion Batteries. *Journal of Power Sources*, **2013**, *233*, 121-130.

365. Ryu, H-H.; Park, K-J.; Yoon, C-S.; Sun, Y-K.; Capacity Fading of Ni-Rich $Li[Ni_xCo_yMn_{1-x-y}]O2$ ($0.6 \leq x \leq 0.95$) Cathodes for High-Energy-Density Lithium-Ion Batteries: Bulk or Surface Degradation?. *Chem. Mater*. **2018,** *30*, 1155−1163.

366. Noh, M.; Cho, J.; Optimized Synthetic Conditions of $LiNi_{0.5}Co_{0.2}Mn_{0.3}O_2$ Cathode Materials for High Rate Lithium Batteries via Co-Precipitation Method. *J. Electrochem. Soc*. **2013**, *160 (1)* A105-A111.

367. Zuo, X.; Fan, C.; Liu, J.; Xiao, X.; Wu, J.; Nan, J.; Effect of tris(trimethylsilyl)borate on the High Voltage Capacity Retention of $LiNi_{0.5}Co_{0.2}Mn_{0.3}O_2$/Graphite Cells. *Journal of Power Sources*. **2013**, *229*, 308-312.

368. Huang, Y.; Jin, F-M.; Chen, F-J.; Chen, L.; Improved Cycle Stability and High-Rate Capability of Li_3VO_4-Coated $Li[Ni_{0.5}Co_{0.2}Mn_{0.3}]O_2$ Cathode Material Under Different Voltages. *Journal of Power Sources*, **2014**, *256*, 1-7.

369. Li, L.; Chen, Z.; Zhang, Q.; Xu, M.; Zhou, X.; Zhu, H.; Zhang, K.; A Hydrolysis-Hydrothermal Route for the Synthesis of Ultrathin $LiAlO_2$-Inlaid $LiNi_{0.5}Co_{0.2}Mn_{0.3}O_2$ as a High-Performance Cathode Material for Lithium Ion Batteries. *J. Mater. Chem. A*. **2015**, *3*, 894-904.

370. Cao, H.; Zhang, Y.; Zhang, J.; Xia, B.; Synthesis and Electrochemical Characteristics of Layered $LiNi_{0.6}Co_{0.2}Mn_{0.2}O_2$ Cathode Material for Lithium Ion Batteries. *Solid State Ionics*. **2005**, *176*, 1207– 1211.

371. Zhang, Y.; Cao, H.; Zhang, J.; Xia, B.; Synthesis of $LiNi_{0.6}Co_{0.2}Mn_{0.2}O_2$ Cathode Material by a Carbonate Co-Precipitation Method and its Electrochemical Characterization. *Solid State Ionics*. **2006**, *177*, 3303–3307.

372. Ju, S.H.; Kang, I-S.; Lee, Y-S.; Shin, W-K.; Kim, S.; Shin, K.; Kim, D-W.; Improvement of the Cycling Performance of $LiNi_{0.6}Co_{0.2}Mn_{0.2}O_2$ Cathode Active Materials by a Dual-Conductive Polymer Coating. *ACS Appl. Mater. Interfaces.* **2014**, *6*, 2546−2552.

373. Zhang, L.; Dong, T.; Yu, X.; Dong, Y.; Zhao, Z.; Li, H.; Synthesis and electrochemical performance of $LiNi_{0.7}Co_{0.15}Mn_{0.15}O_2$ as Gradient Cathode Material for Lithium Batteries. *Materials Research Bulletin*. **2012**, *47*, 3269–3272.

374. Fu, C.; Li, G.; Luo, D.; Li, Q.; Fan, J.; Li, L.; Nickel-Rich Layered Microspheres Cathodes: Lithium/Nickel Disordering and Electrochemical Performance. *ACS Appl. Mater. Interfaces*. **2014**, 6, 15822−15831.

375. Kim, Y. Lithium Nickel Cobalt Manganese Oxide Synthesized Using Alkali Chloride Flux: Morphology and Performance as a Cathode Material for Lithium Ion Batteries. *ACS Appl. Mater. Interfaces.* **2012**, *4*, 2329−2333.

376. Li, L-J.; Wang, Z-X.; Liu, Q-C.; Ye, C.; Chen, Z-Y.; Gong, L.; Effects of Chromium on the Structural, Surface Chemistry and Electrochemical of Layered $LiNi_{0.8-x}Co_{0.1}Mn_{0.1}Cr_xO_2$. *Electrochimica Act.* **2012**, *77*, 89– 96.

377. Xiong, X.; Wang, Z.; Guo, H.; Zhang, Q.; Li, X.; Enhanced Electrochemical Properties of Lithium-Reactive V2O5 Coated on the $LiNi_{0.8-x}Co_{0.1}Mn_{0.1}Cr_xO_2$ Cathode Material for Lithium Ion Batteries at 60°C. *J. Mater. Chem. A*, **2013**, *1*, 1284–1288.

378. Wu, F.; Tian, J.; Su, Y.; Wang, J.; Zhang, C.; Bao, L.; He, T.; Li, J.; Chen, S.; Effect of Ni^{2+} Content on Lithium/Nickel Disorder for Ni-Rich Cathode Materials. *ACS Appl. Mater. Interfaces.* **2015**, *7*, 7702−7708.

379. Lee, E.-S.; Manthiram, A. Smart Design of Lithium-rich Layered Oxide Cathode Compositions with Suppressed Voltage Decay. *J. Mater. Chem. A.* **2014,** *2*, 3932-3939.

380. Pang, W. K.; Lin, H.-F.; Peterson, V. K.; Lu, C-Z.; Liu, C.-E.; Liao, S.-C.; Chen, J.-M. Effects of Fluorine and Chromium Doping on the Performance of Lithium-Rich $Li_{1+x}MO_2$ (M = Ni, Mn, Co) Positive Electrodes. *Chem. Mater.* **2017**, *29*, 10299−10311.

381. Pimenta, V.; Sathiya, M.; Batuk, D.; Abakumou, A. M.; Giaume, D.; Cassiagnon, S.; Larcher, D.; Tarascon, J.-M. Synthesis of Li-Rich NMC: A Comprehensive Study. *Chem. Mater.* **2017**, *29*, 9923−9936.

382. He, Y.-S.; Pei, L.; Liao, X.-Z.; Ma, Z.-F. Synthesis of $LiNi_{1/3}Co_{1/3}Mn_{1/3}O_{2-z}F_z$ Cathode Material from Oxalate Precursors for Lithium Ion Battery. *Journal of Fluorine Chemistry* **2007**, *128*, 139–143.

383. Zheng, J.; Wu, X.; Yang, Y. Improved Electrochemical Performance of $Li[Li_{0.2}Mn_{0.54}Ni_{0.13}Co_{0.13}]O_2$ Cathode Material by Fluorine Incorporation. *Electrochim. Acta* **2013,** *105*, 200-208.

384. Dyer, L. D.; Borie, B. S.; Smith, G. P. Alkali Metal-Nickel Oxides of the Type $MNiO_2$. *J. Am. Chem. Soc.* **1954**, *76*, 1499-1503.

385. Subramaniyam, C. S.; Celio, H.; Shiva, K.; Gao, H.; Goodenough, J. B.; Liu, H. K.; Dou, S. X. Long Stable Cycling of Fluorine-doped Nickel-Rich Layered Cathodes for Lithium Batteries. Sustainable Energy Fuels, **2017**, *1*, 1292-1298.

386. Sinha, N. N.; Munichandraiah, N. Synthesis and Characterization of Carbon-Coated $LiNi_{1/3}Co_{1/3}Mn_{1/3}O_2$ in a Single Step by an Inverse Microemulsion Route. *ACS Appl. Mater. Interfaces.* **2009**, *1*, 1241−1249.

387. Shaju, K. M.; Rao, G. V. S.; Chowdari, B. V. R. Performance of Layered $Li(Ni_{1/3}Co_{1/3}Mn_{1/3})O_2$ as Cathode for Li-Ion Batteries. *Electrochim. Acta* **2002,** *48*, 145-151.

388. Yang, Z.; Zhang, J.; Kintner-Meyer, M. C. W.; Lu, x.; Choi, D.; Lemmon, J. P.; Liu, J. Electrochemical Energy Storage for Green Grid. *Chem. Rev*. **2011**, *111*, 3577–3613.

389. Schipper, F.; Aurbach, D. A Brief Review: Past, Present and Future of Lithium Ion Batteries. *Russ. J. Electrochem.* **2016**, *52*, 1229-1258.

390. Nayak, P. K.; Yang, L.; Brehm, W.; Adelhelm, P. From Lithium-Ion to Sodium-Ion Batteries: Advantages, Challenges, and Surprises. *Angew. Chem. Int. Ed.* **2018**, *57*, 102 – 120.

391. Cao, Y.; Xiao, L.; Choi, W. W. D.; Nie, Z.; Yu, J.; Saraf, L. V.;Yang, Z.; Liu, J. Reversible Sodium Ion Insertion in Single Crystalline Manganese Oxide Nanowires with Long Cycle Life. *Adv. Mater.* **2011**, *23*, 3155–3160.

392. Yuan, D.; Liang, X.; Wu, L.; Cao, Y.; Ai, X.; Feng, J.; Yang, H. A Honeycomb-Layered $Na_3Ni_2SbO_6$: A High-Rate and Cycle-Stable Cathode for Sodium-Ion Batteries. *Adv. Mater*. **2014**, *26*, 6301–6306.

393. Wang, Y.; Xiao, R.; Hu, Y.-S.; Avdeev, M.; Chen, L.; P2-$Na_{0.6}[Cr_{0.6}Ti_{0.4}]O_2$ Cation-Disordered Electrode for High-Rate Symmetric Rechargeable Sodium-Ion Batteries. *Nat. Commun*. 2015, 6, 1-9.

394. Guo, S.; Yu, P. L. H.; Zhu, Y.; Chen, M.; Ishida, M.; Zhou, H. A Layered P2- and O3-Type Composite as a High-Energy Cathode for Rechargeable Sodium-Ion Batteries. *Angew. Chem. Int. Ed.* **2015**, *54*, 5894 –5899.

395. Komaba, S.; Muarat, W.; Ishikawa, T.; Yabuuchi, N.; Ozeki, T.; Nakayama, T.; Ogata, A.; Gotoh, K.; Fujuwara, K. Electrochemical Na Insertion and Solid Electrolyte Interphase

for Hard-Carbon Electrodes and Application to Na-Ion Batteries. *Adv. Funct. Mater*. **2011**, *21*, 3859–3867.

396. Cao, Y.; Xiao, L.; Sushko, M. L.; Wang, W.; Schwenzer, B.; Xiao, J.; Nie, Z.; Saraf, L. V.; Yang, Z.; Liu, J. Sodium Ion Insertion in Hollow Carbon Nanowires for Battery Applications. *Nano Lett.* **2012**, *12*, 3783−3787.

397. Luo, W.; Schardt, J.; Bommier, C.; Wang, B.; Razink, J.; Simonsen, J.; Ji, X. Carbon Nanofibers Derived from Cellulose Nanofibers as a Long-Life Anode Material for Rechargeable Sodium-Ion Batteries. *J. Mater. Chem. A*, **2013**, *1*, 10662–10666.

398. Xiao, L.; Cao, Y.; Henderson, W. A.; Sushko, M. L.; Shao, Y.; Xiao, J.; Wang, W.; Engelhard, M. H.; Nie, Z.; Liu, J. Hard Carbon Nanoparticles as High-Capacity, High-Stability Anodic Materials for Na-Ion Batteries. *Nano Energy* **2016**, *19*, 279–288.

399. Fang, Y.; Xiao, L.; Qian, J.; Ai, X.; Yang, H.; Cao, Y. Mesoporous Amorphous $FePO_4$ Nanospheres as High-Performance Cathode Material for Sodium-Ion Batteries. *Nano Lett*. **2014**, *14*, 3539−3543.

400. Fang, Y.; Xiao, L.; Ai, X.; Cao, Y.; Yang, H. Hierarchical Carbon Framework Wrapped $Na_3V_2(PO_4)_3$ as a Superior High-Rate and Extended Lifespan Cathode for Sodium-Ion Batteries. *Adv. Mater*. **2015**, *27*, 5895–5900.

401. Rui, X.; Sun. W.; Wu, C.; Yu, Y.; Yan, Q. An Advanced Sodium-Ion Battery Composed of Carbon Coated $Na_3V_2(PO_4)_3$ in a Porous Graphene Network. Adv. Mater. **2015**, *27*, 6670–6676.

402. Reynaud, M.; Rousse, G.; Abakumov, A. M.; Sougrati, M. T.; Tendeloo, G. V.; Chotard, J. -N.; Tarascon, J. -M. Design of New Electrode Materials for Li-Ion and Na-Ion Batteries from the Bloedite Mineral $Na_2Mg(SO_4)_2.4H_2O$. *J. Mater. Chem. A*, **2014**, *2*, 2671-2680.

403. Barpanda, P.; Oyama, G.; Nishimura, S.-I.; Chung, S.-C.; Yamada, A. A 3.8-V Earth-Abundant Sodium Battery Electrode. *Nat. Commun.* **2014**, *5*, 1-8.

404. Barpanda, P.; Oyama, G.; Ling, C. D.; Yamada, A. Kröhnkite-Type $Na_2Fe(SO_4)_2{\cdot}2H_2O$ as a Novel 3.25 V Insertion Compound for Na-Ion Batteries. Chem. Mater. **2014**, *26*, 1297-1299.

405. Singh, P.; Shiva, K.; Celio, H.; Goodenough, J. B. Eldfellite, NaFe(SO4)2: An Intercalation Cathode Host for Low-Cost Na-Ion Batteries. *Energy Environ. Sci.* **2015**, *8*, 3000-3005.

406. Qian, J.; Zhou, M.; Cao, Y.; Ai, X.; Yang, H. Nanosized $Na_4Fe(CN)_6$/C Composite as a Low-Cost and High-Rate Cathode Material for Sodium-Ion Batteries. *Adv. Energy Mater.* **2012**, *2*, 410–414.

407. Wang, L.; Lu, Y.; Xu, M.; Cheng, J.; Zhang, D.; Goodenough, J. B. A Superior Low-Cost Cathode for a Na-Ion Battery. *Angew. Chem. Int. Ed.* **2013**, *52*, 1964 –1967.

408. You, Y.; Wu, X.-L.; Yin, Y.-X.; Guo, Y.-G. High-Quality Prussian Blue Crystals as Superior Cathode Materials for Room-Temperature Sodium-Ion Batteries. *Energy Environ. Sci*., **2014**, *7*, 1643–1647.

409. Xiao, L.; Cao, Y.; Xiao, J.; Wang, W.; Kovarik, L.; Nie, Z.; Liu, J. High Capacity, Reversible Alloying Reactions in SnSb/C Nanocomposites for Na-Ion Battery Applications. *Chem. Commun.*, **2012**, *48*, 3321–3323.

410. Qian, J.; Wu, X.; Cao, Y.; Ai, X.; Yang, H.; High Capacity and Rate Capability of Amorphous Phosphorus for Sodium Ion Batteries. *Angew. Chem. Int. Ed.* **2013**, *52*, 4633 – 4636.

411. Wu, L.; Hu, X.; Qian, J.; Pei. F.; Wu, F.; Mao, R.; Ai, X.; Yang, H.; Cao, Y. Sb–C Nanofibers with Long Cycle Life as an Anode Material for High-Performance Sodium-Ion Batteries. *Energy Environ. Sci.*, **2014**, *7*, 323–328.

412. Fang, Y.; Zhang, J.; Xiao, L.; Ai, X.; Cao, Y.; Yang, H. Phosphate Framework Electrode Materials for Sodium Ion Batteries. *Adv. Sci.* **2017**, *4*, 1600392.

413. Kim, j.; Seo, D.-H.; Kim, H.; Park, I.; Yoo, J.-K.; Jung, S.-K.; Park, Y.-U.; Goddard III, W. A.; Kang, K. Unexpected Discovery of Low-Cost Maricite $NaFePO_4$ as a High-Performance Electrode for Na-Ion Batteries. *Energy Environ. Sci.*, **2015**, *8*, 540–545.

414. Langrock, A.; Xu, Y.; Liu, Y.; Ehrman, S.; Manivannan, A.; Wang, C. Carbon Coated Hollow Na_2FePO_4F Spheres for Na-Ion Battery Cathodes. *Journal of Power Sources* **2013**, *223*, 62-67.

415. Deng, X.; Shi, W.; Sunarso, J.; Liu, M.; shao, Z. A Green Route to a Na_2FePO_4F-Based Cathode for Sodium Ion Batteries of High Rate and Long Cycling Life. *ACS Appl. Mater. Interfaces* **2017**, *9*, 16280−16287.

416. Trad, K,; Carlier, D.; Croguennec, L.; Wattiaux, A.; Lajmi, B.; Amara, M. F.; Delmas, C. A Layered Iron(III) Phosphate Phase, $Na_3Fe_3(PO_4)_4$: Synthesis, Structure, and Electrochemical Properties as Positive Electrode in Sodium Batteries. *J. Phys. Chem. C* **2010**, *114*, 10034–10044.

417. Trad, K.; Carlier, D.; Croguennec, L.; Wattiaux, A.; Amara, M, B.; Delmas, C. NaMnFe2(PO4)3 Alluaudite Phase: Synthesis, Structure, and Electrochemical Properties as Positive Electrode in Lithium and Sodium Batteries. *Chem. Mater*. **2010**, *22*, 5554–5562.

418. Chen, H.; Hautier, G.; Jain, A.; Moore, C.; Kang, B.; Doe, R.; Wu, L.; Zhu, Y.; Tang, Y.; Ceder, G. Carbonophosphates: A New Family of Cathode Materials for Li-Ion Batteries Identified Computationally. *Chem. Mater*. **2012**, *24*, 2009−2016.

419. Barpanda, P.; Liu, G.; Ling, C. D.; Tamaru, M.; Avdeev, M.; Chung, S.-C.; Yamada, Y.; Yamada, A. $Na_2FeP_2O_7$: A Safe Cathode for Rechargeable Sodium-ion Batteries. *Chem. Mater*. **2013**, *25*, 3480−3487.

420. Barpanda, P.; Ye, T.; Avdeev, M.; Chung, S.-C.; Yamada, A. A New Polymorph of $Na_2MnP_2O_7$ as a 3.6 V Cathode Material for Sodium-Ion Batteries. *J. Mater. Chem. A*, 2013, 1, 4194–4197.

421. Kim, H.; Park, I.; Lee, S.; Kim, H.; Park, K.-Y.; Park, Y.-U.; Kim, H.; Kim, J.; Lim, H.-D.; Yoon, W.-S.; Kang, K. Understanding the Electrochemical Mechanism of the New Iron-Based Mixed-Phosphate $Na_4Fe_3(PO_4)_2(P_2O_7)$ in a Na Rechargeable Battery. *Chem. Mater*. **2013**, *25*, 3614−3622.

422. Lim, S. Y.; Kim, H.; Chung, J.; Lee, J. H.; Kim, G. B.; Choi, J.-j.; Chung, K. Y.; Cho, W.; Kim, S.-J.; Goddard III, W. A.; Jung, Y.; Choi, J. W. Role of Intermediate Phase for Stable Cycling of $Na_7V_4(P_2O_7)_4PO_4$ in Sodium Ion Battery. *PANS*, **2014**, *111*, 599–604.

423. Deng, C.; Zhang, S. 1D Nanostructured $Na_7V_4(P_2O_7)_4(PO_4)$ as High-Potential and Superior-Performance Cathode Material for Sodium-Ion Batteries. *ACS Appl. Mater. Interfaces* **2014**, *6*, 9111−9117.

424. Kundu, D.; Tripathi, R.; Popov, G.; Makahnouk, W. R. M.; Nazar, L. F. Synthesis, Structure, and Na-Ion Migration in $Na_4NiP_2O_7F_2$: A Prospective High Voltage Positive Electrode Material for the Na-Ion Battery. *Chem. Mater*. 2015, 27, 885−891.

425. Gao, H.; Li, Y.; Park, K.; Goodenough, J. B. Sodium Extraction from NASICON-Structured $Na_3MnTi(PO_4)_3$ through Mn(III)/Mn(II) and Mn(IV)/Mn(III) Redox Couples. *Chem. Mater*. 2016, 28, 6553-6559.

426. Chen, M.; Chen, L.; Liu, Q.; Zhang, B.; Hu, Y.; Gu, Q.; Wang, L.-Z.; Guo, X.; Chou, S.-L.; Dou, S.-X. Carbon-Coated $Na_{3.32}Fe_{2.34}(P_2O_7)_2$ Cathode Material for High-Rate and Long-Life Sodium-Ion Batteries. *Adv. Mater.* **2017**, *29*, 1605535.

427. Belkhiria, M. S.; Laaribi, S.; Amara, A. B. H.; Amara, M. B. Structure of $Na_3Fe(PO_4)_2$ from Powder X-ray Data. *Ann. Chim. Sci. Mat*. **1998**, *23*, 117-120.

428. Morozov, V. A.; Lazoryak, B. I.; Malakho, A. P.; Pokholok, K. V.; Polyakov, S. N.; Terekhina, T. P. The Glaserite-like Structure of Double Sodium and Iron Phosphate $Na_3Fe(PO_4)_2$. *J. Solid State Chem.* **2001**, *160*, 377-381.

429. Livitska, O.; Strutynska, N.; Zatovsky, I.; Slobodyanik, N.; Odinets, E. Nitrate (Chloride) Melts as Media for Crystal growth of complex Phosphates of Alkali and Trivalent Metals. *Journal of Crystal Growth* **2016**, *434* 30–35.

430. Goodenough, J. B.; Park, K. S. The Li-Ion Rechargeable Battery: A Perspective. *J. Am. Chem. Soc.* **2013**, *135*, 1167−1176.

431. Armand, M.; Tarascon, J. M. Building Better Batteries. *Nature* **2008**, *451*, 652-657.

432. Li, Hong.; Wang, Z.; Chen, L.; Huang, X. Research on Advanced Materials for Li-ion Batteries. *Adv. Mater.* **2009,** *21*, 4593-4607.

433. Owen, J. R. Rechargeable Lithium Batteries. *Chem. Soc. Rev.* **1997**, *26*, 259-267.

434. Braun, P. V.; Cho, J.; Pikul, J. H.; King, W. P.; Zhang, H. High Power Rechargeable Batteries. *Curr. Opin. Solid State Mat. Sci.*, **2012**, *16*, 186-198.

435. Thackeray, M. M.; Wolverton, C.; Issacs, E. D. Electric Energy Storage for Transportations – Approaching the Limits of, and Going Beyond, Li-Ion Batteries. *Energy Environ. Sci*., **2012**, *5*, 7854–7863

436. Pearson, K.; Sethuraman, V. A.; Hardwick, L. J.; Hinuma, Y.; Meng, Y. S.; Ven, A.; Srinivasan, V.; Kostecki, R.; Ceder, G. Lithium Diffusion in Graphitic Carbon. *J. Phys. Chem. Lett.* **2010**, *1*, 1176–1180.

437. Erickson, E. M.; Ghanty, C.; Aurbach, D. New Horizons for Conventional Lithium Ion Battery Technology. *J. Phys. Chem. Lett.* **2014**, *5*, 3313−3324.

438. Ohzuku, T.; Ueda, A.; Yamamoto, N. Zero Strain Insertion Material of $Li[Li_{1/3}Ti_{5/3}]O_4$ for Rechargeable Lithium Cells. *J. Electrochem. Soc.* **1995**, *142*, 1431-1435.

439. Wang, G. J.; Gao, J.; Fu, L. J.; Zhao, N. H.; Wu, Y. P.; Takamura, T. Preparation and Characteristic of Carbon-Coated $Li_4Ti_5O_{12}$ Anode Material. *Journal of Power Sources* **2007**, *174*, 1109–1112.

440. Kim, W.; Jeong, Y. U.; Lee, Y. J.; Kim, Y. J.; Song, J. H. Synthesis and Lithium Intercalation Properties of Li_3VO_4 as a New Anode Material for Secondary Lithium Batteries. *Journal of Power Sources* **2013**, *244*, 557-560.

441. Peled, E.; Menachem, C.; Bar-Tow, D.; Melman, A. Improved Graphite Anode for Lithium-Ion Batteries. *J. Electrochem. Soc.* **1996,** *143*, L4-L6.

442. Gaur, K.; Pathak, A. J.; Lal, H. B. Electrochemical Performance and Thermal Stability of $Li_{1.18}Co_{0.15}Ni_{0.15}Mn_{0.52}O_2$ Surface Coated with the Ionic Conductor Li_3VO_4. *J. Mat. Sci.* **1988**, *23*, 4257-4262.

443. Shi, Y.; Zhang, Y.; Liu, L.; Zhang, Z.; Wang, J.; Gao, J.; Chou, S,; Abruña, H. D, Liu, H.; Wexler, D.; Wang, J.; Wu, Y. Rapid Hydrothermal Synthesis of Li_3VO_4 with Different Favored Facets. *J Solid State Electrochem*. **2017**, *21*, 2547–2553.

444. Liang, Z.; Zhao, Y.; Ouyang, L.; Dong, Y.; Kuang, Q.; Lin, X.; Liu, X.; Yan, D. Synthesis of Carbon-Coated Li_3VO_4 and its High Electrochemical Performance as Anode Material for Lithium-ion Batteries. *Journal of Power Sources* **2014**, *252*, 244-247.

445. Jian, Z.; Zheng, M.; Liang, Y.; Zhang, X.; Gheytani, S.; Lan, Y.; Shi, Y.; Yao, Y. Li_3VO_4 anchored graphene nanosheets for long-life and high-rate lithium-ion batteries. *Chem. Commun.*, **2015**, *51*, 229—231.

446. Tartaj, P.; Amarilla J. M.; Vazquez-Santos, M. B. Aerosol-Assisted Synthesis of Colloidal Aggregates with Different Morphology: Toward the Electrochemical Optimization of Li_3VO_4 Battery Anodes Using Scalable Routes. *Chem. Mater*. ***2016***, *28*, 986−993.

447. Zhou, L.; Shen, S.; Peng, X.; Wu, L.; Wang, Q.; Shen, C.; Tu, T.; Huang, L.; Li, J.; Sun, S. New Insights into the Structure Changes and Interface Properties of Li_3VO_4 Anode for Lithium-Ion Batteries during the Initial Cycle by in-Situ Techniques. *ACS Appl. Mater. Interfaces* **2016**, *8*, 23739−23745.

448. Zhang, C.; Liu, C.; Nan, X.; Song, H.; Liu, Y.; Zhang, C.; Cao, G. Hollow−Cuboid Li_3VO_4/C as High-Performance Anodes for Lithium-Ion Batteries. *ACS Appl. Mater. Interfaces* **2016**, *8*, 680−688.

449. Shannon, R. D.; Calvo, C. Refinement of the Crystal Structure of Low Temperature Li_3VO_4 and Analysis of Mean Bond Lengths in Phosphates, Arsenates, and Vanadates. J. Solid State Chem. **1973**, *6*, 538-549.

450. Sing, K. S. W.; Everett, D. H.; Haul, R. A. W.; Moscou, L.; Pierotti, R. A.; Rouquerol, J.; Siemieniewska, T. Reporting Physisorption Data for Gas/Solid Systems *Pure & Appl. Chem.* **1985**, *57*, 603-619.

451. Zhang, C.; Liu, C.; Nan, X.; Song, H.; Liu, Y.; Zhang, C.; Cao, G. Hollow−Cuboid Li_3VO_4/C as High-Performance Anodes for Lithium- Ion Batteries. ACS Appl. Mater. Interfaces **2016**, *8*, 680−688.

452. Choi, N.; Kim, J.; Yin, R.; Kim, S. Electrochemical Properties of Lithium Vanadium Oxide as an Anode Material for Lithium-Ion Battery. *Materials Chemistry and Physics* **2009**, *116*, 603-606.

453. Iwama, E.; Kawabata, N.; Nishio, N.; Kisu, K.; Miyamota, J.; Naoi, W.; Rozier, P.; Simon, P.; Naoi, K. Enhanced Electrochemical Performance of Ultracentrifugation-Derived nc Li_3VO_4/MWCNT Composites for Hybrid Supercapacitors. *ACS Nano* **2016**, *10*, 5398−5404.

454. Yang, Y.; LI, J.; Chen, D.; Zhao, J. Spray Drying-Assisted Synthesis of Li_3VO_4/C/CNTs Composites for High-Performance Lithium Ion Battery Anodes. *J. Electrochem. Soc.* **2017**, *164*, A6001-A6006.

455. Liao, C.; Wen, Y.; Shan, B.; Zhai, T.; Li, H. Probing the Capacity Loss of Li_3VO_4 Anode upon Li Insertion and Extraction. *Journal of Power Sources* **2017,** *348*, 48-56.

456. Pasquier, A. D.; Plitz, I.; Menocal, S.; Amatucci, G. A Comparative Study of Li-Ion Battery, Supercapacitor and Nonaqueous Asymmetric Hybrid Devices for Automotive Applications. *Journal of Power Sources* **2003**, *115*, 171-178.

457. Scrosati, B.; Garche, J. Lithium Batteries: Status, Prospects and Future. *Journal of Power Sources* **2010**, *195*, 2419-2430.

458. Marom, R.; Amalraj, S. F.; Leifer, N.; Jacob, D.; Aurbach, D. A Review of Advanced and Practical Lithium Battery Materials. *J. Mater. Chem.* **2011**, *21*, 9938-9954.

459. Kim, T. H.; Park, J. S.; Chang, S. K.; Choi, S.; Ryu, J. H.; Song, H. K. The Current Move of Lithum Ion Batteries towards the Next Phase. *Adv. Energy Mater.* **2012**, *2*, 860-872.

460. Omar, N.; Daowd, M.; Bossche, P. V.; Omar, H.; Smekens, J.; Coosemens, T.; Mierlo, J. V. Rechargeable Energy Storage Systems for Plug-in Hybrid Electric Vehicles—Assessment of Electrical Characteristics. *Energies* **2012**, *5*, 2952-2988.

461. Manthiram, A. Materials Challenges and Opportunities of Lithium Ion Batteries. *J. Phys. Chem. Lett.* **2011**, *2*, 176-184.

462. Cresc,e A. V.; Xu, K. Electrolyte Additive In Support of 5 V Li Ion Chemistry. *J. Electrochem. Soc.* **2011**, *158* (3), A337-A342.

463. Lee, K. T.; Jeong, S.; Cho, J. Roles of Surface Chemistry on Safety and Electrochemistry in Lithium Ion Batteries. *Chem. Res.* **2013**, *46*, 1161-1170.

464. Park, H.; Shin, D.; Paik, U.; Song, T. Dielectric Polarization of a High-Energy Density Graphite Anode and Its Physicochemical Effect on Li-Ion Batteries. *Ind. Eng. Chem. Res.* **2017**, *56*, 13776-13782.

465. Zhu, G. N.; Wang, Y. G.; Xia, Y. Y. Ti-Based Compounds as Anode Materials for Li-Ion Batteries. *Energy Environ. Sci.* **2012**, *5*, 6652-6667.

466. Li, Q.; Wei, Q.; Sheng, J.; Yan, M.; Zhou, L,; Luo, W.; Sun, R.; Mai, L. Mesoporous Li_3VO_4/C Submicron-Ellipsoids Supported on Reduced Graphene Oxide as Practical Anode for High- Power Lithium-Ion Batteries. *Adv. Sci.* **2015**, *2*, 1500284.

467. Shao, G.; Gan, L.; Ma, Y.; Li, H.; Zhai, T. Enhancing The Performance of Li_3VO_4 by Combining Nanotechnology and Surface Carbon Coating for Lithium Ion Batteries. *J. Mater. Chem. A* **2015**, *3*, 11253-11260.

468. Xu, X.; Niu, F.; Chu, C.; Wang, C.; Yang, J.; Qian, Y. Hierarchically Porous Li_3VO_4/C Nanocomposite as an Advanced Anode Material for High-Performance Lithium-Ion Capacitors. *Journal of Power Sources* **2018**, *384*, 240-248.

469. Liang, Z.; Lin, Z.; Zhao, Y.; Dong, Y.; Kuang, Q.; Lin, X.; Liu, X.; Yan, D. New Understanding of Li3VO4/C as Potential Anode for Li-ion Batteries: Preparation, Structure Characterization and Lithium Insertion Mechanism. *Journal of Power Sources*, **2015**, *274*, 345-354.